UNIVERSITY OF OKLAHOMA

GRADUATE COLLEGE

$SCCO_2$-FLUIDS-ROCK INTERACTIONS IN NANOPOROUS MEDIA: APPLICATIONS IN ENHANCED OIL RECOVERY AND CARBON GEOSTORAGE

A DISSERTATION

SUBMITTED TO THE GRADUATE FACULTY

in partial fulfillment of the requirements for the

Degree of

DOCTOR OF PHILOSOPHY

By

FELIPE A CRUZ
Norman, Oklahoma
2023

$SCCO_2$-FLUIDS-ROCK INTERACTIONS IN NANOPOROUS MEDIA: APPLICATIONS IN ENHANCED OIL RECOVERY AND CARBON GEOSTORAGE

A DISSERTATION APPROVED FOR THE
MEWBOURNE SCHOOL OF PETROLEUM AND GEOLOGICAL ENGINEERING

BY THE COMMITTEE CONSISTING OF

Dr. Chandra S. Rai, Chair

Dr. Heather Bedle

Dr. Benjamin (Bor-Jier) Shiau

Dr. Deepak Devegowda

Dr. Son T. Dang

© Copyright by FELIPE A CRUZ 2023
All Rights Reserved.

Acknowledgments

I would like to express my heartfelt gratitude to the outstanding professors who have shared their expertise and passion to teach the natural sciences in the subsurface. In particular, I would like to extend my sincere thanks to my mentors at the Integrated Core Characterization Center (IC3), Dr. Chandra Rai, Dr. Carl Sondergeld, Dr. Deepak Devegowda, Dr. Son Dang, Dr. Mark Curtis, and Dr. Ali Tinni, for their unwavering guidance, support, and encouragement throughout my research.

I am also deeply grateful to my lab colleagues and friends in Norman, whose camaraderie and shared experiences have made this journey memorable. Their collaboration, feedback, and support have been crucial in shaping my research and personal growth.

Lastly, I am indebted to my family for their unconditional love, patience, and support throughout my academic pursuits. Their encouragement have been the driving force behind my achievements. *Muito obrigado*.

Table of Contents

List of Tables

List of Figures

Abstract

A global effort to reduce atmospheric CO_2 levels and mitigate global warming is ongoing. Carbon capture and storage (CCS) and enhanced oil recovery (EOR) are pivotal technologies for achieving net-zero emissions, further incentivized by U.S. tax benefits. Both practices involve injecting CO_2 into subsurface geological formations, where it transitions into a dense supercritical fluid phase ($scCO_2$). Understanding interactions between $scCO_2$, native fluids, and the subsurface formation, is crucial for optimizing EOR and managing risks in carbon geostorage (CGS). These interactions are particularly complex in nanoporous systems, such as confining zones in CGS, and during cyclic-gas injection (Huff and Puff, or HnP) in unconventional liquid-rich shale reservoirs (ULR).

This dissertation comprises two studies examining the impact of these interactions on HnP-EOR in ULR and the long-term integrity of confining zones in CGS. The first study involves over 20 HnP-EOR tests on preserved ULR samples, coupled with analytical tools to evaluate key parameters affecting crude oil and brine mobilization. Additionally, a shale oil reservoir model was developed to simulate HnP-EOR in ULR and assess net carbon efficiency. In the second study, $scCO_2$ treatments were conducted for 21 days in five confining zones and one storage zone sample under elevated temperature and pressure (150 °F and 3000 psi). A strategy was devised to monitor geochemical reactivity at the surface level down to the micrometer depth of invasion. Before and after treatment, pore size distributions and effective matrix diffusivities were determined. $ScCO_2$-brine-rock wettability and breakthrough tests were conducted under subsurface conditions. Following integration of these two studies with critical literature review, valuable insights into fluid recovery during HnP-EOR in ULR and the integrity of confining zones in CGS are provided.

Chapter 1. Introduction

Carbon dioxide (CO_2) is a heat-trapping gas, or greenhouse gas (GHG), that has primarily contributed to accelerating global warming (NASA 2023). Since the beginning of the 18th century, human activities have raised the level of CO_2 in the atmosphere by 50%. The historical Paris Agreement of 2015 set long-term goals to reduce GHG emissions to limit temperature increase by 2 °C (pushing to 1.5 °C) above pre-industrial levels within this century (UN 2023). To achieve net-zero emissions, carbon capture and storage (CCS) with CO_2 enhanced oil recovery (EOR) are required as long as fossil carbon consumption persists (Davis et al. 2018). CCS is the class of technologies that remove CO_2 from the atmosphere and permanently store it in sinks, such as oceans, soils, and geologic formations. CO_2-EOR refers to the injection of CO_2 in conventional/unconventional oil-bearing formations to mobilize liquid hydrocarbon and provide additional recovery beyond primary production (Farajzadeh et al. 2020).

The injection of CO_2 in geological formations for EOR was first commercially demonstrated in 1972 in Spurry County, Texas, (NETL 2010). Since then, CO_2-EOR projects have been implemented utilizing different injection schemes, including continuous flooding, cyclically, alternating with water (WAG), and others. While continuous CO_2 injection is typically associated with pumping large volumes of CO_2 in conventional reservoirs, the low injectivity of unconventional reservoirs suggests a higher cost-benefit relationship by cyclic injection from a single well. The latter is commonly referred to as Huff-and-Puff (HnP) EOR, where the well is shut-in after injection, allowing the solvent to diffuse into the tight matrix and contact the reservoir oil (soak phase), and then put back on production. In the last decade, CO_2 HnP EOR has been frequently applied to improve the low primary production of unconventional liquid-rich shale

reservoirs (ULR). Such reservoirs are widely abundant throughout the world and the estimated reserves for ULR are in the order of 350 billion barrels of oil and 7300 trillion cubic feet of gas (EIA 2013). Overall, primary production from ULR typically shows a peak in the first few months and is followed by a sharp decline (**Figure 1(a)**), ultimately leading to recovery factors of less than 10% (EIA 2020). In 2016, EOG Resources announced additional recovery factors after associated natural gas HnP in the Eagle Ford play of 30-70% beyond primary production (**Figure 1(b)**) (JPT 2017). Additionally, CO_2-EOR has been incentivized due to revisions in the U.S. Internal Revenue Code (Section 45Q), which benefits companies with tax credits of $60 and $85 per metric ton of CO_2 geologically sequestered with and without EOR, respectively (IEA 2023).

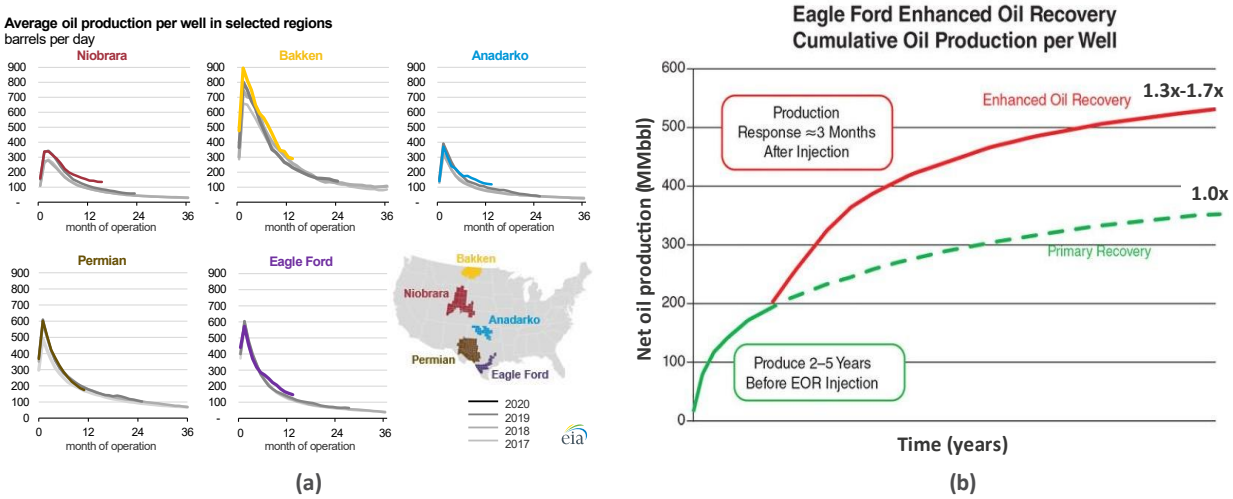

Figure 1. (a) Average oil production per well in the Niobrara, Bakken, Anadarko, Permian, and Eagle Ford shale regions. A steep peak in the first few months is observed followed by a sharp decline (EIA 2020). (b) Cumulative oil production per well in the Eagle Ford projected during primary production (green) and estimated after gas-injection EOR (red) (JPT 2017).

The mechanisms behind the additional production of oil during CO_2-HnP in ULR are tied to CO_2-oil-rock interactions in the nanoporous matrix and attributed to hydrocarbon vaporization, oil

swelling, viscosity reduction, pressure support, interfacial tension reduction, and others (Hoffman and Kovscek 2004, Li et al. 2013, Hemmati-Sarapardeh et al. 2014, Seyyedi et al. 2015, Odiachi et al. 2021). The relative contribution of each HnP-EOR mechanism in ULR is also associated with the reservoir fluid type (Hoffman and Reichhardt 2020). Hydrocarbon vaporization is the most important for high gas-oil ratio (GOR) crude oil, while oil swelling is the most important in low GOR. Viscosity reduction has small significance becoming important only in low GOR, and pressure support provides low recovery regardless of fluid type. Understanding the interplay between CO_2-oil-rock interactions and recovery mechanisms is key to optimizing operational parameters (e.g. injection pressure and rate, soaking and production times, others) during HnP-EOR in ULR.

The U.S. Department of Energy (DoE) has established criteria to assess subsurface formations for carbon geostorage (CGS) which are based on the storage resource (porosity), injectivity (permeability), integrity (long-term containment), and depth (supercritical-CO_2). Deep saline aquifers, depleted conventional oil and gas reservoirs, unmineable coal seams, organic-rich shales, basalt formations, and salt caverns, are considered potential candidates for CGS (NETL 2023). Deep saline reservoirs are deep porous formations underlying sedimentary basins saturated with brine (Celia et al. 2015). They are often envisioned as the most ideal option for CGS given their abundance, excellent storage capacity and injectivity, and reduced risk of leakage due to depth, but suffers from uncertainties in the long-term stability of CO_2 and lack of existing infrastructure (Luo et al. 2022). Depleted conventional oil and gas reservoirs are another promising option based on the existing infrastructure for oil and gas wells, good storage capacity and injectivity, proven geological containment, and CO_2-EOR capability to offset costs (Dai et al. 2017). However, the

potential for induced seismicity and possible groundwater contamination are challenges that increase the difficulty of obtaining permits and meeting regulatory requirements (Newmark et al. 2010, Berentsen and de Pater 2022).

Unmineable coal seams have been proposed for CGS due to the strong affinity of CO_2 to the coal matrix (sorption), permanently storing CO_2, and displacing methane (CH_4) from coal beds as an enhanced gas recovery method (EGR). (Bachu 2007). However, the permeability generated by the set of fracture networks in the coal matrix (cleats) is highly sensitive to stress, therefore it decreases significantly with depth, reducing injectivity. Organic-rich shales are widely available and can also benefit from the adsorption of CO_2 and desorption of hydrocarbon species on organic matter (Li et al. 2019a, Zhao et al. 2023) and are good candidates for EOR/EGR (Fatah et al. 2020). However, their extremely low permeability and possible geochemical reactivity with CO_2 influence the feasibility of CGS implementation (Goodman et al. 2011). Basalt formations are excellent candidates for CGS given the rapid carbon mineralization when CO_2 reacts with silicate minerals in the basalt layers to form stable carbonates (Raza et al. 2022). However, large-scale storage of CO_2 is limited by their geographical distribution. Salt caverns have a large storage capacity and proven technology for underground storage of natural gas with a low risk of leakage (Pajonpai et al. 2022). Nonetheless, the high costs associated with creating infrastructure and their limited geographical distribution affect large-scale deployment.

For each geological formation, the mechanisms that trap CO_2 in the subsurface can be distinct based on their relative trapping contribution and time scale (Zhang and Song 2014). **Figure 2** illustrates the different types of mechanisms, classified into physicochemical, chemical, and physical trapping (Al Hameli et al. 2022). In physical trapping, the supercritical CO_2 ($scCO_2$)

plume is contained by a physical mechanism, such as structural and/or stratigraphic geological feature (static trapping), residual trapping of the $scCO_2$ plume due to brine imbibition, heterogeneity in the petrophysical properties of the storage reservoir (local capillary trapping), and weak physisorption in small pores (sorptive trapping) (Jiang 2011). Chemical trapping consists of geochemical interactions between $scCO_2$ and reservoir fluids/rock, either by dissolving in formation brine or reservoir oil (solubility trapping), dissolving rock minerals generating carbon-bearing ionic species (ionic trapping), chemisorption onto the organic matter of coals and shales (adsorption), or forming stable carbonate minerals by precipitation (mineral trapping) (Ajayi et al. 2019). Physicochemical trapping (i.e. hydrodynamic trapping) is the bridge between the two main classes of mechanisms, whereby the non-wet $scCO_2$ phase is contained hydrodynamically by capillary forces in the caprock (Bachu et al. 2007). Static (structural/stratigraphic) and hydrodynamic are the primary trapping mechanisms in deep saline aquifers and depleted conventional O&G reservoirs, followed by residual (capillary) and solubility (dissolution) as secondary trapping mechanisms (Al Hameli et al. 2022).

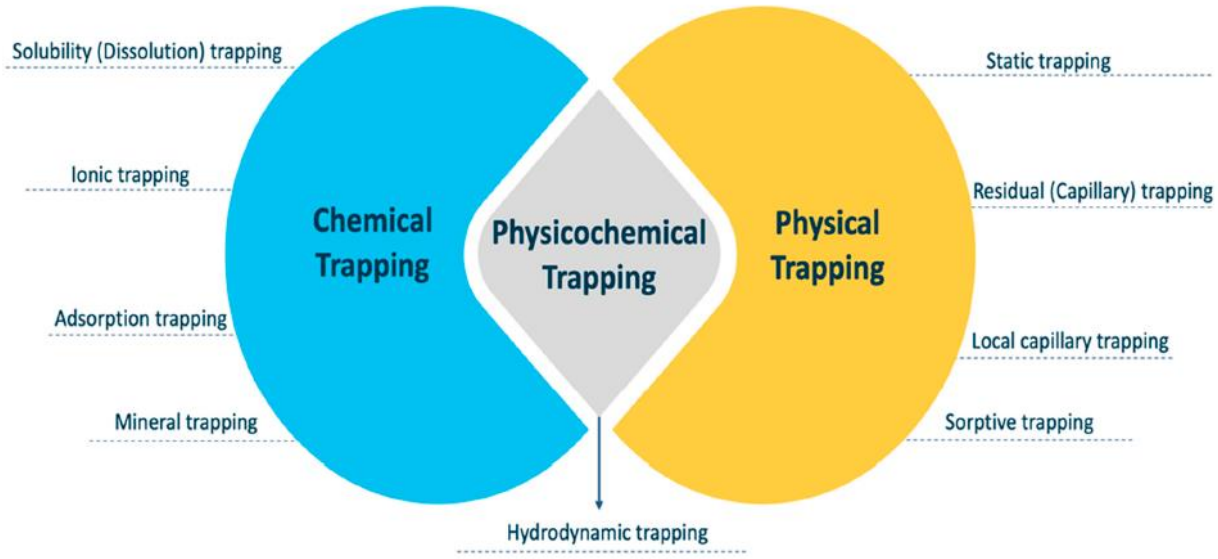

Figure 2. The three classes of trapping mechanisms (physical, chemical, and physiochemical) and their sub-classes during carbon geostorage (Al Hameli et al. 2022).

The trapping mechanisms influence the storage capacity of $scCO_2$ in geological formations (Leung et al. 2014). The US DoE method to estimate storage capacity for CCS projects (Goodman et al. 2011) is derived from the volumetric approach established by the oil and gas industry to estimate the original oil/gas-in-place (Calhoun 1960). A detailed formulation of CO_2 mass at surface conditions that can be stored in saline aquifers is shown in **Equation 1.1**:

$$G_{CO_2} = G_{free} + G_{sol} = AH\emptyset\left\{\frac{43560\times62.42\times(1-S_{wir})\rho_{CO_2}}{B_{g,CO_2}\times2204.62} + \frac{7758\times S_{wir}\times R_{Sw}}{B_w\times6.29}\right\}\times E_{saline} \qquad (1.1)$$

where G_{CO_2} is the mass of CO_2 stored at surface conditions [tonnes], while G_{free} and G_{sol} indicates the contributions of stored $scCO_2$ as a free-phase and dissolved in irreducible brine, respectively. The reservoir volume is represented by the area A [acres], gross thickness H [ft], and total porosity $\emptyset$. For the CO_2 stored as free-phase, 43560, 62.42, and 2204.62, represent conversion factors from acres-ft to ft^3, g/cc to lbs/ft^3, and lb to tonnes, respectively. The storage pore volume for the free-

phase is indicated by $(1 - S_{wir})$, ρ_{CO_2} is the average density of CO_2 at storage conditions [g/cc], and B_{g,CO_2} is the CO_2 formation volume factor to convert volumes from storage to surface conditions [bbl/STB]. For CO_2 dissolved in formation brine, 7758 and 6.29 are conversion factors from acre-ft to barrels (bbl), and bbl to tonnes, respectively. The solution gas-brine ratio (R_{Sw}) indicates the amount of CO_2 that can be dissolved in the brine [scf/bbl], while B_w stands for the brine formation volume factor to convert to surface conditions [bbl/STB]. Lastly, E_{saline} represents the efficiency factor in deep saline storage, which can be further dismembered into a product of efficiency components (**Equation 1.2**) (Bachu et al. 2007):

$$E_{CO_2} = E_{An/At} E_{hn/hg} E_{\emptyset e/\emptyset total} E_A E_L E_g E_d \tag{1.2}$$

where $E_{An/At}$ and $E_{hn/hg}$ are the net-to-total ratios of area and thickness, respectively. $E_{\emptyset e/\emptyset total}$ is the effective porosity. E_A, E_L, E_g are the areal, vertical (layering), and gravitational displacement efficiencies, respectively. They represent the macroscopic displacement efficiency at a reservoir scale. E_A and E_L are influenced by the geologic setting (fault, dipping, heterogeneity, layering). E_g is affected by the density and mobility (relative permeability/viscosity) difference between CO_2 and formation water, since the buoyant $scCO_2$ plume rises within the geologic unit. Lastly, E_d is the microscopic displacement efficiency at the pore scale. It reflects factors such as pore size distribution, wettability, and interfacial tension between fluids (Lake 1989).

The largest uncertainty in the calculation of the $scCO_2$ storage mass in deep saline aquifers is the estimation of the storage efficiency factor (E_{saline}) (Szulczewski and Juanes 2009, Goodman et al. 2011, Thibeau et al. 2014, Bachu 2015, Celia et al. 2015, Wei et al. 2022). Bachu (2015) explained that the variations in E_{saline} (1-10%, sometimes 20%) depend on numerous factors, such

as the storage aquifer characteristics (pressure, temperature, salinity, relative permeabilities, lithology, porosity, heterogeneity, anisotropy, areal extent, and thickness), characteristics of confinement (mainly permeability and capillary entry pressure), and characteristics of the operation (injection rate, injection time, number of wells, well orientation and spacing, and injection strategy).

The storage mass of $scCO_2$ for other geological formations (depleted oil and gas reservoirs, unmineable coal seams, organic-rich shales, basalt formations, salt caverns) are analogous forms to **Equation 1.1**, but incorporate terms related to the specific trapping mechanism of that formation. For example, the storage volume of depleted oil and gas reservoirs includes an efficiency factor that is similar to the CO_2-EOR recovery factor (RF), which can vary widely depending on formation characteristics, operational parameters, thermodynamic conditions, and many other factors (Lake et al. 2019).

In addition to storage capacity, long-term integrity is a key factor during geological CO_2 storage (Busch et al. 2010). The three main concerns related to integrity are (1) wellbore damage and corrosion of pipes and cement (Smith et al. 2011, Lesti et al. 2013, Bai et al. 2016, Pfennig et al. 2021), (2) seepage along pre-existing or reactivated faults and fracture networks (Mortezaei and Vahedifard 2015, Klokov et al. 2018), (3) and leakage associated with capillary breakthrough and molecular diffusion through the brine-saturated confining zone (Fleury et al. 2009, Rezaeyan et al. 2015, Espinoza and Santamarina 2017, Kivi et al. 2021). Interactions between CO_2-fluids-rock are present in all of the above and particularly relevant in the latter. The capillary displacement

pressure in the confining zone can be obtained by the classical Young-Laplace equation (**Equation 1.3**) (Cai et al. 2021, Behroozi 2022):

$$P_c = P_{scCO_2} - P_{brine} = \frac{2\times145\times\gamma\cos\theta}{r} \quad (1.3)$$

where the pressure difference between the non-wetting $scCO_2$ phase (P_{scCO_2}) and the wetting brine phase (P_{brine}) is the capillary pressure (P_c) in psi, γ is the interfacial tension between $scCO_2$ and brine [mN/m], θ is the contact angle between the two fluids and the rock, and r is the connected pore throat radius for capillary breakthrough in nanometers (Chiquet et al. 2007b). Confining zones typically required capillary entry pressures ranging between 870 psi and 5800 psi in order to be considered good seals for CGS (EPA 2013). After the $scCO_2$ pressure in the reservoir exceeds the entry pressure in the caprock, upward fluid migration takes place, and the maximum $scCO_2$ height that can be stored in the caprock (h) is obtained by **Equation 1.4**:

$$h = \frac{2\times145\times\gamma\cos\theta}{0.433\times\Delta\rho r} \quad (1.4)$$

where h is obtained in ft, $\Delta\rho$ is the density difference between brine and $scCO_2$ in the caprock [g/cc], and 0.433 is the conversion factor from g/cc to psi/ft. **Equation 1.4** shows that in addition to $scCO_2$-fluids-rock interactions, knowledge of the fluid densities of $scCO_2$-brine systems in the subsurface is essential to determine the capillary seal capability (van der Meer et al. 2009).

Fluid leakage due to molecular transport (diffusion) of CO_2 through the water-filled, nanopores of the confining zone can become significant due to the long-term nature of geostorage (Brosse et al. 2005, Fleury et al. 2009). The diffusive flow of CO_2 through formation brine saturating the nanoporous confining zone may affect the reactive transport and augment the geochemical reactivity of certain mineral species, which can impact chemo-mechanical and petrophysical

properties (Busch et al. 2008, Henkel et al. 2014, Sanguinito et al. 2018, Goodman et al. 2019). Molecular diffusion has also been documented as the dominant transport property during HnP-EOR in tight porous media such as in organic-rich shales (Dang et al. 2023). In porous media, molecular diffusion is limited by the tortuosity (τ), a property that is governed by the interconnectedness of the pore space (**Equation 1.5**) (Odiachi et al. 2022):

$$D_{AB,eff} = \frac{D_{AB}}{\tau} \quad (1.5)$$

where D_{AB} is the diffusion coefficient of molecule A in the AB mixture and $D_{AB,eff}$ is the effective inter-diffusivity in the porous medium. Tortuosity in conventional formations is highly dependent upon porosity and can increase significantly in porosities of less than 10% (Chen et al. 1977). In unconventional nanoporous media (e.g. shales), the dependence of tortuosity with porosity is less obvious, and other factors such as organic content should be considered to correctly estimate the diffusive loss (Odiachi et al. 2022).

The objective of this dissertation is to investigate the factors controlling the $scCO_2$-fluids-rock interactions in nanoporous media that are relevant to EOR and geostorage. Considerations regarding $scCO_2$-oil-rock interactions during HnP-EOR in ULR are discussed in Chapter 2. The experimental methodology to evaluate the impact of these interactions on HnP-EOR in ULR is discussed in Chapter 3. The results pertaining to HnP-EOR in ULR are presented in Chapter 4. Considerations regarding $scCO_2$-brine-rock interactions during carbon geostorage are discussed in Chapter 5. The experimental methodology to evaluate the impact of these interactions on carbon geostorage is discussed in Chapter 6. Results relevant to carbon geostorage are presented in Chapter 7. Lastly, Chapter 8 discusses the results presented and provides a summary of this work with its main conclusions.

Chapter 2. Considerations: HnP-EOR in ULR

Optimization of HnP-EOR in ULR is a multiscale and multivariable problem. It requires the integration of information from molecular simulations in the nanopore-scale, laboratory experiments in the core-scale, and reservoir simulations in the field-scale. In addition to the multiscale nature, the optimization requires coupling several variables pertaining to fluids (solvent and reservoir oil compositions), rock (sample size and state, petrophysical properties), operational conditions (testing configuration, injection pressure and rate, soaking and production times, number of cycles, temperature), and others. A common approach in research is to break down the problem into smaller problems to understand the primary controls on the recovery of oil. This chapter will discuss the impact of individual variables on the recovery and summarize the current state of art of HnP-EOR in ULR from an experimental standpoint.

Numerous experimental studies investigated the factors impacting the oil recovery efficiency during HnP-EOR in ULR (Gamadi et al. 2013, Song and Yang 2013, Gamadi et al. 2014, Wan et al. 2015, Jin et al. 2017a, Jin et al. 2017c, Jin et al. 2017d, Li et al. 2017a, Song and Yang 2017, Yu et al. 2017, Adel et al. 2018, Atan et al. 2018, Li et al. 2018, Dang 2019, Li et al. 2019b, Kumar et al. 2020, Mamoudou 2020, Mamoudou et al. 2020, Min et al. 2020, Sie and Nguyen 2020, Ghanizadeh et al. 2021, Lu et al. 2021, Mamoudou et al. 2021, Odiachi et al. 2021, Song et al. 2021, Tovar et al. 2021, Zeng et al. 2021, Zhu et al. 2021, Chen et al. 2022, Cruz et al. 2022, Shilov et al. 2022, Sondergeld et al. 2022, Dang et al. 2023, Liu et al. 2023, Yao et al. 2023). Specific to CO_2 HnP-EOR, **Table 1** lists the testing conditions and summary of results, including sample parameters, experimental conditions, minimum miscibility pressure (MMP), and oil recovery factors (RF).

Table 1. List of experimental studies which analyzed the performance of CO_2 during HnP-EOR in unconventional liquid-rich shale reservoirs.

Author	Year	Oil Sample	Rock					T	Pinj	MMP*	ST/PT	Oil RF
			Sample	Size (D/L)	State	K (μD)	Φ (%)	[°F]	[psi]	[psi]	hr	%
Gamadi *et al.*	2014	C_{10}-C_{13} Isoalkanes	Mancos Eagle Ford	Plug (1.5/2")	Resaturated	-	5.0 7.7	95	850-3500 3500	-	24 6-48	10-31 24-41 20-71 61-73
Jin *et al.*	2017	Bakken	Middle Bakken Lower Bakken	Plug (0.5/1.5")	As-received	8-103 5	~5 ~4	230	5000	2530	24	>90 ~32
Li *et al.*	2017	Wolfcamp	Wolfcamp	Plug (2/1.5")	Resaturated	0.3-0.5	6-8	104	1200-2400	1620	6/6	~40-70
Adel *et al.*	2018	Wolfcamp	Wolfcamp	Plug (1")	Resaturated	-	-	155	1400-3500	1925	10	1-49
Min *et al.*	2020	Eagle Ford	Eagle Ford	Crushed (7-8mm)	Preserved	-	5	150	2500	1500	1/1	42
Odiachi *et al.*	2021	Eagle Ford	Eagle Ford	Crushed (7-8mm)	Preserved	0.05	10	150	3500	2500	1/1	50
Ghanizadeh *et al.*	2021	Duvernay	Duvernay	Plug (1.5/2")	Resaturated	0.125	2-3	-	1340	1028	1/4	46

Tovar *et al.*	2021	Wolfcamp	Wolfcamp	Plug (1”)	Preserved (resaturated)	-	6-10	165	2500-3500	3700	22	23-40
					As-received (resaturated)	-	7-8		1200-3100	1925	21	10-26
Zeng *et al.*	2021	Kerosene	Mancos	Plug (1.5/1.5”)	Resaturated	-	-	167	2800-5200	2300	24	~39
Zhu *et al.*	2021	C_{12}	Yanchang Shale	Plug (1/2”)	Resaturated	-	10	140	870-2900	2000	40	18-50
Chen *et al.*	2022	Simulated oil	Lucaogou Shale	Plug (1/1”)	Resaturated	20-4000	8-17	-	2175	-	12	38-85
Dang *et al.*	2023	Eagle Ford	Wolfcamp	Plug (1/1”)	Non-preserved	-	11	95	3750-5000	2750	1/1	35-45
			Eagle Ford Duvernay Eagle Ford		Preserved	-	8.5 6 5	95				20-35

**Minimum miscibility pressure (MMP) determined at experimental temperatures. ST = soak time. PT = production time. RF = recovery factor.*

Effect of sample size

In laboratory HnP-EOR in ULR experiments, the choice of sample size has been proven to influence the oil recovery factor (Dang 2019). Core plug sizes (inch scale) are commonly selected as representative samples of the subsurface (Tovar et al. 2021). However, the ultra-low transport properties in nanoporous systems such as ULR impair the recovery mechanisms (Zhu et al. 2021).This increases the experimental time to achieve ultimate oil recovery on plug samples. As observed in the studies shown in **Table 1**, a single experiment on a plug sample requires multiple cycles of injection, soaking, and production on the scale of days to weeks. Given the multivariable aspect of HnP-EOR, a set of experiments with controlling variables on plug samples requires months and up to a year to be completed. A faster approach to achieve ultimate oil recovery and evaluate multiple variables in shorter time-frame is the use of crushed samples of millimeter-sizes (Dang 2019, Mamoudou 2020, Mamoudou et al. 2020, Min et al. 2020, Mamoudou et al. 2021, Odiachi et al. 2021, Cruz et al. 2022). Crushed samples have enhanced specific surface area favoring the mutual diffusion between solvent and crude oil which has been proven to be a major transport mechanism during HnP-EOR in ULR (Dang et al. 2023). However, this approach yields much higher recovery factors than observed at core-scale thus requiring proper upscaling (Akita et al. 2018, Dang 2019).

Effect of fluid saturations

Most ULR exhibit complex microstructure including a wide range in mineralogy and organic content resulting in fractional wettability where inorganic pores can be oil-wet, water-wet or both, while organic pores are assumed to be oil-wet (Mukherjee et al. 2020). Moreover, the nanometer-sized pores of ULR can induce capillary pressure values in excess of 10,000 psi for a gas-water system (Kale et al. 2010, Sondhi 2011, Donnelly et al. 2016). Additional considerations such as

nanoconfinement (Teklu et al. 2014, Barsotti 2019, Shabib-Asl et al. 2020) and molecular sieving (Zhu et al. 2020, Perez and Devegowda 2020) can interfere with the phase behavior and preferential distribution of hydrocarbons in the nanopores. All of these factors have implications to the accessibility of solvent to hydrocarbon molecules during HnP-EOR in ULR.

Prior to experiments, most studies often choose to resaturate the samples with either reservoir crude oil or oils of simpler composition (e.g. dodecane) (**Table 1)**. Although resaturation in crude oil is beneficial to reduce variations in oil saturations among the samples as compared to non-preserved samples, other considerations such as water saturation (Liu et al. 2023) and exposed surface area (Dang et al. 2023) are neglected during resaturation in crude oil. To better represent native fluid saturations and mitigate fluid loss, use of preserved sample is recommended (Tovar et al. 2021). Additionally, separating the water-phase production from total fluid production is critical to accurately determine the hydrocarbon recovery factor and understand the fluid mobilization mechanisms during HnP-EOR in ULR (Cruz et al. 2022).

Effect of confinement

Most unconventional liquid-rich shale reservoirs exhibit some degree of microcracking associated to the undergoing stages of hydrocarbon generation and migration (Vernik 1994). Microcracks and other low-compliancy features (e.g. fractures) exhibit a strong stress-dependence with permeability (Walsh 1981). During primary production of ULR, the depletion in pore pressure increases the effective stress, which can significantly reduce fracture permeability (Li et al. 2021, He et al. 2022) and also matrix permeability (Vishal and Bakshi 2023). Laboratory experiments coupling artificially-fractured core plugs and HnP-EOR in ULR have shown higher solvent injectivity and faster ultimate recovery factors (Ghanizadeh et al. 2021, Zhu et al. 2021). To

demonstrate the effect of stress-dependence on the oil recovery during HnP-EOR, Dang (2019) conducted experiments without and with confinement (1750 psi effective stress) on twin Duvernay Shale core samples, which exhibited extensive microcracking assessed through CT-scanning. A reduction in the ultimate recovery factor from 30% to 5% was observed when confinement was introduced in the system, highlighting the impact of closing microcracks (i.e. reduction in surface area) to the recovery mechanisms during HnP-EOR in ULR.

Effect of miscibility

A key factor in the optimization of HnP-EOR in ULR is the injection pressure which is associated to the minimum miscibility pressure (MMP) required for the solvent and crude oil phases to form a single-phase upon multiple component-exchanging contacts (Ahmed 1994, Zhang et al. 2019b). Increasing the injection pressure to achieve complete miscibility favors the main recovery mechanisms during HnP-EOR in ULR (Hoffman and Reichhardt 2020). However, during field implementation, the injection pressure is often limited by the number of compressors and can lead to scenarios of partial miscibility which impacts the oil recovery efficiency. Additionally, the effect of nanopore confinement and shift in critical properties of fluids in nanopores can lower the effective MMP and impact the recovery forecast during HnP-EOR in ULR (Teklu et al. 2014, Zhang et al. 2017, Zhang et al. 2019a, Shabib-Asl et al. 2020, Sun et al. 2023a).

Different methodologies have been used to experimentally determine the solvent-crude oil MMP, including the slim-tube test (Yellig and Metcalfe 1980), the rising-bubble method (Elsharkawy et al. 1996), and the vanishing interfacial tension (VIT) technique (Hawthorne et al. 2016). The slim-tube test is a traditional method which relies on the ramp-up and plateau trend in the pressure-oil recovery curve, where recovery continuously increase with injection pressure until eventually

flattening out at the MMP. Although commonly employed, the lack of fundamental physicochemical definition of MMP during slim-tube testing in addition to elevated cost and long-time measurement adversely affects this method (Zhang and Gu 2015, Ahmad et al. 2016). The rising-bubble method offers a more efficient means of estimating MMP, yet the determination of MMP through this method relies on the operator's visual interpretation, introducing subjectivity into the process (Elsharkawy et al. 1996). The VIT technique suppress the previous drawbacks and is based on a physicochemical assumption of the MMP: with increasing pressure, the interfacial tension (hence capillary height as shown in **Equation 1.4**) between the two phases reaches zero at the MMP (Ayirala and Rao 2011). The VIT test stands out as a more efficient and cost-effective alternative to the slim-tube test, as well as the most repeatable method (Hawthorne et al. 2016).

Several factors affect the solvent-crude oil MMP including temperature, solvent composition, oil composition, and asphaltene content (Yang and Gu 2008, Georgiadis et al. 2010a, Moradi et al. 2014, Yang et al. 2015, Li et al. 2017b, Bagalkot et al. 2018, Rouhibakhsh et al. 2018, Shang et al. 2018, Zhang et al. 2018, Ameli et al. 2019, Li et al. 2020a, Rezaei et al. 2021, Golkari et al. 2022, Salehi et al. 2022). Increasing temperature has a decreasing effect on the IFT hence lowering the MMP ((Hemmati-Sarapardeh et al. 2014). Regarding solvent composition, methane (CH_4) shows much larger MMP as compared to CO_2 (Jin et al. 2017b). However, HC-gas enrichment by decreasing CH_4 concentration and increasing ethane (C_2H_6) content can significantly lower MMP (Mukherjee 2020, Min et al. 2020). The MMP of a CO_2-CH_4 binary mixture decreases with increasing CO_2 content, whereas it increases with CO_2 content for a CO_2-C_2H_6 mixture (Choubineh et al. 2019). Furthermore, the composition of the oleic phase including the amount of acidic and basic components also influences the MMP (Lashkarbolooki et al. 2018). As a major drawback,

gas injection in oil reservoirs can lead to asphaltene precipitation, increasing the MMP and decreasing the oil recovery (Kazemzadeh et al. 2015, Shen and Sheng 2017, Li et al. 2020b, Qian et al. 2022). Asphaltene precipitation during gas injection occurs mainly due to contrast between the high carbon-to-hydrogen ratio of asphaltenic compounds as compared to the low molecular weight of paraffinic solvents (Ali et al. 2015, Shen and Sheng 2016). Overall, the complex behavior of multicomponent mixtures highlight the importance of determining the solvent-oil MMP during HnP-EOR

As shown in **Table 1**, some studies investigated the role of injection pressure with respect to the CO_2-crude oil MMP on the oil recovery. Gamadi et al. (2014) tested Eagle Ford and Mancos shale cores, observing increased recovery with rising injection pressure, which eventually plateaued. They approximated the CO_2-mineral oil MMP based on the pressure at which recovery plateaued. Li et al. (2017a) worked with low-permeability Wolfcamp shale cores (300-500 nD) saturated with Wolfcamp oil. Increasing injection pressure up to 200 psi above the measured MMP (slim-tube) enhanced the oil recovery. This was attributed to shale cores' ultra-low permeability, creating an additional pressure gradient from the core's external surface to the region where CO_2 and crude oil interact. Differences in permeability and injection flow rates between slim-tube experiments and actual shale core HnP contributed to the additional pressure drop. Adel et al. (2018) and Tovar et al. (2021) investigated Wolfcamp shale cores from various wells, determining CO_2-crude oil MMPs via slim-tube technique. They reported significantly increased oil recoveries with rising injection pressures, regardless of the MMP. CT-scanning assessed oil and water density changes over time and space, linking increased recovery beyond the MMP to a slow-kinetics, peripheral

vaporization/condensation mechanism at the interface of low-transport shale matrix and high-transport hydraulic fractures.

To minimize energy waste and enhance the oil recovery, the cyclic reinjection of associated produced natural gas (HC-gas) has also been frequently explored (Dang 2019, Kumar et al. 2020, Mamoudou 2020, Min et al. 2020, Sie and Nguyen 2020, Shilov et al. 2022). To understand the role of injection pressure and MMP during HC-gas HnP-EOR in ULR, Dang (2019) conducted experiments using a 72:28 CH_4/C_2H_6 gas mixture on preserved crushed Eagle Ford Shale samples (mm-sized) without confinement. MMPs between HC-gas and Eagle Ford oil were measured via the VIT technique, while total fluid recoveries were measured using NMR T_2. They reported low recoveries below the MMP (<10%), increasing to 25% at the MMP, with no gain at 1000 psi above the MMP. Kumar et al. (2020) performed produced and enriched gas HnP on varying permeability shale samples. They reported a continuous recovery increase beyond the MMP for both gases. Additionaly, enriching 40% of C_2-C_4 in injected gas did not outperform produced gas, even though the enriched gas's MMP was 1000 psi below the produced gas's MMP.

Effect of solvent composition

Based on the differences in MMP between different solvent and crude oil, it is understood that each solvent has a distinct effect on hydrocarbons recovery. To illustrate this effect, the cumulative oil recoveries using different solvents reported by Jin et al. (2017a) and Dang (2019) are shown as a function of time (**Figure 3(a)**) and injection cycles (**Figure 3(b)**), respectively. In **Figure 3(a)**, five tests were conducted on as-received (S_{oil} ~40-60%), core plug samples from the Middle Bakken (~8-100 μD) at 230 °F and injection pressures of 5000 psi, which were larger than the measured MMPs for each solvent apart from N_2 (MMP~15,000 psi). In their study, the following

rank in injection performance was reported: C_2H_6 > CO_2 > 85/15 CH_4/C_2H_6 > CH_4 >> N_2, illustrating the importance of gas-oil miscibility on the recovery. In **Figure 3(b)**, five experiments were performed with cycles of fixed production/soaking times (1/1 hr) on preserved, crushed-sized (7-8 mm) samples from the Eagle Ford at 150 °F, and injection pressures of 1000 psi larger than each solvent-Eagle Ford oil MMP. Similarly to **Figure 3(a)**, the following performances were reported: C_2H_6 > CO_2 > 72/28 CH_4/C_2H_6 ≳ 76/13/11 CH_4/C_2H_6/ C_3H_8 (field gas) > 95/5 CH_4/C_2H_6. These studies indicate the injection of CO_2 recovers more oil as compared to reinjection of associated natural gas (predominantly CH_4-rich) during HnP-EOR in ULR.

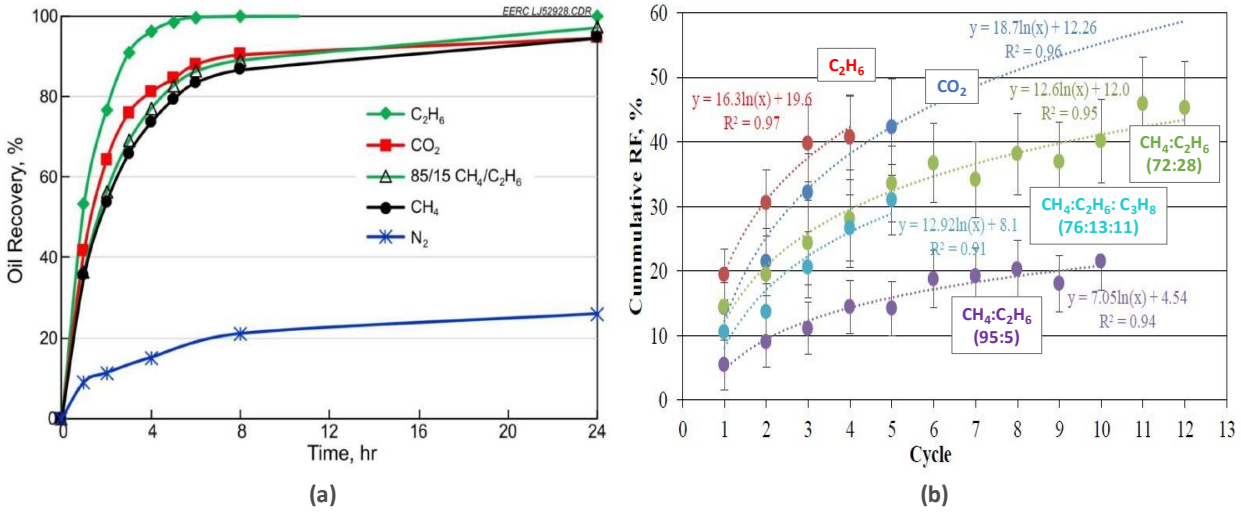

Figure 3. The effect of solvent composition on the oil recovery as function of (a) time and (b) injection cycle. Testing conditions: (a) as-received (S_{oil}~40-60%) core plug samples from Middle Bakken (~8-100 µD) at 230 °F and injection pressure of 5000 psi which is larger than the MMP for the solvents used except N_2 (MMP~ 15,000 psi). Ethane (C_2H_6) shows the best performance, followed by CO_2, methane/ethane mixture (81/15 CH_4/C_2H_6), and methane (CH_4). N_2 exhibits poor performance. (b) preserved crushed-size (7-8 mm) samples from Eagle Ford at 150 °F and injection pressure 1000 psi larger than each solvent-Eagle Ford oil MMP. Similar results as shown in (a), where the larger oil recovery is observed for ethane (C_2H_6), followed by CO_2. The performance of HC-gas mixtures decreases with increasing methane (CH_4) content (after Jin et al. (2017a) and Dang (2019)).

Effect of soaking and production times

The effect of soaking and production times as well as number of cycles on the ultimate oil recovery during HnP-EOR in ULR has also been investigated. Gamadi et al. (2014) noted that longer soaking times, especially above the MMP, led to higher oil recoveries. Additionally, they observed that conducting multiple short soaking cycles outperformed a strategy involving only a few long soaking cycles. Li et al. (2017a) conducted experiments that revealed an increase in oil recovery beyond the MMP when the soaking time was extended from 3 to 6 hours. However, they found that further extending the soak to 9 hours did not yield additional improvements in the ultimate recovery factor. Dang (2019) analyzed preserved crushed samples from the Eagle Ford at injection pressures above the MMP, varying soaking times (1, 3, and 6 hours) with a fixed 1-hour production time. Extending soaking times increased recovery on a cycle-by-cycle basis, especially in the early cycles. However, when analyzing recoveries in terms of residence time (combining soaking and production times), all recovery curves for varying soaking times converged into a single trend. This indicated the preference for shorter soaking times, optimizing gas compressor unit sharing among multiple wells on the same pad. Extending the previous work by Dang (2019), Mamoudou et al. (2020) used preserved plug samples from the Eagle Ford and molecular simulations. Their results substantiated the hypothesis that extended soaking durations did not yield incremental improvements in recovery when compared to shorter soaking periods. Molecular simulations conducted in their study highlighted that the heavier fractions of hydrocarbons remained adsorbed within the shale matrix and were not effectively mobilized with prolonged soaking. These observations were related to the limited solvent penetration depth into the shale matrix, a conclusion in agreement with experimental observations reported by Dang et al. (2019).

Effect of oil composition

As indicated by simulations, the relative contribution of each recovery mechanism during HnP-EOR in ULR is linked to the composition of the oleic phase (Hoffman and Reichhardt 2020). MMP measurements, conducted using the VIT technique with a hydrocarbon gas mixture (72:28 CH_4/C_2H_6), and involving three distinct ULR crude oils, revealed that the MMP increases proportionally with the heaviness of the crude oil (Mukherjee 2020). HnP-EOR experiments employing the same hydrocarbon gas, performed on preserved crushed samples from the Eagle Ford Shale, at pressures both below and above the MMP, have demonstrated that the produced oil is lighter in composition than the native crude oil (Min et al. 2020). Furthermore, the experiments showed that the recovery of heavier fractions slightly increases with injection pressure. These findings align with observations made during experiments conducted on resaturated plug samples from the Wolfcamp Shale, which utilized CO_2 as the solvent (Tovar et al. 2021). In addition, they reported that the oil produced from the shale was lighter than that produced from a resaturated Berea Sandstone plug, suggesting that the limited transport capacity of shale impairs the recovery of heavier fractions. However, detailed quantification of the recovery efficiency of each hydrocarbon fraction during HnP-EOR in ULR in various conditions has not been performed.

To summarize, optimization of HnP-EOR in ULR is complex and involves multiple variables. Key factors affecting oil recovery include sample size, fluid saturations, confinement, miscibility, solvent choice, soaking and production times, and oil composition. Crushed samples allow for faster testing due to enhanced surface area as compared to core plugs, which are more representative but require longer experiments. Preserved samples and confinement are preferred for simulating subsurface conditions. Regarding solvent selection, CO_2 injection tends to

outperform natural gas reinjection. Multiple short-soaking cycles are better than single long soaking time. However, the impact of injection pressure and MMP on the oil recovery and the quantitative recovery of various hydrocarbon fractions in ULR require further exploration.

Chapter 3. Experimental and Modeling Methodology: HnP-EOR in ULR

In this research, an experimental approach was developed to quantify how injection pressure and the minimum miscibility pressure (MMP) influence oil recovery and the efficiency of extracting different hydrocarbon fractions from preserved ULR samples during HnP-EOR (**Figure 4)**. To investigate the impact of nanopore constraints on oil recovery, HnP tests were conducted on both the reservoir crude oil and on crushed rock samples (7-8 mm), using different gas compositions ($scCO_2$, produced field gas, enriched field gas, and immiscible helium gas), and varying injection pressures relative to each solvent-oil MMP (determined with the VIT technique). Before and after each test, petrophysical properties were assessed to examine microstructural changes resulting from solvent-fluid-rock interactions in the nanoporous system. In parallel to experiments, a shale oil reservoir model was developed, calibrated with field data related to the well, reservoir, and fluid properties, to simulate how solvent composition affects oil recovery efficiency during HnP-EOR in ULR.

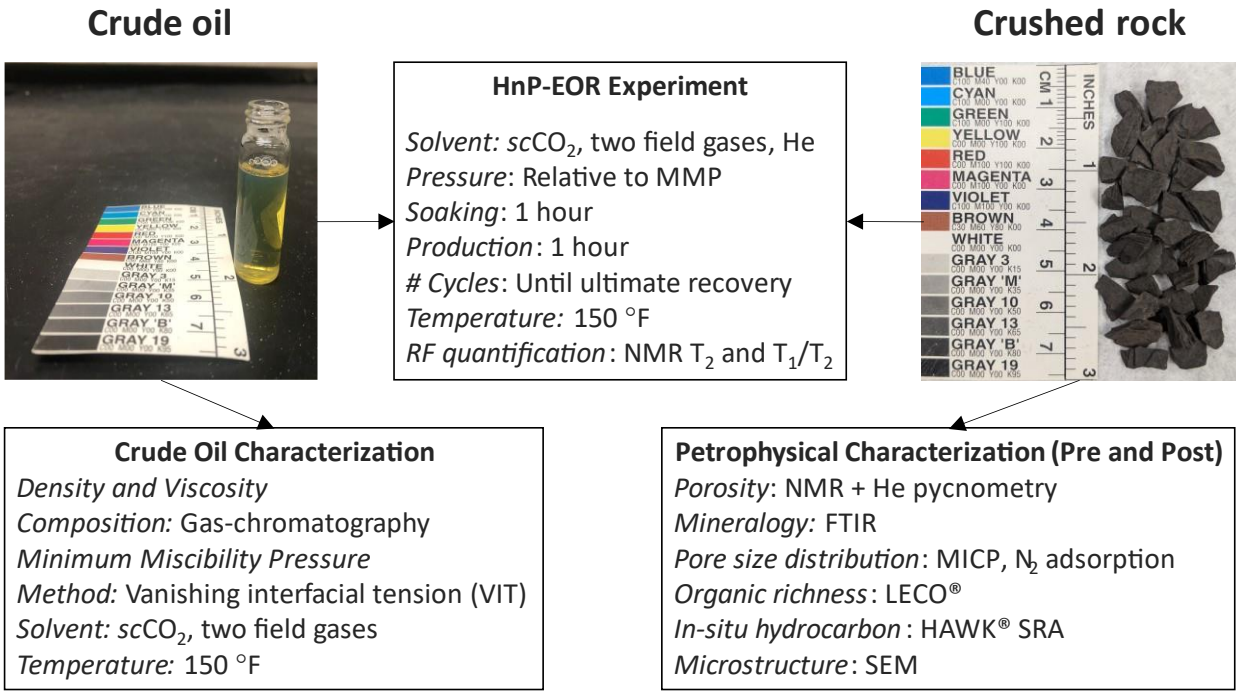

Figure 4. The experimental approach for evaluating the effect of injection pressure and minimum miscibility pressure (MMP) on the oil recovery and hydrocarbon extraction in preserved ULR samples during HnP-EOR. It encompasses HnP tests with varied gas compositions and injection pressures on reservoir crude oil and crushed rock samples. Petrophysical properties were evaluated between tests to analyze microstructural changes due to solvent interactions.

Samples description

Produced crude oil and two wax-preserved core intervals (1 ft long, extracted 15 ft apart) were acquired from a single wellbore in the Eagle Ford Shale. The crude oil had an API gravity of 51° and a dynamic viscosity of 2.2 cP at 150 °F. CT-scanning was used to selected visually homogeneous intervals (4-inch long) from each core. These intervals were labeled as samples EF1 and EF2 in ascending core depth order. Horizontal plugs (1-inch diameter and length) were dry-cored at the centers of these samples and utilized for petrophysical measurements. The remaining

material from each sample was crushed and sieved into 7-8 mm particles and stored in sealed bags (80g each) for use in HnP-EOR experiments.

Table 2 summarizes the petrophysical properties of the two Eagle Ford Shale samples. The total porosities of the preserved samples were determined by the combined measurements of NMR T_2 (liquid-filled porosity) and helium pycnometry (gas-filled porosity) on the core plugs. Mineralogy was determined with transmission-FTIR (Sondergeld and Rai 1994, Ballard 2007). Total organic carbon (TOC) was measured with the LECO® method after acidizing to remove the inorganic carbon. Overall, both shale samples share similarities, mainly composed of carbonates and clays (primarily illite), having porosities and organic-richness (TOC) around 10% and 6wt.%, respectively. In summary, the high porosity and considerable TOC renders the studied Eagle Ford samples as promising candidates for HnP-EOR applications.

Table 2. Total porosity, mineralogy, and total organic carbon (TOC), of the preserved Eagle Ford Shale samples used in the HnP-EOR study.

Sample	Total porosity (%)	Total carbonates (wt.%)	Total clays (wt.%)	Quartz + feldspars (wt.%)	Others (wt.%)	TOC (wt.%)
EF1	10.4	58	21	16	3	6.0
EF2	10.5	57	32	8	4	6.2

The pore size distribution (PSD) of the Eagle Ford crushed samples was obtained in a dry state using two different techniques: mercury injection capillary pressure (MICP) and isothermal nitrogen adsorption. In the case of N_2 adsorption measurements, PSD was derived through density functional theory (DFT) employing a slit-shaped pore model, based on adsorption/desorption

isotherms and hysteresis loop characteristics (Sing 1985, Tian et al. 2020). The MICP pore throat size distributions shown in **Figure 5(a)** indicated a unimodal distribution for both samples with most intrusion occurring in pores throats with a radius below 10 nm. Calculated R_{35} values, representing the characteristic pore radius where 35% of non-wetting phase intrusion occurs (Kolodzie 1980), were notably small (approximately 5 nm), indicating the ultra-tight nature of the samples. N_2 adsorption-based PSD analysis in **Figure 5(b)** revealed a wide distribution across the mesopore (2-50 nm) and macropore (>50 nm) pore volume ranges (Thommes et al. 2015), indicating significant complexity within the nanopore system. Furthermore, the BET specific surface areas (Brunauer et al. 1938) ranged from 2.1 to 2.7 m^2/g for samples EF1 and EF2, respectively. Additionally, Klinkenberg-corrected permeability measurements were conducted in a dry state using nitrogen at pore pressures of 2000 psi and four effective stresses ranging from 2000 to 5000 psi, revealing ultra-low permeabilities in the nanoDarcy range (between 10-40 nD).

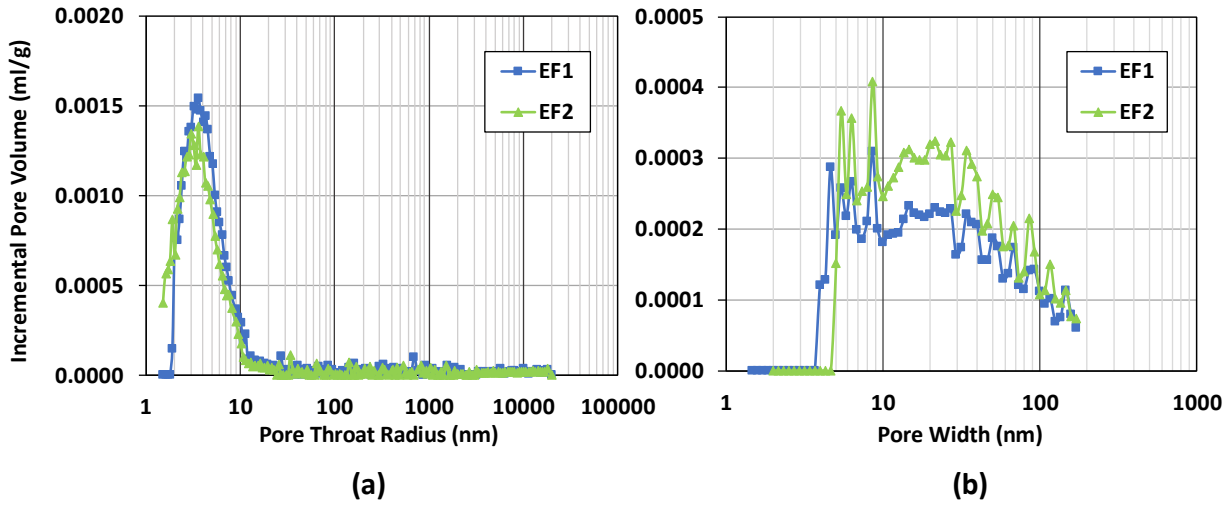

Figure 5. Pore size distributions (PSD) of the Eagle Ford samples obtained in a dry state. (a) mercury injection capillary pressure (MICP). (b) isothermal nitrogen adsorption using density functional theory (DFT) with slit-shape model. The PSD obtained with MICP reveal intrusion occurring below 10 nm indicating that the Eagle Ford samples

are considerable tight. The PSD extracted from N_2 adsorption measurements show a broad range of mesopore and macropore volume, indicating the complexity of the nanoporous system.

The potential mobilization of hydrocarbon fractions during HnP-EOR in ULR was quantitatively assessed using a HAWK® modified dry pyrolysis technique (**Figure 6**) (Dang 2019, Mamoudou 2020). This modified procedure involved breaking down the conventional S1 peak in dry pyrolysis into five distinct sub-peaks through a controlled, stepwise temperature increase. These sub-peaks represent various in-situ fractions of oil present in the shale rock, spanning from lighter, more mobile components below C_{13} (S11) to heavier components ranging from C_{21} to C_{30} (S15) (Abrams et al. 2017). The results indicate a higher abundance of lighter hydrocarbon species compared to the heavier ones in both samples. It also highlights the greater hydrocarbon richness in EF1 compared to EF2. The combined quantity of the five S1 sub-peaks amounts to 15.2 and 12.4 milligrams of hydrocarbons per gram of rock for EF1 and EF2, respectively. These results signify a substantial reservoir of potentially recoverable hydrocarbons for HnP-EOR.

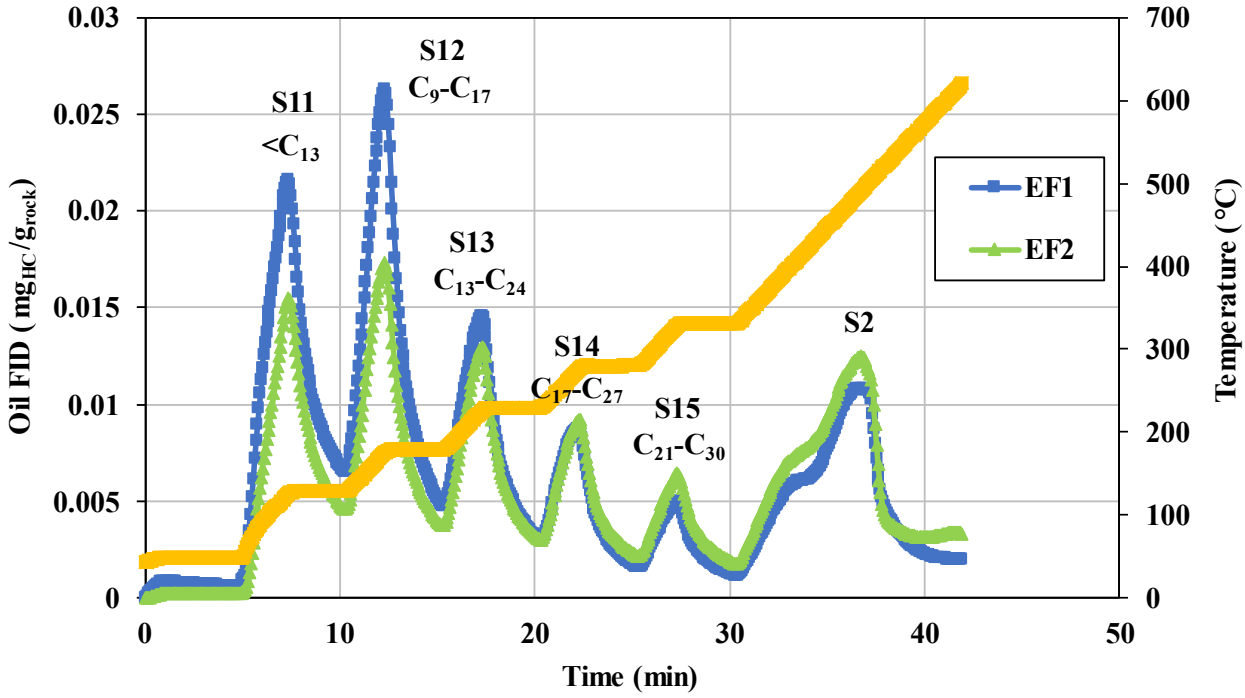

Figure 6. Quantitative assessment of hydrocarbon mobilization during HnP-EOR in ULR using a HAWK® modified dry pyrolysis technique (Dang 2019, Mamoudou 2020). The modification consists of a stepwise temperature program (yellow curve) to subdivide the conventional S1 peak in pyrolysis into five sub-peaks. These sub-peaks represent various in-situ oil fractions, ranging from lighter components below C_{13} (S11) to heavier ones between C_{21} and C_{30} (S15) (Abrams et al. 2017). Results reveal a higher abundance of lighter hydrocarbons than heavier ones in both samples. It also emphasizes EF1's greater hydrocarbon richness compared to EF2.

Hydrocarbon and brine quantification

Proper quantification of residual and recovered hydrocarbon and brine volumes is critical in the evaluation of oil recovery mechanisms and controlling variables during HnP-EOR in ULR (Liu et al. 2023). In this study, NMR T_2 and T_1-T_2 measurements (12 MHz and TE = 0.114 ms) were employed to quantify preserved fluid saturations and separate individual phase recovery factors before and after each HnP cycle. **Figure 7** presents the NMR T_2 and T_1-T_2 map of the two crushed Eagle Ford samples. Their NMR T_2 incremental spectra exhibit bimodal distributions, featuring a

high-amplitude, fast-relaxation peak (0.2 ms), followed by a lower-amplitude, slower-relaxation peak (1 to 10 ms). NMR T_2 analysis of such bimodal distributions suggests the presence of two distinct pore systems or presence of two different fluids in these samples. As shown in **Figure 5**, the combined PSD from MICP and N_2 adsorption confirm the existence of a single primary pore system within the nanometer range. The NMR T_1-T_2 maps, as depicted in **Figure 7**, prove valuable in resolving the fluid-typing challenge. The fast-relaxation peak (0.2 ms) corresponds to a high-amplitude, circular-shaped signal relaxing at low T_1/T_2 ratio (~10), alongside a minor amplitude signal displaying higher T_1/T_2 ratios (T_1/T_2 = 100-1000). In contrast, the second peak observed in the T_2 spectra appears as an elongated signal within the T_1-T_2 maps, consisting of three principal sub-peaks relaxing at distinct intervals. The presence of this elongated signal in the slower-relaxation spectrum suggests the coexistence of hydrocarbons with varying molecular weights saturating the rock, as shown in the HAWK® modified dry pyrolysis in **Figure 6**. Conversely, the fast-relaxation circular signal (T_1/T_2 = 10) may correspond to the brine present in the rock, while the minor amplitude signal at high T_1/T_2 ratios likely represents a portion of the organic matter detectable in the NMR acquisition.

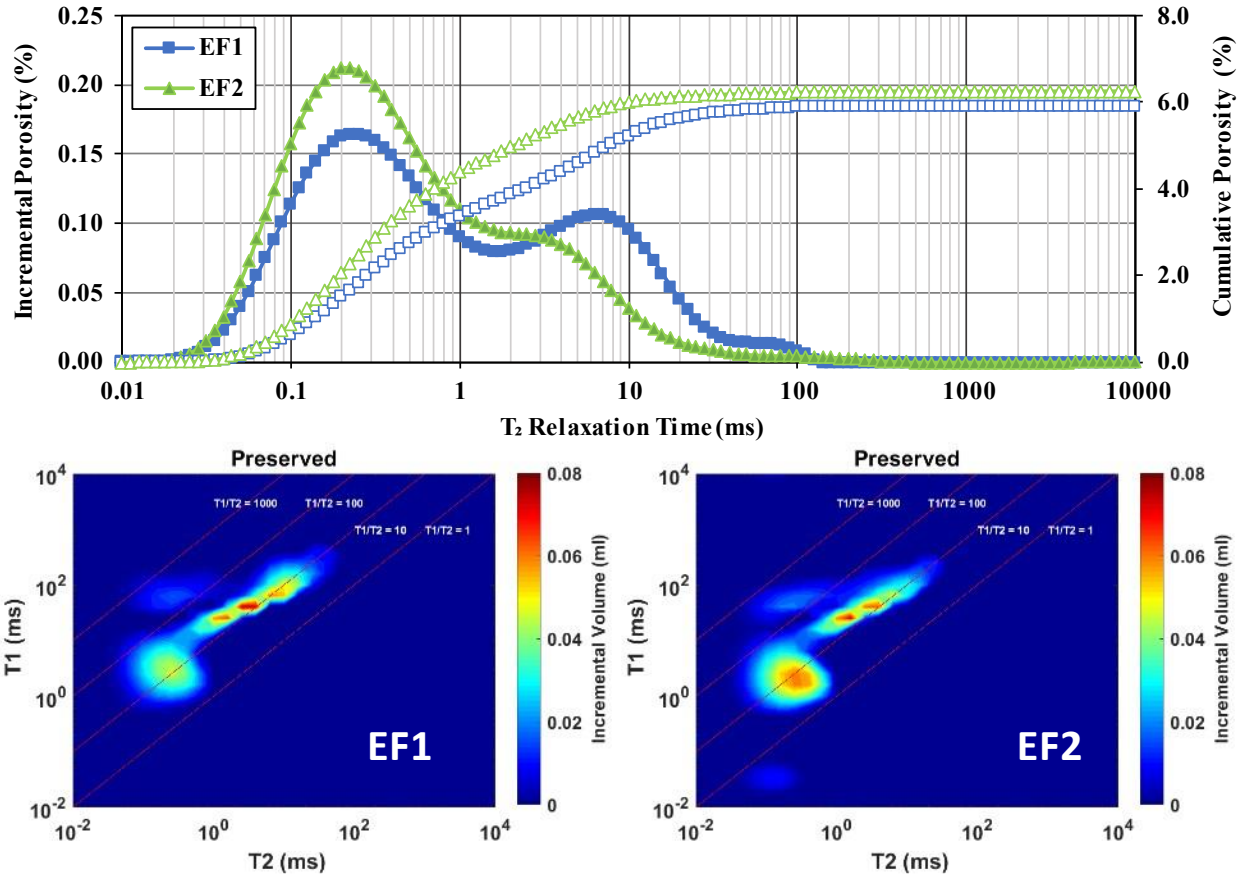

Figure 7. NMR T_2 and T_1-T_2 map of the preserved Eagle Ford samples. The NMR T_2 incremental spectra exhibit a bimodal distribution with a fast-relaxation peak (0.2 ms) and a slower-relaxation peak (1 to 10 ms), suggesting dual pore systems or the presence of two different fluids. As shown in Figure 5, combined PSD results from MICP and N_2 adsorption confirm a primary nanometer-size pore system. NMR T_1-T_2 maps offer fluid-typing insights with a fast-relaxation circular signal potentially representing brine and a slower-relaxation elongated signal indicating a range of hydrocarbons, as observed in the HAWK® modified dry pyrolysis results (Figure 6).

To confirm this hypothesis and separate NMR signatures of hydrocarbons and water, the Eagle Ford preserved plug (1/1" length/diameter) sample underwent spontaneous imbibition for multiple weeks within a doping agent solution ($MnCl_2$, 65 wt.%), which is fairly invisible in NMR acquisition (Gannaway 2014). As the doping agent exhibits miscibility with water and immiscibility with hydrocarbons, it permeates the brine phase, gradually diminishing its NMR

signal, thus enabling precise quantification of relaxation characteristics for each liquid phase saturating the rock. **Figure 8** illustrates NMR T_1-T_2 maps for the doping agent imbibition experiments in the Eagle Ford sample conducted over a 2-month period. Observations reveal negligible changes in the NMR T_1-T_2 maps throughout the 1-month experimental duration, attributed to the low diffusivity within the shale plug, restricting the doping solution's imbibition. After 2 months of imbibition, a notable reduction in the amplitude of the fast-relaxation circular signal emerges, signifying its interaction with the brine phase. The slow-relaxation elongated signal remains largely unaltered, except for a minor amplitude reduction in longer T_2 times (>100 ms), attributed to the natural evaporation of lighter components in the native oil within the preserved plug sample following 2 months of experimentation.

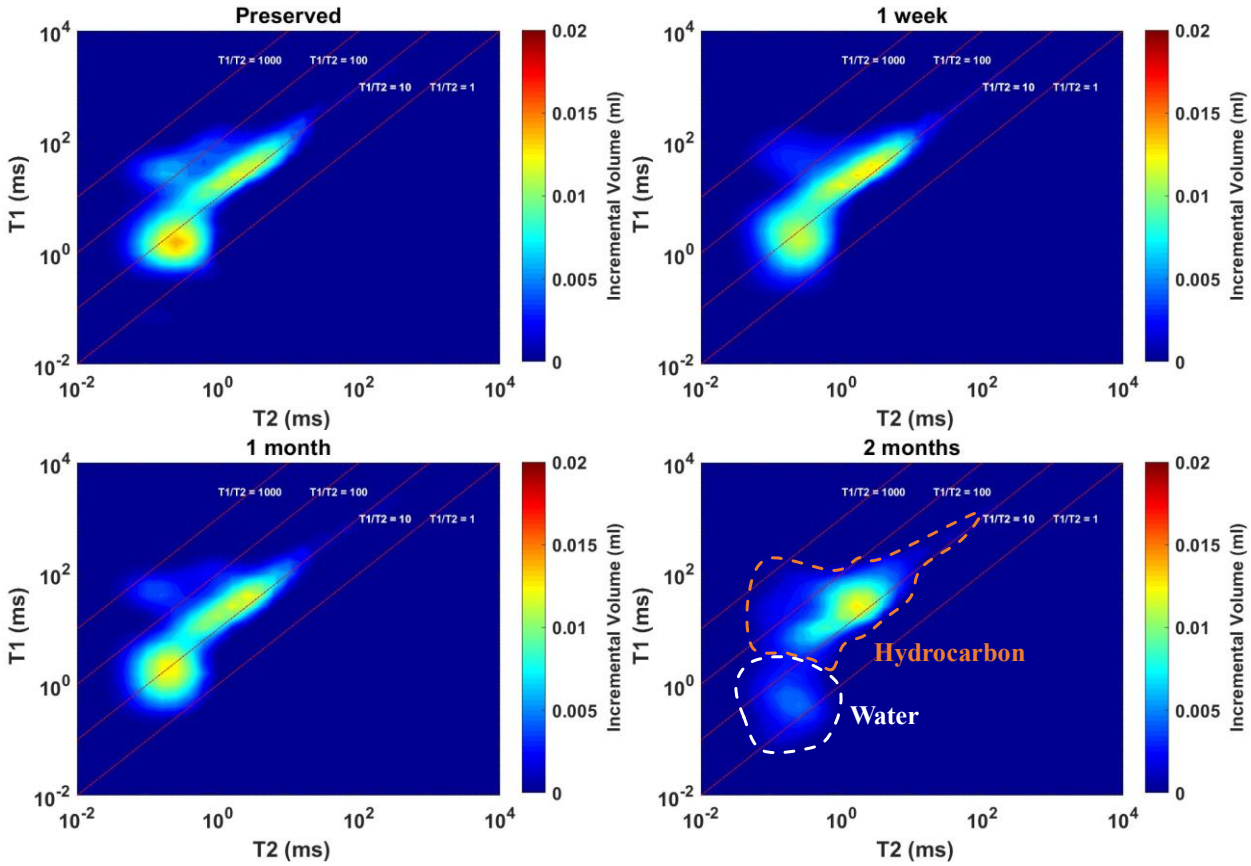

Figure 8. NMR T_1-T_2 maps illustrating the effects of a 2-month imbibition experiment with NMR doping agent solution ($MnCl_2$, 65 wt.%), used to distinguish hydrocarbon and water signals in Eagle Ford shale samples (Gannaway 2014). Initial observations show limited changes within the first month of imbibition attributed to the low diffusivity in shale. After 2 months, a decrease in the fast-relaxation signal suggests interaction with the brine phase, while the slower signal remains largely unaltered.

Following the differentiation of hydrocarbon and water signals using NMR T_1-T_2 data, preserved fluid saturations (i.e., water, oil, and gas) were quantified:

$$\emptyset_{total}\ (\%) = \emptyset_{NMR,T_2} + \emptyset_{helium} \tag{3.1}$$

$$S_{water}\ (\%) = \frac{(\frac{V_{NMR,T_1-T_2(water)}}{V_{NMR,T_1-T_2(total)}}) \times \emptyset_{NMR,T_2}}{\emptyset_{total}} \times 100 \tag{3.2}$$

$$S_{oil}\ (\%) = \frac{(\frac{V_{NMR,T_1-T_2(oil)}}{V_{NMR,T_1-T_2(total)}})\times \emptyset_{NMR,T_2}}{\emptyset_{total}} \times 100 \quad (3.3)$$

$$S_{gas}\ (\%) = 100 - S_{water} - S_{oil} \quad (3.4)$$

where $V_{NMR,T_1-T_2(water)}$, $V_{NMR,T_1-T_2(oil)}$, and $V_{NMR,T_1-T_2(total)}$ represent the NMR T_1-T_2 water, oil, and total volumes, respectively.

Figure 9 illustrates the preserved fluid saturations, indicating that EF2 exhibits slightly higher water saturation relative to EF1 (33% to 26%, respectively), along with barely lower oil saturation (32% to 36%, respectively), as indicated by the preserved rock pyrograms presented in **Figure 6**.

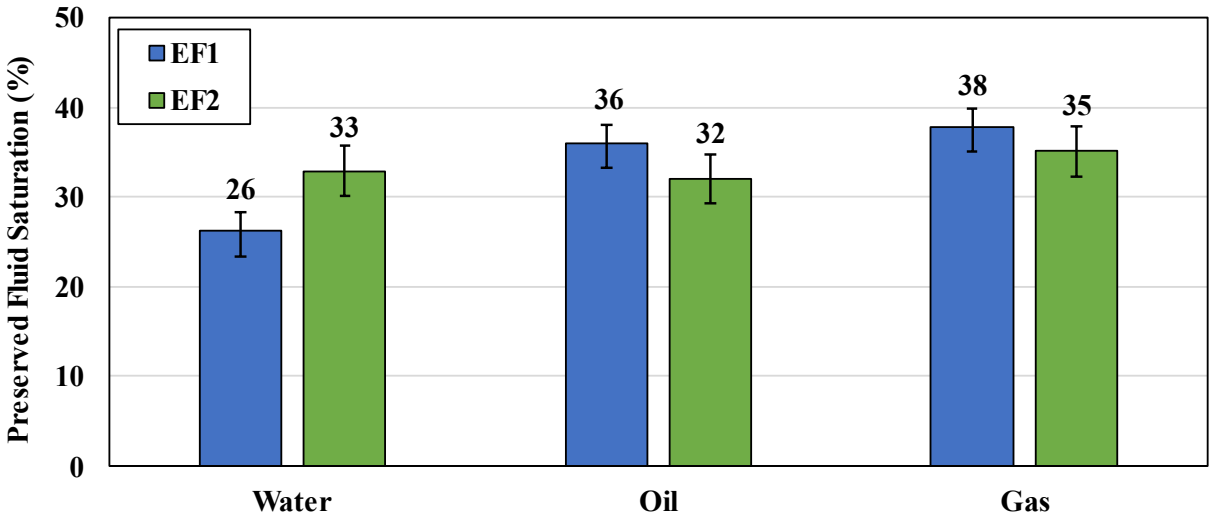

Figure 9. Initial fluid saturations of the preserved Eagle Ford samples were determined with NMR T_1-T_2 and total porosity data. EF2 shows slightly larger water saturation and barely lower oil saturation compared to EF1.

Minimum miscibility pressure (MMP) measurement

The MMPs between each solvent gas and Eagle Ford crude oil were assessed at reservoir temperature (150 °F) using the vanishing interfacial tension (VIT) technique (Hawthorne et al. 2016). Further details of the VIT experimental setup can be found in Mukherjee (2020). This

method uses a small glass tube in a high-pressure, high-temperature cell to visualize the interaction between crude oil and solvent gas (**Figure 10(a)**). By gradually increasing gas pressure, surface tension between the immiscible phases decreases, causing the meniscus height to drop (**Figure 10(b)**). The VIT-MMP is determined when the capillary height disappears, indicating the formation of a single-phase gas-oil system (**Figure 10(c)**). The VIT-MMPs for each solvent-Eagle Ford oil pair measured at reservoir temperature (150 °F) are shown in **Figure 10(d)**. $ScCO_2$ exhibits the lowest MMP at 2500 psi, followed by enriched field gas (C_1: 74%, C_2: 14%, C_{3+}: 12%) at 3450 psi, and produced field gas (C_1: 67%, C_2: 13%, C_{3+}: 20%) at 3850 psi. The enriched field gas was formulated by blending 90 mol% of the produced field gas with 10 mol% of drip liquids from the pipeline. The enrichment in the field gas resulted in a decrease in C1 from 74% to 67% and an increase in the C_{3+} fraction from 12% to 20%.

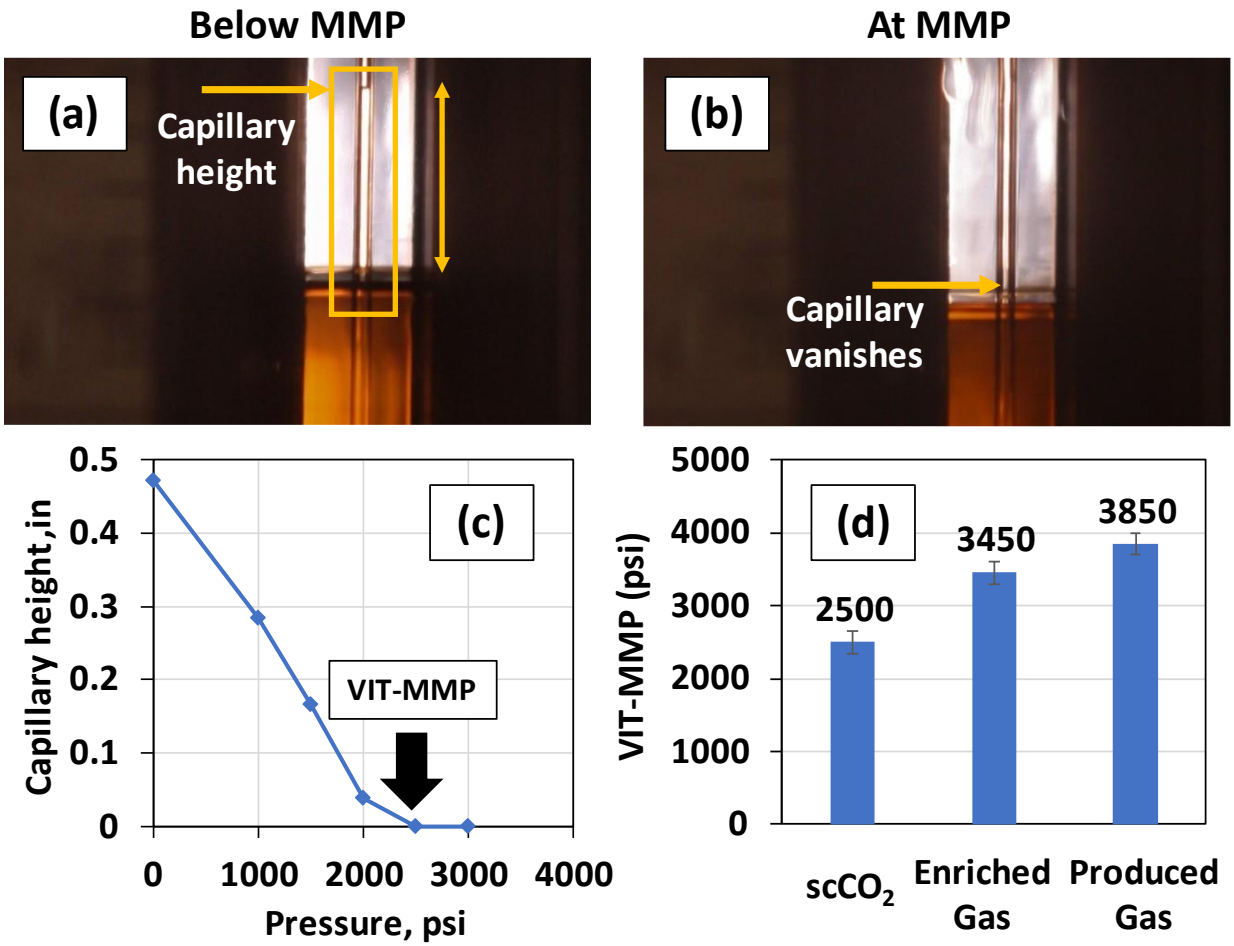

Figure 10. The vanishing interfacial tension (VIT) method to determine minimum miscibility pressure (MMP). (a) Image of the meniscus formed at the interface of solvent gas and crude oil inside the capillary within the HPHT cell at reservoir temperature are shown. (b) As pressure rises, surface tension between the two immiscible phases diminishes, causing a decrease in the capillary height. (c) The VIT-MMP is identified when the capillary height disappears. (d) $scCO_2$ exhibits the lowest MMP (2500 psi), followed by enriched field gas (3450 psi) and produced field gas (3850 psi).

HnP-EOR experiment

The experimental design shown in **Figure 11** was used to conduct the HnP-EOR experiments at the reservoir temperature (150 °F), using different gas compositions ($scCO_2$, produced field gas, enriched field gas, and immiscible helium gas), and various injection pressures relative to each

solvent-oil VIT-MMP. Details of the HnP-EOR experimental setup can be find in Mamoudou (2020). In this study, tests were conducted on both the reservoir crude oil (~3 mL sample) and on the preserved crushed rock (7-8 mm, 80g). Soaking and production times of 1 hour each were selected. The cumulative recovery factor of each liquid phase after an injection cycle ($RF_{cycle,n}$) was determined through NMR measurements using **Equation 3.5**:

$$RF_{cycle,n}\ (\%) = \frac{S_{preEOR} - S_{cycle,n}}{S_{preEOR}} \times 100 \tag{3.5}$$

where S_{preEOR} and $S_{cycle,n}$ are the saturations of the liquid phase before EOR and after a cycle (n). The saturations of each liquid phase were determined with **Equation 3.2** and **3.3**.

To quantify compositional changes of the crude oil after an injection cycle, the residual amount of each alkane present in the crude oil ($V_{alkane,n}$) was calculated by the combination of NMR T_2 (12 MHZ, TE = 0.4 ms) and gas-chromatography, mass-spectrometry (GC-MS) measurements. Further details of the combined NMR and GC-MS framework can be found in Odiachi et al. (2021). Quantification of the residual alkane fraction after an injection cycle is shown in **Equation 3.6**:

$$V_{alkane,n}\ (\%) = \frac{\mathrm{V}_{NMR\,T_2,n} \times N_{alkane,n}}{\mathrm{V}_{NMR\,T_2,preEOR} \times N_{alkane,preEOR}} \times 100 \tag{3.6}$$

where $\mathrm{V}_{NMR\,T_2,n}$ is the NMR T_2 volume of the residual crude oil and $N_{alkane,n}$ is the abundance of the alkane normalized by the total abundance of alkanes after an injection cycle (n), respectively. The product $\mathrm{V}_{NMR\,T_2,preEOR} \times N_{alkane,preEOR}$ is the analogous quantity before EOR.

When ultimate oil recovery is reached after multiple injection cycles, the relative recovery of each hydrocarbon fraction present in the rock was assessed by conducting modified dry pyrolysis measurements on the crushed rock after EOR (**Equation 3.7**):

$$RF_{S_{1i}}\,(\%) = \frac{(S_{1i})_{preEOR} - (S_{1i})_{postEOR}}{(S_{11}+S_{12}+\cdots+S_{15})_{preEOR}} \times 100 \qquad (3.7)$$

where $RF_{S_{1i}}$ is the recovery factor of the S_{1i} fraction. $(S_{1i})_{preEOR}$ and $(S_{1i})_{postEOR}$ are the quantities of the fraction S_{1i} before and after EOR, respectively.

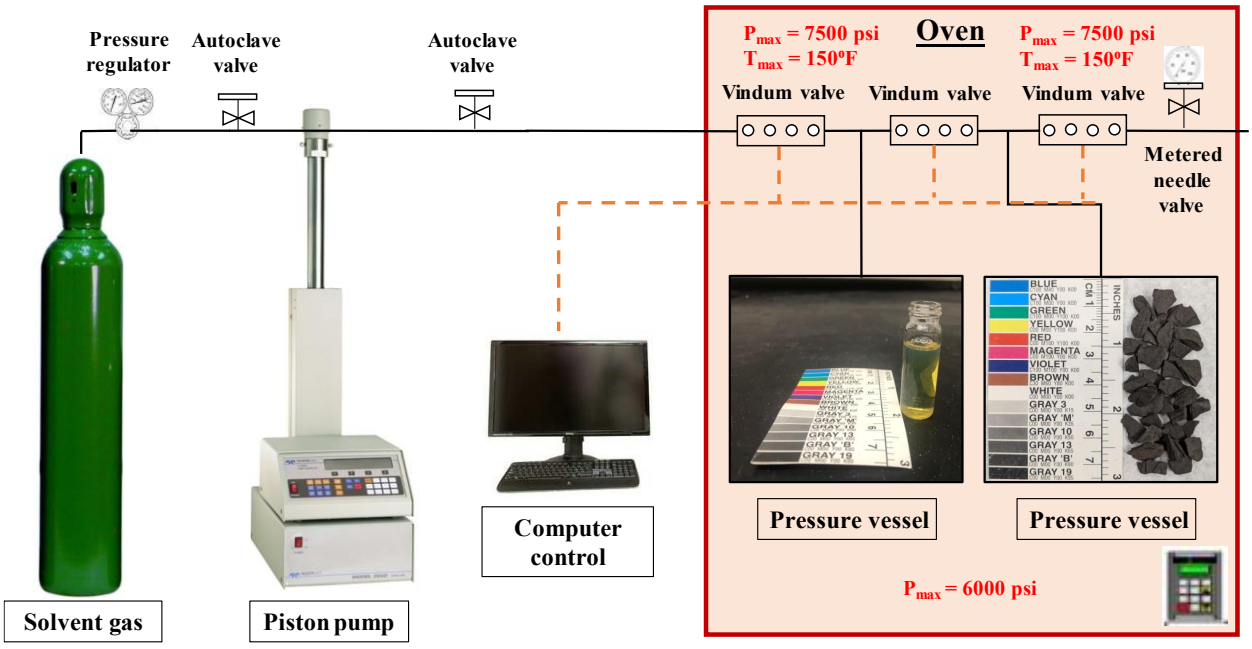

Figure 11. Experimental setup used in the HnP-EOR experiments (Mamoudou 2020). Testing conditions: multiple solvent gases ($scCO_2$, produced field gas, enriched field gas, and immiscible helium gas) at various pressures, reservoir crude oil (~3 mL), preserved crushed rock (7-8 mm, 80 g), soaking and production times of 1hr each, temperature of 150 °F.

Shale oil reservoir model

A shale oil reservoir model was created using CMG (Computer Modeling Group) software to replicate the HnP-EOR process in ULR (**Figure 12**). The model was fine-tuned with field

parameters encompassing reservoir, well, and fluid characteristics from an Eagle Ford Shale oil operation. It features a four-stage, hydraulically-fractured horizontal well with a lateral length of approximately 750 ft, situated in a dual-permeability reservoir. Matrix properties consisted of a porosity-permeability combination of 6%-25 nD, while fractures exhibited porosity-permeability characteristics of 0.06%-40 μD. Additionally, a matrix tortuosity value of 16 was selected based on experimental data (Odiachi et al. 2022). The initial reservoir temperature and pressure were 150 °F and 6000 psi, respectively. Relative permeability and capillary pressure relationships were derived separately, with the reservoir unit located above the water-oil contact.

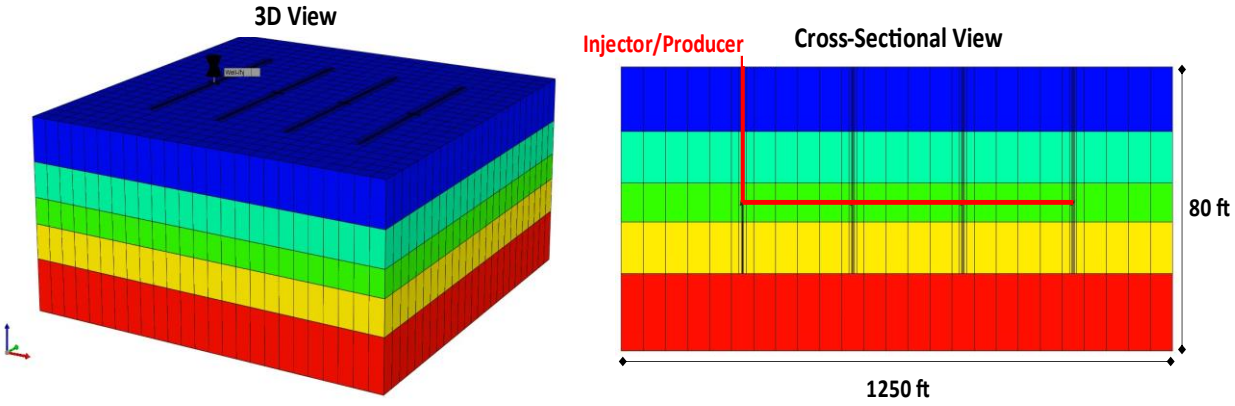

Figure 12. The shale oil reservoir model developed using CMG software to simulate the HnP-EOR process in unconventional liquid-rich shale reservoirs (ULR). The model is calibrated with field parameters for reservoir, well, and fluid properties, gathered from an Eagle Ford Shale oil operation. It features a hydraulically-fractured horizontal well with four stages and a lateral length of approximately 750ft, within a dual-permeability reservoir.

Fluid properties were imported from the CMG WinProp tool, highlighting primary oil constituents lumped into fractions (mol%): C_1: 51%, $C_{2\text{-}6}$: 26%, C_{7+}: 22%. This indicates that the shale oil is relatively light, with a bubble point pressure at the reservoir temperature (150 °F) of 3500 psi. A small fraction of non-hydrocarbon constituents (~1 mol%), including N_2 and CO_2, was included

in the reservoir oil composition. Oil-solvent MMPs at reservoir temperatures were aligned with the measured VIT-MMPs and simulated using the multiple mixing cell method (Ahmadi and Johns 2011) under various conditions of solvent increment and equilibrium gas-oil ratios.

The simulations were performed using a compositional simulator (GEM). Molecular diffusion was included the simulations, where the diffusivity of individual species were determined by Graham's law (Mason and Kronstadt 1967). The simulation constraints included a minimum bottomhole pressure (BHP) of 5500 psi to ensure that the shale oil remained above the bubble point. The maximum BHP was adjusted throughout the injection phase in accordance with each simulation. The simulation commenced with approximately 2.5 years of primary production. Subsequently, the HnP cycles were initiated, comprising a 30-day injection period, followed by a 3-month soaking period, and culminating with a 15-month production phase. In total, a decade of simulated operations encompassed primary production and five HnP-EOR cycles.

Chapter 4. Results: HnP-EOR in ULR

Crude oil HnP-EOR

This study initially investigated oil recovery mechanisms at the bulk phase through HnP-EOR tests conducted on an Eagle Ford crude oil sample. As depicted in **Figure 13**, NMR T_2 spectra (12 MHz, TE = 0.4 ms) were acquired following multiple HnP cycles using $scCO_2$ (**Figure 13(a)**) and produced field gas (**Figure 13(b)**). Both tests were conducted at reservoir temperature (150 °F) and injection pressures 1000 psi greater than the respective solvent-crude oil MMPs (P_{inj},$scCO_2$ = 3500 psi, and P_{inj},produced field gas = 4850 psi).

In the case of the $scCO_2$ test, a substantial reduction in residual volume was observed after the first injection cycle, accompanied by a shift in the T_2 peak towards shorter relaxation times. A similar shift towards faster relaxation occurred in the second cycle, though the reduction in residual volume was notably smaller. The $scCO_2$ test achieved ultimate recovery around 80% after two HnP cycles (**Figure 13(c)**). Conversely, the produced field gas test exhibited a gradual decrease in residual oil volume and shift towards faster relaxation with increasing injection cycles. The produced field gas test required ten cycles to attain an ultimate recovery of approximately 50% (**Figure 13(d)**). The higher and faster oil recovery in indicates that $scCO_2$ has a better HnP performance than produced field gas, as shown in **Figure 3**.

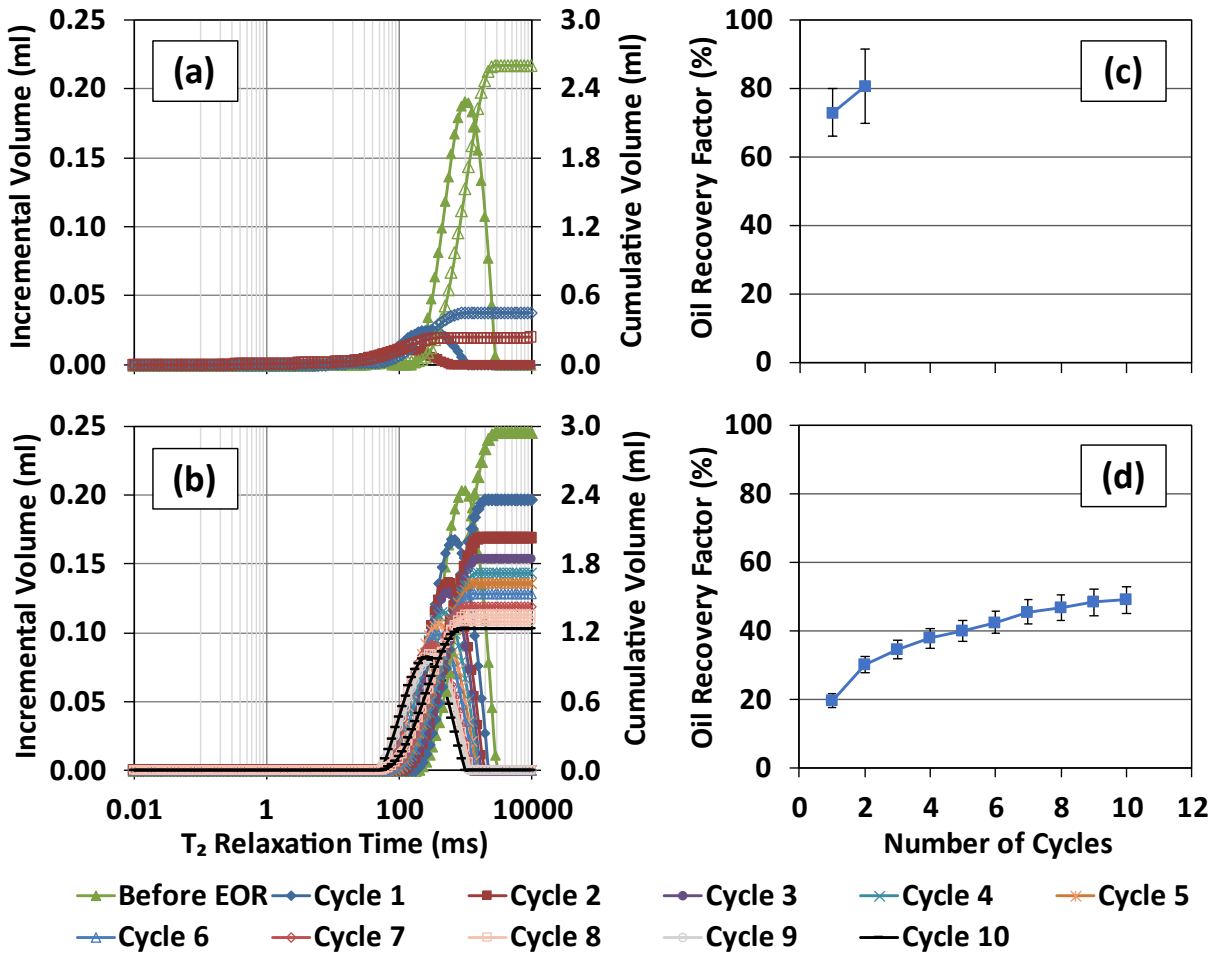

Figure 13. Bulk Eagle Ford crude oil response during HnP-EOR. (a) NMR T_2 spectra of oil during $scCO_2$ HnP showing a substantial reduction in residual volume and a shift towards fast relaxation in the first cycle. (b) NMR T_2 spectra after produced field gas HnP, demonstrating gradual recovery and a shift towards fast relaxation, resulting in a larger residual oil volume compared to $scCO_2$. (c) Oil recovery factor for $scCO_2$ test calculated using **Equation 3.5**, indicating ~80% oil recovery after two cycles (d) Parallel results for produced field gas HnP, with gradual and lower recovery, flattening at ~50%.

The faster relaxation observed after each subsequent injection cycle can be attributed to an increased oil viscosity and a decreased oil diffusion coefficient following EOR. **Figure 14(a)** and **Figure 14(b)** illustrate the derived oil viscosities and oil diffusion coefficients for bulk oil relaxation, calculated using **Equation 4.2** and **4.3**, respectively (Coates et al. 1999):

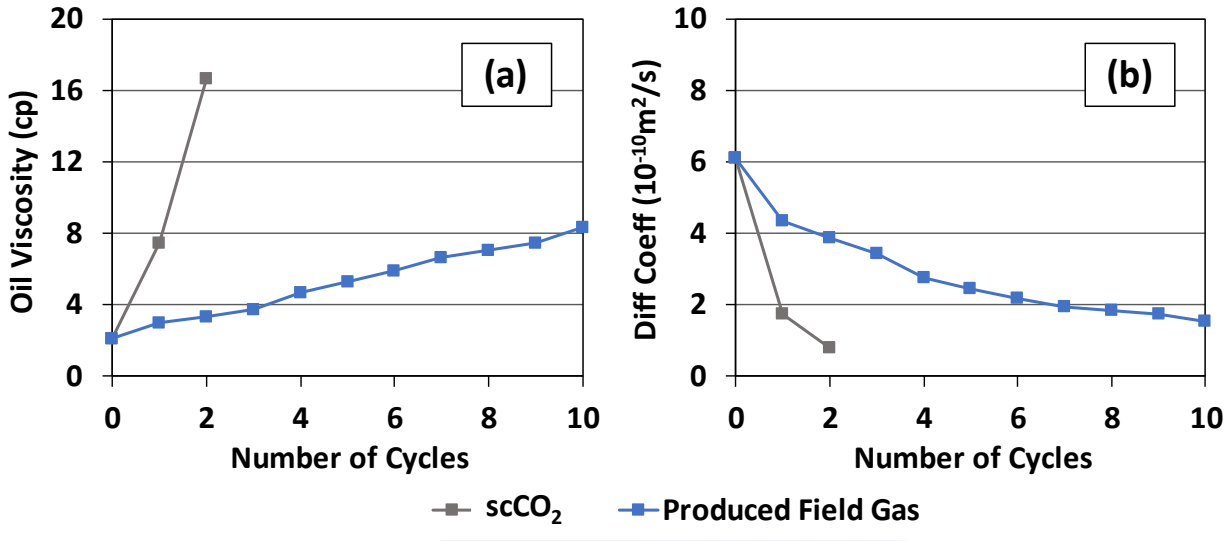

Figure 14. Bulk Eagle Ford crude oil response during HnP-EOR. (a) Computed oil viscosity using **Equation 4.2.** (b) Computed oil diffusion coefficient using **Equation 4.3**. Increase in oil viscosity and decrease in diffusion coefficient associated with increasing oil heaviness during HnP is observed. The trends are more pronounced with $scCO_2$ as compared to produced field gas.

$$\frac{1}{T_{2,bulk}} \cong \frac{1}{T_{2,peak}} \tag{4.1}$$

$$\eta(cp) \cong 0.00713 \frac{T_K}{T_{2,bulk(s)}} \tag{4.2}$$

$$D_o(\frac{m^2}{s}) \cong 1.3 \left(\frac{T_K}{298\eta}\right) \times 10^{-9} \tag{4.3}$$

In these equations, $T_{2,bulk}$ represents the T_2 time corresponding to the peak ($T_{2,peak}$), η signifies the oil viscosity in centipoise (cp), T_K stands for the NMR measurement temperature in Kelvin, and D_o is the oil diffusion coefficient ($\frac{m^2}{s}$). **Figure 13** demonstrates a notable rise in oil viscosity (approximately one order of magnitude) and a reduction in the diffusion coefficient following $scCO_2$ HnP in the bulk oil. Comparatively, the produced field gas test produced less pronounced

trends in oil viscosity and diffusion coefficient. Visual confirmation of a significant increase in oil viscosity during $scCO_2$ HnP is observed based on the before (**Figure 15(a)**) and after (**Figure 15(b)**) images of the crude oil in the glass vial. The increase in oil heaviness within the bulk oil indicates that a vaporization of lighter components from the oil into the solvent phase plays a significant role in the recovery mechanism during HnP-EOR.

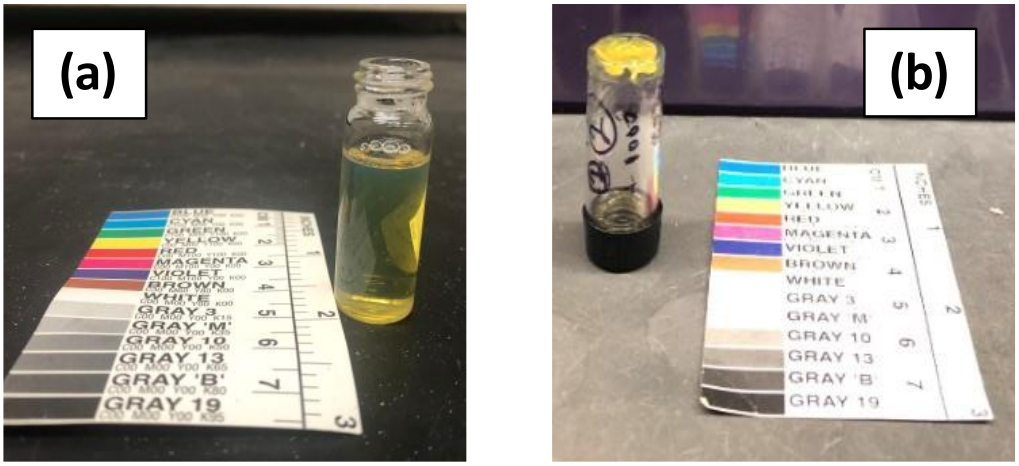

Figure 15. Image comparison between the bulk Eagle Ford oil sample in a glass vial. (a) before $scCO_2$ HnP-EOR. (b) after two injection cycles. There is a notable reduction in oil volume and a substantial increase in viscosity.

Figure 16 displays the outcomes of integrating NMR and GC-MS to quantify the residual volume of individual alkane species within the oil during HnP-EOR. The breakdown of alkanes (up to C_{25}) present in the residual crude oil after $scCO_2$ and produced field gas HnP is shown in **Figure 16(a)** and **Figure 16(b)**, respectively. The residual oil fraction of each alkane was calculated using **Equation 3.6**. During $scCO_2$ HnP, substantial production of hydrocarbon fractions ranging from C_{12} to C_{25} after the initial cycle is observed, leading to a clear reduction in the amount of these fractions remaining in the oil. Interestingly, during the second cycle, there is a preference for producing lighter fractions up to C_{19}, while the recovery of heavier fractions decreases, and no

production occurs above C_{24}. This suggests that the vaporization of heavier compounds during HnP-EOR mainly occurs in initial cycles and depends on the quantity of lighter phases present in the oil. A similar trend in the produced field gas test is observed (**Figure 16(b)**), where most of the recovery for heavier fractions happens during the first cycle, followed by gradual production of lighter species in subsequent cycles. Overall, the composition of the remaining crude oil becomes progressively heavier with each additional injection cycle, regardless of the solvent selected.

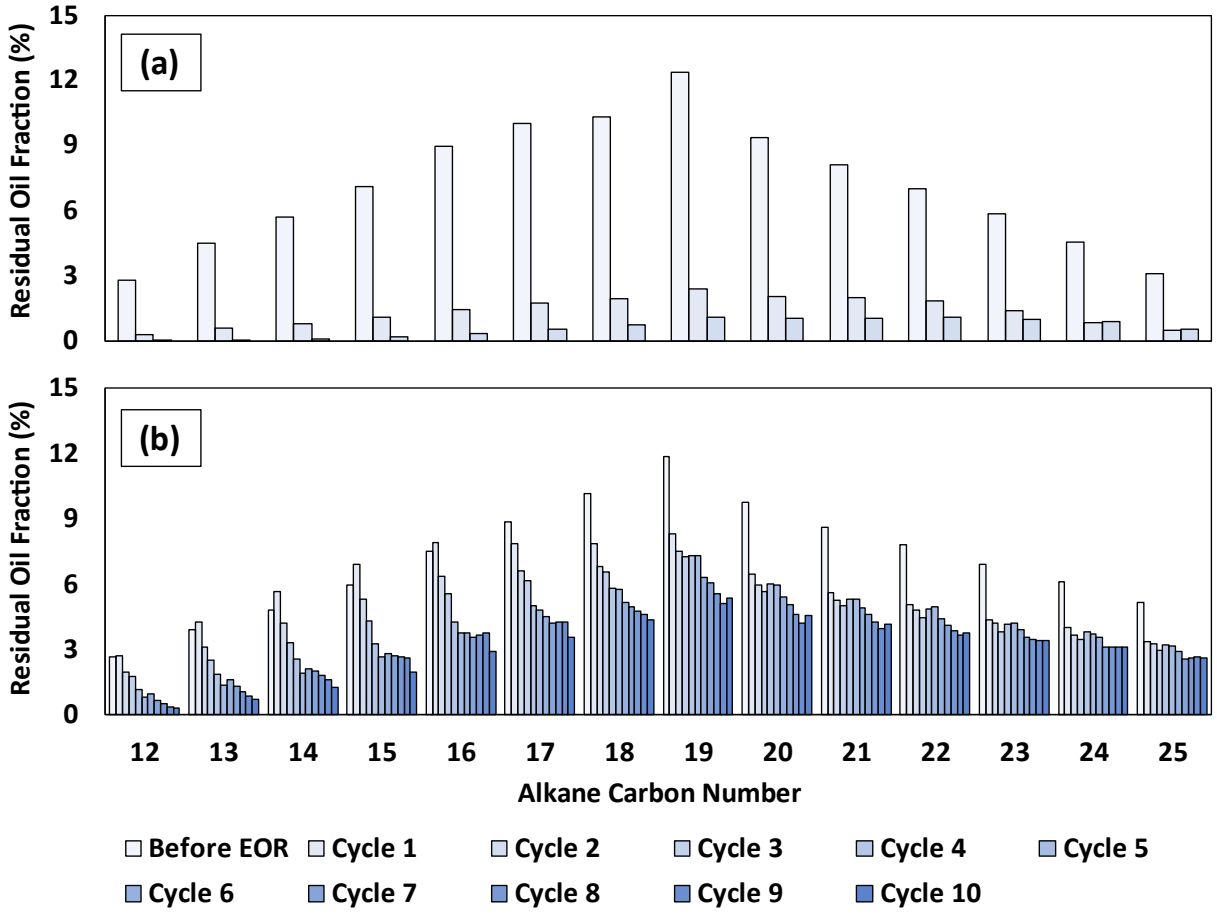

Figure 16. Effect of HnP-EOR on crude oil composition, obtained after integrating NMR and GC-MS data. (a) and (b) display alkane distributions during $scCO_2$ and produced field gas HnP, respectively. After the initial $scCO_2$ HnP cycle, there is substantial production of hydrocarbon fractions (C_{12} to C_{25}), reducing residual volumes. During the

second cycle, preference for lighter fractions up to C_{19} is observed, with reduced recovery for heavier fractions (none above C_{24}). Produced field gas test show a similar trend, with the majority of heavy fraction recovery in the first cycle and gradual production of lighter species in subsequent cycles. Overall, remaining crude oil becomes heavier with each injection cycle, regardless of the solvent used.

Simultaneously with the HnP-EOR tests, MMP measurements with the residual crude oil were conducted using the VIT-technique, as explained in **Figure 10**. Based on the gradual HnP performance, this study was conducted with produced field gas at a pressure of 1000 psi above the initial MMP (4850 psi) and at reservoir temperature (150 °F). The aim was to assess how the increasing heaviness of the oil during HnP affects the solvent-crude oil miscibility, as determined by VIT-MMP measurements. **Figure 17(a)** illustrates capillary height-pressure curves after each injection cycle. At lower pressures (<2000 psi), these curves fairly align with the original solvent-crude oil curve (with an experimental error margin). However, distinctions emerge at higher pressures (>3000 psi) and after a few cycles, as higher pressures are required to make the capillary height vanish. **Figure 17(b)** reveals that the gradual production of light fractions and the increasing heaviness of the oil over injection cycles result in an increase in the solvent-residual oil MMP. For instance, after six injection cycles, the MMP for the residual oil is approximately 800 psi higher than the original crude oil-solvent MMP. This suggests that the vaporization mechanism leads to higher injection pressure to achieve miscibility in subsequent cycles, impacting ultimate recovery.

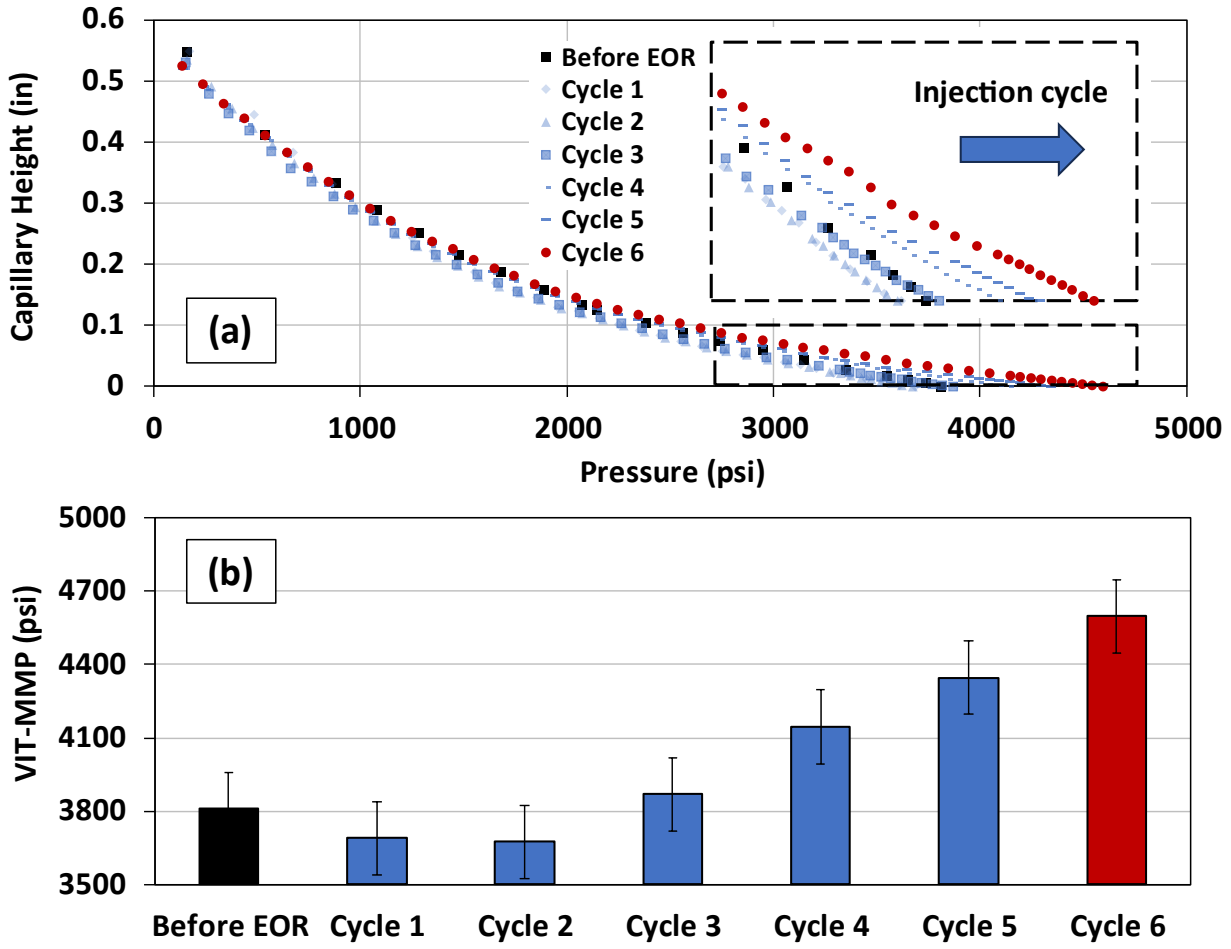

Figure 17. Impact of HnP cycles on the solvent-residual crude oil MMP determined with the VIT technique. Given the gradual oil recovery, these HnP tests were conducted using produced field gas at 1000 psi above the original MMP and 150 °F. (a) Capillary height-pressure curves after several injection cycles. At lower pressures (<2000 psi), curves closely align with the original solvent-crude oil MMP. However, distinctions became evident at higher pressures (>3000 psi) and after few injection cycles, requiring elevated pressures to reach single-phase. (b) Increasing oil heaviness during cycles lead to increased solvent-residual oil MMP. After six cycles, the MMP is approximately 800 psi higher than the original MMP, suggesting impairment on miscibility and impacting oil recovery.

Crushed rock HnP-EOR

Similarly, to the bulk crude oil HnP-EOR tests, equivalent experiments were conducted using preserved crushed rock samples (7-8 mm) from the same well in the Eagle Ford Shale. **Figure 18** provides an overview of the incremental and cumulative volumes acquired through NMR during the $scCO_2$ HnP test, performed at an injection pressure 1000 psi higher than the $scCO_2$-Eagle Ford oil MMP ($P_{inj,scCO_2}$ = 3500 psi). In **Figure 18(a)**, the decrease in residual volumes is evident for the two primary peaks across successive injection cycles. Cumulative volume profiles reveal that the most substantial volume reduction occurs within the initial two cycles. NMR T_1-T_2 maps, before and after six injection cycles (**Figure 18(a)** and **Figure 18(b)** respectively), indicate significant depletion in both water and oil volumes after six injection cycles, leading to ultimate oil recovery.

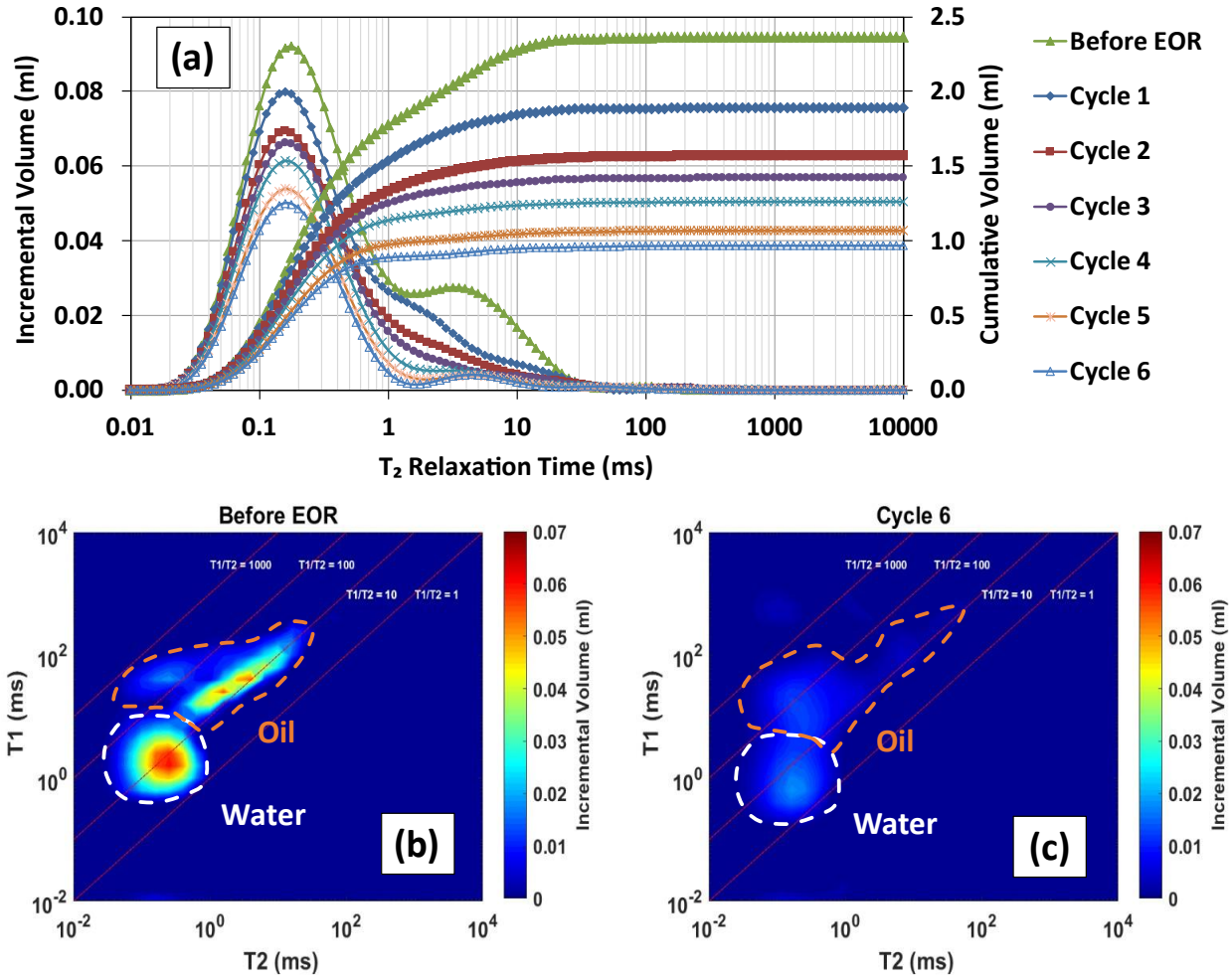

Figure 18. NMR results for the $scCO_2$ HnP test on the Eagle Ford crushed samples (7-8 mm) at injection pressure of 1000 psi above the $scCO_2$-Eagle Ford oil MMP (P_{inj} = 3500 psi). (a) T_2 distribution showing a reduction in volume for the two primary peaks, with a major decrease in the first two cycles. NMR T_1-T_2 maps before HnP (b) and after six HnP cycles (c) highlight significant reduction in oil and water volumes.

Upon achieving ultimate oil recovery after the sixth cycle, residual oil within the rock underwent Soxhlet extraction, followed by GC-MS analysis (Odiachi et al. 2021). **Figure 19(a)** presents the alkane volumes of crude oil extracted from the shale rock before and after six $scCO_2$-HnP cycles, determined by **Equation 3.6**. Similar to the results in the bulk oil $scCO_2$ HnP test under identical experimental conditions (**Figure 16(a)**), a preference for vaporizing lighter fractions is evident,

accompanied by reduced recovery of heavier fractions above C_{19}. Notably, in the shale sample, there was no production of heavier fractions above C_{24}, even after six injection cycles. Additionally, the composition of the remaining crude oil within the shale rock following HnP was assessed using a modified pyrolysis protocol demonstrated in **Figure 6**. Analysis of mobile hydrocarbon fractions, as depicted in **Figure 19(b)**, reveals the same preference for lighter fractions and limited recovery of heavier fractions. These observations suggest that the nanoporous nature of shale rock introduces constraints in mobilizing heavier fractions during HnP-EOR.

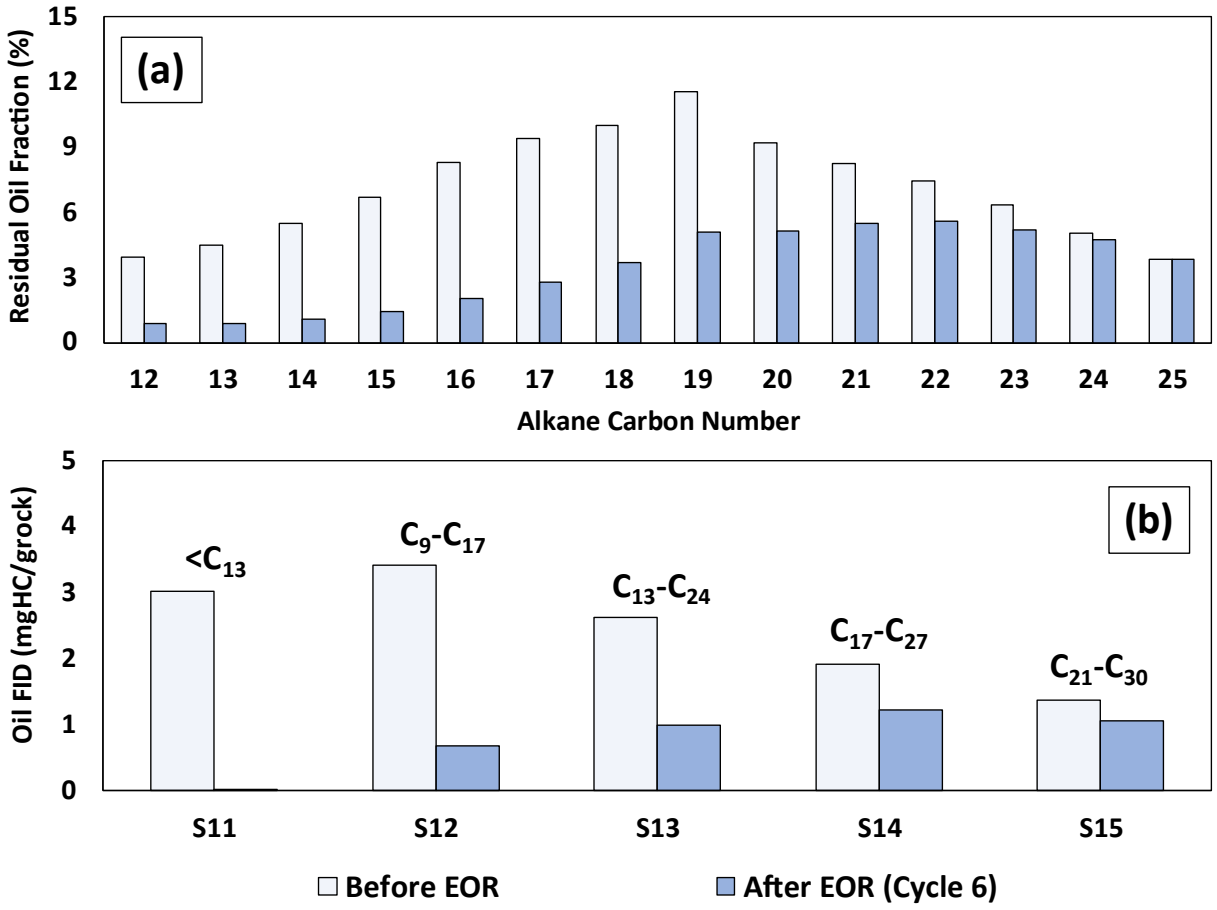

Figure 19. (a) Alkane volume analysis of crude oil extracted from shale rock before and after six $scCO_2$-HnP cycles, highlighting the preference for vaporizing lighter fractions and minimal recovery of heavier fractions above C_{19}. No production of heavier fractions above C_{24} occurred, even after six cycles. (b) Composition of the residual crude oil

within the shale rock after HnP-EOR, analyzed using a modified pyrolysis protocol. The results demonstrate the same preference for lighter fractions and limited recovery of heavier fractions, indicating constraints in mobilizing these heavier fractions within the nanoporous shale rock system.

Furthermore, extensive testing was conducted on the two Eagle Ford samples (EF1 and EF2), varying solvent composition ($scCO_2$, produced field gas, enriched field gas, and immiscible helium gas) and injection pressures. The tests were terminated when no significant increase in oil recovery occurred after two consecutive cycles, leading to variations in the total number of cycles among the tests. Notably, the crushed sample tests achieved considerably higher oil recovery factors than those typically observed in the field due to enhanced surface areas and absence of confining stress (Dang 2019).

Figure 20(a) and **Figure 20(b)** depict the cumulative oil recoveries for tests conducted on sample EF1 using produced and enriched field gases, respectively. Both gases exhibit increasing oil recovery with rising pressure, extending beyond the measured VIT-MMP for each solvent-Eagle Ford oil pair. In the EF1 produced field gas tests, a slight increase in oil recovery is observed as injection pressure rises from 1000 psi below the MMP to the MMP, followed by significantly higher recovery at 1000 psi above the MMP. Conversely, the EF1 enriched field gas tests show a gradual increase in oil recovery below the MMP to the MMP, extending to pressures up to 2000 psi above the MMP. However, it is worth noting that the enriched field gas tests did not display the same level of recovery amplification above the MMP as observed for the produced field gas tests. In fact, the oil recovery for the enriched field gas test at the highest pressure of 2000 psi above the MMP (5450 psi) was lower (~56%) than that of the produced field gas test (~65%) at 1000 psi above the MMP (4850 psi).

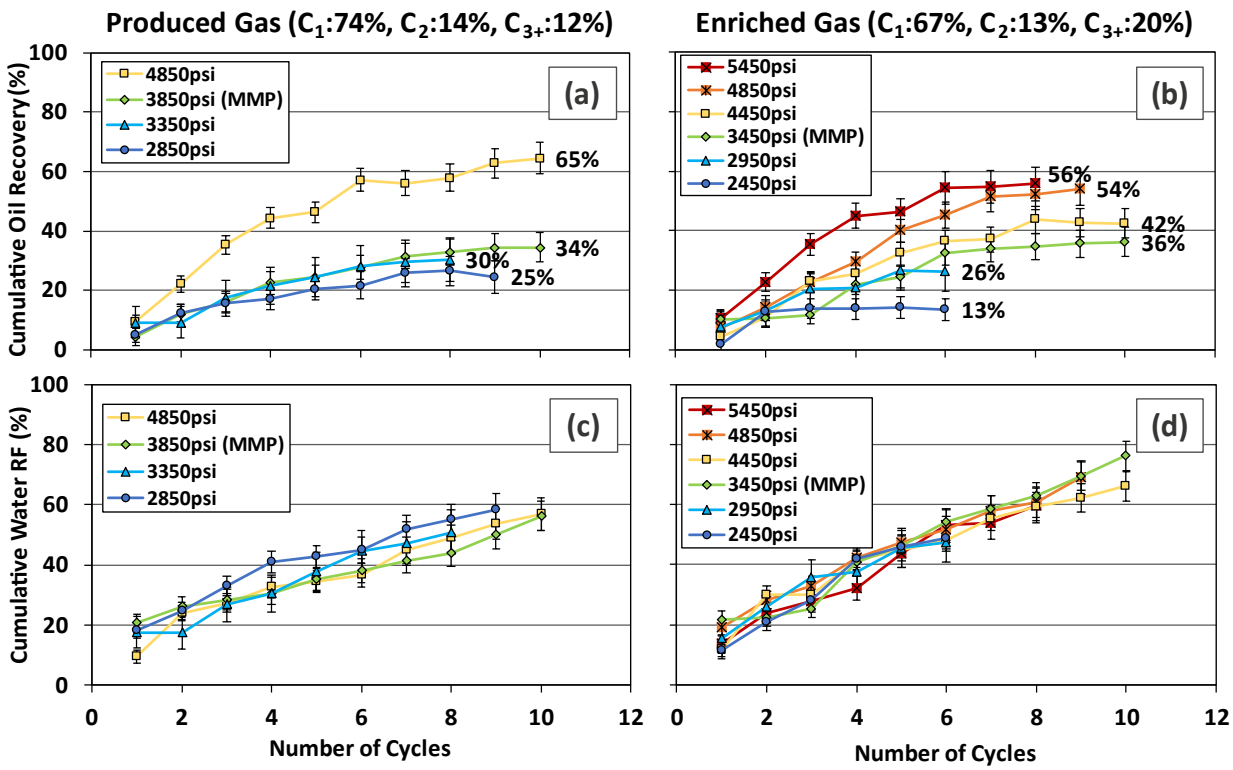

Figure 20. Overview of oil and water recovery during HnP tests on EF1 in varying solvent compositions and injection pressures. (a) oil recovery with produced field gas. (b) oil recovery with enriched field gas. (c) water recovery with produced field gas. (d) water recovery with enriched field gas.

The cumulative water production for tests conducted on sample EF1 using produced and enriched field gases is depicted in **Figure 20(c)** and **Figure 20(d)**, respectively. In these tests, water production exhibits a monotonically linear increase after each injection cycle, persisting through the later cycles. The results indicate that the composition of the field gas or injection pressure do not have a substantial impact on water production. The lack of correlation between water production and injection pressure suggests that capillary displacement is not the underlying mechanism driving the observed fluid production. Therefore, the trend in water production can be attributed to external diffusion of water during each injection cycle, which involves cyclic heating to reservoir temperature and exposure to low-humidity solvent gas.

Figure 21(a) through **Figure 21(d)** present analogous results for oil and water recoveries in produced and enriched field gas tests performed on sample EF2. Three additional tests were conducted on this sample: one using $scCO_2$ at 1000 psi above the MMP (P_{inj} = 3500 psi) as previously depicted in **Figure 18**, and two tests using immiscible helium (He) gas at the same minimum and maximum absolute pressures as the produced field gas tests (P_{inj} = 2850 psi and P_{inj} = 4850 psi). The He tests aimed to isolate the effects of pressure support and miscibility on oil recovery using an immiscible gas. Overall, sample EF2 exhibits similar trends to sample EF1: oil recoveries increase with injection pressure, extending beyond the MMP, and this effect is more pronounced in the produced field gas tests. Water production shows a monotonically linear increase with the injection cycles, with no discernible impact of the field gas composition or injection pressure. The results for the $scCO_2$ test at 3500 psi show faster oil recovery at lower absolute pressure compared to the field gases at high pressure (>4450 psi). A slightly larger water production trend is observed for $scCO_2$ (**Figure 21(d)**), likely due to the larger water diffusion coefficient in $scCO_2$ compared to hydrocarbon phase (Kravanja et al. 2018b). In contrast, the low oil recovery in the He gas tests conducted at the full range of injection pressures (2850 psi to 4850 psi) suggests that solvent-oil miscibility plays a critical role in controlling oil recovery. In fact, the immiscible He gas HnP at the highest injection pressure (4850 psi) yielded lower oil recovery (22%) than the produced field gas HnP (31%) at the lower pressure (2850 psi).

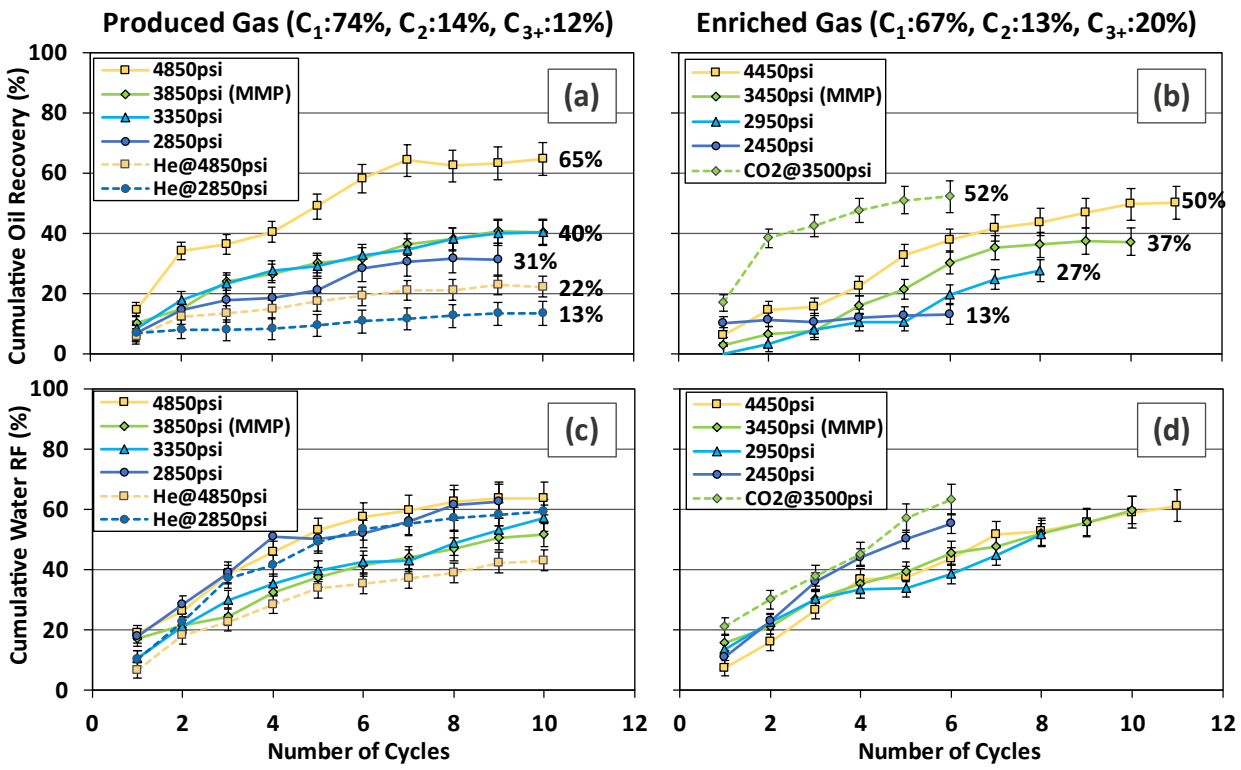

Figure 21. Analogous plots to Figure 20 for the HnP tests conducted on sample EF2. (a) oil recovery with produced field gas and helium (He). (b) oil recovery with enriched field gas and $scCO_2$. (c) water recovery with produced field gas and helium (He). (d) water recovery with enriched field gas and $scCO_2$.

Figure 22 summarizes cumulative oil recoveries for EF1 and EF2 (**Figure 22(a)** and **Figure 22(b)**, respectively) and water production for EF1 and EF2 (**Figure 22(c)** and **Figure 22(d)**, respectively) at the conclusion of the sixth injection cycle, which marked the furthest point for which all samples underwent HnP. A positive linear correlation between injection pressure and oil recovery is evident for both field gases, extending beyond the respective solvent-crude oil MMPs. In contrast, water production shows no significant relationship with injection pressure, indicating that capillary displacement is not a dominant driver for water removal. Injecting below each field gas-crude oil MMP shows no substantial difference in the performance of the field gases. However, produced field gas exhibits better performance than enriched field gas at injection pressures above the MMP.

Notably, immiscible He gas tests exhibit lower oil recovery than field gases, with $scCO_2$ outperforming the field gases. At injection pressures above the MMP, the average oil recovery for produced field gas is nearly three times higher than immiscible He gas and is similar to $scCO_2$ at a lower pressure (4850 psi compared to 3500 psi). Interestingly, even at injection pressures lower than the MMP, produced field gas performance remains approximately twice as high as immiscible helium gas. These observations underscore the influence of partial and complete miscibility on oil recovery and the better performance of $scCO_2$ as a solvent during HnP-EOR in ULR.

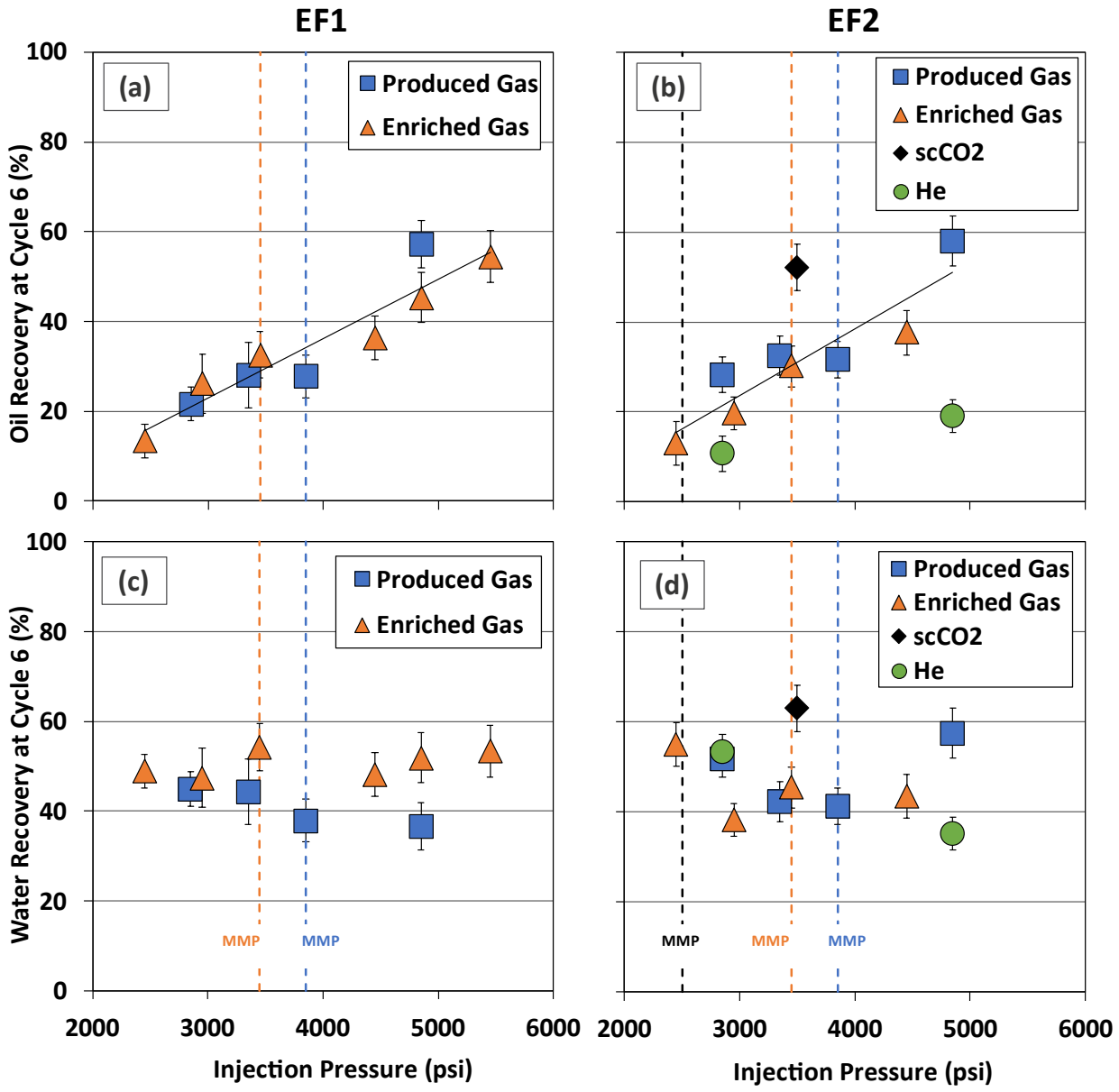

Figure 22. Cumulative recoveries at the sixth cycle, representing the maximum cycle reached in all samples. (a) EF1 oil recovery, with a positive linear trend for field gases extending beyond the MMP. (b) EF2 oil recovery, showing similar trends to EF1, including He gas lower performance and $scCO_2$ higher performance than field gas. (c) and (d) depict water production for both samples, with no pressure-related trend.

Figure 23 illustrates the relative contribution of movable hydrocarbon fractions (S11 to S15) to the total oil recovery in EF1 (left side) and EF2 (right side) determined through modified dry

pyrolysis. Relative recovery factors were calculated using **Equation 3.7**. The results emphasize that lighter fractions (S11 and S12) up to C_{17} significantly contribute to oil recovery, representing 40-60% of the total recovered oil. Importantly, the linear correlation between oil recovery and injection pressure, as shown in **Figure 22**, predominantly pertains to the lighter fractions (S11 and S12) and diminishes for heavier fractions (S13 to S15). Similar to **Figure 22**, immiscible He gas demonstrates lower performance compared to field gases, while $scCO_2$ exhibits higher performance than field gases. Additionally, there is no clear trend for the recovery of heavy fractions. The findings from modified dry pyrolysis indicate that variations in oil recovery during HnP EOR are driven by the preferential vaporization of lighter species in oil under favorable miscible conditions.

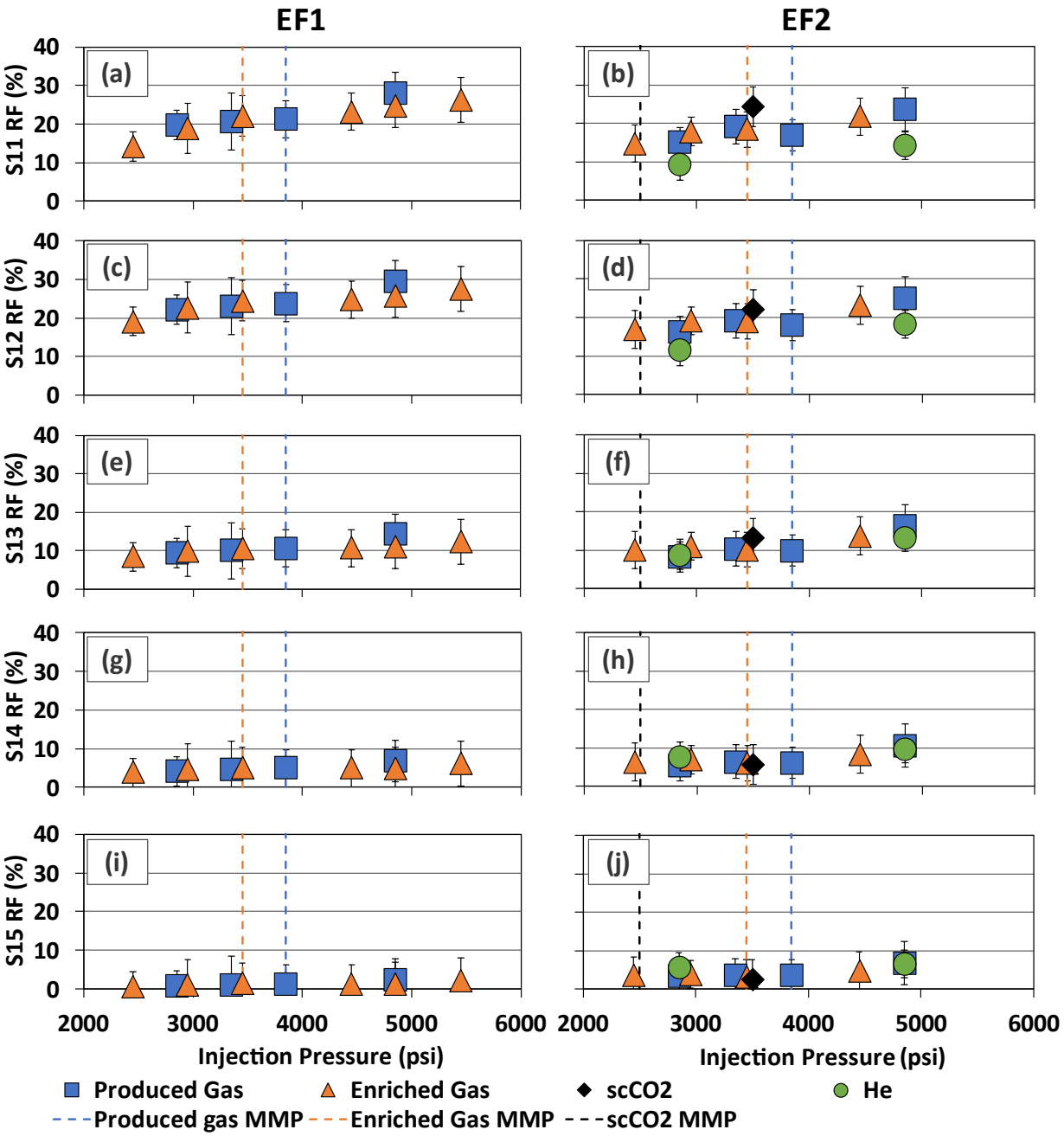

Figure 23. Relative contribution of the five movable hydrocarbon subpeaks (S1) in modified dry pyrolysis to the total oil. EF1 and EF2 results are shown on the left and right side, respectively. Notably, the lighter fractions of the oil within S11 and S12 (up to C_{17}) significantly influence overall oil recovery, irrespective of the miscibility condition. In tests with immiscible helium gas, lighter oil fractions exhibit lower recovery compared to field gases, while $scCO_2$ outperforms field gas. No trend is observed for the heavier oil fractions.

Petrophysical characterization results following HnP-EOR tests using produced and enriched field gases on both Eagle Ford samples are discussed in **Appendix A**. In summary, MICP pore throat size distributions and isothermal N_2 adsorption pore size distributions reveal an increase in nanopore volume due to fluid removal. Notably, the N_2 adsorption PSD appears to better reflect the effect of increasing pressure and fluid removal on enhancing nanopore volume. SEM images of a high-recovery sample (EF2, produced field gas, 4850 psi or 1000 psi above the MMP) before and after HnP-EOR, indicate that organic matter regions exhibit reduced porosity, likely due to a film coating that clogs organic pores due to HnP process. Further analysis with cross-section images obtained from FIB-SEM suggest that pore blockage primarily occurs at the surface, with deeper porosity remaining unaffected. Molecular dynamics insights (Perez and Devegowda 2020) suggest that heavy hydrocarbon fractions adhere to the surface due to their lower energy, potentially forming the observed film in the SEM images. Overall, no major alterations in the microstructure are observed after HnP-EOR in all field gas tests performed.

Shale oil reservoir HnP-EOR

Compositional simulations within the shale oil reservoir model were employed to gain insights into solvent efficiency and the carbon intensity of HnP-EOR operations in ULR. Following 2.5 years of primary production with very low recovery (~1%), various HnP scenarios were simulated. These scenarios involved different solvent compositions (produced and enriched field gases, and $scCO_2$) and increasing injection pressures above the initial average reservoir pressure (6000 psi). Notably, CMG WinProp phase behavior simulations confirmed the miscibility of the three solvents with crude oil at the initial average reservoir pressure of 6000 psi and a temperature of 150 °F.

Figure 24 illustrates the outcomes of these scenarios for the three solvents at injection pressures of 6000 psi, 8000 psi, and 10000 psi. Cumulative oil recoveries over time (**Figure 24(a)**) exhibit enhanced performance with rising injection pressures, aligning with experimental results. However, the consistent linear trends observed in **Figure 24(b)** imply that incremental oil recoveries remain relatively stable after each cycle, in contrast to the experimental results that showed oil recovery curves flattening over time. This variance can be attributed to the considerably larger surface in the crushed sample experiments compared to the shale oil reservoir model. Extending the simulation duration beyond a decade of operation could potentially reveal a similar flattening in the recovery curve, although this would be computationally intensive.

Nonetheless, the compositional simulation results indicate that, unlike the experiments, produced field gas displays lower performance compared to enriched field gas and $scCO_2$. Moreover, at higher injection pressures, $scCO_2$ exhibits a slight advantage over enriched field gas, showing the best performance. The differences in field gas performance between the shale oil reservoir model and experiments may be attributed to underlying factors such as methane adsorption (Wang et al. 2019) and nanopore confinement (Du and Nojabaei 2021), which were not considered in the simulations. Molecular dynamics simulations could potentially provide insights into these effects and the disparities in field gas performance at elevated pressures (Perez and Devegowda 2020).

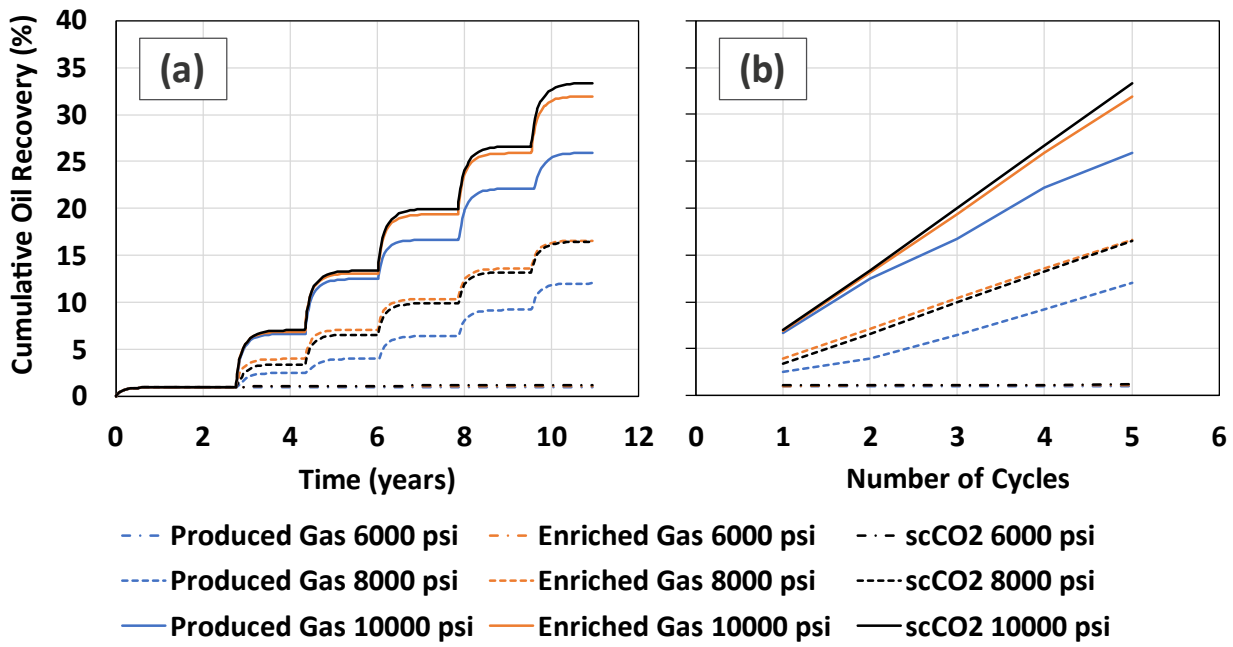

Figure 24. Simulation results using three solvents at different injection pressures (6000 psi, 8000 psi, and 10000 psi). (a) increasing pressure leads to higher cumulative oil recoveries over time, aligning with experimental results. (b) consistent linear trends in incremental oil recoveries, unlike the experiments that showed flattening curves over increasing cycles. This difference is due to the larger surface area in experiments. The simulations indicate that, contrary to experiments, produced field gas performs worse than enriched field gas and $scCO_2$. Additionally, at higher pressures, $scCO_2$ appears to show the best performance.

To assess the carbon intensity of the $scCO_2$ HnP-EOR process in ULR, the moles of CO_2 injected and produced were analyzed at varying injection pressures, as shown in **Figure 25**. **Figure 25(a)** and **Figure 25(b)** display the amount of injected $scCO_2$ as a function of time and the number of cycles, respectively. Corresponding results for the amount of produced $scCO_2$ are depicted in **Figure 25(c)** and **Figure 25(d)**. As pressure increases, the quantities of injected and produced $scCO_2$ also rise, primarily due to compressibility and increased solubility in the oil at elevated pressure. In **Figure 25(b)**, the amount of $scCO_2$ injected shows a linear increase with the number of cycles at the same injection pressure. However, an upward deviation from this linear trend is

evident in **Figure 25(d)** at high pressures, indicating excess recovery of the initial CO_2 present in the crude oil (~1mol%) as injection pressure rises.

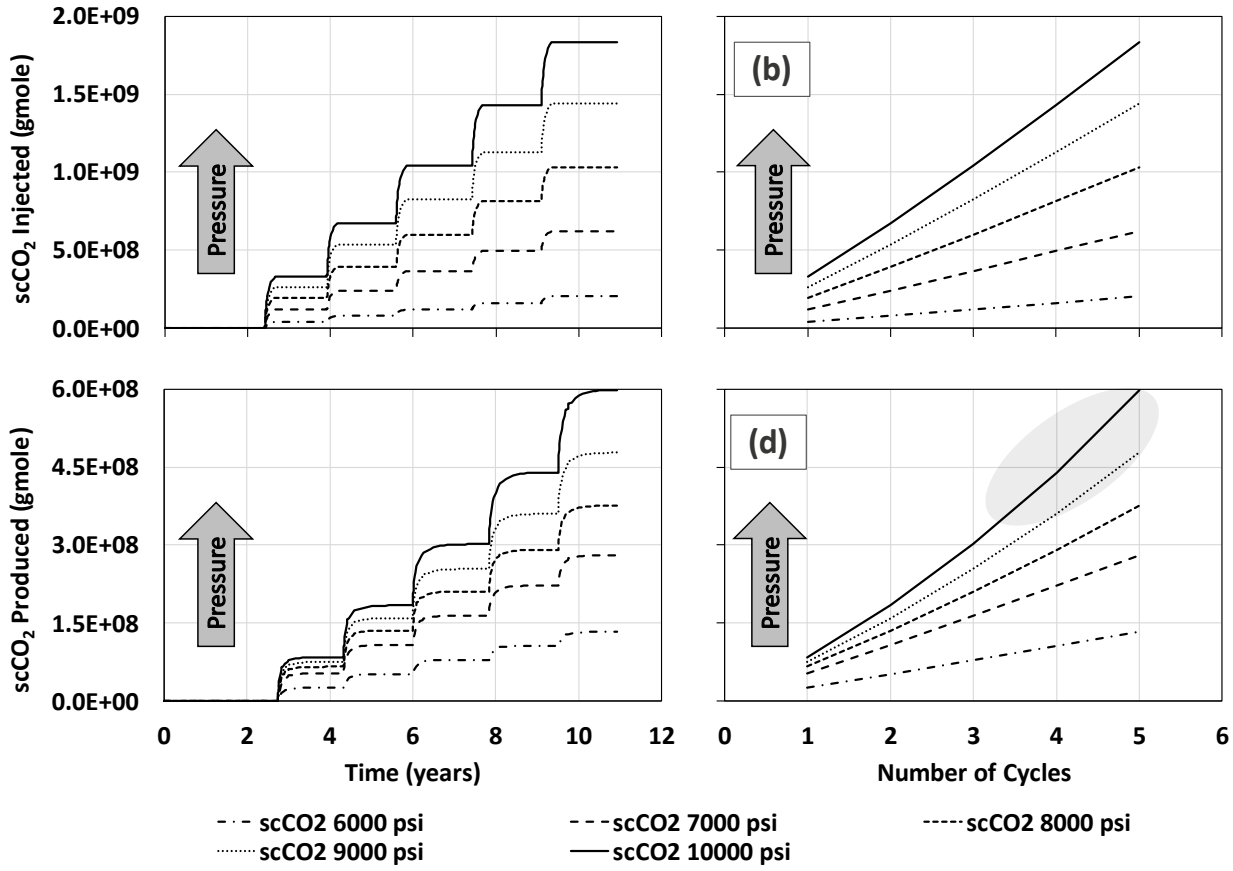

Figure 25. Insights into the amount of $scCO_2$ injected and produced (in gmoles) under different scenarios. (a) and (b) cumulative $scCO_2$ injected over time and across cycles. (c) and (d) corresponding results for $scCO_2$ produced. Increasing pressure leads to higher quantities of injected and produced $scCO_2$, influenced by compressibility, and enhanced solubility in the oil at elevated pressures. In (b), a linear increase in the amount of injected $scCO_2$ is observed with the number of cycles at a consistent injection pressure. However, (d) shows an upward deviation from this linear trend at high pressures, indicating the excess recovery of the initial $scCO_2$ content in the crude oil as injection pressure rises.

Figure 26 presents the ratio of produced to injected $scCO_2$ at varying injection pressures, offering insight into carbon intensity. Higher values indicate substantial recovery of injected $scCO_2$ during

the "puff" stage, while lower ratios suggest greater $scCO_2$ storage and a less carbon-intensive process. The findings reveal that, as injection pressure rises, the ratio of produced-to-injected $scCO_2$ decreases, reflecting improved $scCO_2$ solubility and a less carbon-intensive operation. Furthermore, at identical pressures, the ratio remains relatively consistent at the conclusion of each additional "puff" cycle. Nevertheless, at elevated pressures, a slight rise in this ratio over successive cycles is observed, aligning with the upward deviation from the linear trend in production presented in **Figure 25(d)**. After five HnP cycles or a decade of operation, this ratio converges to approximately 33%, indicating that in the model, roughly 67% of the injected $scCO_2$ is stored in the subsurface.

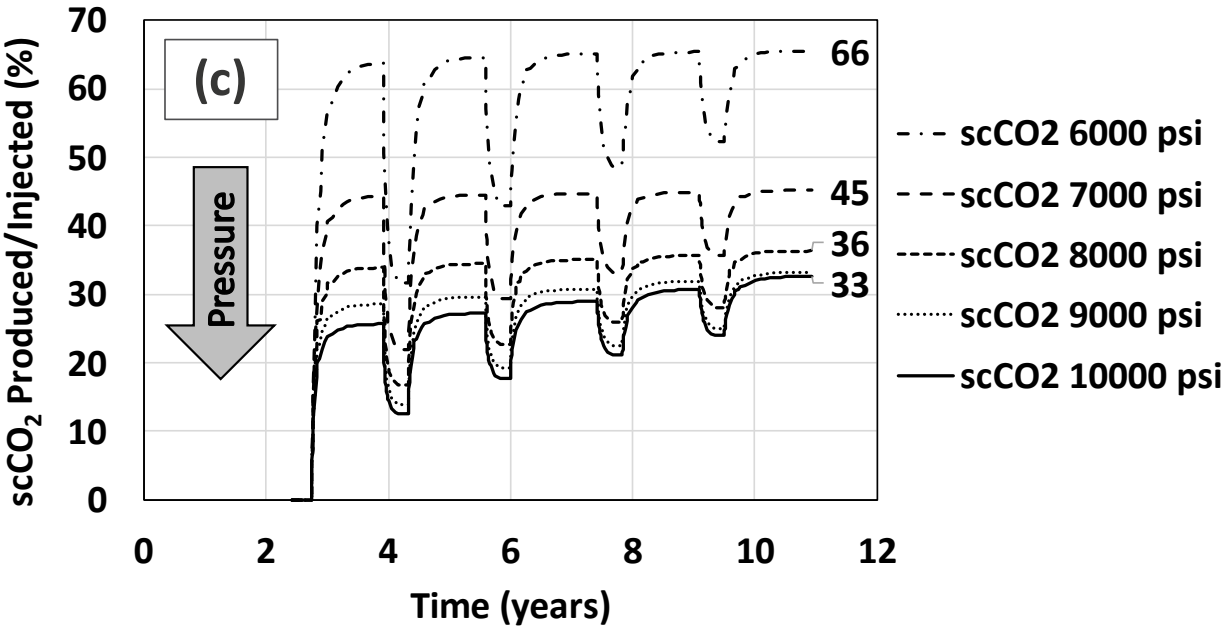

Figure 26. Ratio of produced to injected $scCO_2$ at varying injection pressures. Higher values indicate recovery of injected $scCO_2$, implying carbon intensity, while lower ratios suggest increased $scCO_2$ storage and less carbon intensity. Results show that with rising injection pressure, the ratio decreases due to enhanced $scCO_2$ solubility, indicating a less carbon-intensive process. At the same pressure, the ratio remains fairly constant after each cycle, but at high pressures, it exhibits a slight increase over successive cycles. After five HnP cycles or a decade of

operation, the ratio converges to about 33%, implying that approximately 67% of injected $scCO_2$ is stored underground.

Chapter 5. Considerations: CO_2-Geostorage

The examination of interactions between $scCO_2$, fluids, and rock is fundamental to ensuring the effectiveness and sustainability of carbon geostorage (CGS), a critical strategy for combatting global warming and achieving net-zero emissions. A specific focus of this examination pertains to the interactions between CO_2 and brine in the subsurface, as these interactions have the potential to induce geochemical reactions within the storage and confining zones, consequently affecting the efficiency and integrity of CGS (Gaus et al. 2005, Rosenbauer et al. 2005, Espinoza et al. 2011). This chapter aims to provide an up-to-date overview of the essential CO_2-fluid-rock interactions relevant to CO_2 geostorage and to explore the potential ramifications of induced geochemical reactivity on these properties, as well as their implications for the efficiency and integrity of CGS.

Phase behavior

Understanding the PVT properties of CO_2 as a free-phase in the subsurface is essential in the design of a CO_2-geostorage project (Smit et al. 2014). **Figure 27** illustrates the phase diagram of pure CO_2 within the range of pressure and temperature conditions typically encountered in sedimentary basins (Zhao et al. 2015c). The minimum injection depth for CO_2 storage is approximately 800 m, equivalent to the critical pressure of CO_2 (P_c ~ 1070 psi), considering a standard hydrostatic gradient (0.433 psi/ft). Beyond the critical point, CO_2 enters the supercritical region, displaying increased density (**Figure 28**) (van der Meer et al. 2009, Span and Wagner 2015). The rise in CO_2 density (ρ_{CO_2}) with depth beyond 800 m augments both the volume of stored $scCO_2$ within the reservoir (**Equation 1.1**) and the capillary seal height (h) (**Equation 1.4**). Nevertheless, deep

injection leads to elevated compressor expenses, necessitating consideration of an optimal injection depth window (Vilarrasa and Rutqvist 2017).

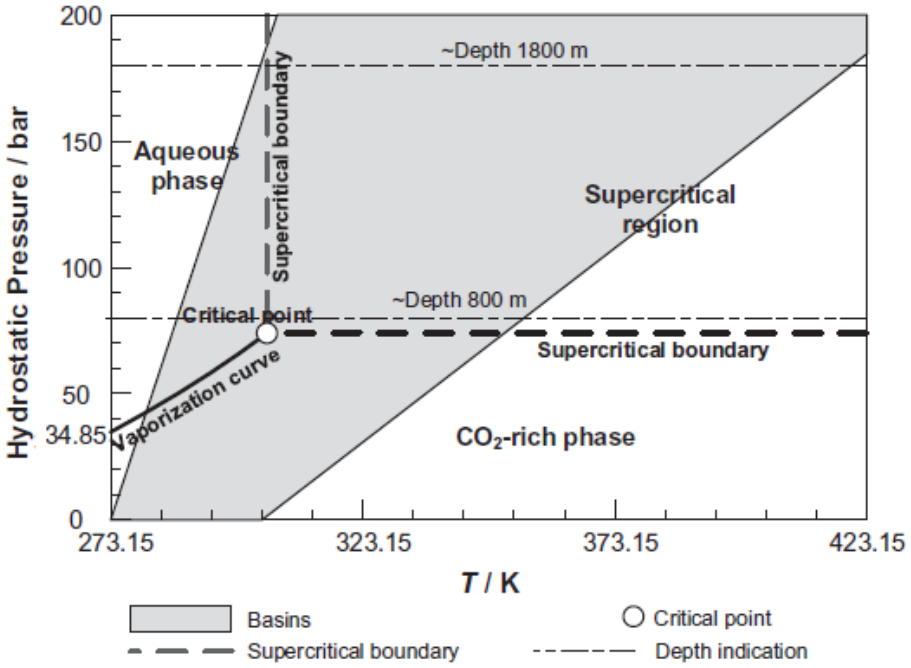

Figure 27. Phase behavior of CO_2 and the pressure-temperature envelope in sedimentary basins (Zhao et al. 2015c).

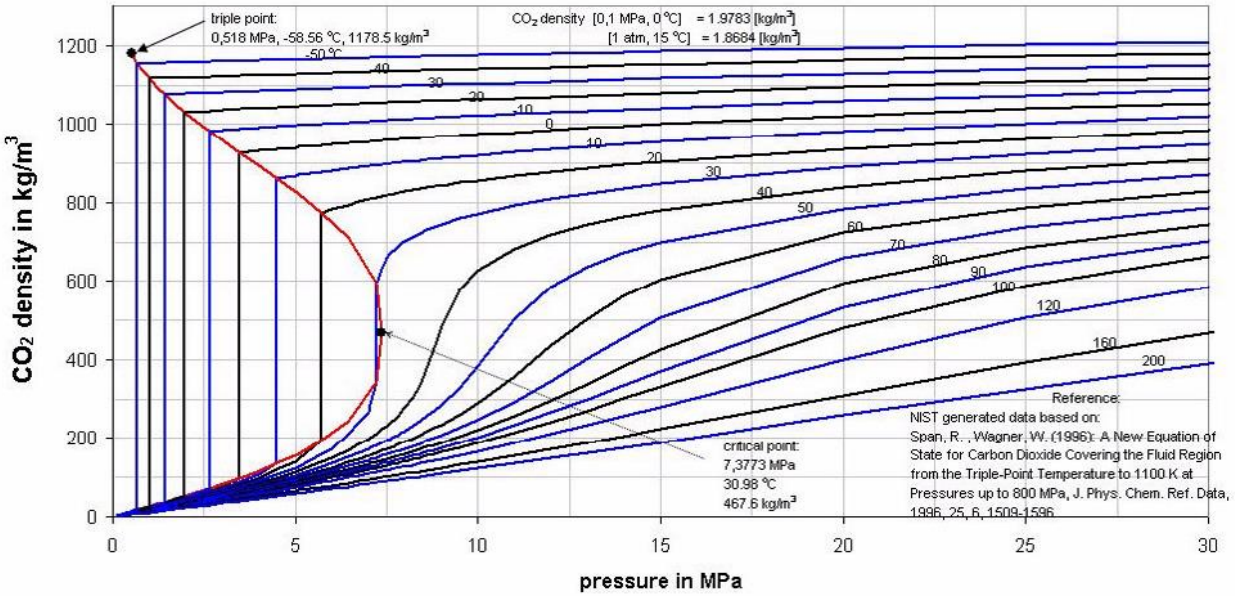

Figure 28. PVT properties of pure CO_2 (van der Meer et al. 2009, Span and Wagner 2015).

In the binary CO_2-H_2O system, the interaction between the components can result in phase densities that differ from those of pure components. King et al. (1992) found no significant difference between the density of a water-saturated CO_2 phase and that of pure CO_2 at 77 °F. Hebach et al. (2002) extended this observation to higher pressures (up to 4350 psi) and temperatures (up to 122 °F). However, the density of the CO_2-rich aqueous phase can significantly exceed that of the pure aqueous phase due to the dissolution of CO_2 in water, leading to the formation of carbonic acid species with a higher molecular density than H_2O (Garcia 2001). Spycher et al. (2003) developed a model that accurately predicts the density of the CO_2-rich water phase, extending the work of King et al. (1992) to high temperatures and pressures of up to 212 °F and 8700 psi (**Equation 5.1**):

$$\frac{1}{\rho_{W,sat}} = \frac{(1-w)}{\rho_{W,PC}} + \frac{w}{\rho^*_{CO_2}} \tag{5.1}$$

where $\rho_{W,sat}$ is the density of the CO_2-saturated water phase, w is the mass fraction of dissolved CO_2, $\rho_{W,PC}$ is the density of the pure water, $\rho^*_{CO_2}$ is the inverse of the partial specific volume of dissolved CO_2 in water. Parkinson and De Nevers (1969) showed that the quantity $\rho^*_{CO_2}$ is weakly dependent on the amount of dissolved CO_2, and for temperatures below 572 °F, independent of pressure. In the range of temperatures of 32 °F < T < 212 °F, $\rho^*_{CO_2}$ is also nearly independent of temperature, being close to 1260 kg/m^3. In deep saline aquifers, the increased density of brine promotes convective mixing between phases, facilitating a more uniform distribution of injected CO_2 throughout the storage reservoir (Ennis-King and Paterson 2005, Emami-Meybodi and Hassanzadeh 2015).

The mutual solubility of the CO_2-water/brine system under subsurface conditions has been experimentally investigated in several studies (Weiss 1974, King et al. 1992, Diamond and Akinfiev 2003, Spycher et al. 2003, Duan et al. 2006, Zhao et al. 2015c, Zhao et al. 2015b, Zhao et al. 2015a, Steel et al. 2016, Chabab et al. 2021). **Figure 29** illustrates the pressure-composition diagram of the CO_2-H_2O system at temperatures up to 212 °F and pressures up to 4350 psi (Zhao et al. 2015c). On the left side of the graph (circles), the mole fraction of CO_2 in the aqueous phase is represented, while on the right side (triangles), it indicates the mole fraction of CO_2 in the gas phase. The three-phase lines denote the vicinity of the critical point (T_c ~ 304 K, P_c ~ 73 bar). Under subsurface conditions (above the critical point), the change in the composition of the CO_2-rich gas phase is negligible (x_{CO_2}: 1 to ~0.995). In contrast, the mole fraction of dissolved CO_2 in H_2O increases with rising pressure and decreasing temperature. At 323 K and 150 bar (122 °F and 2175 psi), the mole fraction of dissolved CO_2 in the aqueous phase is approximately 2.2 mol% (x_{CO_2}~0.022).

Utilizing **Equation 5.1** and pure component data from NIST Chemistry WebBook (Shen 2023), the density of the aqueous phase increases by nearly 2 wt.% (from 994.5 to 1015.2 kg/m^3 for pure H_2O and CO_2-rich H_2O, respectively). In brine systems, the solubility of the non-polar CO_2 substance diminishes with an elevated salt concentration in the aqueous phase, a phenomenon known as the "salting-out effect" (Steel et al. 2016, Ho and Ilgen 2017, Chabab et al. 2021). Detailed discussion on the influence of ion composition on the solubility of CO_2 in brine is given by Zhao et al. (2015b).

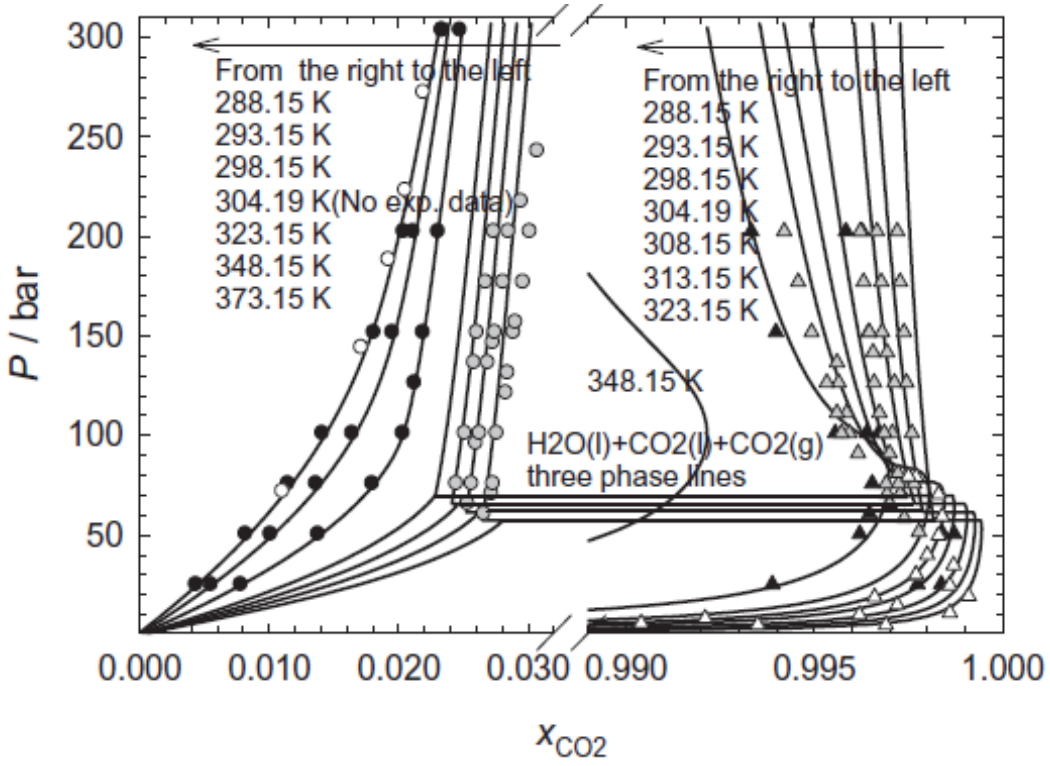

Figure 29. Pressure-composition phase diagram for the CO_2-H_2O system at P-T conditions applicable to CO_2 storage. In this diagram, the circles correspond to the mole fraction of CO_2 in the aqueous phase, while the triangles indicate the mole fraction of CO_2 in the gas phase (Zhao et al. 2015c).

Interfacial tension

The interfacial tension between carbon dioxide and water/brine systems has been extensively studied (Massoudi and King 1974, Chun and Wilkinson 1995, da Rocha et al. 1999, Hebach et al. 2002, Park et al. 2005, Akutsu et al. 2007, Sutjiadi-Sia et al. 2008, Chiquet et al. 2007b, Bachu and Brant Bennion 2009, Bachu and Bennion 2009, Chalbaud et al. 2009, Aggelopoulos et al. 2010, Georgiadis et al. 2010b, Aggelopoulos et al. 2011, Bikkina et al. 2011, Li et al. 2012, Pereira et al. 2016). Experimental determination of the interfacial tension primarily relies on two traditional techniques: the capillary-rise method and axisymmetric drop shape analysis (ADSA). These methods fundamentally hinge on solving the Young-Laplace equation at the interface

between the gas and water (Behroozi 2022). Overall, drop-shape analysis is the preferred method due to its superior accuracy, broad measurement range, and better reproducibility (Xing et al. 2013).

For conducting CO_2-water/brine interfacial tension measurements using ADSA, two configurations are employed: (a) pendant-drop, and (b) rising-drop/bubble (**Figure 30**). The nomenclature "drop/bubble" is adopted for the rising technique to account for the phase behavior of CO_2 below and above the critical point. In the pendant-drop configuration, a sufficiently large droplet of water/brine is carefully extruded through a needle under a surrounding CO_2 phase. Alternatively, the rising-drop/bubble configuration is the systematic opposite (CO_2 droplet/bubble submerged into an external aqueous phase). In both cases, gravity forces acting on the drop/bubble are balanced by the interfacial forces between the two fluid phases.

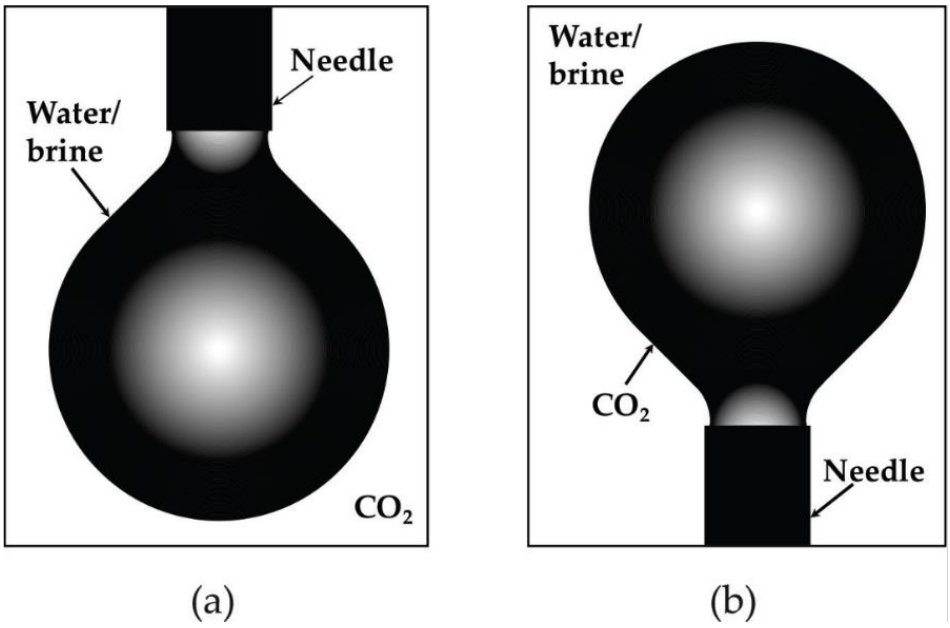

Figure 30. The two experimental configurations to determine the CO_2-water/brine IFT using ADSA. (a) aqueous droplet in the surrounding CO_2 phase (pendant-drop) and (b) CO_2 droplet/bubble in the surrounding aqueous phase (rising-drop/bubble) (Prem and Imran 2018).

After fluid-equilibrium has been established (i.e., no mass transfer and no chemical reaction between the two phases), the interfacial tension is determined based on **Equation 5.2**, whose mathematical derivation can be found elsewhere (Andreas et al. 1938, Hansen and Rødsrud 1991, Río and Neumann 1997, Yeow et al. 2008, Berry et al. 2015):

$$\gamma = \frac{(\Delta\rho)gR_o^2}{\beta} \tag{5.2}$$

Here, γ represents the interfacial tension, $\Delta\rho$ is the density difference between the two fluids, g is the gravity constant, R_o is the radius of curvature at the drop/bubble apex, and β is a shape factor. The shape factor corresponds to the dimensionless Bond number, which characterizes the ratio of gravitational forces to surface forces. Precise determination of the interfacial tension relies on accurate density values for the fluid phases (Hebach et al. 2002, Chiquet et al. 2007b, Pereira et al. 2016) and calculation of the size parameters, R_o and β. These size parameters are obtained through proper system calibration and iterative fitting of the drop contour (Bashforth 1883). A large value of β (indicating the dominance of gravity forces over surface forces) results in a "pendant-shaped" drop, providing a unique combination of R_o and γ and reducing numerical errors. In contrast, "spherical-shaped" drops generate lower β values, leading to multiple combinations of R_o and γ and increased measurement errors (Neeson et al. 2014). Therefore, it is generally recommended to measure the interfacial tension in the gravity-dominated regime.

Several other factors in the experimental design should be considered to obtain reproducible interfacial tension data. These include placing the thermocouple as close as possible to the droplet/bubble phase (Kvamme et al. 2007), thorough solvent cleaning between tests to prevent contamination (Prem and Imran 2018), adequate pre-equilibration times between the two fluid

phases (Hebach et al. 2002, Yang et al. 2005), and measuring the interfacial tension as soon as it reaches equilibrium to minimize prolonged evaporation of the droplet phase (Tewes and Boury 2004).

Table 3 provides comprehensive information on the measurement conditions of the selected studies, encompassing measurement techniques, gas and liquid phase compositions, equilibration methods and times, methods used for evaluating the densities of each phase, reported density difference ranges, temperature and pressure ranges, aqueous phase molalities, and reported interfacial tension values. The selection criteria for the studies included in this analysis are based on two main factors: (1) pre-equilibration of both fluid phases, and (2) the availability of experimental measurements or modeling of aqueous-phase density, along with the inclusion of reported density difference.

Table 3. Measurement conditions for CO_2-water/brine IFT data selected in this study.

Reference	Technique	Liquid	Equilibration		Fluid densities		T	P	M	IFT
			Method	Time	Method	$\Delta\rho$ [kg/m^3]	[°F]	[psi]	[mol/kg]	[mN/m]
Chalbaud et al. (2009)	RD/B	H_2O+NaCl	GC	min	theoretical	95-980	77-212	700-3700	0.1-2.7	25-48
Chiquet et al. (2007b)	PD	H_2O, H_2O+NaCl	MV	min	measured	40-900	95-230, 95	700-6500	0, 0.3	23-46, 30-45
Aggelopoulos et al. (2010)	RD/B	H_2O+$CaCl_2$	GC	24hr	theoretical	90-1110	77-212	750-3700	0.05-2.7	28-56
Aggelopoulos et al. (2011)	RD/B	H_2O+NaCl+$CaCl_2$	GC	24hr	theoretical	90-1050	77-212	750-3800	0.1-3	27-54
Bikkina et al. (2011)	PD	H_2O	SV	24hr	theoretical	110-970	77-140	200-3000	0	22-61
Li et al. (2012)	PD	H_2O+NaCl+KCl	SV	min	theoretical	40-1120	77-347	300-7300	1-5	19-66
Pereira et al. (2016)	PD	H_2O	SV	min	measured	55-990	77-200	50-10000	0	13-69

Technique: PD=pendant-drop, RD/B=rising-drop/bubble.

Equilibration: GC=gas cap, MV=mixing vessel, SV=static vessel.

Multiple experimental investigations have explored the impact of pressure and temperature on the interfacial tension (IFT) between pure water and CO_2. **Figure 31** provides a synthesized representation of the IFT data collected from **Table 3**, showing variations in response to changes in pressure and temperature. When proper experimental protocols are followed, which include pre-equilibration and accurate density determinations, a notable consensus emerges in the literature regarding the trends in CO_2-H_2O IFT, predominantly concerning pressure.

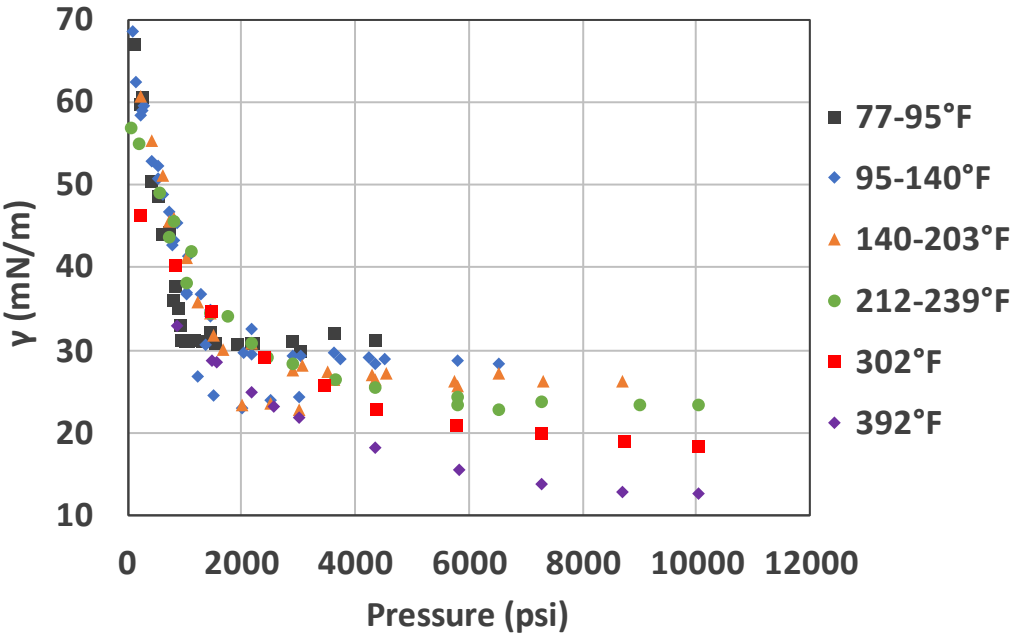

Figure 31. Averaged CO_2-H_2O IFT as function of pressure and at different temperatures using the dataset from Table 3. Notably, the IFT exhibits a distinct shift in the linear trend with pressure, especially below and above its critical point. The IFT in the supercritical CO_2 region also appears to decrease at elevated temperatures.

Below the CO_2 critical point ($P_c \approx 1070$ psi) and above the critical temperature ($T_c \approx 88$ °F), where CO_2 exists as a gas, IFT exhibits a steep and linear decrease with increasing pressure along the same isotherm. This phenomenon is primarily attributed to the increased gas solubility in the so-called Henry regime (Chiquet et al. 2007b). In contrast, above the critical point but below boiling point of H_2O (212 °F at standard pressure), the IFT undergoes a gradual reduction with increasing

pressure, eventually reaching a pseudo plateau at around 26 mN/m (Chalbaud et al. 2009, Hebach et al. 2002). The relatively weak decline in IFT with pressure in the supercritical CO_2 state is due to its *liquid-like* characteristics and substantially reduced compressibility (Georgiadis et al. 2010b). Pereira et al. (2016) highlighted that this trend transition becomes less evident with increasing temperature, especially beyond 212 °F. According to their findings, elevated temperatures can lower the pseudo plateau IFT of 26 mN/m to 18.4 mN/m (at 302 °F) and further to 12.6 mN/m (at 392 °F).

When considering temperatures below the boiling point of H_2O, the CO_2-H_2O IFT shows a less pronounced trend with temperature along the same isobar. This can be attributed to three main competing factors as temperature increases (Xing et al. 2013): the weakening of intermolecular forces lead to IFT reduction, while greater decrease in bulk CO_2 phase density (in comparison to H_2O phase density) yields increased density differences, which added to the reduced gas solubility, contribute to IFT increase. These competing effects have led to inconsistencies in the literature concerning measured trends of CO_2-H_2O IFT with temperature (see Chiquet et al. (2007b), Bachu and Bennion (2009), Georgiadis et al. (2010b)). In practical applications, these variations imply minor IFT deviations with temperature, which are overshadowed by the more significant IFT impact of pressure. Nevertheless, **Figure 31** underscores the need to account for temperature effects on IFT during CO_2 storage in deep reservoirs where high temperature conditions may occur (Pereira et al. 2016).

The impact of salinity in the aqueous phase on the CO_2-H_2O IFT interfacial tension has been a subject of investigation by various researchers (Chiquet et al. 2007b, Bachu and Bennion 2009, Chalbaud et al. 2009, Aggelopoulos et al. 2010, Aggelopoulos et al. 2011, Li et al. 2012). **Figure**

32, based on Chalbaud et al. (2009), presents the CO_2-H_2O IFT in the presence of sodium chloride as a function of molality (M = moles of solute per kilogram of solvent), pressure, and temperature. With increasing temperature (from 81 °F up to 212 °F), the transition between the two CO_2-H_2O IFT trends with pressure (initial significant decrease followed by flattening) extends to higher pressures, regardless of the salt concentration. Prior to reaching the pseudo plateau IFT, an increase in NaCl molality results in a linear IFT increase in comparison to pure H_2O. This increase becomes more pronounced at elevated temperatures. Beyond the pseudo plateau, the average IFT increase with molality compared to pure H_2O becomes temperature-independent (at $81\ °F \leq T \leq 212\ °F$), maintaining a consistent slope ($\frac{\delta\gamma}{M} = 1.43$) (**Figure 33**).

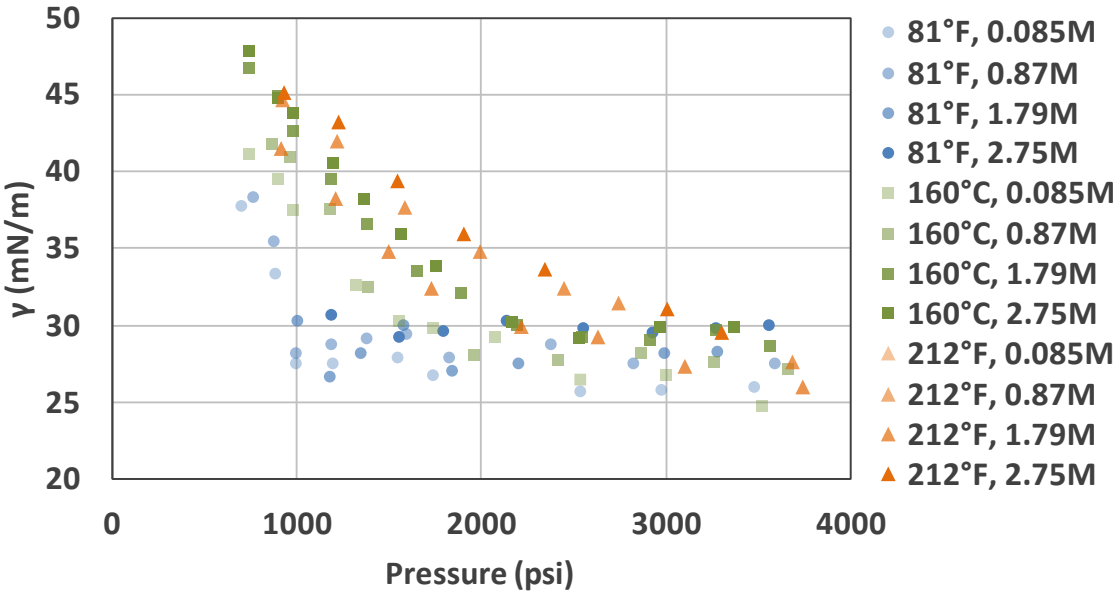

Figure 32. CO_2-brine (NaCl) IFT as function of molality, pressure, and temperature (Chalbaud et al. 2009).

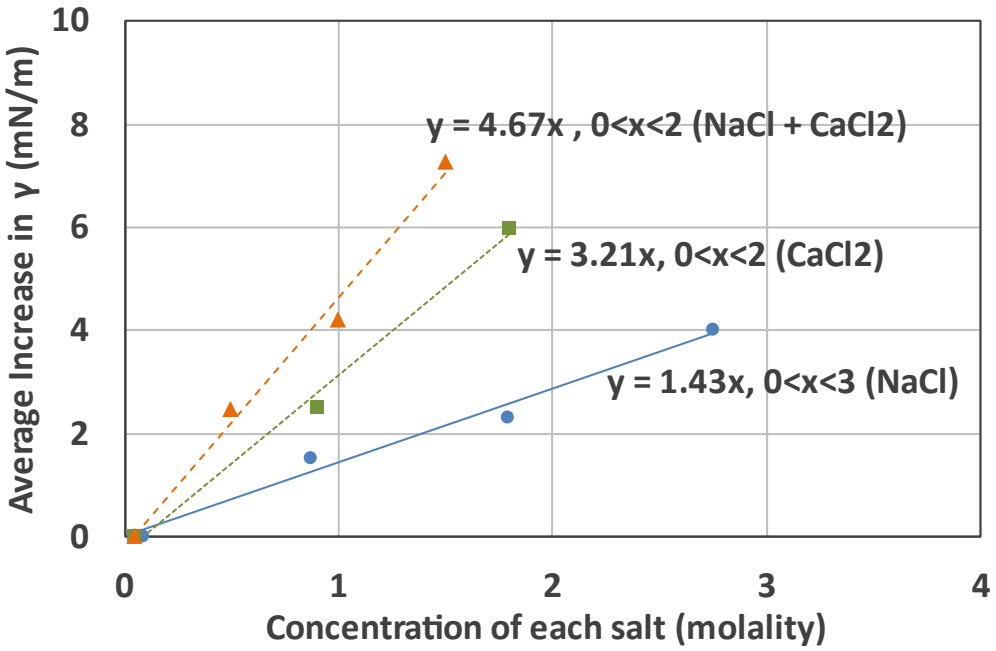

Figure 33. Effect of salt valence and molality on the CO_2-H_2O IFT (Aggelopoulos et al. 2011). The IFT data represent the averages of the pseudo plateau IFTs for each temperature (81 °F, 160 °F, 212 °F). The average IFT increase is relative to the pseudo plateau IFT of pure water ($\sim\gamma_{H_2O}\sim 26 mN/m$).

Figure 33 also illustrates the impact of salt valence on CO_2-brine IFT. Aggelopoulos et al. (2010) and Aggelopoulos et al. (2011) examined the effect of salt composition on the IFT by conducting measurements under the same pressure and temperature conditions as Chalbaud et al. (2009) using $CaCl_2$ and an equimolar mixture of NaCl and $CaCl_2$. They observed a more substantial increase in the average pseudo plateau IFT when using $CaCl_2$ ($\frac{\delta\gamma}{M} = 3.21$). Interestingly, the average increase in the pseudo plateau IFT for an equimolar mixture of NaCl and $CaCl_2$ closely approximated the sum of the individual IFT increases for each salt alone ($\frac{\delta\gamma}{M} = 4.67 \sim 3.21 + 1.43$). This linear increase in IFT with salt molality and valence is attributed to the presence of structure-making cations and structure-breaking anions concentrated at the gas-water interface (Soleymanzadeh et al. 2021). Structure-making cations can effectively align the dipoles in H_2O molecules and become

solvated in the bulk aqueous phase (Leroy et al. 2010). A reduction in these cations at the interface leads to an attraction of water molecules towards the bulk phase, consequently increasing interfacial tension (Pegram and Record 2007). Chalbaud et al. (2009) proposed that this increase in IFT with brine is proportional to the ratio of cation charge (z^+) to the cation surface area (r^2). However, Mutailipu et al. (2018) examined the influence of the main cations present in formation brine (e.g. Na^+, K^+, Ca^{2+}, Mg^{2+}) on CO_2-IFT and did not observe a significant variation in IFT with respect to cation valence. The $\frac{z^+}{r^2}$ ratio follows the Hofmeister sequence (Hyde et al. 2017):

$$Cs^+ < Rb^+ < NH_4^+ < K^+ < Na^+ < Li^+ < Ca^{2+} < Mg^{2+}$$

The presence of impurities (e.g. H_2S, SO_2, N_2, Ar, CH_4, H_2) in the CO_2 stream and its effect on the water/brine IFT has been experimentally investigated by Shah et al. (2008), Saraji et al. (2014), Al-Yaseri et al. (2015), Kravanja et al. (2018a), Liu et al. (2016), and Dalal Isfehani et al. (2023), respectively. The total amount of impurities (vol.%) in the CO_2 stream can be as large as 5-10%, especially in the oxy-fuel and pre-combustion capture processes (Oosterkamp and Ramsen 2008). Shah et al. (2008) reported similar trends in the H_2S-H_2O IFT to the CO_2-H_2O IFT. γ_{H_2S} decreases with increasing pressure levelling off around 9-10 mN/m at higher pressures (P > 1700 psi) and higher temperatures (T > 161 °F). The pseudo plateau γ_{H_2S} was close to 30-40% of the pseudo plateau γ_{CO_2}, stressing the effect of acid gas on the H_2O IFT. The CO_2-H_2S mixture with H_2O (70:30 mol% H_2S:CO_2) was observed to be similar in IFT to the molar averages of the CO_2-H_2O and H_2S-H_2O binary mixture IFTs. Similarly, Saraji et al. (2014) observed a linear decrease in the CO_2-brine IFT with increasing SO_2 content (up to 6 wt.%) of 29 mN/m (pure CO_2) as low as 18 mN/m at 3000 psi, 140 °F, and 1 M brine.

On the other hand, Al-Yaseri et al. (2015) reported an N_2-CO_2 mixture IFT (50:50 mol% N_2:CO_2) with brine (0.5 wt.% NaCl) of around 41 mN/m at 1900 psi and 113 °F. This value was much closer to the pure CO_2-brine IFT as compared to N_2-brine (39 mN/m to 61 mN/m, respectively). Kravanja et al. (2018a) also reported no significant difference in the CO_2 IFT with formation brine by including Ar (0-10 vol.%) as compared to pure CO_2 IFT (P up to 5800 psi, T: 104-194 °F). As an application for CO_2 storage in depleted gas reservoirs, Liu et al. (2016) measured the CH_4-CO_2 IFT with brine (NaCl) over a wide range of pressures, temperatures, and salinities (P up to 5000 psi, T:77-257 °F, M up to 3.5 M). They reported that adding CH_4 to the mixture increases the CO_2-brine IFT over the entire experimental conditions. Focusing on cushion gas mixing in hydrogen geo-storage applications, Dalal Isfehani et al. (2023) evaluated the H_2-CO_2 mixture IFT with brine at subsurface conditions. Interestingly, their results show that $\gamma_{H_2-CO_2}$ decreases linearly with CO_2 content at lower concentrations, followed by a non-linear trend at higher CO_2 concentrations.

Most studies attempted to derive a functional form for the IFT between pure CO_2 or CO_2-gas mixtures and brine based on the molar Parachor model (**Equation 5.3**) (Sugden 1921):

$$\gamma^{1/4} = \frac{P}{M}(\rho_L - \rho_V) \tag{5.3}$$

where γ is the interfacial tension between the two phases, P is the Parachor of the component, M is its molar mass, and ρ_L and ρ_V are the densities of the liquid and vapor phases in equilibrium, respectively.

The Parachor is a temperature-independent additive property associated with the structural components (atoms and functional groups) of a molecule (Zhelezny et al. 2009). Quayle (1953) extensively characterized the Parachor for various organic compounds. To describe the IFT for the

pure CO_2-brine system, Chalbaud et al. (2009) employed the Parachor model below the critical point (high $\Delta\rho$), followed by two components above the critical point (low $\Delta\rho$). This model accounts for the pseudo plateau IFT and the linear increase with salinity. Liu et al. (2016) developed a robust correlation for gas mixtures (CH_4+CO_2), considering gas composition, temperature, pressure, density differences, individual molecular weights, and individual Parachor coefficients. They reported enhanced accuracy in predicting the CO_2-CH_4 mixture IFT with brine, surpassing commonly used correlations in the petroleum industry for hydrocarbon/water systems (Weinaug and Katz 1943, Ramey and Firoozabadi 1988, Corbett 2000, Sutton 2009). Molecular dynamics studies have corroborated the work from Liu et al. (2016) and provided insights into the behavior of IFT in more complex HC-CO_2-brine systems (Narayanan Nair et al. 2022, Choudhary et al. 2021, Yang et al. 2019).

Several authors have proposed that $\Delta\rho$ is the primary control on the behavior of the CO_2-H_2O/brine IFT (Chalbaud et al. 2009, Bikkina et al. 2011, Li et al. 2012, Pereira et al. 2016). Therefore, in **Figure 34**, the selected IFT dataset in **Table 3** were plotted as a function of $\Delta\rho$. It indicates that the CO_2-H_2O/brine IFT-$\Delta\rho$ curve follows a bilinear trend, decreasing steeply from larger $\Delta\rho$ to the vicinity of the critical point ($\Delta\rho$ ~ 600 kg/m^3), and then mildly declining until it flattens at lower $\Delta\rho$. Furthermore, an increase in brine salinity (M > 1) shifts IFT-$\Delta\rho$ curve, resulting in a higher pseudo plateau IFT. Conversely, an increase in temperature (T > 212 °F) shifts the IFT-$\Delta\rho$ curve downwardly, reducing the pseudo plateau IFT. As both formation brine salinity and temperature generally increase with depth (Réveillère 2013), these two factors tend to offset one another. **Figure 34** suggests that subsurface CO_2-H_2O/brine IFTs are expected to be in the range of ~25-30 mN/m, at subsurface conditions of elevated pressure, temperature, and salinity.

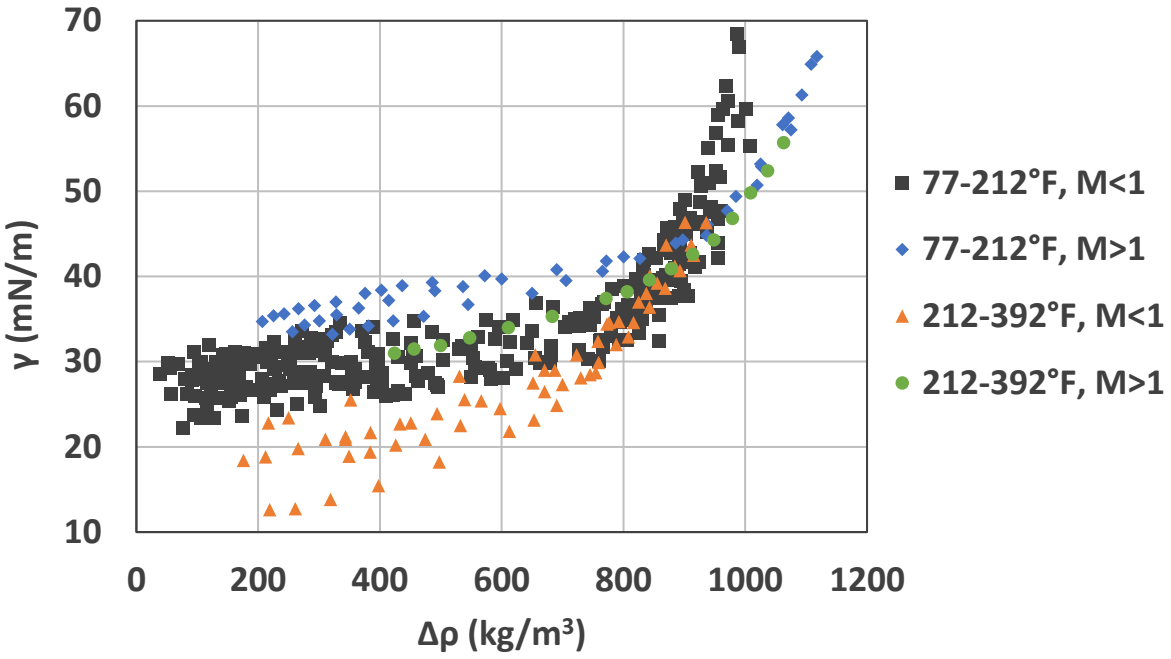

Figure 34. CO_2-H_2O/brine IFT as a function of the density difference at varying temperature and salinity (M). The IFT-$\Delta\rho$ curve follows a bilinear trend above and below the critical point ($\Delta\rho$ ~ 600 kg/m^3). Increasing salinity and temperature shifts the curve upwardly and downwardly, respectively. Given that both formation brine salinity and temperature typically increase with depth (Réveillère 2013), these two variables balance each other, leading to subsurface IFTs in the range of ~25-30 mN/m.

CO_2-geostorage in depleted oil and gas reservoirs involves considering additional effects such as the co-interaction with both the crude oil and brine. Studies focused on the IFT of the CO_2-oil-water/brine ternary system, particularly concerning carbonated water injection EOR, have been conducted (Yang et al. 2005, Bagalkot and Hamouda 2018, Lashkarbolooki et al. 2018, Nowrouzi et al. 2019, Samara et al. 2022, Yang et al. 2022). These studies generally converge on three key findings when CO_2 is introduced to the system: (i) the crude oil-water/brine IFT decreases (ii) the reduction becomes more pronounced with increasing pressure beyond the critical point of CO_2 and

tends to level off at higher pressures, and (iii) the IFT diminishes with increasing temperature, with temperature having a greater effect than pressure.

The effect of oil composition has been investigated by Lashkarbolooki et al. (2018), using both light and heavy crude oil with reservoir brine. They observed greater reduction in IFT for heavy oil compared to the light oil at identical pressures and temperatures. Furthermore, the influence of temperature was more pronounced in the case of heavy oil IFT than in light oil. These variations were attributed to the diffusion of natural surfactants (e.g. asphaltenes) to the water/oil interface as CO_2 selectively dissolves and diffuses within the oleic phase. Regarding the effect of brine salinity, Nowrouzi et al. (2019) conducted experiments varying salt concentration and type. Their general observation was that increased salinity led to higher CO_2-oil-brine IFT. Moreover, the specific nature and type of salt had distinct impacts on the time-dependent behavior and magnitude of the IFT alteration induced by CO_2.

Contact angle of CO_2-fluid-rock systems

Carbon geostorage (CGS) involves capillary processes affected by the wetting behavior of fluids. These processes influence the microscopic displacement efficiency of formation brine by $scCO_2$ (**Equation 1.2**) and the capillary sealing capacity of the caprock (**Equations 1.3** and **1.4**). In the context of CGS, water-wettability over $scCO_2$ is preferred. This preference restricts the upward vertical migration of $scCO_2$ and enhances residual trapping within the reservoir (Al-Khdheeawi et al. 2018, Iglauer et al. 2015b, Rahman et al. 2016). Moreover, it contributes to structural trapping, consequently reducing the risk of $scCO_2$ breakthrough within the confining zone (Espinoza and Santamarina 2017, Stavropoulou and Laloui 2022).

To assess wettability in a three-phase solid-fluid-fluid system, the contact angle (CA) is a widely accepted measurement (Good and Mittal 1993). **Figure 35** illustrates common techniques for measuring CA relevant to CGS. The configurations include (a) a brine/oil droplet surrounded by a CO_2 phase (sessile-drop), (b) a CO_2 droplet/bubble encased by a brine/oil phase (captive-bubble), (c) and (d) alternative setups to measure dynamic contact angles on tilted plates, and (e) and (f) depict the advancing and receding contact angles for brine/oil droplets on horizontal substrates. It is important to note that the terminology "advancing" and "receding" is contingent on the displacing phase and the configuration of the test. In sessile drop measurements, the advancing CA corresponds to brine displacing the CO_2 phase (imbibition), while the receding CA pertains to drainage (CO_2 displacing brine). Conversely, in captive-bubble measurements, advancing signifies drainage by CO_2, while receding represents imbibition by brine (Iglauer et al. 2015a, Arif et al. 2019).

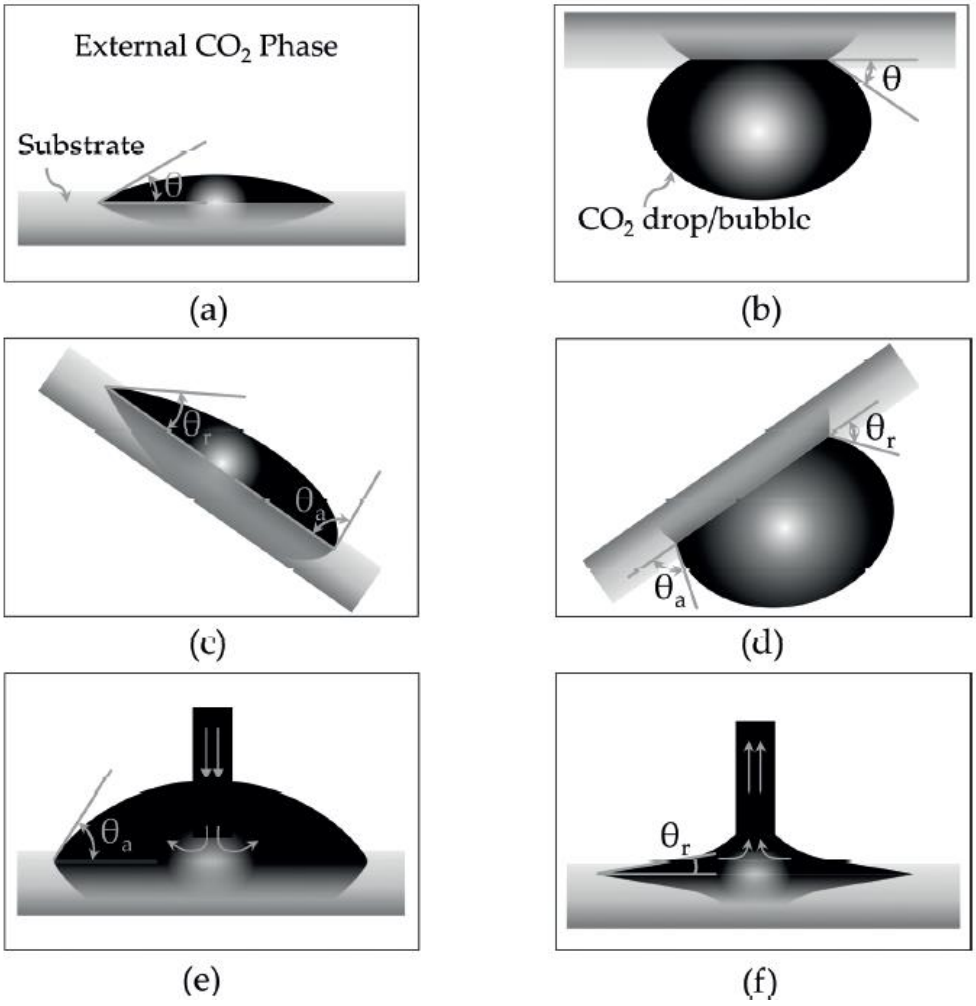

Figure 35. Common direct techniques to measure static (θ) and dynamic (advancing θa, and receding θr) contact angles in CO_2-geostorage. (a) brine/oil droplet on an external CO_2 phase (sessile-drop), (b) CO_2 droplet/bubble on an external brine/oil phase (captive-bubble), (c) sessile-drop on a tilted plate, (d) captive-bubble on a tilted plate, (e) advancing brine/oil droplet on a horizontal plate, (f) receding oil/brine droplet on a horizontal substrate (Prem and Imran 2018).

Recent advancements in contact angle (CA) measurements include the use of synthetic micromodels and micro-computed tomography (μ-CT) applied to rock core samples. These methods enable direct quantification of CA at the pore scale, which is relevant to CO_2 storage (Kim et al. 2012, Andrew et al. 2014, Lv et al. 2017, AlRatrout et al. 2018). Synthetic micromodels

allow for fast and cost-effective visualization of fluid displacement and screening tests. However, this approach falls short in capturing the surface chemistry and microstructure of rocks and is constrained by pressure and temperature conditions (Lifton 2016, Jacobs 2019). μ-CT in-situ CA measurements on rock samples have emerged as a solution to the limitations of microfluidics, providing pore-scale visualization of CA. Nevertheless, these measurements require the doping of the pore fluid, which is a notable drawback (Santini et al. 2013). As an alternative to direct wettability measurements, nuclear magnetic resonance (NMR) offers the advantage of overcoming the limitations associated with micromodels and μ-CT. NMR provides valuable structural insights into CO_2-brine-rock surface interactions (Baban et al. 2021, Baban et al. 2022).

Numerous studies have directly quantified the equilibrated CO_2-brine-rock contact angles as functions of various system conditions, including pressure, temperature, salinity, on diverse pure mineral and rock surfaces (**Table 4)** (Chiquet et al. 2007a, Yang et al. 2008, Espinoza and Santamarina 2010, Bikkina 2011, Mills et al. 2011, Tonnet et al. 2011, Broseta et al. 2012, Jung and Jiamin 2012, Kim et al. 2012, Farokhpoor et al. 2013, Saraji et al. 2013, Wang et al. 2013, Andrew et al. 2014, Iglauer et al. 2014, Kaveh et al. 2014, Saraji et al. 2014, Chaudhary et al. 2015, Iglauer et al. 2015a, Liu et al. 2015, Al-Yaseri et al. 2016, Lv et al. 2016, Roshan et al. 2016, Shojai Kaveh et al. 2016, Al-Yaseri et al. 2017, Arif et al. 2017, Botto et al. 2017, Guiltinan et al. 2017, Lv et al. 2017, Tudek et al. 2017, Alnili et al. 2018, Pan et al. 2018a, Arif et al. 2019, Mutailipu et al. 2019, Yekeen et al. 2020, Baban et al. 2021, Hashemi et al. 2021, Al-Yaseri et al. 2022, Baban et al. 2022, Song et al. 2022).

Table 4. Measurement conditions for equilibrated CO_2-water/brine contact angle (CA) data arranged by substrate studied.

Reference	Liquid	Substrate	Technique		T	P	M	CA
			Method	CA type	[°F]	[psi]	[mol/kg]	[°]
Chiquet et al. (2007a)	H_2O+NaCl	Quartz	CB	θ_R	95	140-1500	0.1-1	20-27
Espinoza and Santamarina (2010)	H_2O, H_2O+NaCl	Quartz	SD	Θ_S	77	15-1450	0-3.4	20-42
Bikkina (2011)	H_2O	Quartz	SD	Θ_S	104	200-2900	0	39-51
Mills et al. (2011)	Mixed brine	Quartz	CB	Θ_S	104	840-1840	0-0.6	27-37
Kim et al. (2012)	H_2O+NaCl	Quartz	MM	Θ_S	113	1225	1-5	66-75
Jung and Jiamin (2012)	H_2O, H_2O+NaCl	Quartz	SD	Θ_S	113	15-3630	0-5	33-68
Broseta et al. (2012)	H_2O+NaCl	Quartz	CB	Θ_A, θ_R	95	60-2200	0.1-7	35-95
Wang et al. (2013)	H_2O, H_2O+NaCl	Quartz	CB	Θ_S	86-122	1000-2900	0-1.2	21-27
Farokhpoor et al. (2013)	H_2O, H_2O+NaCl	Quartz	SD	Θ_S	97-151	15-3630	0-0.8	10-22
Saraji et al. (2013)	H_2O	Quartz	CB	Θ_A, θ_R	95-140	500-1700	0	7-34
Iglauer et al. (2014)	H_2O	Quartz	SD-TP	Θ_S	74-122	15-2170	0	0-82
Chaudhary et al. (2015)	H_2O+NaBr	Quartz	μ-CT	Θ_S	140	2000	3.1	26
Liu et al. (2015)	H_2O+NaCl	Quartz	SD	Θ_A, θ_R	81-104	432	0.1	5-92
Al-Yaseri et al. (2016)	H_2O	Quartz	SD-TP	Θ_A, θ_R	73-158	15-2900	0	7-49
Botto et al. (2017)	Mixed brine	Quartz	CB	Θ_S	104	140-3630	5.1	22-43
Lv et al. (2016)	H_2O, H_2O+KI	Quartz	SD, μ-CT	Θ_A, θ_R	104	140-3630	0-5.1	22-72
Mutailipu et al. (2019)	H_2O, H_2O+NaCl	Quartz	SD	Θ_S	122-212	700-2180	0-2	16-38
Espinoza and Santamarina (2010)	H_2O, H_2O+NaCl	Calcite	SD	Θ_S	25	15-1450	0-3.4	30-42
Bikkina (2011)	H_2O	Calcite	SD	Θ_S	77	725-2900	0	38-47

Mills et al. (2011)	Mixed brine	Calcite	CB	Θ_S	104	840	0.6*	27
Broseta et al. (2012)	H_2O+NaCl	Calcite	CB	Θ_A, θ_R	95	150-2200	0.1	35-75
Wang et al. (2013)	H_2O	Calcite	CB	Θ_S	86-122	1000-2900	0	21-27
Farokhpoor et al. (2013)	H_2O, H_2O+NaCl	Calcite	SD	Θ_S	97	15-2900	0-0.8	10-18
Arif et al. (2017)	H_2O, H_2O+NaCl	Calcite	SD	Θ_A, θ_R	73-158	15-2900	0-3.4	9-122
Kaveh et al. (2014)	H_2O	Sandstone	CB	Θ_S	113	80-1740	0	14-24
Iglauer et al. (2015a)	H_2O+NaCl+KCl	Various caprock	SD-TP	Θ_R	122	2170	4.2	44-68
Botto et al. (2017)	Mixed brine	Sandstone	CB	Θ_S	104	2900-3630	5.2	50-82
Tudek et al. (2017)	H_2O+KI	Sandstone	CB, μ-CT	Θ_S	72	1500	0.6	30-92
Alnili et al. (2018)	H_2O, H_2O+$CaCl_2$	Sandstone	SD	Θ_S, Θ_A, θ_R	95-158	720-2900	0-1.8	45-85
Mutailipu et al. (2019)	H_2O+NaCl	Sandstone	SD	Θ_S	122-212	700-2180	2	7-40
Kaveh et al. (2014)	H_2O, H_2O+NaCl	Silica-rich shale	CB	Θ_S	113-122	110-2170	0-4.2	11-49
Guiltinan et al. (2017)	H_2O+NaBr	Barnett shale	x-CT	Θ_S	68-140	2000	5	7-29
Yang et al. (2008)	Mixed brine	Limestone	SD	Θ_S	81-136	15-2900	-	32-99
Tonnet et al. (2011)	H_2O+NaCl	Calcite-rich shale	CB	θ_R	284	120-2030	0.8	12-17
Andrew et al. (2014)	H_2O+KI	Limestone	μ-CT	Θ_S	122	1450	0.4	41
Al-Yaseri et al. (2017)	H_2O+$CaCl_2$	Dolomite	SD-TP	Θ_A, θ_R	95-158	15-2900	1.8	16-93
Mutailipu et al. (2019)	H_2O+NaCl	Limestone	SD	Θ_S	122-212	700-2180	2	2-53

Technique: CB=captive-bubble, SD=sessile-drop, MM=micromodel, SD-TP=sessile-drop and tilting plate, μ-CT=micro-computed tomography, x-CT=x-ray computed tomography.

CA type: Θ_S=static, Θ_A=advancing, Θ_R=receding.

Figure 36 presents the static and dynamic CO_2-water/brine-mineral contact angles as a function of pressure, spanning temperatures ranging from above the critical point of CO_2 (95 °F) up to 158 °F, and various salt molalities up to 7 M, using data compiled from **Table 4**. Substantial variation in CO_2-water systems' contact angles for pure minerals is observed at the same pressure. This disparity, as documented by Iglauer et al. (2014), is primarily attributed to differences in surface cleaning procedures. Building on this research, Al-Yaseri et al. (2022) further investigated the issue and reported significant alterations in wetting behavior when cleaning oil-wet rocks with toluene and water-wet rocks with acetone. These studies emphasize that air plasma is an effective method for surface decontamination. Nevertheless, **Figure 36** indicates that pure quartz and calcite minerals are water-wet related to CO_2 ($\theta < 90°$) under low-pressure conditions. Generally, most studies reveal increasing contact angles with rising pressure, and in the case of pure calcite, the surface may revert to CO_2-wet ($\theta < 90°$). However, it is worth noting that Bikkina (2011) and Mutailipu et al. (2019) reported slightly decreasing contact angles with pressure.

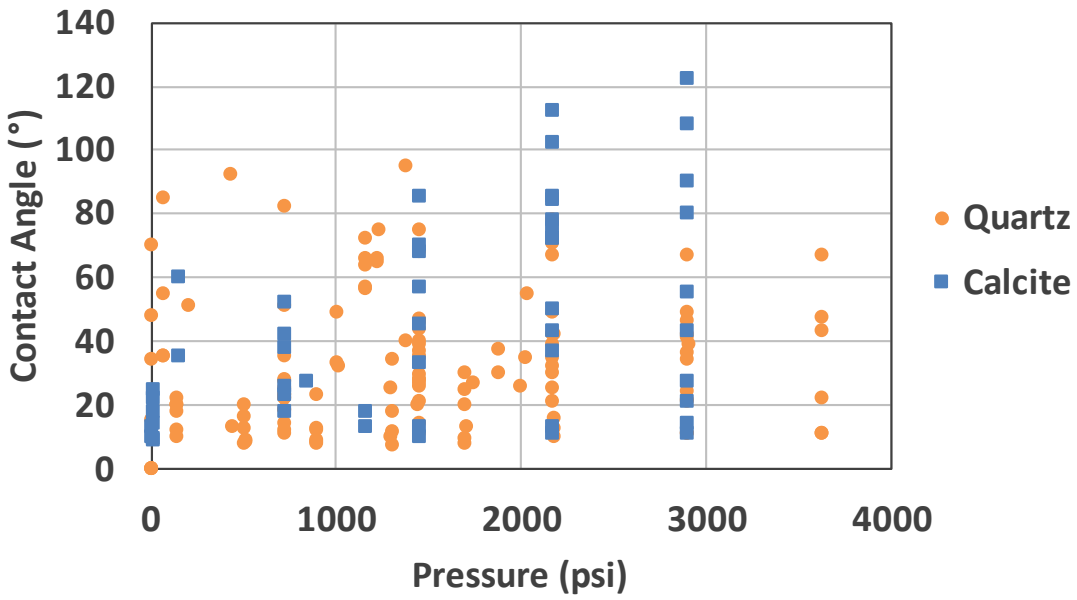

Figure 36. CO_2-water/brine contact angle values for quartz and calcite at the range of temperatures from 95-158 °F and molalities up to 7 based on the literature data shown in Table 4.

Figure 37 illustrates the influence of pressure on CO_2-brine contact angles for real-rock samples listed in **Table 4**, including sandstones, carbonates (limestones and dolomites), various mineralogies of caprocks, and an organic-rich shale (Barnett). The temperature range considered matches that of **Figure 36** (95-158 °F), and only brine molalities exceeding 1M are included to minimize clay-water interactions. Notably, the pressure-dependent increasing behavior extends to real-rock samples, with carbonate samples showing larger contact angles than sandstones at higher pressures, possibly indicating a reversion in wetting behavior. Caprock samples exhibit contact angles similar to the trend observed in sandstone. The data for the organic-rich shale (Barnett) at 2000 psi shows considerably lower CA values, which could be attributed to the measurement technique (x-CT in contrast to drop shape analysis).

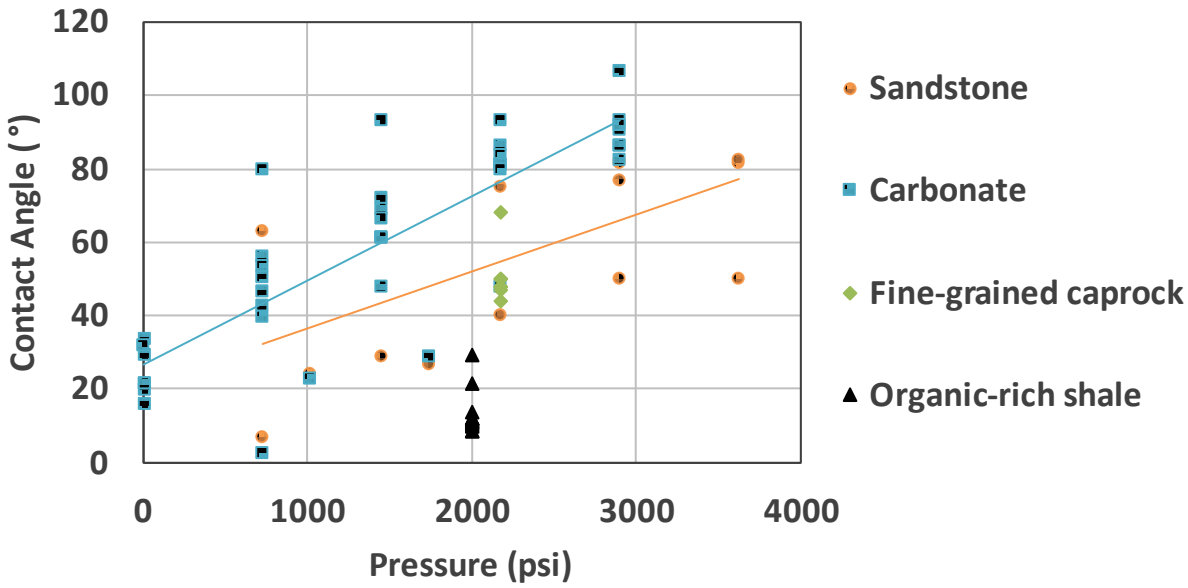

Figure 37. CO_2-brine-rock contact angle values at the range of temperatures from 95-158 °F and molalities higher than 1 for various lithologies based on the literature data shown in Table 4.

In **Figure 38**, the impact of salt concentration on CO_2-brine(NaCl)-mineral contact angles is depicted at similar temperatures (113-122 °F) and a pressure of 2175 psi (15 MPa). Studies

consistently report an increase in contact angles of pure minerals with increasing salt molality, signifying a reduction in water-wettability in the presence of salt. The mechanisms behind this increase in contact angle are attributed to the higher ionic strength, ion adsorption on the surface, and variations in the magnitude of zeta potential (Roshan et al. 2016, Pan et al. 2018a). However, the influence of salinity on the CO_2-brine contact angle of real-rocks remains uncertain. Shojai Kaveh et al. (2016) reported no change in the CO_2 contact angle of silica/dolomite-rich shale caprocks when a 1 M NaCl solution was used instead of pure H_2O. Alnili et al. (2018) observed a slight decrease in the CO_2 contact angle of a Warro sandstone (90 wt.% quartz). The inconsistencies between CO_2 contact angles of pure minerals and real rocks are attributed to factors such as the mineralogy of the real rock, surface roughness, and a decrease in electrostatic repulsion due to the reduction of pH resulting from CO_2 dissolution in the aqueous phase (Chiquet et al. 2007a, Yekeen et al. 2020).

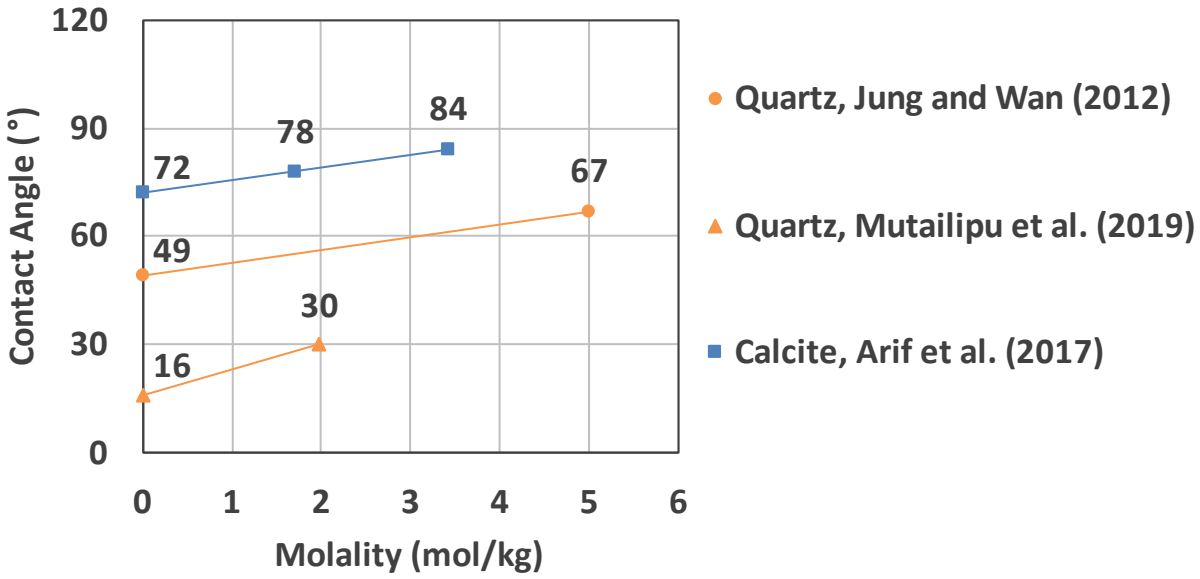

Figure 38. Effect of salt molality on the CO_2-brine(NaCl)-mineral contact angle data at the range of temperatures from 113-122 °F for quartz and calcite (Table 4).

Despite numerous studies on CO_2-water/brine-rock contact angles, the influence of temperature on contact angle remains uncertain (Arif et al. 2019, Yekeen et al. 2020). **Figure 39** presents CO_2-H_2O contact angle values obtained at 2175 psi (15 MPa) as a function of temperature, drawing from multiple studies listed in **Table 4**. Quartz samples exhibit increasing contact angles with increasing temperature (Farokhpoor et al. 2013, Iglauer et al. 2014, Al-Yaseri et al. 2016, Mutailipu et al. 2019), while calcite (Arif et al. 2017) and carbonate (Yang et al. 2008) display a decreasing trend with temperature. Roshan et al. (2016) underscored the non-trivial nature of temperature-dependent contact angle behavior, which is influenced by factors such as Van der Waals potentials, ionic concentration of the solution, interfacial tension between fluids, dielectric constant, valence of the ion, and various other considerations.

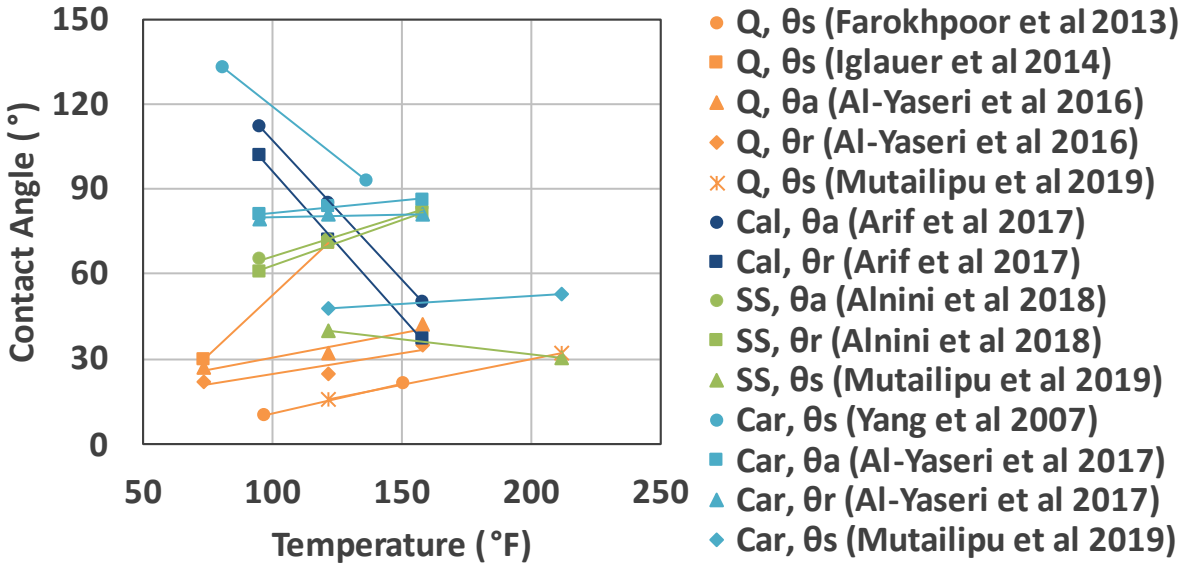

Figure 39. Effect of temperature on the CO_2-water-rock contact angle data at the pressure of 2175 psi (15 MPa) and various lithologies (Table 4). Q=quartz, Cal=calcite, SS=sandstone, Car=carbonate.

As an application to CO_2-geostorage in depleted oil and gas reservoirs, some studies have explored the wettability of crude oil-formation brine systems in the presence of CO_2 (Yang et al. 2008,

Jaeger et al. 2010, Ameri et al. 2013, Al-Mutairi et al. 2014, Seyyedi et al. 2015, Nowrouzi et al. 2019, Park et al. 2020, Yekeen et al. 2021). These studies reveal a consistent trend of decreasing contact angles between crude oil and formation brine when CO_2 is introduced, promoting water-wettability, especially in carbonate systems. Furthermore, an increase in pressure leads to an increase in contact angles, indicating a less water-wet state. This reduction in contact angle (increasing water-wettability) with CO_2 enrichment positively impacts oil displacement in depleted oil reservoirs (Samara et al., 2022) and contributes to increasing the capillary threshold in the caprock (Stavropoulou and Laloui 2022).

Molecular diffusion in CO_2-fluid systems

Several researchers have posited that the molecular diffusion of CO_2 within formation brine and crude oil can significantly affect capillary sealing in saline aquifers and depleted reservoirs, accelerate the dissolution kinetics of CO_2 into brine, and induce geochemical reactions in subsurface minerals (Busch et al. 2008, Henkel et al. 2014, Sanguinito et al. 2018, Goodman et al. 2019). Various techniques have been employed to measure the diffusion coefficients of CO_2 in aqueous systems. These techniques encompass bubble solution rates (Epstein and Plesset 1950, Krieger et al. 1967, Ng and Walkley 1969, Kravanja et al. 2018b, Kravanja et al. 2018a), the pressure decay method (Yang and Gu 2006, Azin et al. 2013, Zarghami et al. 2017), fluorescence-based methods (Hirai et al. 1997, Sell et al. 2013), Raman spectroscopy (Lu et al. 2013, Perera et al. 2018), and Taylor dispersion (Cadogan et al. 2014). The conditions for measuring the CO_2 diffusion coefficient in aqueous solutions are summarized in **Table 5**.

.

Table 5. Measurement conditions for CO_2 diffusion coefficient in water or brine solutions.

Author	Technique	Liquid	T	P	M	D_{AB}
			[°F]	[psi]	[mol/kg]	[10^{-9} m^2/s]
Ng and Walkley (1969)	Bubble rate of solution	H_2O	77	15	0	1.99
Hirai et al. (1997)	Laser-induced fluorescence	H_2O	77	4264-5685	0	1.25-1.45
Yang and Gu (2006)	Pressure decay method	Mixed brine	81-136	700-1100	*	170-270
Azin et al. (2013)	Pressure decay method	Mixed brine	104-113	850-1000	*	10-45
Sell et al. (2013)	Fluorescence/microfluidics	H_2O, H_2O+NaCl	77	72-720	0-5	0.56-1.86
Lu et al. (2013)	Raman spectroscopy	H_2O	32-392	1450-6530	0	0.76-16.1
Cadogan et al. (2014)	Taylor dispersion	H_2O	77-302	1750-7150	0	2.0-12.3
Zarghami et al. (2017)	Pressure decay method	H_2O, mixed brine	122	2540-3120	0, *	3.6-8.3
Perera et al. (2018)	Raman spectroscopy	H_2O, H_2O+NaCl	122	1305	0-5	1.7-3.1

** Formation brine molality not mentioned*

The impact of pressure on the diffusivity of CO_2 in aqueous systems is depicted in **Figure 40**. It is evident that pressure has a minimal effect on CO_2 diffusion in water, regardless of the measurement technique. The diffusion coefficients at 77 °F range from 1.2-2.3 x 10^{-9} m^2/s. Kravanja et al. (2018b) have demonstrated that the diffusion coefficient of H_2O in CO_2 is nearly one order of magnitude larger (~10^{-8} m^2/s), primarily because water possesses a smaller hydrodynamic radius than carbon dioxide. Regarding CO_2-geostorage in depleted oil and gas reservoirs, analysis of five different crude oils by Cui et al. (2023) reveals that the diffusivity of CO_2 in crude oil also increases with rising pressure due to a synergistic effect with decreasing density. Overall, their CO_2 diffusion coefficients in oil fall within the range of 10^{-9} m^2/s, similar to the diffusivity in water.

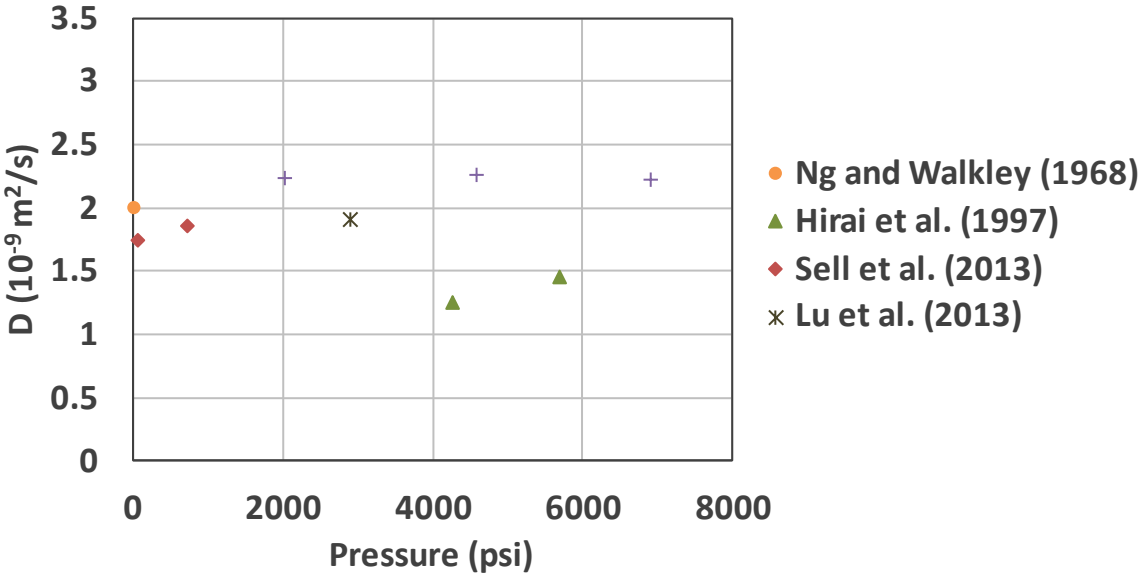

Figure 40. Effect of pressure on the CO_2 diffusion coefficient in pure water at 77 °F. Data source: Table 5.

In relation to other parameters, both salinity (**Figure 41**) and temperature (**Figure 42**) exhibit a linear dependence on diffusivity. Perera et al. (2018) have proposed that the diffusivity of CO_2 in H_2O can be modeled using the Stokes-Einstein relationship (**Equation 5.4**):

$$D = k_B T/(n_{SE}\pi\mu a) \quad (5.4)$$

where D is the diffusion coefficient, k_B is the Boltzmann constant, T is the absolute temperature, n_{SE} is the Stokes-Einstein number, μ is the viscosity of the solution, a is the hydrodynamic radius of the solute. Thus, the linear decrease in diffusivity with increasing salt molality is attributed to the linear increase in the viscosity of the aqueous solution as the salt content rises. The linear increase in diffusivity with increasing temperature is associated with enhancement in the thermal motion of molecules, which is the basis for diffusion.

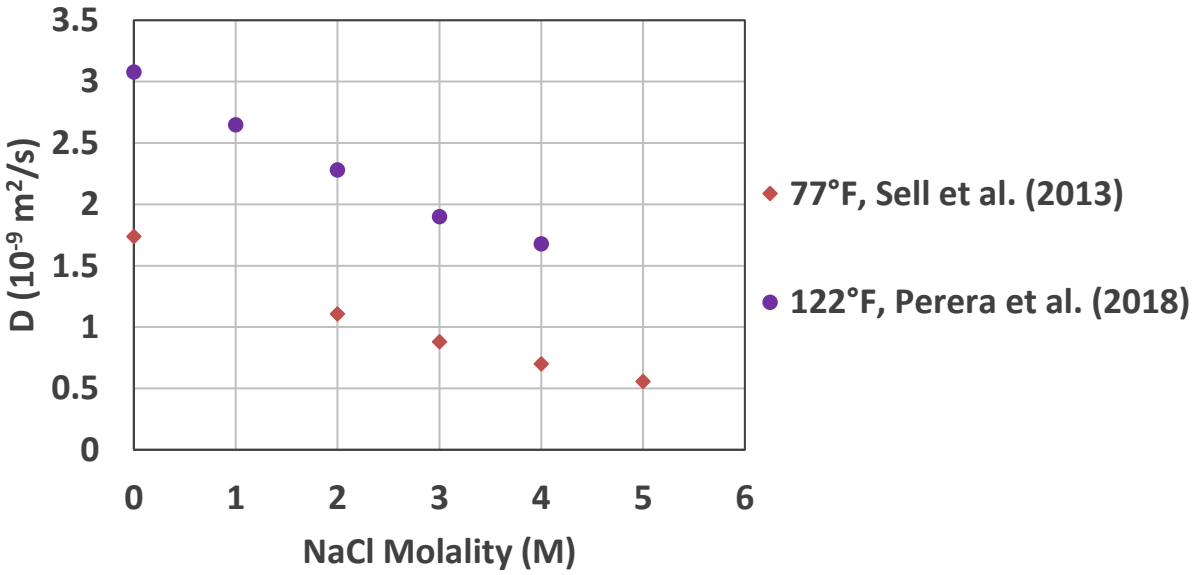

Figure 41. Effect of salinity on the CO_2 diffusion coefficient in NaCl brine at 77 and 122 °F. Data source: Table 5.

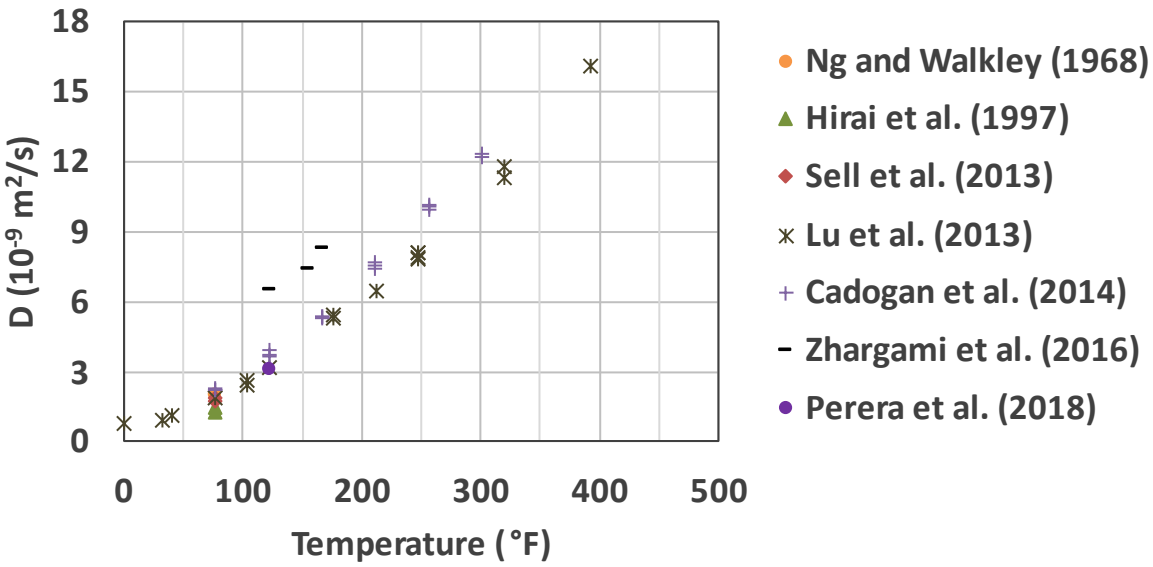

Figure 42. Effect of temperature on the CO_2 diffusion coefficient in pure water. Data source: Table 5.

The computation of the effective diffusivity of CO_2 within brine-saturated porous media takes into account the interconnectedness of the diffusion pathway, often characterized by tortuosity, as outlined in **Equation 1.5**. Experimental investigations have provided data on the effective CO_2 diffusion coefficients (D_{eff}) within brine-saturated confinement zones under various conditions (Hildenbrand and Krooss 2003, Krooss et al. 2005, Busch et al. 2008, Fleury et al. 2009, Wollenweber et al. 2009, Berne et al. 2010, Amann et al. 2011, Edlmann et al. 2013, Fleury et al. 2013). These experiments typically encompass a temperature range of 70-120 °F and pore pressures of up to approximately 1500 psi.

It is noteworthy that certain studies have incorporated different levels of confinement in their measurements, introducing complexity to the analysis. This complexity arises from the documented decrease in the effective diffusivity of gas within fine-grained rocks as the effective stress increases (Sun et al. 2023b). For example, Busch et al. (2008) conducted measurements at a constant effective stress of approximately 870-1000 psi, whereas Wollenweber et al. (2009) and

Amann et al. (2011) operated at higher constant effective confinement levels of approximately 1500 psi and 2500 psi, respectively.

Overall, the effective CO_2 diffusion coefficients in brine-saturated confining zones within the specified conditions typically fall within the range of 10^{-10} to 10^{-12} m²/s (Song and Zhang, 2013). These values are generally one to three orders of magnitude smaller than the CO_2 diffusivity in water, which is approximately 10^{-9} m²/s under the same measurement conditions (**Figure 40**, **Figure 41**, and **Figure 42)**. The notably slow effective diffusion of CO_2 within brine-saturated confinement zones suggests that the rate of diffusive leakage is minimal (Gaus et al. 2005). However, certain experiments have indicated that mineral dissolution resulting from geochemical reactivity might increase the pore space of confining zones, thereby potentially enhancing the effective diffusivity and leakage of CO_2 (Busch et al. 2008, Wollenweber et al. 2009).

Geochemical reactivity in CO_2-brine-rock systems

The subsurface interaction between CO_2 and brine can instigate geochemical reactions with the storage and confining zone, potentially influencing the microscopic displacement and trapping mechanisms relevant to carbon geostorage (CGS). These geochemical reactions are commonly categorized as short-term and long-term reactions (Gaus et al. 2005, Gaus 2010). In the early stages, CO_2 dissolves in brine, leading to the formation of carbonic acid, which subsequently ionizes into carbonate and bicarbonate ions, resulting in a reduction of pH to approximately 3 (Gaus et al. 2005, Rosenbauer et al. 2005, Espinoza et al. 2011):

$$CO_2\,(gas) + H_2O \rightleftharpoons H_2CO_3 \tag{5.5}$$

$$H_2CO_3 \rightleftharpoons H^+ + HCO_3^- \tag{5.6}$$

$$HCO_3^- \rightleftharpoons H^+ + CO_3^- \quad (5.7)$$

The increase in H^+ concentration in the brine due to CO_2 dissolution accelerate reaction with carbonate minerals based on their fast reaction mechanism in acidic environments (Palandri and Kharaka 2004). Calcite exhibits the largest dissolution rate among carbonates, being ~2–3 and ~3–4 orders of magnitude faster than dolomite and siderite, respectively (Pokrovsky et al. 2009, Golubev et al. 2009, Dresel 1989). In the presence of excess H^+ ions, carbonate mineral reactions take the following form:

$$CaCO_3\ (\text{calcite}) + H^+ \rightleftharpoons Ca^{2+} + HCO_3^- \quad (5.8)$$

$$CaMg(CO_3)_2\ (\text{dolomite}) + 2H^+ \rightleftharpoons Ca^{2+} + Mg^{2+} + 2HCO_3^- \quad (5.9)$$

$$FeCO_3\ (\text{siderite}) + H^+ \rightleftharpoons Fe^{2+} + HCO_3^- \quad (5.10)$$

In the example of calcite dissolution, the reactant is consumed quickly, and the reaction ceases at an equilibrium pH of 4.5–5.0 (Gaus et al. 2005, Espinoza et al. 2011). On the other hand, the dissolution of aluminosilicates (e.g. feldspars, micas, and clays) can persist over significantly longer periods, thereby stabilizing the pH at around 8. Reaction between felspars and carbonic acid arising from CO_2 dissolution lead to the formation of secondary minerals (primarily kaolinite) and release of cations in the brine (Tutolo et al. 2015). Conversely, the reaction between carbonic acid and clays mainly involves ion exchange and water adsorption processes rather than direct carbonation reactions (Espinoza and Santamarina 2012). A secondary reaction is the alteration of feldspars in high calcium ion concentration deriving from carbonate dissolution on top of naturally existing in the brine before CO_2 injection (Gunter et al. 1997, Gaus et al. 2005). An example is the

dissolution of albite consuming Ca^{2+} and leading to the precipitation of calcite and kaolinite (Gaus et al. 2005):

$$2NaAlSi_3O_8\ (albite) + CO_2 + 2H_2O + Ca^{2+} \rightleftharpoons 4SiO_2\ (chalcedony) + CaCO_3\ (calcite) + Al_2Si_2O_5(OH)_4\ (kaolinite) + 2Na^+ \quad (5.11)$$

According to **Equation 5.11**, CO_2 can be sequestered in the form of calcite. Alternatively, the secondary reaction of anorthite (Ca-rich feldspar) is quicker than albite and can sequester CO_2 without requiring Ca+ ions in the brine (Gaus et al. 2005):

$$CaAl_2Si_2O_8\ (anorthite) + CO_2 + 2H_2O \rightleftharpoons CaCO_3\ (calcite) + Al_2Si_2O_5(OH)_4\ (kaolinite) \quad (5.12)$$

The reaction rates of aluminosilicates are notably slower when contrasted to carbonate mineral reactions. Furthermore, the reactivity of silicate minerals, such as quartz, is even slower and remains independent of pH conditions (Espinoza et al. 2011, Kaszuba et al. 2013). Overall, these reactions can take up to thousands of years to occur (Gaus et al. 2005, Espinoza et al. 2011). Pyrite, a frequently encountered mineral in confinement zones (e.g. shales), can undergo complex reaction pathways influenced by CO_2, potentially leading to oxidation processes (Vaziri Hassas and Miller 2019).

In summary, this chapter delves into the fundamental CO_2-fluid-rock interactions pertinent to carbon geostorage (CGS). Regarding phase behavior within the CO_2-H_2O system, the mutual solubilities of components can result in phase densities deviating from those of pure systems, especially in the case of the aqueous phase. Accurate density determination assumes critical importance, influencing the assessment of capillary seal capability and the CO_2-H_2O interfacial tension, which is predominantly governed by the density difference. In storage conditions

characterized by the presence of supercritical CO_2, the $scCO_2$-H_2O IFT reaches a pseudoplateau at approximately 25-30 mN/m. This pseudoplateau IFT is anticipated to exhibit relative stability with increasing depth (corresponding to elevated pressure, temperature, and salinity), attributable to counteracting effects between these properties. The consistent behavior of interfacial tension aids in the estimation of both $scCO_2$-brine capillary pressure and seal capability. Furthermore, it has been shown that the wettability of the $scCO_2$-brine-rock system is influenced by mineralogy, with carbonate minerals demonstrating reduced water-wettability in comparison to sandstones.

This chapter also addresses the impact of CO_2 dissolution in brine, resulting in acidification that can initiate various geochemical reaction pathways. Such reactions have the potential to induce alterations in mineral content and distribution within both storage and confining rock. Mineralogical changes, in turn, can lead to modifications in both the wettability of the $scCO_2$-brine-rock system and pore size distribution hence transport properties. Recent studies have revealed alterations in these properties after geochemical reactivity in both the storage zone (Seyyedi et al. 2020, Wang et al. 2020, Kim et al. 2023) and the confining zone (Mouzakis et al. 2016, Qin et al. 2017, Pan et al. 2018b, Sanguinito et al. 2018, Goodman et al. 2019, Fatah et al. 2021, Gholami et al. 2021, Qin et al. 2022, Medina et al. 2023, Wang et al. 2023). Additionally, it has been suggested that geochemical reactivity may affect the effective diffusion of CO_2 (Medina et al. 2023, Montegrossi et al. 2023), impacting the CO_2 diffusive leakage in the confining zone.

In conclusion, geochemical reactions are a significant concern with regard to the long-term integrity of CO_2 geostorage. Most studies have approached the geochemical effects using crushed samples, which offer an enhanced surface area and significantly magnify the impact of reactivity. To the best of the present work's knowledge, a quantitative workflow for comprehending the extent

and influence of geochemical reactivity on the transport and petrophysical properties of intact rock samples has yet to be developed. Such a study has the potential to provide valuable insights into gauging the scope of geochemical reactions and their effects on critical properties relevant to CGS.

Chapter 6. Experimental Methodology: CO_2-Geostorage

In this study, an experimental approach was developed to quantify the impact of geochemical reactivity induced by $scCO_2$-brine interactions on petrophysical and transport properties relevant to carbon geostorage (CGS) **(Figure 43)**. To investigate the extent of geochemical reactions and their implications for CGS, confining zone samples with varying petrophysical properties and two different orientations (i.e., horizontal and vertical) were selected. Following sample preparation, characterization of petrophysical and transport properties were performed. After pre-characterization, the samples were subjected to $scCO_2$ treatment. Following $scCO_2$ treatment, the same characterization was conducted to assess the extent of geochemical reactions and their implications for controlling properties relevant to CGS.

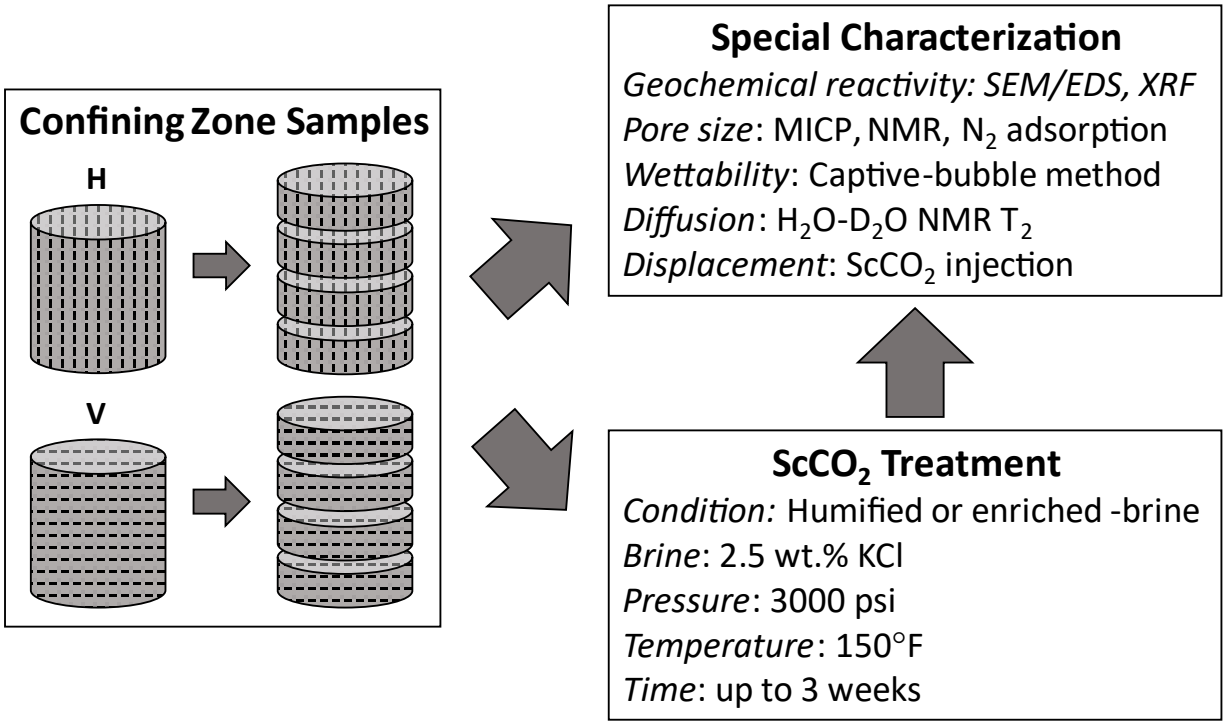

Figure 43. Experimental setup illustrating the quantification of geochemical reactivity's impact on petrophysical and transport properties in the context of carbon geostorage (CGS). Confining zone samples with varying petrophysical

characteristics and orientations (horizontal and vertical) were selected for analysis. Characterization before and after $scCO_2$ treatment enables the assessment of geochemical reaction extents and their implications for properties governing CGS.

Samples description

For this study, five confining zone samples and one sandstone storage zone sample were selected (**Table 6**). Horizontal and vertical plugs, each approximately 1-inch in diameter and length, were extracted in their "as-received" condition. Subsequently, the plugs underwent cleaning via Soxhlet extraction, utilizing an 80/20 toluene/methanol solution to extract hydrocarbons, water, and salt. Afterward, they were dried at 212 °F until a constant weight was achieved. The assessment of petrophysical properties followed the protocol described in **Chapter 3**: mineralogy was determined using FTIR (detailed mineral content can be found in **Appendix B**), total organic carbon (TOC) content was measured using the LECO® method, and porosity were determined through combination of NMR T_2 and helium pycnometry measurements.

Table 6. Mineralogy, total organic carbon (TOC), and porosity, of the samples used in this study.

Sample	Formation	Quartz (wt.%)	Feldspars (wt.%)	Total clays (wt.%)	Total carbonates (wt.%)	Others (wt.%)	TOC (wt.%)	Porosity (%)
S1	Navajo	79	1	14	6	0	-	9.3
S2	Meramec	42	12	27	19	0	-	7.1
S3	Uinta	7	5	27	58	3	2.0	5.9
S4	Utica	7	12	74	6	1	0.7	8.1
S5	Woodford	67	9	16	6	2	8.7	8.3

S6	Eagle Ford	6	7	8	71	8	4.7	4.5

To prepare the samples for measurements, four adjacent thin disks with a length of ¼ inch were extracted from each plug. To minimize heterogeneity within the same plug, multiple X-ray fluorescence (XRF) measurements were performed on the surface of each disk, confirming low elemental variation. To reduce surface roughness, the measurement surface of each disk underwent fine polishing, progressing to 2400 grit sandpaper, followed by ion-milling (Fischione 1060 SEM, Export, USA). Subsequently, the ion-milled surface of each sample was characterized with SEM coupled with energy dispersive X-ray spectroscopy (EDS). Imaging procedure to evaluate sample surface geochemical reactivity is detailed in Curtis et al. (2023).

Subsequent to the pre-characterization phase, the samples were divided into two groups, and these groups were replicated following the $scCO_2$ treatment. The first group aimed to examine alterations in wettability and pore size distribution in horizontal samples within the $scCO_2$-brine-rock system, and it involved the selection of samples S1 to S3 (**Table 6**). The second experimental group was focused on evaluating changes in transport properties, performing molecular diffusion measurements and $scCO_2$ breakthrough tests in both horizontal and vertical samples (S4 through S6). After the initial round of experiments, the samples underwent $scCO_2$ treatment. Subsequently, identical measurements were conducted on each sample post-treatment to assess alterations resulting from $scCO_2$-brine-rock interactions.

$ScCO_2$ treatment

To establish the experimental conditions for the $scCO_2$ treatment, a target injection depth of 2000 meters was selected. Assuming a hydrostatic pressure gradient for brine of approximately 1.05

MPa per 100 meters and a temperature gradient of around 24 °C per kilometer, conditions of approximately 20.7 MPa and 65 °C (150 °F) were determined at the injection depth. An exposure time of 21 days was selected, as it has been deemed sufficient to observe short-term geochemical reactions within confining zones, such as carbonate dissolution/precipitation (Mouzakis et al. 2016, Miller et al. 2016, Sanguinito et al. 2018, Goodman et al. 2019, Wang et al. 2023) and possible clay interactions (Qin et al. 2017, Sanguinito et al. 2018). It is noteworthy that due to the rates of mineral reactions, quartz dissolution (Gholami et al. 2021) or secondary feldspar alteration (Gaus et al. 2005) are not anticipated to be observed during this time frame, as these reactions may require up to 6 to 19 months to occur, respectively.

Following the establishment of exposure conditions, individual pressure reactors (Parr Instrument, Moline, USA) were selected, capable of withstanding pressures and temperatures up to 58 MPa and 350 °C, respectively. Thorough cleaning of the reactors between each test was performed using toluene, isopropanol, and acetone to prevent cross-contamination. For the samples' treatment, $scCO_2$ was humified and introduced gradually into each pressure reactor using a piston pump (Teledyne ISCO, Lincoln, USA) at a slow pressure gradient of approximately 0.4 MPa per hour to prevent micro fracturing of the samples. Pressure and temperature were continuously monitored throughout the process. After exposure, the system was gradually cooled and depressurized at the same rate as injection, and the samples were subsequently utilized in further measurements.

To evaluate the influence of the brine-to-rock volume ratio on the extent of geochemical reactivity, samples in each group underwent different brine-to-rock volume ratio conditions. In the first group, the samples were submerged in a 2.5 wt.% KCl solution, with a brine-to-rock volume ratio of approximately 10:1. Meanwhile, the second group of samples was subjected to pressure

saturation in the KCl brine up to 5000 psi in a separate system, carefully transferred to each specific pressure reactor, and exposed to the humified-$scCO_2$ treatment without immersion in excess brine. These two treatment conditions are referred to in this study as $scCO_2$-enriched brine and humified-$scCO_2$, respectively.

Pore size distribution measurement

Porosity and pore size distribution measurements were carried out both before and after the $scCO_2$ treatment on the samples from group 1. Pore throat size distributions (PTSD) were determined using MICP measurements on cleaned and dried thin disk samples, utilizing the AutoPore IV system (Micromeritics, Norcross, USA). This porosimeter is capable of handling pressures up to 60,000 psi, enabling the assessment of nanopore throat radii up to 1.5 nm. Pore size measurements via NMR T_2 were assessed using the GeoSpec II system (Oxford Instruments, Abingdon, United Kingdom) on thin disk samples pressure saturated in brine. To enhance the signal-to-noise ratio (SNR), three disks were stacked in each NMR measurement. An echo spacing of 200 μs was selected for sample 1 (storage zone), while a 100 μs echo spacing was used for samples 2 and 3 (confining zones). Additionally, isothermal nitrogen (N_2) adsorption measurements were conducted on the confining zones (samples 2 and 3) to evaluate alterations in nanopore structure. In preparation for the N_2 adsorption measurements, each sample was crushed and sieved to micrometer sizes ranging from 250 to 425 μm. The N_2 adsorption pore size distributions were determined through density functional theory (DFT) using a slit-shaped model. Specific surface areas were calculated using the Brunauer–Emmett–Teller (BET) method by fitting the adsorption data within the low relative pressure range (0.05–0.35).

Contact angle measurement

As discussed in **Chapter 5**, various configurations have been employed for the measurement of contact angles in subsurface conditions within $scCO_2$-brine-rock systems (Prem and Imran 2018). The captive-bubble technique was specifically chosen (**Figure 44**) to maintain sample brine saturation during measurements and prevent potential desiccation when surrounded by an $scCO_2$ environment.

The contact angle measurements were carried out using a DSA100 drop shape analyzer (Krüss GmbH, Hamburg, Germany) combined with a high-pressure, high-temperature (HPHT) unit (Eurotechnica, Bargteheide, Germany), featuring maximum working pressures and cell temperatures of 69 MPa and 200 °C, respectively. Prior to the measurement, each brine-saturated sample from group 1 was securely mounted on a custom-made, chemically inert holder made of PEEK material. This holder allowed the sample to pass through a needle with a known outside diameter of approximately 1.587 mm, ensuring proper alignment with the sample's center. This alignment step facilitated the contact of the $scCO_2$ bubble with the ion-milled surface of the sample, minimizing the influence of surface roughness on the contact angle (θ) and reducing lateral heterogeneity.

Subsequently, approximately 30 mL of brine was introduced into the system to cover the top surface of the sample. The unit was gradually heated to target temperature (150 °F). $ScCO_2$ was injected from the top (gas-cap), enabling diffusion into the brine while maintaining a constant pressure of 20.7 MPa, which was also continuously monitored. Following a period of fluid equilibration (approximately 2 hours), a single $scCO_2$ bubble was gently extruded from the needle using a separate dosing unit. Image calibration was performed, and the software (ADVANCE,

version 1.10.0) recorded the static $scCO_2$-brine-rock contact angle over time. The same procedure was repeated on the group 1 samples after $scCO_2$ treatment.

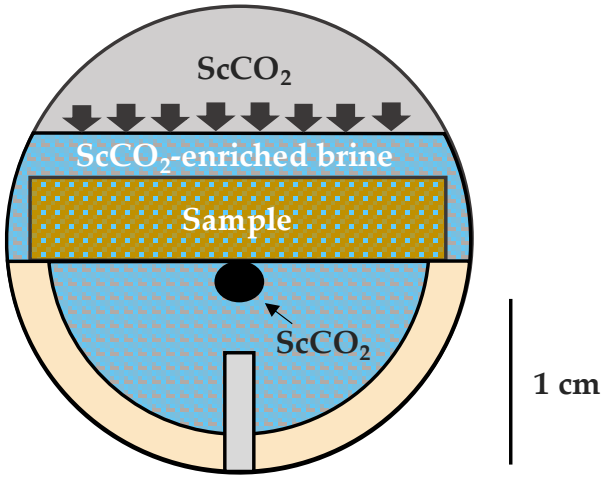

Figure 44. $ScCO_2$-brine-rock captive-bubble measurement system, with approximate dimensions in centimeters. The brine surrounding the rock sample is enriched with $scCO_2$ diffusing downward from the "gas-cap" region, maintained at specified pressure and temperature conditions. Upon reaching equilibration, a single $scCO_2$ bubble is gently extruded from the needle at the bottom, making contact with the central region of the ion-milled lower surface of the sample.

Molecular diffusion measurement

The horizontal and vertical thin disk samples in group 2 underwent molecular diffusion and $scCO_2$ breakthrough tests both before and after $scCO_2$ treatment. To evaluate effective diffusivity along a specific sample orientation (either horizontal or vertical), a thin layer of chemically resistant epoxy resin (J-B Weld™) was applied to the lateral sides of the samples prior to the diffusion measurements. This epoxy layer restricted radial diffusion, maintaining the concentration gradient along the main axis of each thin disk sample.

Following the epoxy application, the samples were gradually pressurized to 5000 psi in synthetic brine to enhance brine saturation. After achieving brine saturation, effective molecular diffusion

on the samples was assessed using an NMR T_2 H_2O-D_2O diffusion protocol, as described in previous work (Odiachi et al. 2022). For this diffusion assessment, a D_2O brine solution with the same salinity (2.5 wt.% KCl) was selected as the diffusing substance due to its invisibility under H^+ NMR. Consequently, this methodology facilitates the determination of the effective diffusion coefficient of D_2O within the porous medium. This determination is made by monitoring the reduction in NMR volume over time as the surrounding D_2O brine diffuses through the sample, concurrently mixing with the H_2O brine previously saturating the sample.

In this study, the signal-to-noise ratio (SNR) of the thin disk samples was improved by utilizing three samples in each NMR T_2 measurement (TE = 100 μs). These three samples were placed in a glass vial without contacting each other, submerged in approximately 40 mL of D_2O solution, and continuous NMR T_2 measurements were conducted over time. Given the sample conditions (i.e., epoxy-coated sides), the non-steady-state diffusion of D_2O through the porous medium is simplified into a 1D axial diffusion problem, and the mathematical solution for the effective D_2O diffusion coefficient is detailed in **Appendix C**. The tortuosity of the samples was further determined using both **Equation 1.5** and the diffusion coefficients of D_2O-H_2O mixtures at laboratory temperature (Baur et al. 1959, Odiachi et al. 2022). The identical NMR T_2 H_2O-D_2O diffusion protocol was applied to the samples after $scCO_2$ treatment to assess possible changes arising from $scCO_2$-brine-rock interactions.

$ScCO_2$ breakthrough test

Investigating gas breakthrough within brine-saturated nanoporous media, as observed in confining zones within carbon geostorage (CGS), can be a time-intensive process (Fleury and Brosse 2018).

The precise determination of breakthrough pressure (P_{BT}) in such media is typically accomplished using a pressure stepwise technique (Stavropoulou and Laloui 2022).

Figure 45 illustrates a schematic representation of the experimental setup, designed to emulate $scCO_2$-brine displacement within brine-saturated confining zones under subsurface conditions. The system comprises three pumps, designated for upstream gas, upstream brine, and confining pressure, all connected to a vertical core holder. The outlet of the core holder is connected to a back pressure regulator, which serves to maintain a constant pore pressure throughout the test. The outlet of the core holder is also connected to a brine-filled pipette at atmospheric pressure, allowing for the visual observation of gas breakthrough. The entire test procedure is documented through the use of a camera.

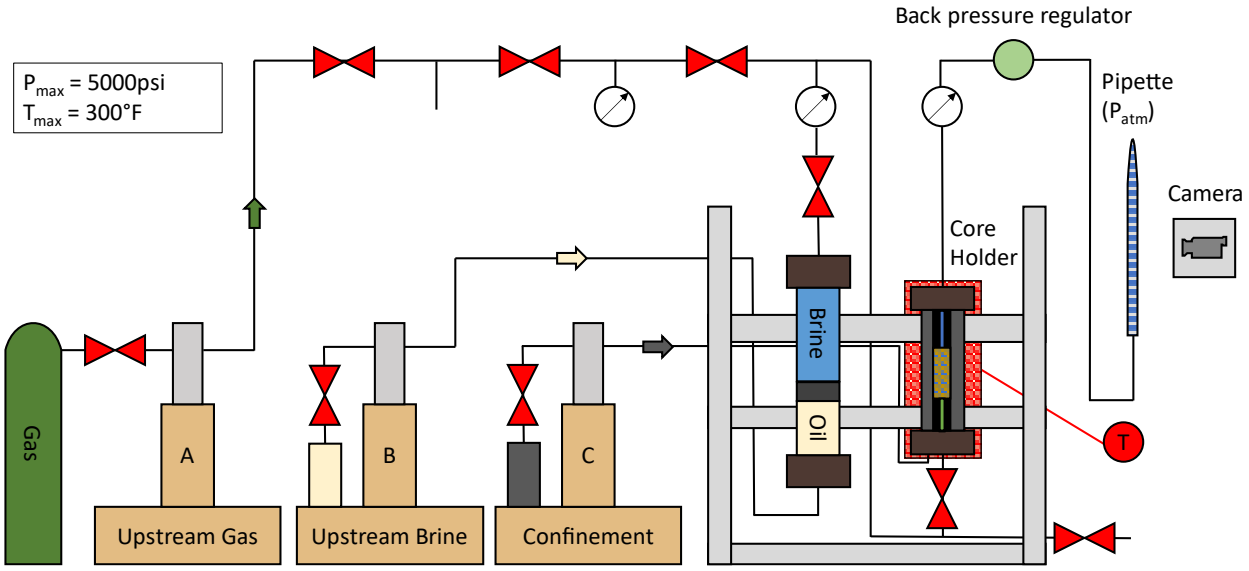

Figure 45. Schematic drawing for the $scCO_2$ breakthrough system.

Before each test, the pore pressure lines undergo a thorough flush with deionized water, followed by nitrogen (N_2) to minimize any residual salt presence within the system. Subsequently, brine (2.5 wt.% KCl) is displaced through an accumulator up to the core holder's inlet. In a separate

system, a thin disk sample is slowly pressure-saturated in brine at 5000 psi, ensuring maximal brine saturation before the commencement of the test. Following this, the sample is affixed within a rubber jacket and positioned inside the core holder. A net confinement pressure of 600 psi is applied to enable the sealing of the jacket around the sample.

Brine is then introduced into the saturated sample at a controlled rate (0.01 mL/hr), and the increase in pipette volume is carefully monitored. The core holder is heated to reach the target temperature of 150 °F. The back pressure regulator is regulated to downstream pressure of 1400 psi, a level exceeding the critical pressure of CO_2. Subsequently, $scCO_2$ is introduced upstream at a slightly higher pressure than downstream, displacing brine in the upstream lines. Following this, the injection of $scCO_2$ occurs incrementally, with each pressure increment set at 100 psi, while maintaining a net confinement pressure of 600 psi. The system's pressure and pump volumes are continuously monitored throughout the process.

The gradual dissolution and diffusion of CO_2 into the brine saturating the rock sample lead to a progressive reduction in pump volume over time. Once the injection pump volume stabilizes, the next pressure increment is initiated. It is important to note that this entire process is laborious, and a single test on a shale core plug may span from weeks to months to reach completion. Both before and after the $scCO_2$ treatment, $scCO_2$ breakthrough tests were conducted on the thin disk samples within group 2. These tests were carried out to gain insights into potential changes in $scCO_2$ breakthrough pressures resulting from the geochemical reactivity induced by $scCO_2$-brine-rock interactions.

Chapter 7. Results: CO_2-Geostorage

Geochemical reactivity

Figure 46 presents backscattered electron (BSE) images of the group 1 samples (S1 to S3), captured over identical areas both before and after $scCO_2$-enriched brine treatment (3000 psi, 150 °F, 3 weeks). In **Figure 46(a)** to **Figure 46(c)**, the microstructures before treatment are depicted for samples S1, S2, and S3, respectively. Subsequent images (**Figure 46(a)** to **Figure 46(f)**) portray the same areas for each sample after the treatment. Prior to treatment, sample S1 is primarily composed of quartz grains, with some clays (including illite, chlorite, and kaolinite) filling the pore spaces. Sample S2 is characterized by the presence of silicates, aluminosilicates, and minor amounts of carbonates. Meanwhile, S3 exhibits a dominant carbonate-rich composition, encompassing clays, limited silicates, and pyrite (depicted in white).

Following the treatment, no significant geochemical reactivity is discernible in sample S1, with the exception of salt precipitation. In contrast, sample S2 exhibits preferential dissolution of carbonate minerals (highlighted in red), while the primary silicate and aluminosilicate framework remains largely intact. Given the elevated carbonate content in sample S3 (**Table 6**), substantial surface alteration is evident due to the dissolution of carbonates post-treatment. Notably, other potentially reactive minerals, such as clays and pyrite, remain unaltered throughout this process.

Figure 47 presents BSE images of a highly reactive region within sample S3, both before (**Figure 47(a)**) and after (**Figure 47(a)**) $scCO_2$-treatment. In **Figure 47(c)**, spatial elemental mapping conducted prior to treatment using energy-dispersive x-ray spectroscopy (EDS) reveals a predominance of calcite with minor traces of silicate and dolomite. After treatment, **Figure 47(d)** shows that the only carbonate undergone dissolution is calcite, while dolomite remains unaffected.

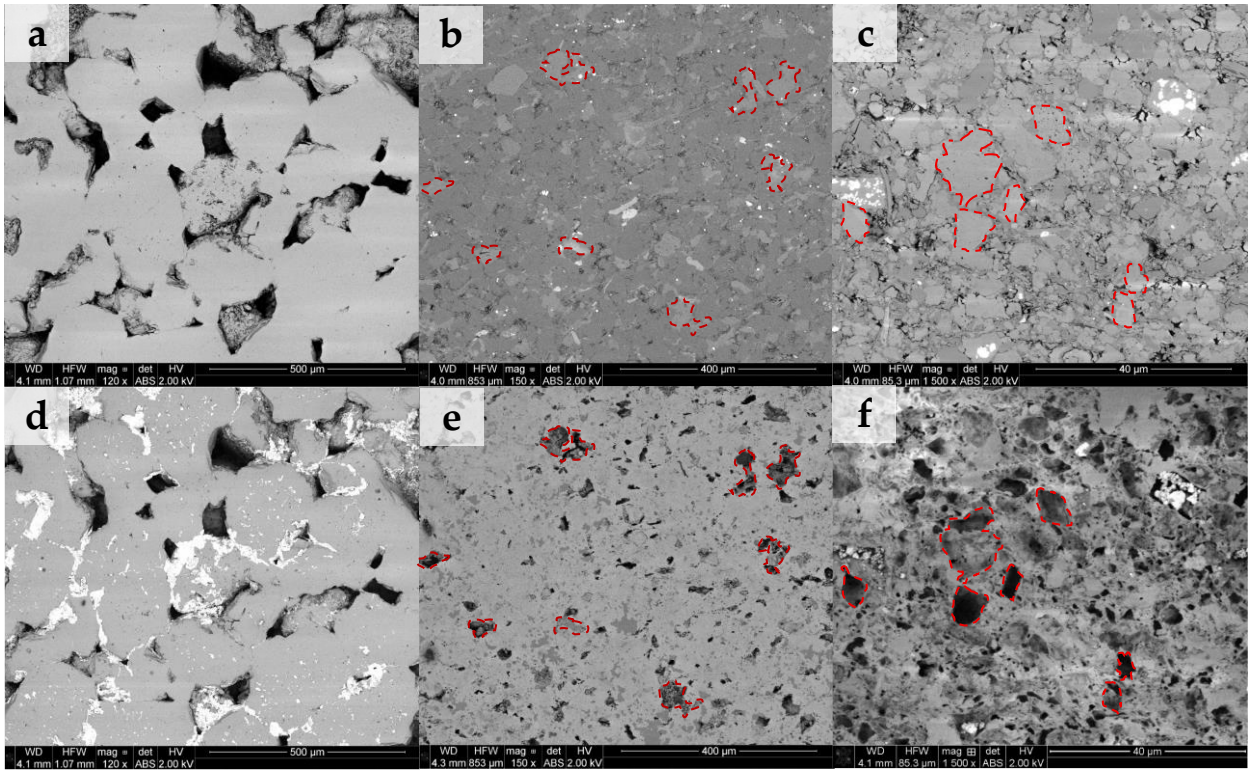

Figure 46. Backscattered images (BSEs) of group 1 samples captured at the same areas both before and after $scCO_2$-enriched brine treatment (3000 psi, 150 °F, 3 weeks). (a–c) represent areas before treatment for samples S1, S2, and S3, respectively. Their same areas after treatment are sequentially shown in (d–f). Sample S1 exhibits minimal evidence of geochemical reactivity, except for the presence of salt precipitation. In contrast, the images of sample S2 reveal a notable preferential dissolution of carbonate minerals, emphasized in red, while the overall silicate and aluminosilicate framework remains intact. The images of sample S3 display significant surface alteration resulting from the dissolution of carbonates, which aligns with the sample's higher initial carbonate content. Interestingly, other potentially reactive minerals, such as clays and pyrite, appear to remain unaltered during the process.

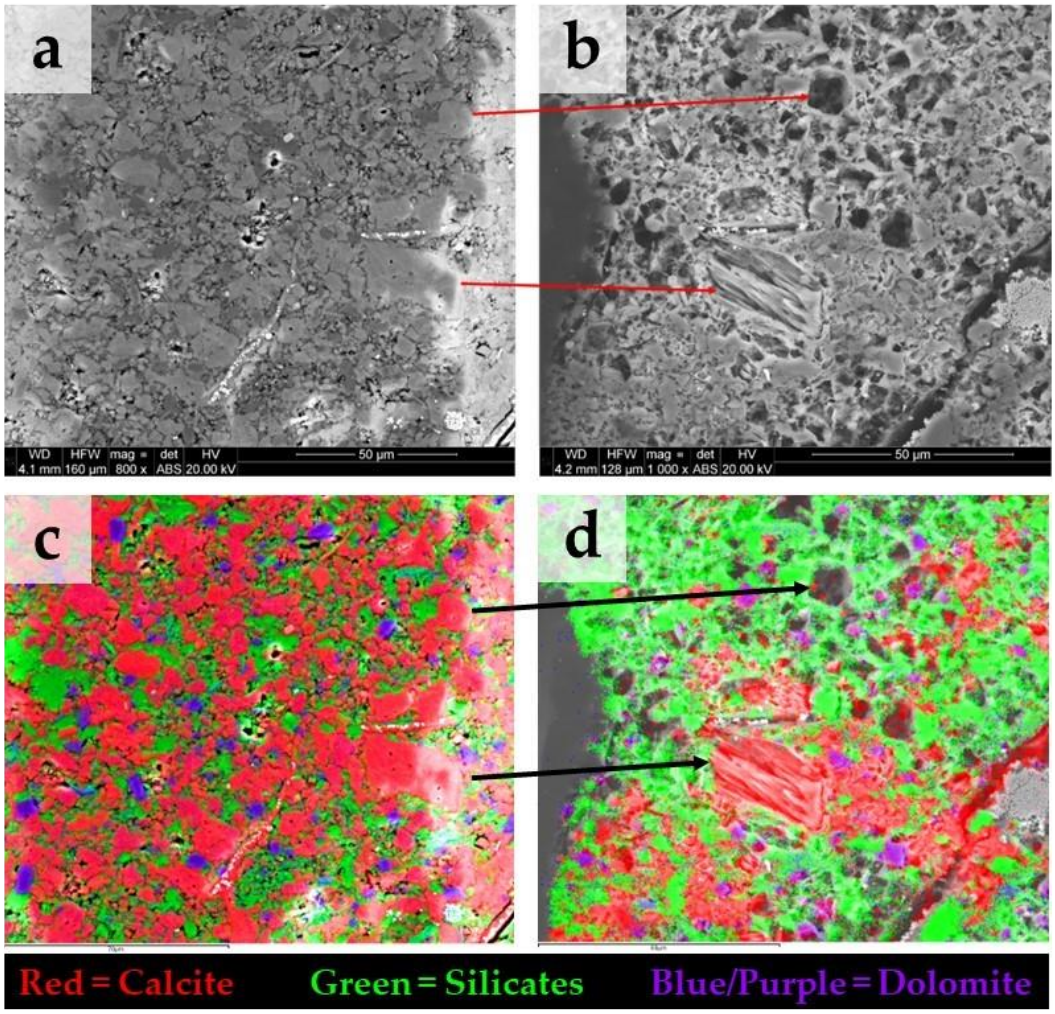

Figure 47. BSE images captured before (a) and after (b) treatment, depicting the same region of sample S3 and highlighting significant alteration resulting from carbonate dissolution. Please note that in (b), a slight displacement of the image relative to (a) has occurred, but the arrows indicate corresponding calcite grains. In (c), spatial elemental mapping conducted with energy-dispersive x-ray spectroscopy (EDS) prior to treatment reveals the predominant presence of calcite with minor amounts of dolomite. In (d), following treatment, it is evident that only calcite has undergone dissolution, while dolomite remains unchanged.

Figure 48 presents the relative oxide concentration data obtained from x-ray fluorescence (XRF) measurements on group 2 samples, both before and after $scCO_2$ treatment extending up to 3 weeks. Multiple XRF measurements were conducted on the top surface of each thin disk sample. The columns in the figure represent the average relative concentrations, while the error bars denote the standard deviation. Specifically, **Figure 48(a)**, **Figure 48(b)**, and **Figure 48(c)**, illustrate the XRF results for group 2 samples S4, S5, and S6, respectively.

Before treatment, the XRF analysis aligns with the FTIR mineralogy data provided in **Table 6**: S4 is rich in aluminosilicates, S5 is predominantly composed of silicates, and S6 contains a notable amount of carbonates. Post-treatment, the XRF results indicate minimal alteration in the surface composition of samples S4 and S5, which consist mainly of silicates and aluminosilicates. However, for sample S6, a substantial decrease in the relative concentration of CaO is observed, reducing from 42 wt.% prior to treatment to 22 wt.% and further to 15 wt.% after a total treatment time of 1 and 3 weeks, respectively. This reduction in CaO content is accompanied by a relative increase in other prevalent oxides, such as SiO_2.

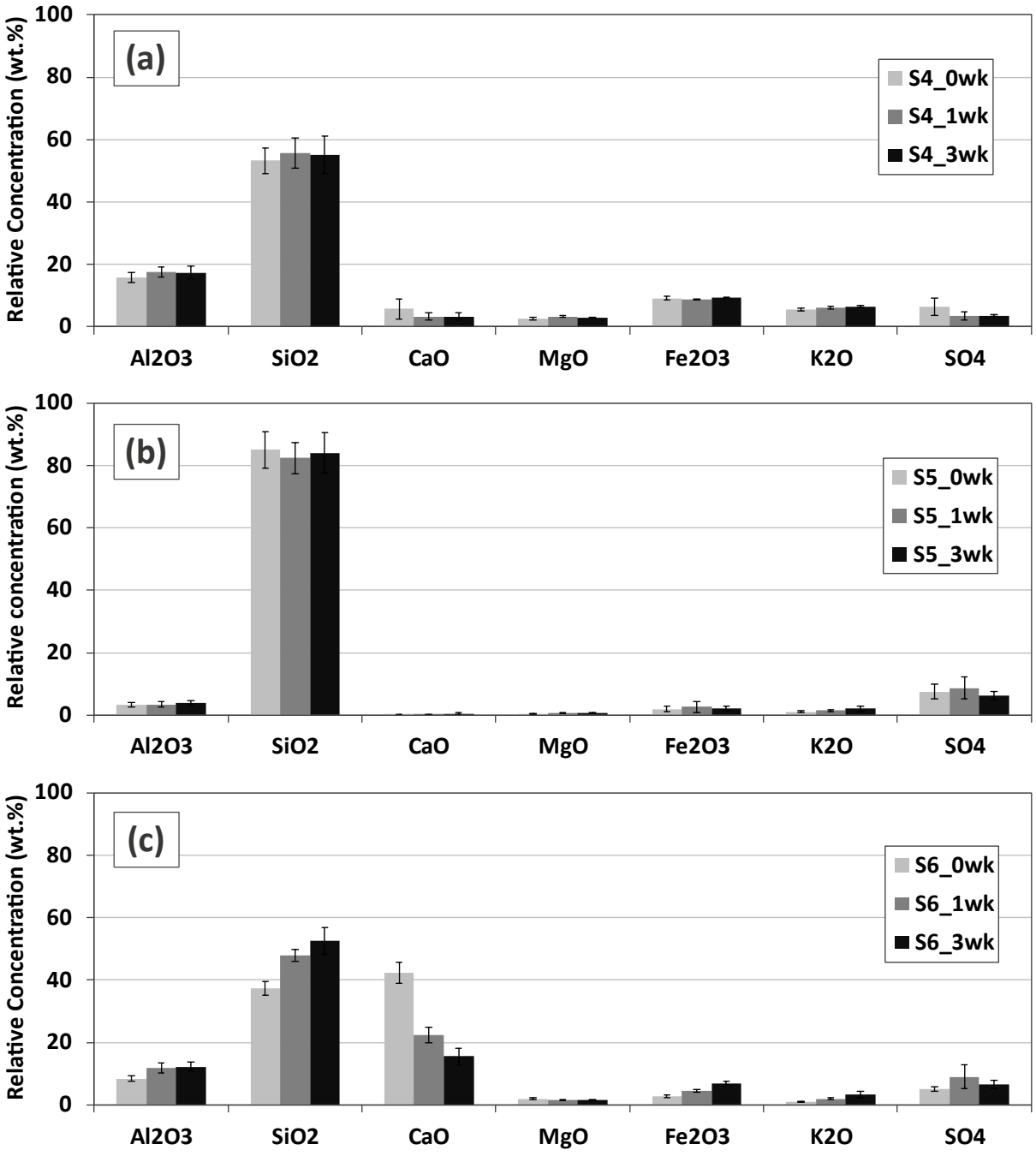

Figure 48. XRF analysis of oxide concentrations for group 2 samples before and after $scCO_2$ treatment. The results for samples S4, S5, and S6, are depicted in (a), (b), and (c), respectively. S4 and S5 are primarily composed of aluminosilicates and silicates, respectively. S5 has significant carbonate content. After treatment, minimal changes

in the surface composition of samples S4 and S5 are seen. However, sample S6 exhibits a significant reduction in the relative concentration of CaO, along with slight relative increase in SiO_2.

To estimate the extent of geochemical reactivity within depth, an additional shale horizontal sample (**Table 2**) underwent a 7-day treatment under identical conditions as the group 2 samples. Following treatment, the sample's surface underwent a series of XRF measurements, complemented by fine polishing using 2400 grit sandpaper. Throughout the polishing process, changes in relative depth were meticulously recorded with a digital caliper (resolution 10 μm).

Figure 49 provides a comprehensive view of the relative surface concentration of major oxides as a function of depth from the initial surface. The dashed lines represent the average relative concentration of each oxide prior to treatment. After treatment, a reduction in the relative concentration of CaO is seen, coupled with a slight increase in SiO_2, consistent with the observations in **Figure 48**.

Remarkably, after a series of polishing-XRF steps, the average surface concentrations converge toward the elemental composition present before treatment, occurring at an approximate depth of ~150 μm. Using the reacted distance of penetration (x) and the square root relationship with time and diffusion coefficient for a one-dimensional diffusion of a substance into a semi-infinite medium having constant surface concentration (Crank 1979):

$$x \sim 2\sqrt{Dt} \rightarrow D \sim \frac{x^2}{4t} \sim \frac{(150\mu m)^2}{4(7 \times 24 \times 60 \times 60s)} \sim 9.3 \times 10^{-15}\left(\frac{m^2}{s}\right) \quad (1)$$

An estimated $scCO_2$ reaction-diffusion coefficient in the order of $\sim 10^{-15}\left(\frac{m^2}{s}\right)$ is obtained. Considering the bulk $scCO_2$-H_2O diffusion coefficient at 150 °F of ~ $10^{-9}\left(\frac{m^2}{s}\right)$, the estimated

reaction-diffusion coefficient is about five to six orders of magnitude smaller than the bulk diffusion coefficient of $scCO_2$ in H_2O.

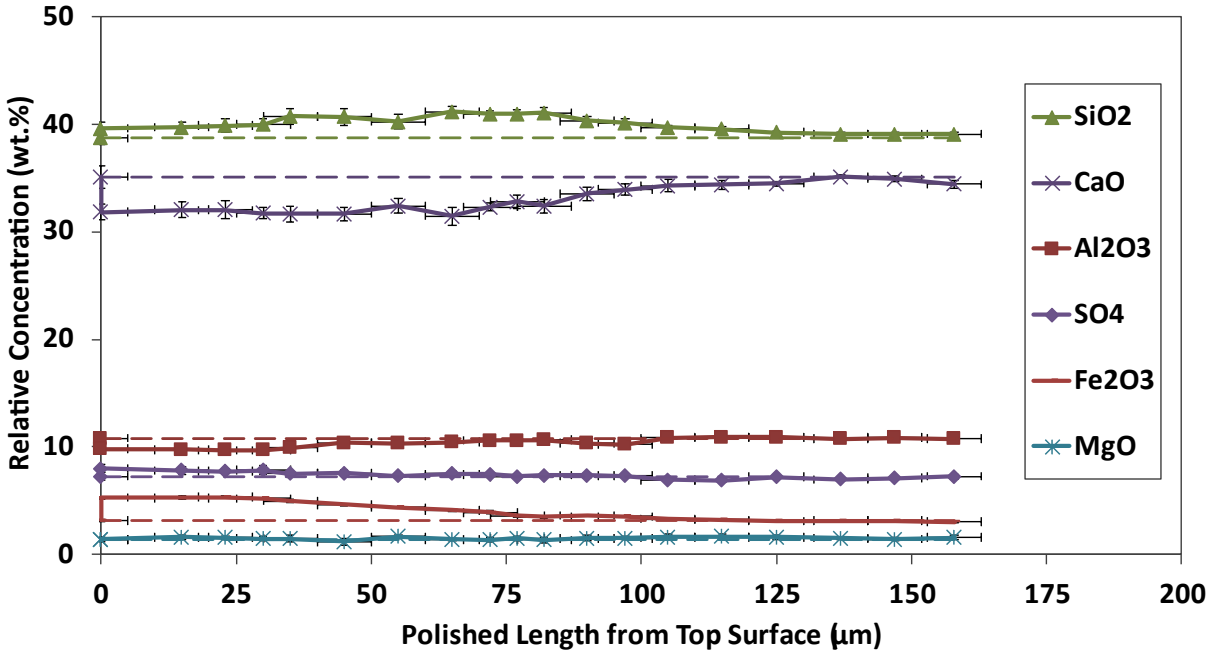

Figure 49. Estimation of reacted depth after $scCO_2$ treatment (7 days) through multiple surface XRF measurements and fine polishing (2400 grit sandpaper) steps. An additional horizontal shale sample rich in carbonates (Eagle Ford) was selected. The dashed lines represent the surface concentration of each oxide before treatment. After treatment, the surface concentration of CaO reduces as observed in Figure 48. Following a series of XRF measurements coupled with fine-polishing, the surface concentrations converge to the original elemental composition at around 150 µm deep from the original surface.

The combined results from XRF analysis in **Figure 48** and **Figure 49**, as well as SEM and EDS findings in **Figure 46** and **Figure 47**, collectively indicate that the observed geochemical reactivity in these samples predominantly manifests at the surface. The results also indicate preferential dissolution of calcite, while other species remain unaltered.

ScCO₂-brine-rock wettability

Figure 50 provides an overview of contact angle measurements for the scCO₂-brine-rock system conducted on group 1 samples, both before and after scCO₂ treatment. Before treatment, samples S1, S2, and S3 exhibit contact angles of 42 ± 1°, 37 ± 1°, and 35 ± 2°, respectively. These values align with those found in the literature for similar experimental conditions involving sandstones, caprock, and source rocks (**Figure 37**). Notably, these rocks maintain their water-wettability even at higher pressures of approximately up to 20 MPa. Post-scCO₂ treatment, minimal changes in contact angles are evident, despite the significant surface reactivity observed in sample S3 (**Figure 47**). Additionally, trapping of surface bubbles can also be noted on sample S3, which develops during the fluid-equilibration phase, suggesting potential geochemical reactions occurring at the surface as the brine becomes saturated with scCO₂.

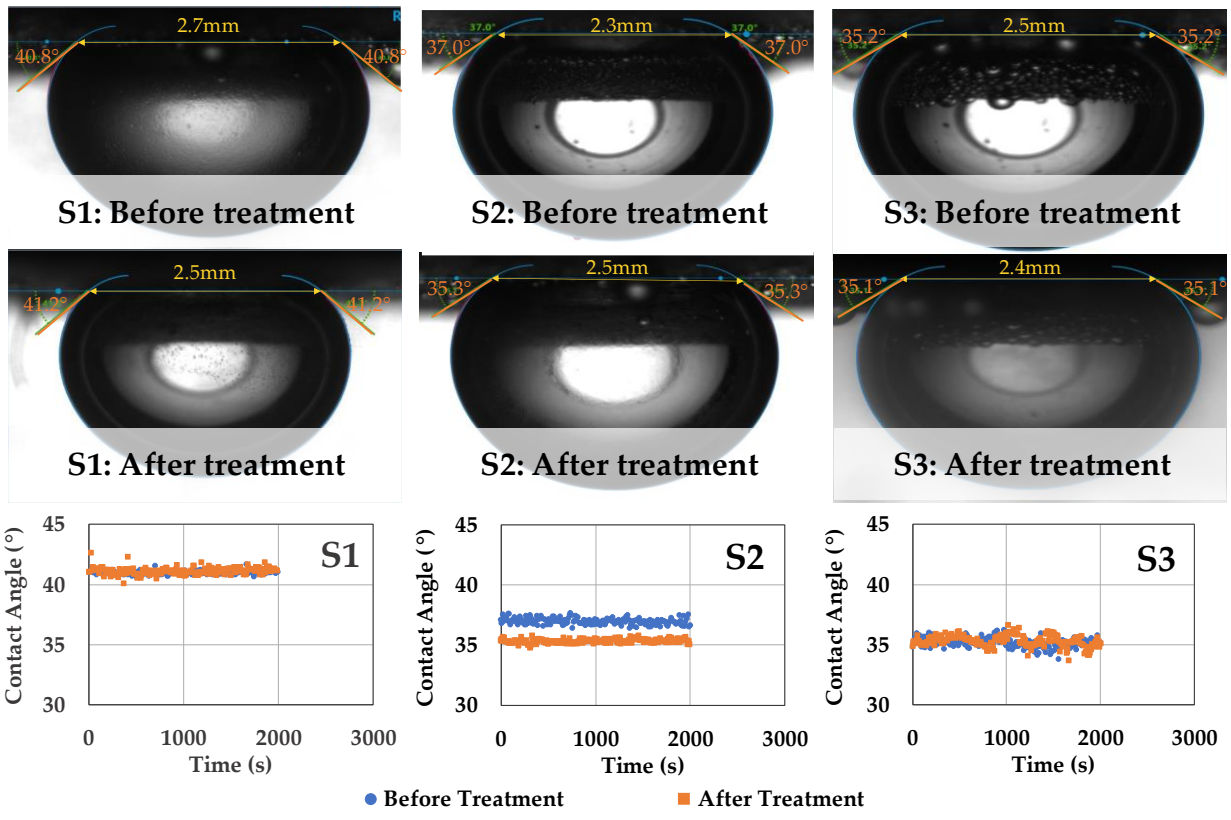

Figure 50. A summary of contact angle measurements in the $scCO_2$-brine-rock captive-bubble system, conducted on group 1 samples before and after $scCO_2$ treatment. The equilibrated contact angles remain unchanged, demonstrating the samples' consistent water-wettability, even under elevated pressure (~20 MPa) and temperature (150 °F) conditions, and after undergoing geochemical reactivity.

Pore size distribution

The thin disk samples from group 1 underwent a detailed analysis of pore size distribution in the bulk rocks using three techniques, mercury injection capillary pressure (MICP), nuclear magnetic resonance (NMR), and N_2 adsorption, both before and after $scCO_2$ treatment. **Figure 51** illustrates the incremental and cumulative pore throat size distributions (PTSDs) obtained from MICP analysis. **Figure 51(a)**, **Figure 51(b)**, and **Figure 51(c)**, depict the incremental curves for samples S1, S2, and S3, respectively, while their cumulative curves are sequentially presented in **Figure 51(d)**, **Figure 51(e)**, and **Figure 51(f)**. For the storage zone sample, S1, the PTSD indicates initial intrusion within the 2–10 µm pore throat size range, followed by a dominant peak between 200 and 600 nm. In contrast, the confining zone samples, S2 and S3, exhibit considerably lower pore throat range, with a main peak at approximately 6–10 nm and 2–4 nm, respectively. After $scCO_2$ treatment, minimal changes are observed in the PTSD of samples S1 and S2. Sample S3 shows minor alterations, with a slight increase in amplitude in the pore range of 100–1000 nm, followed by a reduction in the main peak at 1–10 nm.

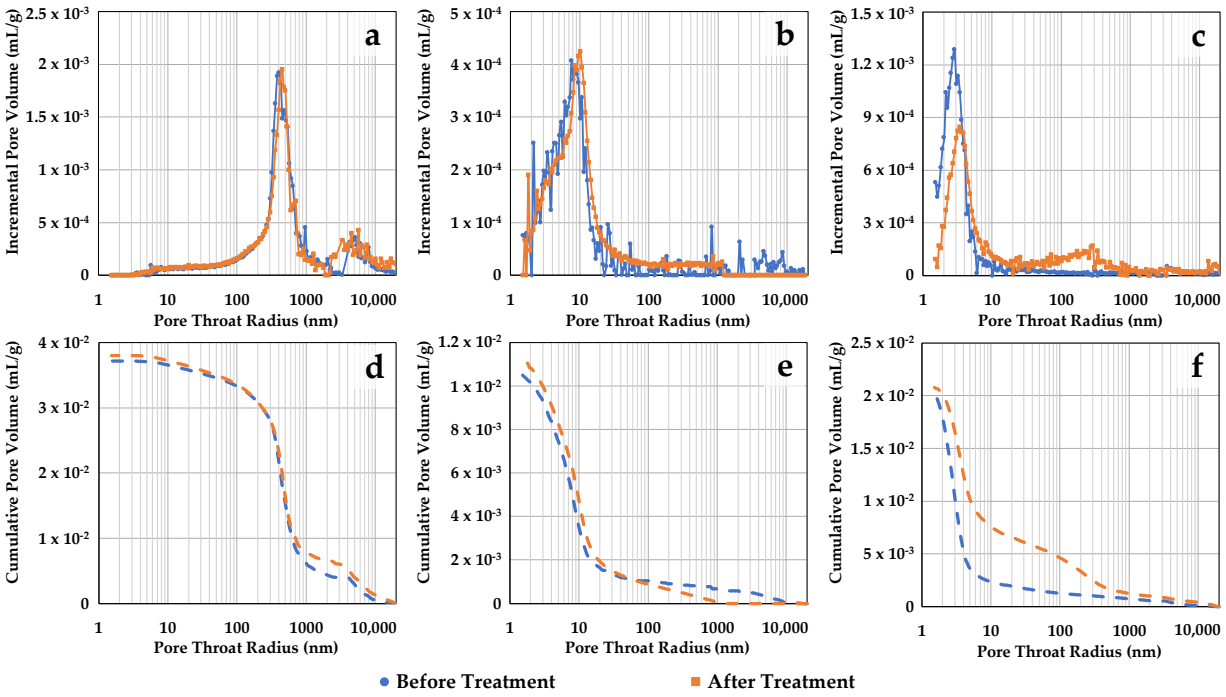

Figure 51. Pore throat size distributions (PTSDs) obtained with MICP on group 1 samples before and after $scCO_2$ treatment. The incremental curves for samples S1, S2, and S3 are shown in (a–c), respectively. Their cumulative curves are sequentially represented in (d–f). Overall, minimal changes are observed in the PTSD of the samples, except for a slight increase in amplitude within the 100–1000 nm range for sample S3, followed by a decrease in the 1–10 nm range.

Figure 52 presents the NMR T_2 data for group 1 samples before and after $scCO_2$ treatment. **Figure 52(a)**, **Figure 52(b)**, and **Figure 52(c)**, represent the incremental curves for samples S1, S2, and S3, while their cumulative curves are sequentially displayed in **Figure 52(d)**, **Figure 52(e)**, and **Figure 52(f)**. Before treatment, the storage zone sample, S1, displays a primary peak at around 100 ms T_2 relaxation, while the main peaks for confining samples S2 and S3 occur at shorter T_2 times of approximately 1.1 ms and 0.8 ms, respectively. In the confining zone samples, the second small peak above 100 ms is observed and most likely represents brine trapped in surface irregularities. Overall, the pore size distributions inferred through NMR exhibit no significant

changes in the three samples after treatment, with sample S3 displaying a small inflection in the spectrum after treatment around 1–20 ms, which does not substantially affect cumulative porosity within this range.

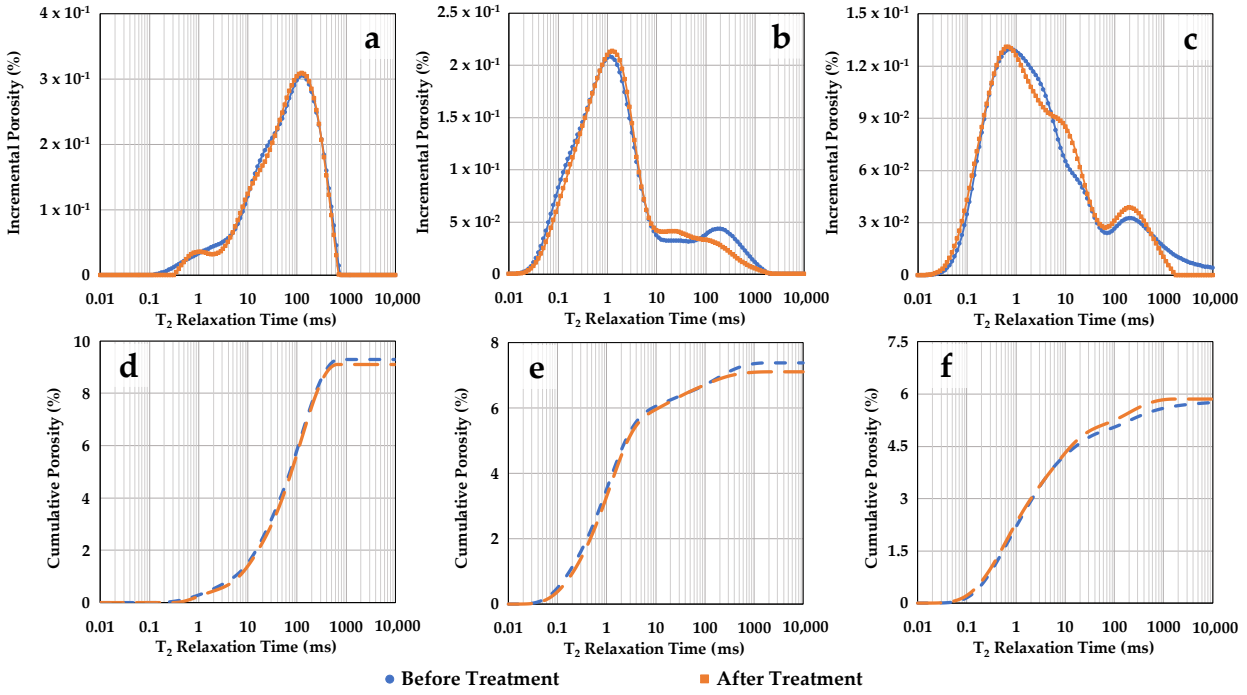

Figure 52. NMR T_2 data on group 1 samples before and after $scCO_2$ treatment. The incremental curves for samples S1, S2, and S3 are shown in (a–c), respectively. Their cumulative curves are sequentially represented in (d–f). Overall, the NMR T_2 data for the samples exhibit negligible changes, with the exception of a minor inflection observed around 1–20 ms for sample S3, which does not significantly impact its cumulative porosity.

Figure 53 displays N_2 adsorption and desorption isotherms for confining zone samples S2 and S3, both before (**Figure 53(a)**) and after (**Figure 53(b)**) $scCO_2$ treatment. These isotherms, along with hysteresis loop analysis, provide insights into pore structure and connectivity in tight porous media (Wang et al. 2017, Tian et al. 2020, Fuhua et al. 2023). Before treatment, both samples exhibit type IV isotherm characteristics with a distinct hysteresis loop, indicating capillary condensation in meso/macro-pores (Thommes et al. 2015). There is no limiting uptake at high relative pressures

(p/p^0), signifying an H3 hysteresis loop with slit-shaped pores forming plate-like structures (Sing 1985). A wider hysteresis loop for sample S3 suggests a more complex pore network. Following treatment, minimal changes in adsorption behavior are observed. Pore size distribution (PSD) analysis using density functional theory (DFT) reveals main peaks in the mesopore region (20–40 nm) for S2 and broader distribution for S3, with a more substantial fine-mesopore volume (2–20 nm) than S2. After treatment, no significant alterations in PSD or BET surface areas are observed. Sample S3 shows a slight decrease in mesopore volume, followed by a minor increase in the fine-mesopore range, resulting in a slight decrease in surface area. However, these differences are relatively small and do not significantly impact cumulative pore volumes in the nanopore range.

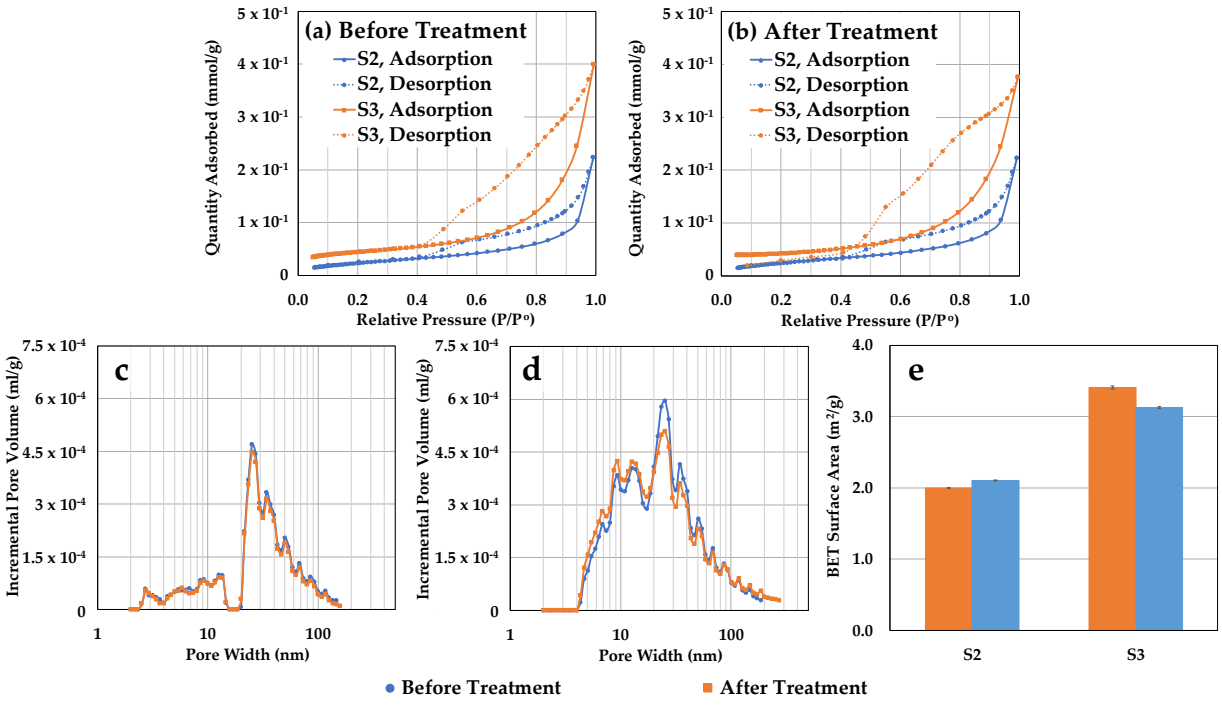

Figure 53. Isothermal N_2 adsorption results for the confining zone samples S2 and S3 before and after $scCO_2$ treatment. Before treatment, isotherms in (a) exhibit type IV characteristics with significant hysteresis loops, and S3 displays higher adsorption. After treatment, as seen in (b), isotherms maintain their shapes, indicating minimal changes in adsorption behavior. Incremental pore volume curves for S2, presented in (c), show a primary mesopore

peak (20–40 nm) that remains consistent post-treatment. In (d), the incremental pore volume curves for S3 reveal a broader distribution with more fine mesopores (2–20 nm) compared to S2, and slight pore size distribution changes post-treatment. Notably, (e) illustrates that the increased fine mesopores in S3 result in a larger BET surface area, with minor alterations after treatment.

Molecular diffusion

Figure 54 presents the NMR T_2 H_2O-D_2O diffusion measurement results for sample S4 (horizontal) prior to $scCO_2$ treatment. In **Figure 54(a)**, the NMR T_2 incremental and cumulative volumes during D_2O imbibition in the brine-saturated sample are shown as a function of time. Before D_2O imbibition, the NMR spectrum exhibits a single peak at around 0.8 ms, indicating rapid relaxation associated with small pore sizes. As time progresses during D_2O imbibition (invisible to H+ NMR), the T_2 spectra decrease. After approximately 810 minutes, D_2O diffusion ceases, leaving just under 0.2 mL of unexchanged H_2O brine in the sample. A shift in T_2 peak towards faster relaxation after D_2O imbibition indicate diffusion limitation in smaller pore sizes.

In **Figure 54(b)**, the ratio of measured D_2O volume that has diffused into the sample to the initial sample H_2O volume is plotted against the square root of time. Vertical error bars are related to the NMR volume error (Mamoudou 2020), while horizontal error bars account for the error in the NMR acquisition time. In the early-time region, the measured D_2O volume fraction entering the medium follows a linear relationship with the square root of time, flattening at longer times, and reaching a maximum imbibed volume fraction of approximately 0.8.

Figure 54(b) also presents the imbibed D_2O volume normalized by the volume fraction at the end of diffusion, a necessary step for fitting the non-steady state 1D diffusion (**Equation C.4**). This normalization allows for the derivation of the effective D_2O diffusion coefficient in the porous

medium (3.6 x 10^{-10} m^2/s), as shown in **Figure 54(c)**. The diffusion fitting criteria in shale align with previous work (Odiachi et al. 2022). Using the calculated effective D_2O diffusion coefficient, along with the bulk D_2O-H_2O diffusion coefficient value (2.2 x 10^{-9} m^2/s at 25 °C) (Baur et al. 1959) and **Equation 1.5**, a tortuosity value for horizontal sample S4 is determined to be 6.1.

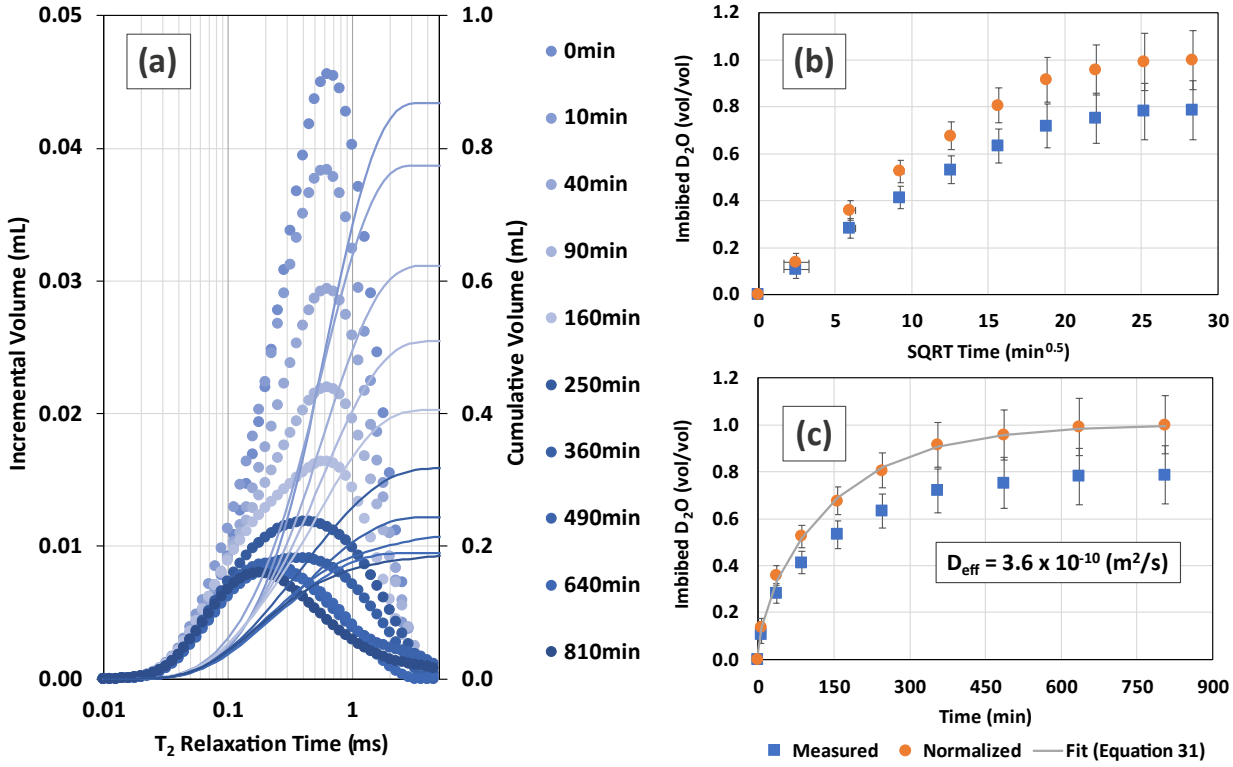

Figure 54. NMR T_2 H_2O-D_2O diffusion measurement for horizontal sample S4 before $scCO_2$ treatment. (a) NMR T_2 incremental and cumulative volumes during D_2O imbibition are plotted as function of relaxation time, with an initial peak around 0.8 ms indicating rapid relaxation due to small pores. As time progresses, D_2O diffusion ceases after about 810 minutes. A shift in T_2 peak toward faster relaxation indicate limited D_2O diffusion in smaller pore sizes. (b) ratio of measured D_2O volume that diffused into the sample to the initial sample H_2O volume, and imbibed D_2O volume normalized by the volume fraction at the end of diffusion, are plotted against the square root of time. Vertical error bars account for NMR volume errors, and horizontal error bars represent NMR acquisition time errors. In the early-time region, the D_2O volume fraction follows a linear relationship with the square root of time, reaching

a maximum imbibed volume fraction of about 0.8. (c) the normalized imbibed D_2O volume is used to derive the effective D_2O diffusion coefficient (3.6×10^{-10} m^2/s) in the porous medium. Using this coefficient, along with the bulk D_2O-H_2O diffusion coefficient (2.2×10^{-9} m^2/s at 25 °C) and **Equation 1.5**, a tortuosity value of 6.1 is determined for horizontal sample S4.

Figure 55 provides an overview of NMR T_2 H_2O-D_2O diffusion outcomes for group 2 samples, considering both horizontal and vertical orientations, before $scCO_2$ treatment. The normalized D_2O volumes as a function of the square root of time for samples S4, S5, and S6 are displayed in **Figure 55(a)**, **Figure 55(b)**, and **Figure 55(c)**, respectively. Notably, S4 and S6 exhibit faster horizontal diffusion compared to the vertical orientation, with sample S6, originating from an outcrop, showing less orientation-dependent variation.

In **Figure 55(d)**, effective diffusion coefficients (D_{eff}) for D_2O in both orientations are presented. These results reveal that D_{eff} can be up to three times larger in the horizontal orientation compared to the vertical orientation. Additionally, D_{eff} along the vertical orientation are similar amongst the samples. **Figure 55(e)** illustrates calculated tortuosities using bulk D_2O-H_2O diffusion coefficients and **Equation 1.5**. Here, it is evident that tortuosities in the vertical orientation can be up to four times larger than those in the horizontal orientation.

To explore the influence of anisotropy on the diffusive characteristics of the confining zones, the compressional wave velocities of both horizontal and vertical samples were assessed, as depicted in **Figure 56(a)**. These P-wave velocities were measured in the "as-received state" and under low confining pressure (250 psi). Notably, the results reveal that samples S4 and S6 exhibit higher P-wave velocities in the horizontal direction compared to the vertical orientation. In contrast, sample S5 displays relatively less anisotropy, aligning with the findings in **Figure 55**. **Figure 56(b)** shows

the ratio between horizontal and vertical P-wave velocities against the measured ratio of effective diffusion coefficients presented in **Figure 55(d)**. These results elucidate a correlation between P-wave anisotropy and anisotropy in diffusive properties in the confining zones. Additionally, the largest anisotropy in diffusivity and P-wave velocity observed in sample S4 correlates with an increasing clay content (illite > 50 wt.%) (Table 7).

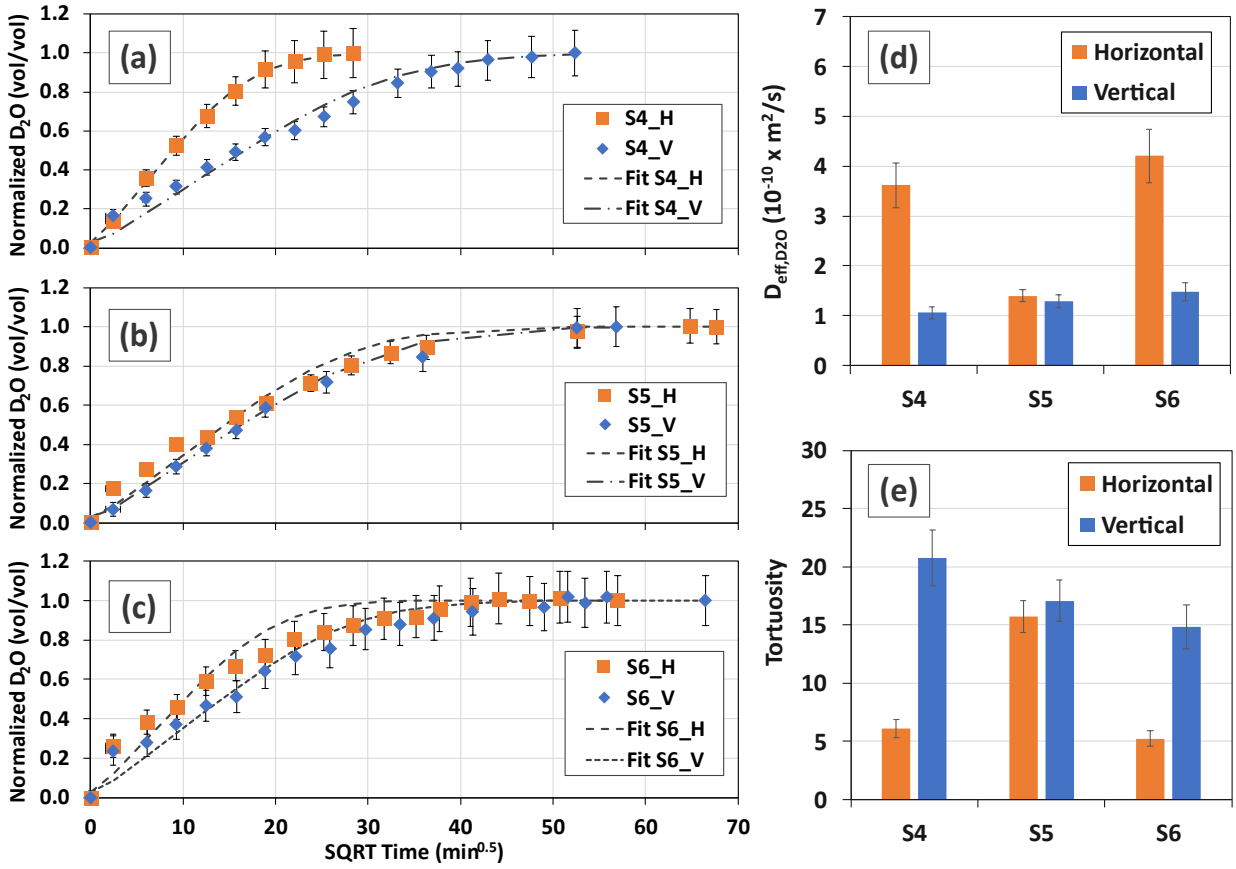

Figure 55. NMR T_2 H_2O-D_2O diffusion data for group 2 samples, considering both horizontal and vertical orientations, pre-$scCO_2$ treatment. Normalized D_2O volumes as a function of the square root of time for samples S4, S5, and S6 are shown in (a), (b), and (c), respectively. S4 and S6 exhibit notably faster horizontal diffusion, with S6 demonstrating less orientation-dependent variation due to its outcrop origin. In (d), effective diffusion coefficients (D_{eff}) are compared between both orientations, revealing up to threefold differences. Vertical D_{eff} values are

consistent across samples. (e) Depicts tortuosity calculations based on bulk diffusion coefficients, indicating up to fourfold greater values for the vertical orientation.

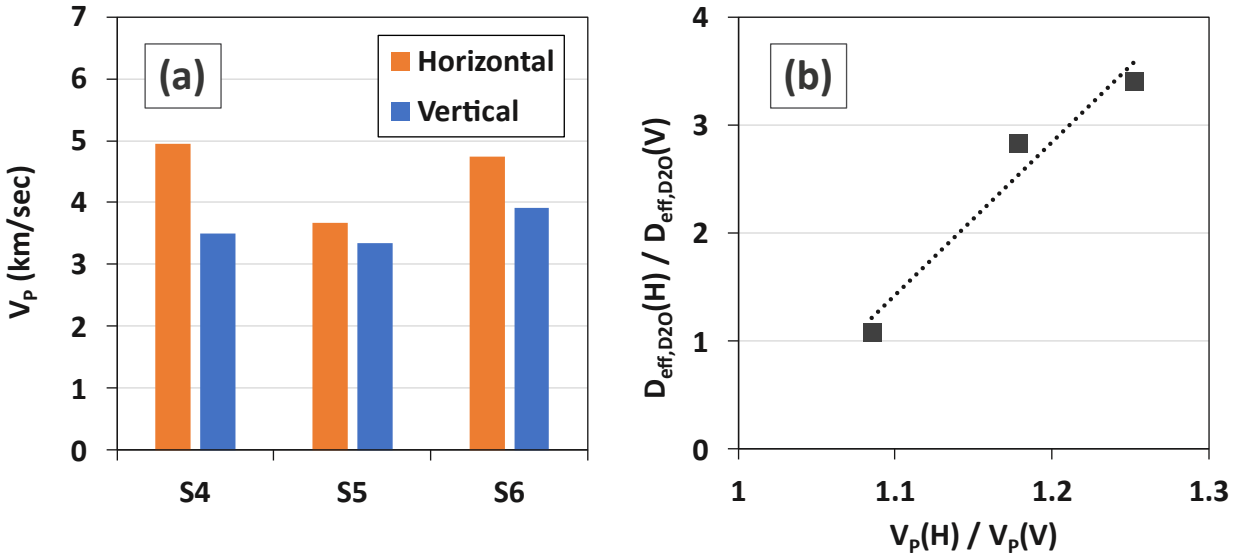

Figure 56. Impact of anisotropy on confining zone diffusion characteristics. In (a), compressional wave velocities for horizontal and vertical samples are shown under "as-received" and low confining pressure (250 psi). Notably, S4 and S6 exhibit higher horizontal P-wave velocities, while S5 displays less anisotropy. (b) illustrates the linear relationship between the ratio of horizontal to vertical P-wave velocities and the measured ratio of effective diffusion coefficients from Figure 55(d).

Subsequent to initial diffusion assessment, group 2 samples underwent $scCO_2$ treatment for a duration of 3 weeks. **Figure 57** summarizes NMR T_2 H_2O-D_2O outcomes in horizontal samples from group 2, both before and after $scCO_2$ treatment. The normalized D_2O volumes as a function of the square root of time for horizontal samples S4, S5, and S6 are presented in **Figure 57(a)**, **Figure 57(b)**, and **Figure 57(c)**, respectively. Their effective D_2O diffusion coefficients (D_{eff}) are depicted in **Figure 57(d)**. S4 exhibits increased diffusivity post-treatment, while S5 maintains consistent diffusivity. Interestingly, S6 initially displays reduced diffusivity after 1 week of treatment, which gradually approaches its original diffusivity after 3 weeks. The calculated

tortuosities, as shown in **Figure 57(e)**, reflect the trends observed in the effective diffusion coefficients of the samples.

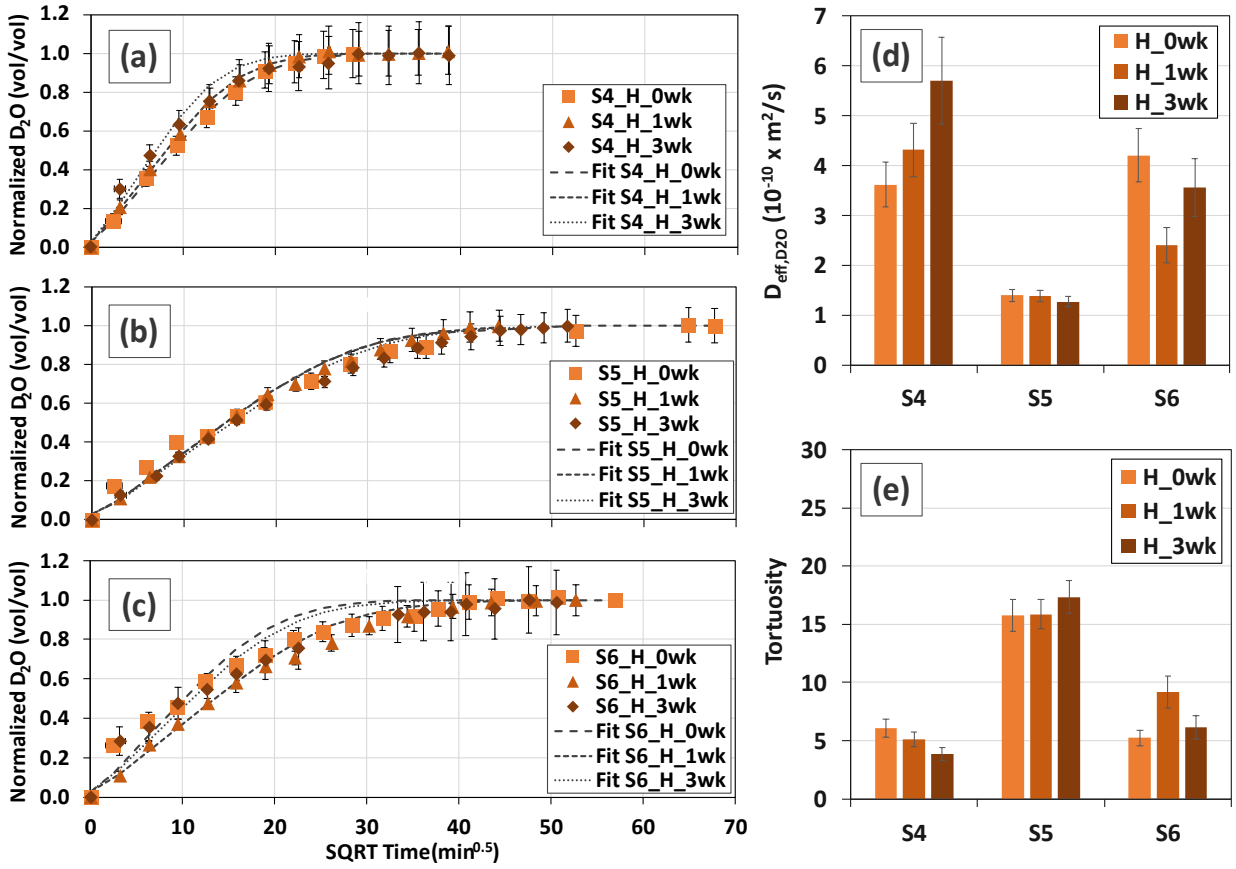

Figure 57. NMR T_2 H_2O-D_2O results for horizontal group 2 samples before and after $scCO_2$ treatment. (a) to (c) present normalized D_2O volumes versus the square root of time for samples S4, S5, and S6, respectively. (d) effective D_2O diffusion coefficients (D_{eff}). (e) calculated tortuosities. Following treatment, S4 displays increased diffusivity, S5 maintains consistent diffusivity, and S6 initially exhibits reduced diffusivity after 1 week, followed by increased diffusivity after 3 weeks. Tortuosity trends align with the changes in effective diffusion coefficients.

Similarly to **Figure 57**, **Figure 58** presents a summary of NMR T_2 H_2O-D_2O results in vertical samples before and after $scCO_2$ treatment. Comparable trends in diffusivity and tortuosity changes during treatment are observed in vertical samples when compared to horizontal samples. Sample

S4 exhibits increased diffusivity (reduced tortuosity) after treatment, while S5 retains its pre-treatment characteristics. S6 displays reduced diffusivity after 1 week, followed by an increase after 3 weeks, reflecting fluctuations in tortuosity (initial increase, subsequent decrease).

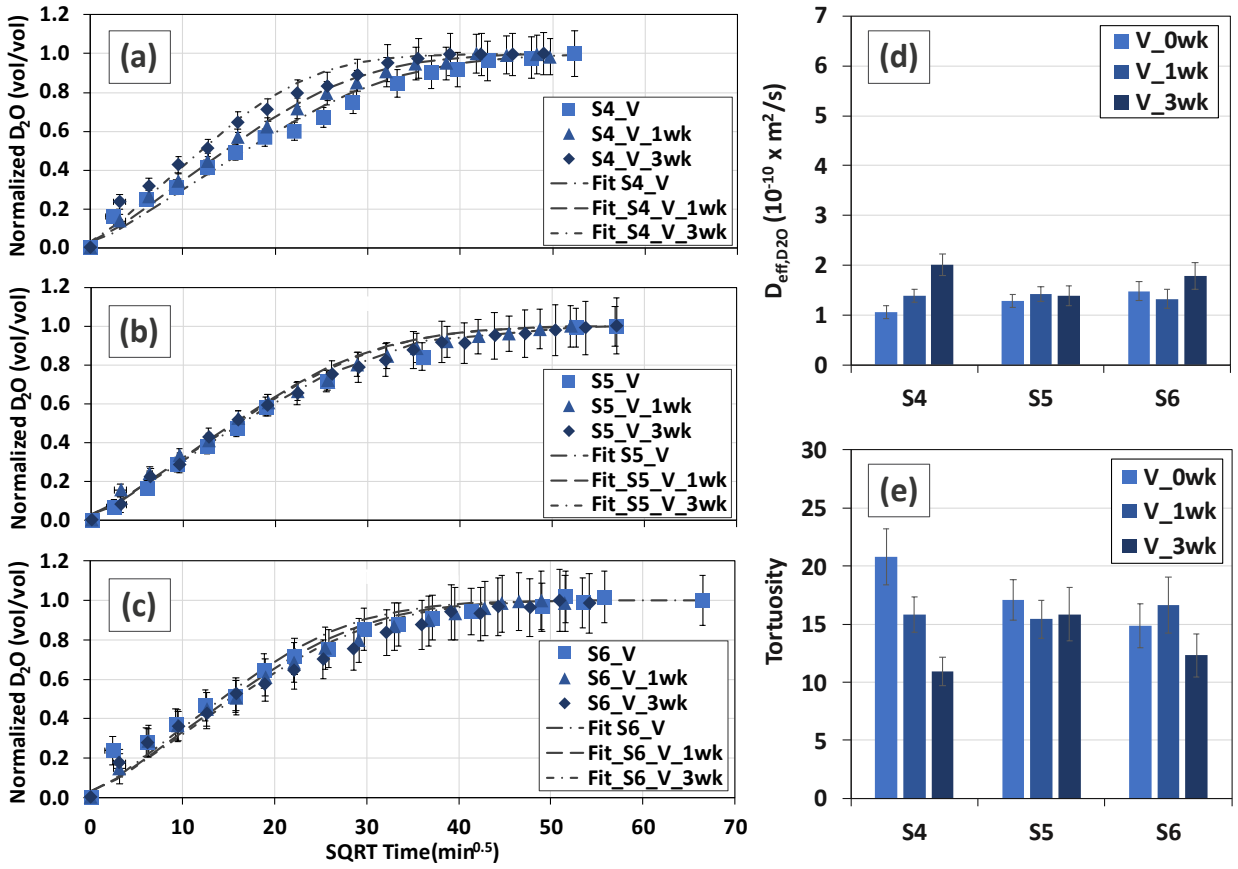

Figure 58. NMR T_2 H_2O-D_2O results for vertical group 2 samples before and after $scCO_2$ treatment. (a) to (c) present normalized D_2O volumes versus the square root of time for samples S4, S5, and S6, respectively. (d) effective D_2O diffusion coefficients (D_{eff}). (e) calculated tortuosities. Comparable trends in diffusivity and tortuosity changes during treatment are observed for vertical samples as compared to horizontal (Figure 57). S4 shows increased diffusivity (lower tortuosity) after treatment, S5 remains consistent, and S6 experiences fluctuations in both diffusivity and tortuosity.

To further understand the factors influencing the trends in diffusivity during $scCO_2$ treatment, **Figure 59** presents a summary of the ratios of total D_2O volumes diffused into the samples relative to their H_2O volumes before D_2O imbibition. These results suggest that the volume of D_2O diffusing into the samples remains relatively consistent throughout the $scCO_2$ treatment. Additionally, the endpoints of diffusion exhibit consistency between horizontal and vertical samples. Specifically, samples S4 and S5 experience the exchange of nearly 80% of their initial H_2O volume with D_2O, while sample S6 exchanges approximately 60-70%.

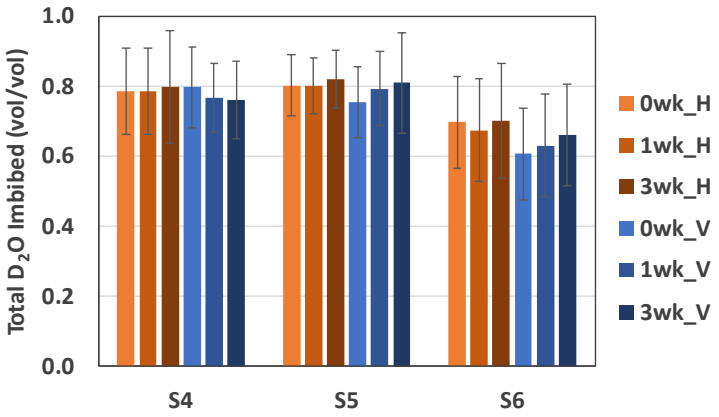

Figure 59. The ratios of total D_2O volumes diffused into the samples compared to their initial H_2O volumes during $scCO_2$ treatment. These ratios suggest that the volume of D_2O diffusing into the samples remains consistent throughout the treatment. Notably, the endpoints of diffusion exhibit uniformity between horizontal and vertical samples. Samples S4 and S5 exchange roughly 80% of their initial H_2O volume for D_2O, while sample S6 exchanges around 60-70%.

NMR T_2 H_2O-D_2O diffusion results for group 2 samples, encompassing both horizontal and vertical orientations, are given in **Appendix D**. **Table 8** presents the measured effective D_2O diffusion coefficients, tortuosities, and estimates of effective $scCO_2$ diffusion coefficients under the subsurface conditions defined in this study (150 °F, 3000 psi, and ~1 M salinity brine). These estimated effective $scCO_2$ diffusion coefficients can be employed to forecast the extent of CO_2

diffusion within the confining zone. An illustration of the concentration-distance profile over time is provided in **Figure 66(a)** and **Figure 66(b)** using diffusivities for sample S4 before and after 3 weeks of $scCO_2$ treatment, respectively. Without including short-term geochemical reactivity, $scCO_2$ does not diffuse beyond roughly 5 meters into the confining zone after 100 years. The inclusion of short-term geochemical reactivity slightly increases the diffusion length from 5 meters to 7 meters, indicated by the small changes in diffusivity observed.

$ScCO_2$ breakthrough test

The intricate nature of CO_2-fluid-rock interactions, especially in complex rock systems such as shales, can yield diverse results during the displacement of brine by $scCO_2$, as previously observed in the literature (Hildenbrand and Krooss 2003, Wollenweber et al. 2009, Edlmann et al. 2013). In preparation for extensive $scCO_2$ breakthrough testing, initial validation experiments were conducted in less complex systems. For these experiments, synthetically-made ceramic sample (Cobra Technologies BV, Netherlands) with specific pore size (~50 nm pore diameter) and quartz-rich sandstone/siltstone rocks were selected. The tests were carried out at room temperature, and the porous materials were saturated with a straightforward 2.5 wt.% KCl solution, utilizing N_2 as the displacing phase. Simultaneously, the pore size distribution of these porous materials was determined through mercury injection capillary pressure (MICP) analysis on twin samples.

Figure 60 illustrates the summary of a constant-flowrate N_2-brine breakthrough test conducted on the nanoporous ceramic sample (1" diameter, ~1/4" thickness) at room temperature. **Figure 60(a)** depicts the pressures' profiles (e.g. inlet or upstream, and outlet or downstream) and the constant flow rate of 0.1 mL/min. Prior to N_2 injection, a net confining pressure of 1000 psi was applied. During injection, the inlet pressure builds up due to existing capillary forces in the N_2-brine-pore

interface that restrains N_2 displacement of brine. The outlet pressure is maintained roughly at ~1550 psi. When the pressure difference between the inlet and outlet (**Figure 60(b)**) reaches a value of ~560 psi, a gas bubble in the outlet pipette is observed, indicating N_2 breakthrough. Following breakthrough, a short two-phase flow period of N_2 and brine (ΔP~620 psi) takes place, which is followed by a longer N_2 single-phase flow period where ΔP reduces gradually, and then reduces to zero when injection ceases. **Figure 60(c)** depicts the outlet pipette in three different time steps (from left to right): (i) before injection, showing a stagnant brine-air interface; (ii) at ΔP~560 psi, where the bubble at the interface indicates gas breakthrough; (iii) at ΔP~620 psi, where two-phase flow of N_2 gas and brine is observed.

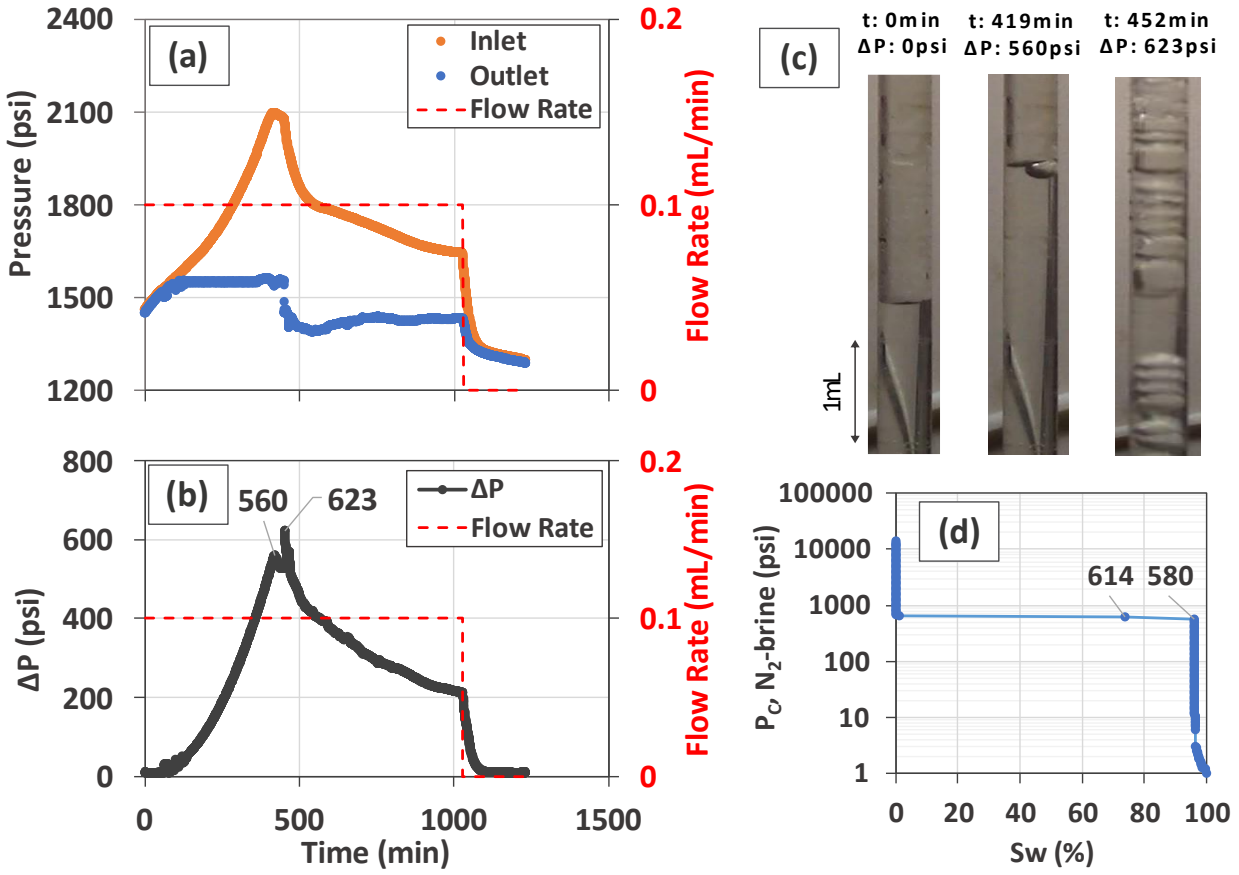

Figure 60. Summary of the N_2-brine breakthrough test on a nanoporous ceramic membrane (1" diameter, ~1/4" thickness) at room temperature. (a) inlet and outlet pressures during a constant flow rate injection (0.1 mL/min). A net 1000 psi pressure was applied. When the pressure difference reached ~560 psi (b), indicating N_2 breakthrough, a gas bubble was observed in the outlet pipette (c). This was followed by a two-phase flow (N_2 and brine) and a subsequent N_2 flow period until injection ceased. (d) the capillary pressure (Pc) curve obtained through MICP shows a breakthrough pressure similar to that observed (P_{BT} ~ 560 psi to 580 from MICP).

Figure 60(d) shows the capillary pressure (Pc) curve for the ceramic sample obtained with MICP. The results indicate that the measured N_2-brine breakthrough pressure (P_{BT} ~ 560 psi) is similar to the breakthrough pressure estimated using the MICP-derived pore size distribution (~580 psi) for the nanoporous system.

Equations 7.1 and **7.2** detail the conversion between the Pc of a Hg-air interface to N_2-brine and $scCO_2$-brine, respectively:

$$P_{c,N_2:H_2O} = \frac{\gamma_{N_2:H_2O} \times \cos\theta_{N_2:H_2O}}{\gamma_{Hg:air} \times \cos\theta_{Hg:air}} \times P_{c,Hg:air} \approx \left| \frac{\left(\frac{72mN}{m}\right) \times \cos(0°)}{\left(\frac{485mN}{m}\right) \times \cos(130°)} \right| \times P_{c,Hg:air} \approx 0.23 P_{c,Hg:air} \quad (7.1)$$

$$P_{c,scCO_2:H_2O} = \frac{\gamma_{scCO_2:H_2O} \times \cos\theta_{scCO_2:H_2O}}{\gamma_{Hg:air} \times \cos\theta_{Hg:air}} \times P_{c,Hg:air} \approx \left| \frac{\left(\frac{27mN}{m}\right) \times \cos(35°)}{\left(\frac{485mN}{m}\right) \times \cos(130°)} \right| \times P_{c,Hg:air} \approx 0.07 P_{c,Hg:air} \quad (7.2)$$

assuming a N_2–brine γ of 72 mN/m and θ of 0° (Song and Fan 2022), $scCO_2$–brine γ of 27 mN/m and θ of 35° for this work experimental conditions, and Hg–air γ of 485 mN/m and θ of 130° (laboratory conditions). **Equations 7.1** and **7.2** indicate that the N_2–brine and $scCO_2$–brine capillary pressures (Pc) at the experimental conditions is about ~4.5 and ~14 times smaller than laboratory Hg–air Pc, respectively.

In **Figure 61(a)**, the Hg-air capillary pressure curves for samples S4 and S6 are presented prior to $scCO_2$ treatment. Subsequently, **Figure 61(b)** transforms these capillary pressure curves into $scCO_2$-brine interfaces using **Equation 7.2**. The analysis of their inflection points indicate $scCO_2$ displacement pressures of approximately 1200 psi for S4 and 1800 psi for S6, respectively. **Figure 61(c)** and **Figure 61(d)** display micro-CT slices of S4 and S6 following treatment, where no

discernible microcracks are observed. However, sample S5 exhibited noticeable fractures and was excluded from further measurements.

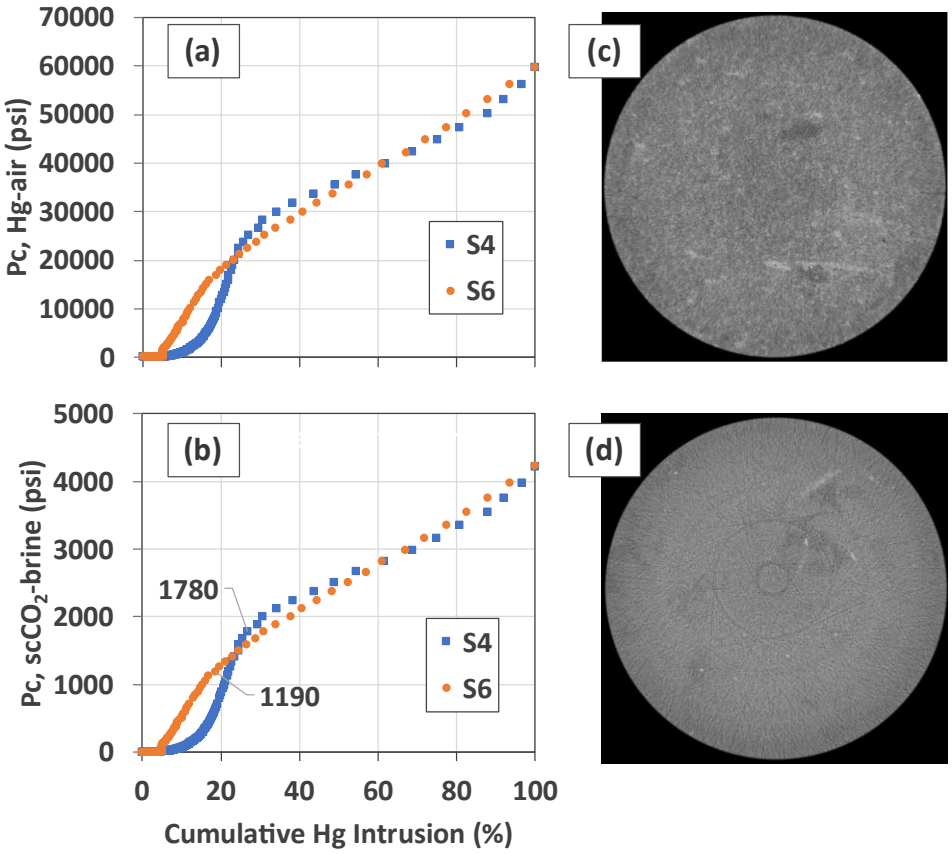

Figure 61. (a) Hg-air capillary pressure curves for samples S4 and S6 before $scCO_2$ treatment. (b) conversion to $scCO_2$-brine interfaces, indicating displacement pressures of approximately 1200 psi for S4 and 1800 psi for S6. (c) and (d) after treatment, micro-CT slices of S4 and S6 exhibit structural integrity with no observable microcracks.

Figure 62 provides an overview of the stepwise pressure $scCO_2$ breakthrough experiments conducted on samples S4 and S6 at reservoir temperature (150 °F), both before and after $scCO_2$ treatment. **Figure 62(a)** and **Figure 62(b)** present the results for S4 and S6 before treatment, respectively. These experiments involved applying injection pressures up to 4500 psi higher than the outlet pressures. Such differential pressures are higher than the expected displacement

pressures for $scCO_2$ shown in **Figure 61(b)**. While a reduction in pump volumes was observed, no visual indication of breakthrough was apparent during these tests. It is important to mention that these initial experiments were conducted at larger incremental pressures (~500 psi) and for short injection time (~2 days).

The same experiments on S4 and S6 were performed after $scCO_2$ treatment (**Figure 62(c)** and **Figure 62(d)**, respectively). Extended experimental durations of up to 10 days and small incremental pressure (100 psi) were applied. Maximum injection pressures reached approximately 800 psi higher than the outlet pressure by the end of the tests. These tests revealed a significant reduction in pump volumes (>4 mL), exceedingly more than 10 times the sample pore volume (~0.4 mL). Despite the decrease in pump volumes, no visual indication of breakthrough was observed in the post-treatment tests.

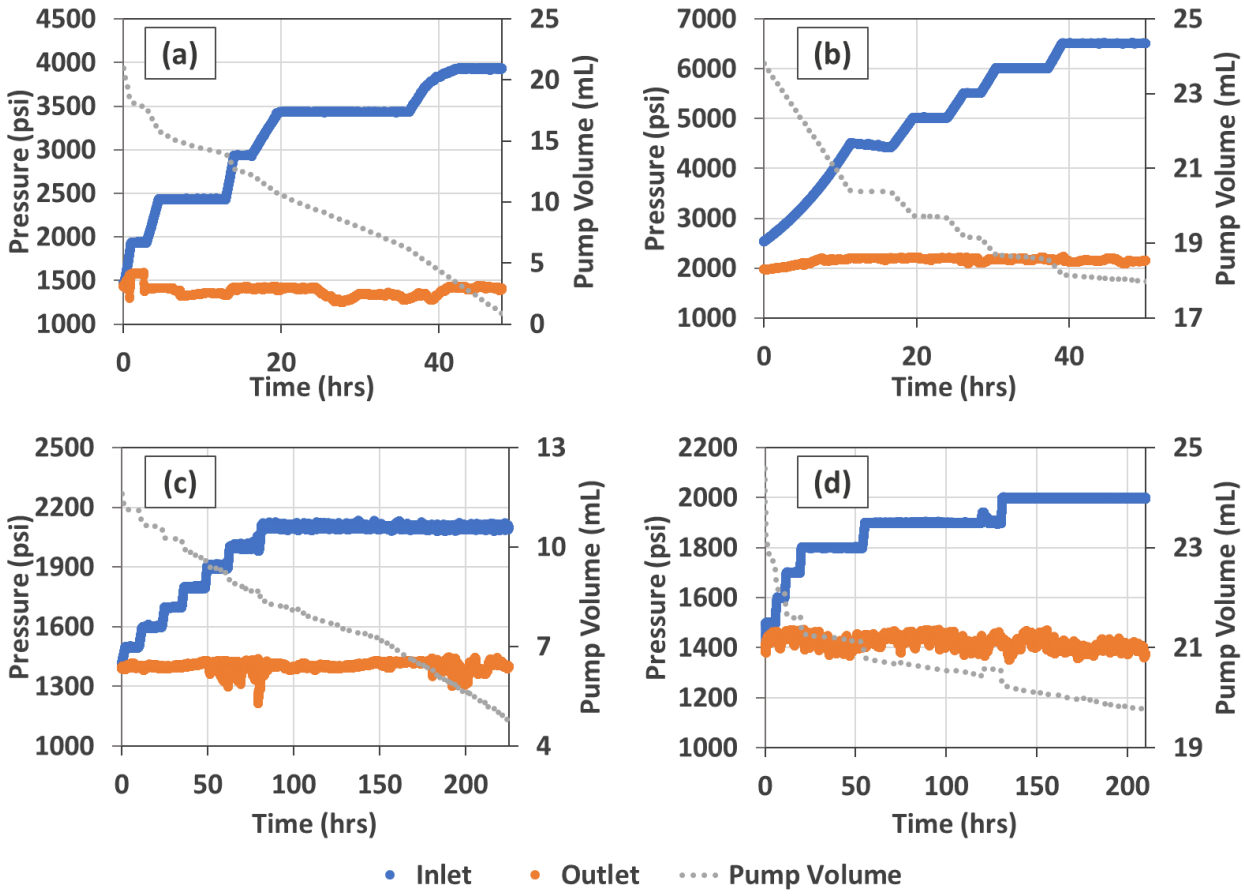

Figure 62. Overview of stepwise pressure $scCO_2$ breakthrough experiments conducted on samples S4 and S6. The tests were carried out at reservoir temperature (150 °F), both before and after $scCO_2$ treatment. (a) and (b) results for S4 and S6 before treatment. Injection pressures reaching up to 4500 psi higher than the outlet pressures were applied in these experiments. Despite observing a reduction in pump volumes, no visual indication of breakthrough was detected during these tests. (c) and (d) same experiments on S4 and S6 after $scCO_2$ treatment, with extended experimental durations of up to 10 days. Maximum injection pressures reached approximately 800 psi higher than the outlet pressure. These tests revealed a significant reduction in pump volumes, exceeding 10 times the sample pore volume. No visual indication of breakthrough was observed in the post-treatment tests.

Chapter 8. Discussion

Relevance of sample scale, transport properties, and experimental results in nanoporous systems

As observed throughout this study, assessing the influence of $scCO_2$-fluid-rock interactions on fluid mobilization in nanoporous systems involves the integration of knowledge spanning pore, core, and reservoir scales. In nanoporous frameworks such as unconventional liquid-rich shale reservoirs (ULR) and confining zones relevant to carbon geostorage (CGS), excessive capillary pressures are encountered, which can reach up to 10,000 psi for gas-water systems (Bustin et al. 2008). High capillary pressure scenarios significantly impede pressure-driven fluid flow, making concentration-driven flow, i.e., diffusion, a relevant transport mechanism (Dang et al. 2023).

Diffusive flow, where substances move from regions of high concentration to low concentration, is contingent on the diffusion coefficient (diffusivity) of the substance. The Stokes-Einstein relationship (**Equation 5.4**) establishes a direct proportionality between the diffusivity of a molecule in a dilute solution (e.g. water) with temperature, and an inverse proportionality with the solution's viscosity and the size of the molecule. When applied to a system, the total amount of diffusing molecules in a given time is also affected by the system's surface area. Consequently, the influence of diffusional transport is amplified in systems with augmented specific surface areas, as is the case in laboratory experiments conducted with crushed-size samples.

Throughout this research, it was demonstrated that diffusive flow in nanoporous systems, especially when coupled with enhanced surface-area crushed-sized samples, can substantially magnify responses in laboratory measurements. As reported in Chapter 4, the 21 HnP-EOR in ULR tests using crushed-sized samples (7-8 mm) resulted in significantly higher and faster fluid recoveries than those expected in real-world field applications. Similarly, within the context of

CGS, studies involving $scCO_2$ treatments in confining zones using micrometer-sized crushed samples have reported notable geochemical alterations driven by CO_2 dissolution and diffusion in brine (Mouzakis et al. 2016, Qin et al. 2017, Pan et al. 2018b, Sanguinito et al. 2018, Goodman et al. 2019, Fatah et al. 2021, Gholami et al. 2021, Qin et al. 2022, Medina et al. 2023, Wang et al. 2023).

In the context of this research, the findings in Chapter 7, involving relatively larger-scale samples (inch-sized) as compared to previous $scCO_2$ treatment studies, reveal that geochemical reactivity within nanoporous confining zones is limited to a shallow region near the sample surface, preserving the bulk rock properties. The data presented in **Figure 49** indicate that the diffusivity of the reacted zone at a treatment temperature of 150 °F is on the order of 9×10^{-15} m^2/s. This value is roughly 4-5 orders of magnitude smaller than the effective $scCO_2$ diffusivities in brine-saturated confining zones at similar conditions, as estimated in **Table 8**. Notably, a recent experimental study has also demonstrated significantly lower reacted zone diffusivity as compared to effective $scCO_2$ diffusivity in shale formations (Montegrossi et al. 2023). Moreover, an integration of the tortuosity measurements after short-term geochemical reactivity from this study with literature-based CO_2-H_2O diffusion coefficients in subsurface conditions, suggests that even after 100 years of injection, the CO_2 molecule does not penetrate beyond approximately 7 meters into any of the studied confining zones (**Figure 66(b)**). It is important to note that the diffusion measurements were conducted under unconfined state, and the effective diffusivity of CO_2 (hence depth of penetration) is expected to decrease even further under subsurface conditions of effective stress (Sun et al. 2023b).

Another example of the influence of available surface area on diffusive transport is highlighted in the doping agent experiment on the Eagle Ford preserved plug sample (**Figure 8**). In this case, it required up to two months for the water-soluble solution (65% $MnCl_2$) to diffuse through the brine in the preserved core plug at laboratory conditions of unconfined stress and room temperature. Overall, while crushed-size samples offer faster experimentation, it is imperative to exercise caution when directly extrapolating experimental findings to field or reservoir-scale models.

Interplay between injection pressure, miscibility, and diffusivity during HnP-EOR in ULR

The determination of the minimum miscibility pressure (MMP) between a solvent and crude oil, whether experimentally using reservoir crude oil samples or established through compositional simulations, is a critical design parameter in the planning of miscible gas injection for EOR. In the MMP determination at reservoir temperature using the vanishing interfacial tension technique (**Figure 10**), it was observed that $scCO_2$ exhibits a lower MMP compared to enriched or produced field gases, requiring less pressure to form a single-phase with crude oil. Furthermore, the findings from the static HnP-EOR tests performed on crude oil at reservoir temperature indicate that $scCO_2$ outperforms produced field gas when injected at the same relative pressure above their respective VIT-MMPs (**Figure 13**). A comprehensive analysis combining NMR and GC-MS reveals a preferential production of lighter fractions in both tests, resulting in an increase in the heaviness of the residual oil following each HnP cycle (**Figure 16**). The increase in heaviness of residual oil has a progressive effect on the solvent-residual oil MMP (**Figure 17**). By injecting produced field gas above the original solvent-crude oil MMP, it is estimated that the MMP increases by up to 800 psi after six HnP cycles on the crude oil.

Introducing a shale rock into the system has a significant impact to HnP-EOR, as demonstrated by systematic analysis of the residual oil fraction through two quantitative techniques: NMR integrated with GC-MS and modified dry pyrolysis. Compositional analysis of the extracted residual oil after $scCO_2$ HnP-EOR (**Figure 19(a)**) combined with in-situ hydrocarbon assessment after 21 HnP-EOR tests (**Figure 23**) indicate substantial compositional differences in the reservoir crude oil before and after HnP-EOR. With the inclusion of the shale rock system in the $scCO_2$ HnP-EOR test, negligible recovery of heavier fractions above C_{25} is observed (**Figure 19**). Without the shale rock system and for the same experimental conditions (P_{inj} of 1000 psi above original MMP and 150 °F), these fractions are largely produced within the 1st injection cycle (**Figure 16(a)**).

The integration of these findings suggests that the effect of MMP increase during HnP-EOR in bulk oil, as illustrated in **Figure 17**, is even more pronounced within the shale rock system. A linear increase in oil recovery with injection pressure extending beyond the original gas-oil MMP is observed in the 18 tests using two hydrocarbon gases (produced and enriched field gases) on two preserved shale samples (**Figure 22**). In contrast, the two immiscible helium tests conducted at a 2000 psi pressure difference, resulting in much lower oil recovery than with hydrocarbon gases, imply a low contribution of pressure-driven oil compressibility effects and a strong implication of a diffusion-driven mechanism to oil recovery. The monotonic increase in water recovery after each cycle and its lack of correlation with pressure indicate a negligible effect of pressure displacement on water production. Water recovery is likely associated with a concentration difference when the dry solvent gas is cyclically injected, and the diffusion of water to the solvent phase is further enhanced by an increase in experimental temperature to 150 °F.

Hence, the observation of linear oil recovery with injection pressure, even above the original MMP, is potentially influenced by the combination of two effects: (i) after each cycle, the MMP of the solvent-residual oil increases due to a significant rise in residual oil heaviness, and (ii) there is a linear increase in the diffusion coefficient of hydrocarbon gas molecules, primarily CH_4, in crude oil with increasing pressure. The latter phenomenon is attributed to a synergistic effect arising from the reduction in oil viscosity and density (as discussed by Jamialahmadi et al. (2006)). It is important to note that the substantial water production observed in the 21 HnP-EOR tests does not exhibit a similar trend with pressure, as diffusion of molecules in water systems is minimally affected by pressure (**Figure 40**). Moreover, the self-diffusivity of a water molecule significantly exceeds that of long-chain hydrocarbon molecules, which explains the differences in recovery amounts between the two fluids during the HnP experiments.

In summary, the HnP-EOR tests conducted on preserved samples demonstrated an enhanced performance of $scCO_2$ injection when compared to the linear trend observed with field gases. The results further suggest a slightly superior performance of produced field gas compared to enriched field gas. The earlier finding aligns with the shale oil reservoir HnP-EOR model, which incorporates diffusive transport, and support the experimental observation of $scCO_2$'s efficiency as a solvent (**Figure 24**). Moreover, the HnP-EOR model revealed additional oil recoveries with injection pressures extending beyond each solvent-crude oil MMP, as observed in the experiments. In fact, MMP determination using compositional simulations confirmed miscibility between the three solvents and crude oil at the initial reservoir conditions of 150 °F and 6000 psi. However, it is important to acknowledge that the HnP-EOR model indicated a relatively lower performance of produced field gas in comparison to enriched field gas. Discrepancies between the experimental

and modeling results for the recoveries of the two hydrocarbon (HC) gases may be attributed to the influence of other mechanisms that were not explicitly accounted for in the model, such as nanoconfinement and adsorption effects.

In the $scCO_2$ HnP-EOR simulations using the shale oil reservoir model, an assessment of net carbon efficiency reveals compelling insights. After five HnP-EOR cycles over a span of 10 years, when operating at an injection pressure of 6000 psi, the produced-to-injected $scCO_2$ ratio stands at approximately 66% (**Figure 26**). As injection pressure rises, this ratio significantly decreases, reflecting improved $scCO_2$ solubility in the reservoir oil and a less carbon-intensive operation. When the injection pressure is elevated to 10,000 psi, the ratio converges to roughly 33%, signifying that around 67% of the injected $scCO_2$ is sequestered in the subsurface after 10 years. It is worth noting that incorporating additional factors into the model, such as $scCO_2$ adsorption on kerogen, may lead to further improvements in this analysis.

Impact of geochemical reactivity on capillary displacement and effective diffusion during CGS

Geochemical reactions resulting from the dissolution of $scCO_2$ in brine have been experimentally demonstrated to induce microstructural changes in both storage zones (Seyyedi et al. 2020, Wang et al. 2020, Kim et al. 2023) and confining zones (Mouzakis et al. 2016, Qin et al. 2017, Pan et al. 2018b, Sanguinito et al. 2018, Goodman et al. 2019, Fatah et al. 2021, Gholami et al. 2021, Qin et al. 2022, Medina et al. 2023, Wang et al. 2023) even over relatively short treatment durations, typically a few weeks. These effects on storage zones are often observed through $scCO_2$-enriched brine dynamic injection tests in limestone core samples. Notably, substantial dissolution (resulting in wormholes) is observed near the core plugs' inlet, followed by limited precipitation in the distal region. While dynamic tests are valuable for assessing geochemical impacts in high-flow regions,

the duration of reactivity is extended because "fresh" reactant species (e.g., H+) continue to be supplied in open flow systems.

Conversely, investigations into the geochemical alterations of confining zones are typically conducted via static $scCO_2$ treatments in closed systems using crushed samples of micrometer size. Significant geochemical reactivity is evidenced by the preferential dissolution (and precipitation) of carbonate minerals, which subsequently influence pore size distributions. However, the remarkably low effective diffusivity observed within nanoporous confining zones leads to the establishment of concentration gradients of reactant species (e.g., H+) across the sample. During the diffusion process through the sample, these reactant species are actively involved in geochemical reactions, particularly in fast-kinetics reactions such as the dissolution of calcite through an acid mechanism (as represented by **Equation 5.8**). This active participation depletes their concentration in distal regions of the core sample, thus generating a diffusion-reaction concentration gradient of these species. The diffusion-reaction concentration gradient plays a pivotal role in promoting surface reactivity and intensifying reactions within systems characterized by high specific surface areas, such as crushed samples.

Overall, modeling studies on reactive transport demonstrate that geochemical reactions driven by $scCO_2$ diffusion within nanoporous confining zones are anticipated to impact properties over timescales spanning hundreds to thousands of years (Gaus et al. 2005). To address the challenge of prolonged experimental durations, a promising strategy involves the combination of quantitative analytical tools capable of concurrently monitoring these alterations at the surface level, down to the nanometer, micrometer, and millimeter depths of invasion.

In Chapter 7, the influence of geochemical reactions is quantified through surface characterization and three distinct pore size distribution (PSD) measurements performed on thin disk samples. Scanning electron microscopy (SEM) with energy-dispersive X-ray spectroscopy (EDS) analysis and X-ray fluorescence (XRF) measurements reveals calcite dissolution preferentially occurring at the sample's surfaces, while other potentially reactive minerals such as dolomite, clays, and pyrite remain unaltered. Moreover, aside from salt precipitation, the sandstone storage zone exhibited minimal reactivity. Experimental studies conducted over comparable timeframes and under analogous conditions also reported preferential carbonate reactivity of confining zones (Mouzakis et al. 2016, Miller et al. 2016, Sanguinito et al. 2018, Goodman et al. 2019, Wang et al. 2023) and minimal quartz reactivity in storage zones (Wigand et al. 2008, Lu et al. 2012, Shi et al. 2019, Kim and Makhnenko 2022, Kim et al. 2023). However, it is conceivable that extended treatment periods (0.5–1.5 years) might reveal some level of reactivity with quartz, as reported in previous studies (Rathnaweera et al. 2016, Gholami et al. 2021).

Although evident surface reactivity of carbonate-rich confining zones is observed, minimal alterations are detected in the PSDs of the bulk rocks obtained through mercury injection capillary pressure (MICP), nuclear magnetic resonance (NMR), and nitrogen (N_2) adsorption following treatment. Consistent minor changes are identified in the case of the carbonate-rich sample S3: MICP indicates a slight increase in the amplitude within the 100–1000 nm range, followed by a decrease in the main peak within the 1–10 nm range (**Figure 51**). NMR T_2 spectrum exhibits a small inflection around the 1–20 ms range (**Figure 52**), and N_2 adsorption demonstrates a modest increase in the primary peak within the 20–40 nm range, followed by a slight reduction in the fine-mesopores spanning 1–20 nm (**Figure 53**).

An alteration in surface mineralogy driven by calcite dissolution could change surface hydrophilicity and impact the wettability in the $scCO_2$-brine-rock system. However, the fluid-equilibrated $scCO_2$-brine-rock contact angles here reported are little influenced by the reactivity occurring at the surface (**Figure 50**). The rocks here studied maintain their water-wettability at high pressure conditions (~20 MPa) and even after moderate or strong surface reactivity. Calcite dissolution in the forms of etching and pitting could locally increase the surface roughness (**Figure 46(f)**), which has been found to decrease contact angle in hydrophilic surfaces of pure minerals (e.g., quartz, calcite) (Arif et al. 2017, Al-Yaseri et al. 2016). However, in fine-grained heterogeneous surfaces such as confining zones, the large difference in scale between the static $scCO_2$ bubble (millimeter-size) and grain-size (micrometer to nanometer) accounts for small roughness changes due to dissolution that could impact the contact angle. Here, it is also found that using NMR to assess wettability alteration due to dissolution in nanoporous media (Tinni et al. 2015, Mukherjee et al. 2020) is experimentally challenging because the geochemical reactivity observed does not appear to influence the surface relaxivity of the bulk rock (**Figure 52**).

The NMR T_2 H_2O-D_2O diffusion measurements on horizontal and vertical (i.e. parallel and perpendicular to bedding, respectively) confining zone samples reveal compelling insights. Before $scCO_2$ treatment, a faster effective D_2O diffusion on the horizontal samples (~ 3.6-4.2 x 10^{-10} m^2/s) was observed as compared to vertical orientation (~ 1.1-1.5 x 10^{-10} m^2/s) for the samples extracted from the subsurface (S4 and S6) (**Figure 55**). However, the outcrop sample (S5) exhibit much lower orientation-dependent variation, with both horizontal and vertical diffusivities (~ 1.3-1.4 x 10^{-10} m^2/s) in the range of vertical diffusivities on subsurface samples. To explore the influence of anisotropy on the diffusivity of confining zones, P-wave velocities were measured in all samples

in the ”as-received state” and under low confining pressure (250 psi) (**Figure 56(a)**). The results in **Figure 56(b)** indicate a correlation between P-wave anisotropy and diffusivity anisotropy in confining zone samples under low effective stress. The highest anisotropy in diffusive and acoustic properties was observed in the clay-rich sample S4 (illite > 50 wt.%) (Table 7).

Combined with the bulk D_2O-H_2O diffusivity value at room temperature (2.2 x 10^{-9} m^2/s at 25 °C) (Baur et al. 1959) and **Equation 1.5**, the findings reveal tortuosity ranges of 5.2 to 6.1 in the horizontal orientation and 14.8 to 20.8 in the vertical orientation for the subsurface samples (**Figure 55**). These variations in tortuosity with orientation indicate that diffusive leakage estimations and reactive-transport models could be overestimating the vertical effective $scCO_2$ diffusivity in confining zones in roughly 3-4 times if relying on tortuosity measurements conducted on horizontal samples. Additionally, the diffusivity anisotropy of confining zones (i.e. faster horizontal diffusion) is a factor that should be accounted for during estimation of diffusive leakage parallel to bedding along a fault penetrating a confining zone. Risk of leakage along a fault has been critically evaluated during CGS (Xiao et al. 2024), although experimental and modeling studies have indicated that geological faults can undergo self-sealing, primarily due to calcite precipitation, leading to a reduction in fault leakage (Jung et al. 2014, Patil et al. 2017, Miocic et al. 2019).

After $scCO_2$ treatment, the effective D_2O diffusivity of horizontal samples (**Figure 57**) and vertical samples (**Figure 58**) exhibit different responses. The clay-rich subsurface sample (S4) shows consistent increase in diffusivity (i.e. decrease in tortuosity) over treatment time, irrespective of orientation. In contrast, the quartz-rich outcrop sample (S5) demonstrates minimal changes in diffusivity over time in either orientation. The carbonate-rich subsurface sample (S6) shows a

distinct pattern, with a temporary reduction in diffusivity after one week of treatment, followed by an increase after three weeks. In comparison to the existing literature, Wollenweber et al. (2009) documented a slight increase in the effective $scCO_2$ diffusivities (ranging from 7.8 x 10^{-11} to 1.2 $\cdot 10^{-10}$ m^2/s) for a confining zone sample after undergoing treatment (at ~115 °F and pressure below 1300 psi) over a duration of 240 hours. The observed changes were attributed to alterations in mineral composition and texture, particularly the dissolution and precipitation of carbonates. Similarly, in repeated $scCO_2$ diffusivity measurements (performed at ~122 °F and pressures between 870-1015 psi), Busch et al. (2008) reported a slight increase in $scCO_2$ diffusivity (from 3.1 to 4.8 x 10^{-11} m^2/s). This increase was interpreted as potentially being associated with interactions between CO_2 and clay minerals in their initial measurement.

Here, elemental composition changes measured through XRF surface analysis over the treatment period, as depicted in **Figure 48**, revealed alterations only in the case of sample S6, specifically a reduction in CaO content. This suggests that the observed increase in diffusivity in sample S4 is unlikely to be attributed to geochemical mineral alteration. Furthermore, examination of the total diffused volume over time, as presented in **Figure 59**, indicates a lack of significant alterations in any of the samples, signifying the preservation of the exchangeable brine-filled pore volume over the course of treatment. It is possible that the enhanced diffusivity on S4 post-$scCO_2$ treatment is attributed to other interactions between clay minerals and CO_2 (e.g. absorption and ion exchange), as documented by Espinoza and Santamarina (2012). For the quartz-rich sample (S5), the negligible changes in diffusivity align with the observed lack of quartz reactivity, as depicted in **Figure 46**. In the case of the carbonate-rich sample (S6), the fluctuations observed in diffusivity, in conjunction with the reduction in CaO content during treatment, suggest a potential combined

mechanism involving surface calcite dissolution and possible subsurface precipitation. This mechanism may also be inferred from the consistent minor alterations in pore size observed in the carbonate-rich sample (S3) (**Figure 51**, **Figure 52**, and **Figure 53**). Overall, although slight changes in diffusivity were observed after treatment, **Figure 66** suggests small impact in the estimation of long-term $scCO_2$ diffusive penetration in the confining zone.

Significant insights were gained from the $scCO_2$ breakthrough experiments performed on brine-saturated thin disk confining zone samples under subsurface conditions of elevated pressure and temperature. A validation experiment using a thin disk nanoporous ceramic sample with a specific pore diameter of approximately 50 nm exhibited a breakthrough pressure (P_{BT}) consistent with the value determined through MICP pore size distribution (P_{BT} ~ 560 psi, $P_{BT,MICP}$ ~ 580 psi) (**Figure 60**). This validation test employed nitrogen (N_2) at room temperature, which has higher surface tension and a smaller contact angle, resulting in a larger capillary pressure, compared to $scCO_2$ under subsurface conditions (as determined by **Equations 7.1** and **7.2**). In this validation test, a visual indication of gas breakthrough was observed after approximately 500 minutes of injection. Subsequently, a two-phase flow of N_2 and brine occurred, followed by single-phase N_2 flow.

Conversely, the $scCO_2$ breakthrough experiments conducted on intact confining zone samples (S4 and S6) at subsurface conditions, both before and after $scCO_2$ treatment, and under low net confinement (600 psi), did not reveal $scCO_2$ displacing brine within the samples (**Figure 62**). Prior to $scCO_2$ treatment, these experiments involved applying substantial differential pressures, with inlet pressures exceeding outlet pressures by up to 4500 psi. These pressures were at least 2000 psi greater than the breakthrough pressures predicted by MICP measurements on the same samples in their dry state (**Figure 61(b)**). It is essential to note that before treatment, the experiments were

conducted with large incremental pressure steps of approximately 500 psi and for relatively short injection durations, spanning around 2 days.

Following $scCO_2$ treatment, the pressure increments were reduced to 100 psi, and the experiments extended for up to 10 days, with differential pressures reaching up to 800 psi. Notably, at high pressures, the tests revealed a significant reduction in pump volumes, exceeding 10 times the pore volume of the samples (more than 4 mL compared to ~0.4 mL). However, despite the decrease in pump volumes, no visual indications of $scCO_2$ displacing brine were observed in the post-treatment tests. Based on the trend between pump volume with time (**Figure 62**), it is hypothesized that the reduction in pump volume observed is associated with slow molecular diffusion of $scCO_2$ saturating the outlet brine in the experimental setup.

In contrast to initial expectations, the absence of $scCO_2$ displacing brine in confining zones, even under conditions of elevated pressures, is a well-documented phenomenon in previous experimental investigations (Hildenbrand and Krooss 2003, Amann et al. 2011, Edlmann et al. 2013, Kivi et al. 2022). The findings of Hildenbrand and Krooss (2003) revealed that certain experiments on confining zones exhibited no discernible breakthrough of the $scCO_2$ phase during capillary pressure tests, attributing the results to a slow molecular diffusion process. Amann et al. (2011) conducted $scCO_2$ breakthrough tests where only diffusive gas transport was observed, and effective $scCO_2$ diffusion coefficients appear to increase with time. Based on the apparent diffusivity, they suggested that a period of 170 days would be required to establish nearly steady state conditions during the test.

Edlmann et al. (2013) provided further insights indicating that $scCO_2$ does not flow through tight natural caprock fractures even under substantial differential pressures exceeding 7400 psi.

However, they noted that below the critical point where CO_2 transitioned into its gas phase, gaseous CO_2 readily traversed the caprock fractures. Kivi et al. (2022) conducted experiments with large differential pressure (4930 MPa), which drove $scCO_2$ into caprock specimens. However, the relative permeability increase along the drainage path was insufficient to enable effective advancement of free-phase $scCO_2$, rendering it nearly immobile. This observation led to the conclusion that the sealing capacity of caprock is unlikely to be compromised by rapid capillary breakthrough. Instead, it was revealed that $scCO_2$ dissolved in brine predominantly migrates over extended timescales, driven by the inherently slow molecular diffusion in confining zones.

Notably, certain experiments conducted on tight samples did indicate CO_2 breakthrough. However, these experiments were performed either using sediment packs comprising sand, silt, and clay materials (as seen in Espinoza and Santamarina (2017)) or by injecting CO_2 in either gaseous or liquid phases (as observed in Stavropoulou and Laloui (2022)). When integrating the findings of this research study with those from the existing literature, it becomes evident that a complex interplay between capillary displacement and molecular diffusion processes governs the dynamics of $scCO_2$ transport in confining zones.

Conclusions

In this dissertation, two sets of studies involving $scCO_2$-fluids-rock interactions in nanoporous media, particularly relevant to enhanced oil recovery (EOR) in unconventional liquid-rich shale reservoirs (ULR) and carbon geostorage (CGS), were performed. The first study combined laboratory experiments and modeling to optimize key properties related to the Huff-and-Puff EOR operation in ULR. The second study delved into the effect of geochemical reactions, arising from $scCO_2$-brine-rock interactions, on the transport and petrophysical properties of confining zones during CGS. The integration of these two studies provided the following conclusions:

- The specific surface area of laboratory samples intensifies the magnitude of responses pertaining to fluid mobilization, especially in nanoporous systems where concentration-driven flow is a relevant transport mechanism. The large and fast oil and water recovery factors (typically above 50 %) during the 21 HnP-EOR tests in ULR using crushed-sized samples (7-8 mm) demonstrate this concept. Conversely, short-term geochemical reactivity in nanoporous confining zones using inch-sized samples (i.e. lower specific area) appears to be limited to a region near the sample surface, preserving the bulk rock properties. Moreover, the results indicate that the apparent diffusivity of the reacted zone is 4-5 orders of magnitude smaller than the effective $scCO_2$ diffusivity in the confining zone (9×10^{-15} to $5\text{-}15 \times 10^{-10}$ m^2/s, respectively). Integration of these results suggests that even after a century of injection, the CO_2 molecule penetration appears to be limited to around 7 meters deep in the studied confining zones including the effect of short-term geochemical reactivity. The limited penetration is expected to decrease even further under subsurface conditions of effective stress.

- During HnP-EOR in ULR, $scCO_2$ outperforms the positive linear trend in oil recovery with injection pressure for both produced and enriched field gases. The 21 tests conducted in the shale rock coupled with bulk oil tests indicate preferential production of lighter fractions, resulting in an increase in oil heaviness after each cycle. The increase in oil heaviness after each cycle results in a rise in the solvent-residual oil MMP. Given the oil compositional differences, this phenomenon appears to be more pronounced when the shale matrix is introduced. Therefore, the linear oil recovery trend with injection pressure, even above the original MMP, is possibly attributed to a combination of increasing solvent-residual oil MMP and the linear rise in diffusion coefficients of hydrocarbon gases in crude oil with pressure. The experimental findings of $scCO_2$ solvent efficiency align with the shale oil reservoir HnP-EOR model. The simulations indicate an increase in net carbon efficiency as injection pressure rises, with roughly 67% of the injected $scCO_2$ sequestered in the subsurface at 10,000 psi injection pressure after 10 years of operation.
- The CGS $scCO_2$ treatment study reveals clear evidence of geochemical reactivity, particularly in carbonate-rich confining zones. Calcite dissolution is preferentially observed at the surface. Despite surface reactivity, the water-wettability in the $scCO_2$-brine-systems measured by the captive-bubble technique is preserved. Minimal alterations in pore size distribution (PSD) of the intact bulk rocks are observed through three different PSD measurements. The diffusion measurements show anisotropy in the diffusivity of confining zones, with horizontal diffusion faster than vertical diffusion in subsurface samples. A correlation between P-wave anisotropy and diffusivity anisotropy is documented. The highest anisotropy observed correlates with increasing clay content. The response of diffusivity to $scCO_2$ treatment varies among different

samples. Clay-rich subsurface samples exhibit an increase in diffusivity after treatment, while quartz-rich outcrop samples show minimal changes. The carbonate-rich subsurface sample exhibits a distinct pattern, with a temporary reduction in diffusivity followed by further increase. Although slight changes in diffusivity are observed after $scCO_2$ treatment, the predicted impact on $scCO_2$ diffusive leakage in confining zones appears to be small. The $scCO_2$ breakthrough experiments on brine-saturated thin disk confining zone samples under subsurface conditions highlight the complexity of $scCO_2$ transport. Contrary to initial expectations, $scCO_2$ did not displace brine in the confining zones, even under high pressures. This phenomenon has been observed in previous research and underscores the importance of molecular diffusion in confining zones during CGS.

Recommendations for Future Work

While this dissertation has contributed to the comprehension of scCO2-fluids-rock interactions within nanoporous systems and their applications in EOR and geostorage, it is crucial to acknowledge the existing limitations of this work. Identifying these limitations is essential for guiding future research endeavors. In this context, the following suggestions are proposed:

- In the first study involving HnP-EOR in ULR using various solvents under varying miscibility conditions, it is advisable to validate the outcomes obtained in crushed-sized experiments through the utilization of hydraulically-fractured core samples. Testing under conditions of confinement and pore pressure resembling those in subsurface HnP-EOR operations is recommended. This approach enhances the accuracy of estimating absolute values for crude oil and brine recovery factors during HnP-EOR and facilitates the upscaling to reservoir scale. However, it is important to acknowledge a potential limitation associated with this approach, specifically the prolonged experimental duration required to observe fluid recovery in such conditions. Additionally, the suggestion of real-time quantification of fluid phase recovery factors under pressurized conditions akin to subsurface environments is proposed. The reservoir simulations performed can be enhanced by incorporating additional factors such as nanoconfinement, adsorption onto shales, and geochemical interaction with reservoir brine.
- In the second study pertaining to the long-term integrity of confining zones during CGS, it is advised to prolong the duration of $scCO_2$ treatment, extending it to a scale of months or even up to a year. This prolonged treatment duration aims to enhance confidence in the limited propagation of short-term geochemical reactivity within nanoporous confining zone systems. Additionally, it is recommended to incorporate supplementary measurements, including

profilometry, to precisely ascertain the depth of reaction propagation and estimate reaction-diffusion coefficient. Profilometry measurements should also be performed to estimate the impact of surface roughness resulting from geochemical reactivity on captive-bubble wettability assessments. To refine effective diffusivity measurements, it is suggested to conduct them under pressurized conditions that mimic confinement and pore pressure, providing a more accurate estimation of effective $scCO_2$ diffusivities and long-term diffusive leakage. In the context of $scCO_2$ breakthrough tests, pre-equilibrating the outlet brine with $scCO_2$ is recommended to minimize pump volume loss via diffusion and gain deeper insights into $scCO_2$ displacing brine saturating confining zones. Furthermore, it is advisable to collect the outlet brine post-experiment and perform inductively coupled plasma (ICP) measurements to elucidate mineralogical changes in sample composition following exposure to $scCO_2$. These additional measures and considerations aim to enhance the comprehensiveness and reliability of the study's findings.

References

Abrams, M.A., Gong, C., Garnier, C. et al. 2017. A new thermal extraction protocol to evaluate liquid rich unconventional oil in place and in-situ fluid chemistry. *Marine and Petroleum Geology* **88**: 659-675. https://doi.org/10.1016/j.marpetgeo.2017.09.014.

Adel, I.A., Tovar, F.D., Zhang, F. et al. 2018. The Impact of MMP on Recovery Factor During CO2 – EOR in Unconventional Liquid Reservoirs. Paper presented at the SPE Annual Technical Conference and Exhibition, Dallas, Texas, USA, 2018/9/24/. SPE. https://doi.org/10.2118/191752-MS.

Aggelopoulos, C.A., Robin, M., Perfetti, E. et al. 2010. CO2/CaCl2 solution interfacial tensions under CO2 geological storage conditions: Influence of cation valence on interfacial tension. *Advances in Water Resources* **33** (6): 691-697. https://doi.org/10.1016/j.advwatres.2010.04.006.

Aggelopoulos, C.A., Robin, M., and Vizika, O. 2011. Interfacial tension between CO2 and brine (NaCl + CaCl2) at elevated pressures and temperatures: The additive effect of different salts. *Advances in Water Resources* **34** (4): 505-511. https://doi.org/10.1016/j.advwatres.2011.01.007.

Ahmad, W., Vakili-Nezhaad, G., Al-Bemani, A.S. et al. 2016. Uniqueness, repeatability analysis and comparative evaluation of experimentally determined MMPs. *Journal of Petroleum Science & Engineering* **147**: 218-227. https://doi.org/10.1016/j.petrol.2016.06.023.

Ahmadi, K. and Johns, R. 2011. Multiple Mixing-Cell Method for MMP Calculations. *SPE Journal* **16** (04): 733-742. https://doi.org/10.2118/116823-PA.

Ahmed, T.H. 1994. Prediction of CO2 Minimum Miscibility Pressures. *Proc.*, SPE Latin America/Caribbean Petroleum Engineering Conference. https://doi.org/10.2118/27032-MS.

Ajayi, T., Gomes, J.S., and Bera, A. 2019. A review of CO2 storage in geological formations emphasizing modeling, monitoring and capacity estimation approaches. *Petroleum Science* **16** (5): 1028-1063. https://doi.org/10.1007/s12182-019-0340-8.

Akita, E., Moghanloo, R.G., Davudov, D. et al. 2018. A Systematic Approach for Upscaling of the EOR Results from Lab-Scale to Well-Scale in Liquid-Rich Shale Plays. Paper presented at the SPE Improved Oil Recovery Conference. https://doi.org/10.2118/190188-MS.

Akutsu, T., Yamaji, Y., Yamaguchi, H. et al. 2007. Interfacial tension between water and high pressure CO2 in the presence of hydrocarbon surfactants. *Fluid Phase Equilibria* **257** (2): 163-168. https://doi.org/10.1016/j.fluid.2007.01.040.

Al-Khdheeawi, E.A., Vialle, S., Barifcani, A. et al. 2018. Effect of wettability heterogeneity and reservoir temperature on CO2 storage efficiency in deep saline aquifers. *International Journal of Greenhouse Gas Control* **68**: 216-229. https://doi.org/10.1016/j.ijggc.2017.11.016An experimental investigation of wettability alteration during CO2 immiscible flooding.

Al-Mutairi, S.M., Abu-Khamsin, S.A., Okasha, T.M. et al. 2014. An experimental investigation of wettability alteration during CO2 immiscible flooding. *Journal of Petroleum Science & Engineering* **120**: 73-77. https://doi.org/10.1016/j.petrol.2014.05.008.

Al-Yaseri, A., Abbasi, G.R., Yekeen, N. et al. 2022. Effects of cleaning process using toluene and acetone on water-wet-quartz/CO2 and oil-wet-quartz/CO2 wettability. *Journal of*

Petroleum Science & Engineering **208**: 109555. https://doi.org/10.1016/j.petrol.2021.109555.

Al-Yaseri, A., Sarmadivaleh, M., Saeedi, A. et al. 2015. N2+CO2+NaCl brine interfacial tensions and contact angles on quartz at CO2 storage site conditions in the Gippsland basin, Victoria/Australia. *Journal of Petroleum Science & Engineering* **129**: 58-62. https://doi.org/10.1016/j.petrol.2015.01.026.

Al-Yaseri, A.Z., Lebedev, M., Barifcani, A. et al. 2016. Receding and advancing (CO2+brine+quartz) contact angles as a function of pressure, temperature, surface roughness, salt type and salinity. *The Journal of Chemical Thermodynamics* **93**: 416-423. https://doi.org/10.1016/j.jct.2015.07.031.

Al-Yaseri, A.Z., Roshan, H., Zhang, Y. et al. 2017. Effect of the Temperature on CO2/Brine/Dolomite Wettability: Hydrophilic versus Hydrophobic Surfaces. *Energy & Fuels* **31** (6): 6329-6333. https://doi.org/10.1021/acs.energyfuels.7b00745.

Al Hameli, F., Belhaj, H., and Al Dhuhoori, M. 2022. CO2 Sequestration Overview in Geological Formations: Trapping Mechanisms Matrix Assessment. *Energies* **15** (20): 7805. https://www.mdpi.com/1996-1073/15/20/7805.

Ali, M., Dahraj, N.U., and Haider, S.A. 2015. Study of Asphaltene Precipitation during CO2 Injection in Light Oil Reservoirs. *Proc.*, SPE/PAPG Pakistan section Annual Technical Conference. https://doi.org/10.2118/181130-MS.

Alnili, F., Al-Yaseri, A., Roshan, H. et al. 2018. Carbon dioxide/brine wettability of porous sandstone versus solid quartz: An experimental and theoretical investigation. *Journal of Colloid and Interface Science* **524**: 188-194. https://doi.org/10.1016/j.jcis.2018.04.029.

AlRatrout, A., Blunt, M.J., and Bijeljic, B. 2018. Spatial Correlation of Contact Angle and Curvature in Pore-Space Images. *Water Resources Research* **54** (9): 6133-6152. https://doi.org/10.1029/2017WR022124.

Amann, A., Waschbüsch, M., Bertier, P. et al. 2011. Sealing rock characteristics under the influence of CO2. *Energy Procedia* **4**: 5170-5177. https://doi.org/10.1016/j.egypro.2011.02.494.

Ameli, F., Hemmati-Sarapardeh, A., Tatar, A. et al. 2019. Modeling interfacial tension of normal alkane-supercritical CO2 systems: Application to gas injection processes. *Fuel* **253**: 1436-1445. https://doi.org/10.1016/j.fuel.2019.05.078.

Ameri, A., Kaveh, N.S., Rudolph, E.S.J. et al. 2013. Investigation on Interfacial Interactions among Crude Oil–Brine–Sandstone Rock–CO2 by Contact Angle Measurements. *Energy & Fuels* **27** (2): 1015-1025. https://doi.org/10.1021/ef3017915.

Andreas, J.M., Hauser, E.A., and Tucker, W.B. 1938. Boundary Tension by Pendant Drops. *The Journal of Physical Chemistry* **42** (8): 1001-1019.

Andrew, M., Bijeljic, B., and Blunt, M.J. 2014. Pore-scale contact angle measurements at reservoir conditions using X-ray microtomography. *Advances in Water Resources* **68**: 24-31. https://doi.org/10.1016/j.advwatres.2014.02.014.

Arif, M., Abu-Khamsin, S.A., and Iglauer, S. 2019. Wettability of rock/CO2/brine and rock/oil/CO2-enriched-brine systems: Critical parametric analysis and future outlook. *Advances in Colloid and Interface Science* **268**: 91-113. https://doi.org/10.1016/j.cis.2019.03.009.

Arif, M., Lebedev, M., Barifcani, A. et al. 2017. CO2 storage in carbonates: Wettability of calcite. *International Journal of Greenhouse Gas Control* **62**: 113-121. https://doi.org/10.1016/j.ijggc.2017.04.014.

Atan, S., Ajayi, A., Honarpour, M. et al. 2018. The Viability of Gas Injection EOR in Eagle Ford Shale Reservoirs. Paper presented at the SPE Annual Technical Conference and Exhibition, Dallas, Texas, USA, 2018/9/24/. SPE. https://doi.org/10.2118/191673-MS.

Ayirala, S.C. and Rao, D.N. 2011. Comparative Evaluation of a New Gas/Oil Miscibility-Determination Technique. *Journal of Canadian Petroleum Technology* **50** (9/10): 71-81. https://doi.org/10.2118/99606-PA.

Azin, R., Mahmoudy, M., Raad, S. et al. 2013. Measurement and modeling of CO2 diffusion coefficient in Saline Aquifer at reservoir conditions. *Open Engineering* **3** (4): 585-594. https://doi.org/10.2478/s13531-012-0069-2.

Baban, A., Al-Yaseri, A., Keshavarz, A. et al. 2021. CO2 – brine – sandstone wettability evaluation at reservoir conditions via Nuclear Magnetic Resonance measurements. *International Journal of Greenhouse Gas Control* **111**: 103435. https://doi.org/10.1016/j.ijggc.2021.103435.

Baban, A., Keshavarz, A., Amin, R. et al. 2022. Impact of Wettability Alteration on CO2 Residual Trapping in Oil-Wet Sandstone at Reservoir Conditions Using Nuclear Magnetic Resonance. *Energy & Fuels* **36** (22): 13722-13731. https://doi.org/10.1021/acs.energyfuels.2c02933.

Bachu, S. 2007. Carbon dioxide storage capacity in uneconomic coal beds in Alberta, Canada: Methodology, potential and site identification. *International Journal of Greenhouse Gas Control* **1**: 374-385. https://doi.org/10.1016/S1750-5836(07)00070-9.

Bachu, S. 2015. Review of CO2 storage efficiency in deep saline aquifers. *International Journal of Greenhouse Gas Control* **40**: 188-202. https://doi.org/10.1016/j.ijggc.2015.01.007.

Bachu, S. and Bennion, D.B. 2009. Interfacial Tension between CO2, Freshwater, and Brine in the Range of Pressure from (2 to 27) MPa, temperature from (20 to 125) °C, and Water Salinity from (0 to 334 000) mg·L−1. *Journal of Chemical and Engineering Data* **54** (3): 765-775. https://doi.org/10.1021/je800529x.

Bachu, S., Bonijoly, D., Bradshaw, J. et al. 2007. CO2 storage capacity estimation: Methodology and gaps. *International Journal of Greenhouse Gas Control* **1** (4): 430-443. http://pubs.er.usgs.gov/publication/70031669.

Bachu, S. and Brant Bennion, D. 2009. Dependence of CO2 -brine interfacial tension on aquifer pressure, temperature and water salinity. *Energy Procedia* **1** (1): 3157-3164. https://doi.org/10.1016/j.egypro.2009.02.098.

Bagalkot, N. and Hamouda, A.A. 2018. Interfacial tension and CO2 diffusion coefficients for a CO2 + water and n-decane system at pressures of 10 to 160 bar. *RSC Advances* **8** (67): 38351-38362. https://doi.org/10.1039/C8RA03690J.

Bagalkot, N., Hamouda, A.A., and Isdahl, O.M. 2018. Dynamic interfacial tension measurement method using axisymmetric drop shape analysis. *MethodsX* **5**: 676-683. https://doi.org/10.1016/j.mex.2018.06.012.

Bai, M., Zhang, Z., and Fu, X. 2016. A review on well integrity issues for CO2 geological storage and enhanced gas recovery. *Renewable & Sustainable Energy Reviews* **59**: 920-926. https://doi.org/10.1016/j.rser.2016.01.043.

Ballard, B. 2007. Quantitative Mineralogy of Reservoir Rocks Using Fourier Transform Infrared Spectroscopy. Paper presented at the SPE Annual Technical Conference and Exhibition, Anaheim, California, U.S.A., 2007/1/1/. SPE. https://doi.org/10.2118/113023-STU.

Barsotti, E. 2019. Capillary Condensation in Shale: A Narrative Review. Paper presented at the SPE Annual Technical Conference and Exhibition, Calgary, Alberta, Canada, 2019/9/23/. SPE. https://doi.org/10.2118/199768-STU.

Bashforth, F. 1883. *An attempt to test the theories of capillary action by comparing the theoretical and measured forms of drops of fluid. With an explanation of the method of integration employed in constucting the tables which give the theoretical forms of such drops, by J. C. Adams*. England: England: University Press, 1883.

Baur, M.E., Garland, C.W., and Stockmayer, W.H. 1959. DIFFUSION COEFFICIENTS OF H2O-D2O MIXTURES. *Journal of the American Chemical Society* **81** (12): 3147-3148. https://doi.org/10.1021/ja01521a058.

Behroozi, F. 2022. A Fresh Look at the Young-Laplace Equation and Its Many Applications in Hydrostatics. *The Physics Teacher* **60** (5): 358-361. https://doi.org/10.1119/5.0045605.

Berentsen, C. and de Pater, C.H. 2022. Seismicity Induced by Cooling of CCS Reservoirs. Paper presented at the SPE EuropEC - Europe Energy Conference featured at the 83rd EAGE Annual Conference & Exhibition. https://doi.org/10.2118/209685-MS.

Berne, P., Bachaud, P., and Fleury, M. 2010. Diffusion Properties of Carbonated Caprocks from the Paris Basin. *Oil & Gas Science and Technology* **65** (3): 473-484. https://doi.org/10.2516/ogst/2009072.

Berry, J.D., Neeson, M.J., Dagastine, R.R. et al. 2015. Measurement of surface and interfacial tension using pendant drop tensiometry. *Journal of Colloid and Interface Science* **454**: 226-237. https://doi.org/10.1016/j.jcis.2015.05.012.

Bikkina, P. 2011. Contact angle measurements of CO2-water-quartz/calcite systems in the perspective of carbon sequestration. *International Journal of Greenhouse Gas Control* **5**: 1259-1271. https://doi.org/10.1016/j.ijggc.2011.07.001.

Bikkina, P.K., Shoham, O., and Uppaluri, R. 2011. Equilibrated Interfacial Tension Data of the CO2–Water System at High Pressures and Moderate Temperatures. *Journal of Chemical and Engineering Data* **56** (10): 3725-3733. https://doi.org/10.1021/je200302h.

Botto, J., Fuchs, S.J., Fouke, B.W. et al. 2017. Effects of Mineral Surface Properties on Supercritical CO2 Wettability in a Siliciclastic Reservoir. *Energy & Fuels* **31** (5): 5275-5285. https://doi.org/10.1021/acs.energyfuels.6b03336.

Broseta, D., Tonnet, N., and Shah, V. 2012. Are rocks still water-wet in the presence of dense CO2 or H2S? *Geofluids* **12** (4): 280-294. https://doi.org/10.1111/j.1468-8123.2012.00369.x.

Brosse, E., Bildstein, O., and Rudy, S. 2005. Gas-Water-Rock Interactions Induced by Reservoir Exploitation, CO2 Sequestration, and Other Geological Storage. *Oil & Gas Science and Technology* **60**: 9-18. https://doi.org/10.2516/ogst:2005002.

Brunauer, S., Emmett, P.H., and Teller, E. 1938. Adsorption of Gases in Multimolecular Layers. *Journal of the American Chemical Society* **60** (2): 309-319. https://doi.org/10.1021/ja01269a023.

Busch, A., Alles, S., Gensterblum, Y. et al. 2008. Carbon dioxide storage potential of shales. *International Journal of Greenhouse Gas Control* **2** (3): 297-308. https://doi.org/10.1016/j.ijggc.2008.03.003.

Busch, A., Amann, A., Bertier, P. et al. 2010. The Significance of Caprock Sealing Integrity for CO2 Storage. *Society of Petroleum Engineers - SPE International Conference on CO2 Capture, Storage, and Utilization 2010*. https://doi.org/10.2118/139588-MS.

Bustin, R.M., Bustin, A.M.M., Cui, A. et al. 2008. Impact of Shale Properties on Pore Structure and Storage Characteristics. Paper presented at the SPE Shale Gas Production Conference, Fort Worth, Texas, USA, 2008/1/1/. SPE. https://doi.org/10.2118/119892-MS.

Cadogan, S.P., Maitland, G.C., and Trusler, J.P.M. 2014. Diffusion Coefficients of CO2 and N2 in Water at Temperatures between 298.15 K and 423.15 K at Pressures up to 45 MPa. *Journal of Chemical and Engineering Data* **59** (2): 519-525. https://doi.org/10.1021/je401008s.

Cai, J., Jin, T., Kou, J. et al. 2021. Lucas–Washburn Equation-Based Modeling of Capillary-Driven Flow in Porous Systems. *Langmuir* **37** (5): 1623-1636. https://doi.org/10.1021/acs.langmuir.0c03134.

Calhoun, J.C. 1960. *Fundamentals of Reservoir Engineering*, Rev. edition. Norman : University of Oklahoma Press.

Celia, M.A., Bachu, S., Nordbotten, J.M. et al. 2015. Status of CO2 storage in deep saline aquifers with emphasis on modeling approaches and practical simulations. *Water Resources Research* **51** (9): 6846-6892. https://doi.org/10.1002/2015WR017609.

Chabab, S., Ahmadi, P., Théveneau, P. et al. 2021. Measurements and Modeling of High-Pressure O 2 and CO 2 Solubility in Brine (H 2 O + NaCl) between 303 and 373 K and Pressures up to 36 MPa. *Journal of Chemical and Engineering Data* **66** (1): 609-620. https://doi.org/10.1021/acs.jced.0c00799.

Chalbaud, C., Robin, M., Lombard, J.M. et al. 2009. Interfacial tension measurements and wettability evaluation for geological CO2 storage. *Advances in Water Resources* **32** (1): 98-109. https://doi.org/10.1016/j.advwatres.2008.10.012.

Chaudhary, K., Guiltinan, E.J., Cardenas, M.B. et al. 2015. Wettability measurement under high P-T conditions using X-ray imaging with application to the brine-supercritical CO2 system. *Geochemistry, Geophysics, Geosystems* **16** (9): 2858-2864. https://doi.org/10.1002/2015GC005936.

Chen, L.L.-y., Katz, D.L., and Tek, M.R. 1977. Binary gas diffusion of methane-nitrogen through porous solids. *AIChE Journal* **23** (3): 336-341. https://doi.org/10.1002/aic.690230317.

Chen, Y., Zhi, D., Qin, J. et al. 2022. Experimental study of spontaneous imbibition and CO2 huff and puff in shale oil reservoirs with NMR. *Journal of Petroleum Science & Engineering* **209**: 109883. https://doi.org/10.1016/j.petrol.2021.109883.

Chiquet, P., Broseta, D., and Thibeau, S. 2007a. Wettability alteration of caprock minerals by carbon dioxide. *Geofluids* **7** (2): 112-122. https://doi.org/10.1111/j.1468-8123.2007.00168.x.

Chiquet, P., Daridon, J.-L., Broseta, D. et al. 2007b. CO2/water interfacial tensions under pressure and temperature conditions of CO2 geological storage. *Energy Conversion and Management* **48** (3): 736-744. https://doi.org/10.1016/j.enconman.2006.09.011.

Choubineh, A., Helalizadeh, A., and Wood, D.A. 2019. The impacts of gas impurities on the minimum miscibility pressure of injected CO2-rich gas–crude oil systems and enhanced oil recovery potential. *Petroleum Science* **16** (1): 117-126. https://doi.org/10.1007/s12182-018-0256-8.

Choudhary, N., Anwari Che Ruslan, M.F., Narayanan Nair, A.K. et al. 2021. Bulk and Interfacial Properties of the Decane + Brine System in the Presence of Carbon Dioxide, Methane, and Their Mixture. *Industrial & Engineering Chemistry Research* **60** (30): 11525-11534. https://doi.org/10.1021/acs.iecr.1c01607.

Chun, B.-S. and Wilkinson, G.T. 1995. Interfacial tension in high-pressure carbon dioxide mixtures. *Industrial & Engineering Chemistry Research* **34** (12): 4371-4377. https://doi.org/10.1021/ie00039a029.

Coates, G.R., Xiao, L., and Prammer, M.G. 1999. NMR logging: principles and applications (in English). http://books.google.com/books?id=vptTAAAAMAAJ.

Corbett, P. 2000. PVT and Phase Behaviour of Petroleum Reservoir Fluids: Ali Danesh, Elsevier, 1998, ISBN 0 444 82196 1, 220 NLG (approx. £83). *Marine and Petroleum Geology* **17**: 558–559. https://doi.org/10.1016/S0264-8172(99)00062-8.

Crank, J. 1979. *The Mathematics of Diffusion*: Clarendon Press.

Cruz, F., Mamoudou, S., and Tinni, A. 2022. The Impact of Gas-Oil Miscibility on Oil Recovery During Huff-and-Puff EOR in Organic-Rich Shales. Paper presented at the SPE Annual Technical Conference and Exhibition. https://doi.org/10.2118/210028-MS.

Cui, X., Liu, Z., Cui, P. et al. 2023. A novel methodology for measurement of the diffusion coefficient between CO2 and oil based on quantification of the oil droplet swelling behavior. *Colloids and Surfaces A: Physicochemical and Engineering Aspects* **656**: 130485. https://doi.org/10.1016/j.colsurfa.2022.130485.

Curtis, M., Mamoudou, S., Cruz, F. et al. 2023. Effects of CO2 Exposure on Unconventional Reservoir Rock Microstructure. *Proc.*, SPE/AAPG/SEG Unconventional Resources Technology Conference. https://doi.org/10.15530/urtec-2023-3864852.

da Rocha, S.R.P., Harrison, K.L., and Johnston, K.P. 1999. Effect of Surfactants on the Interfacial Tension and Emulsion Formation between Water and Carbon Dioxide. *Langmuir* **15** (2): 419-428. https://doi.org/10.1021/la980844k.

Dai, Z., Viswanathan, H., Xiao, T. et al. 2017. CO2 Sequestration and Enhanced Oil Recovery at Depleted Oil/Gas Reservoirs. *Energy Procedia* **114** (C): 6957-6967. https://doi.org/10.1016/j.egypro.2017.08.034.

Dalal Isfehani, Z., Sheidaie, A., Hosseini, M. et al. 2023. Interfacial tensions of (brine + H2 + CO2) systems at gas geo-storage conditions. *Journal of Molecular Liquids* **374**: 121279. https://doi.org/10.1016/j.molliq.2023.121279.

Dang, S. 2019. *Understanding the fundamental drive mechanisms for huff-and-puff enhanced oil recovery in tight formations*. Ph.D Dissertation, University of Oklahoma. https://hdl.handle.net/11244/322858

Dang, S., Mamoudou, S., Rai, C. et al. 2023. Experimental Observation of Diffusion as the Main Drive Mechanism in Unconventional Shales. *Proc.*, SPE/AAPG/SEG Unconventional Resources Technology Conference. https://doi.org/10.15530/urtec-2023-3864848.

Dang, S.T., Sondergeld, C.H., and Rai, C.S. 2019. Interpretation of Nuclear-Magnetic-Resonance Response to Hydrocarbons: Application to Miscible Enhanced-Oil-Recovery Experiments in Shales. *SPE-168971-PA* **22** (1): 302-309. https://doi.org/10.2118/191144-PA.

Davis, S.J., Lewis, N.S., Shaner, M. et al. 2018. Net-zero emissions energy systems. *Science* **360** (6396): eaas9793. https://www.science.org/doi/abs/10.1126/science.aas9793.

Diamond, L.W. and Akinfiev, N.N. 2003. Solubility of CO 2 in water from −1.5 to 100 °C and from 0.1 to 100 MPa: evaluation of literature data and thermodynamic modelling. *Fluid Phase Equilibria* **208** (1): 265-290. https://doi.org/10.1016/S0378-3812(03)00041-4.

Dresel, P.E. 1989. *The dissolution kinetics of siderite and its effect on acid mine drainage*. Ph.D Dissertation, The Pennsylvania State University, United States -- Pennsylvania. https://www.osti.gov/biblio/6918291

Du, F. and Nojabaei, B. 2021. A diffusion-based compositionally-extended black oil model to investigate produced gas re-injection EOR in Eagle Ford. *Fuel* **306**: 121711. https://doi.org/10.1016/j.fuel.2021.121711.

Duan, Z., Sun, R., Zhu, C. et al. 2006. An improved model for the calculation of CO2 solubility in aqueous solutions containing Na+, K+, Ca2+, Mg2+, Cl−, and SO42. *Marine Chemistry* **98** (2-4): 131-139. https://doi.org/10.1016/j.marchem.2005.09.001.

Edlmann, K., Haszeldine, S., and McDermott, C.I. 2013. Experimental investigation into the sealing capability of naturally fractured shale caprocks to supercritical carbon dioxide flow. *Environmental Earth Sciences* **70** (7): 3393-3409. https://doi.org/10.1007/s12665-013-2407-y.

EIA. Drilling Productivity Report (DPR). *U.S. Energy Information Administration*, https://www.eia.gov/todayinenergy/detail.php?id=48676.

EIA, E.I.A.-. Technically Recoverable Shale Oil and Shale Gas Resources: An

Assessment of 137 Shale Formations in 41 Countries outside the United States, https://www.eia.gov/analysis/studies/worldshalegas/pdf/overview.pdf.

Elsharkawy, A.M., Poettmann, F.H., and Christiansen, R.L. 1996. Measuring CO2 Minimum Miscibility Pressures: Slim-Tube or Rising-Bubble Method? *Energy & Fuels* **10** (2): 443-449. https://doi.org/10.1021/ef940212f.

Emami-Meybodi, H. and Hassanzadeh, H. 2015. Two-phase convective mixing under a buoyant plume of CO2 in deep saline aquifers. *Advances in Water Resources* **76**: 55-71. https://doi.org/10.1016/j.advwatres.2014.11.011.

Ennis-King, J.P. and Paterson, L. 2005. Role of Convective Mixing in the Long-Term Storage of Carbon Dioxide in Deep Saline Formations. *SPE Journal* **10** (3): 349-356. https://doi.org/10.2118/84344-PA.

EPA. Underground Injection Control (UIC) Program Class VI Well Site Characterization Guidance. *Environmental Protection Agency (EPA)*, https://www.epa.gov/sites/default/files/2015-07/documents/epa816r13004.pdf.

Epstein, P.S. and Plesset, M.S. 1950. On the Stability of Gas Bubbles in Liquid-Gas Solutions. *The Journal of Chemical Physics* **18** (11): 1505-1509.

Espinoza, D.N., Kim, S.H., and Santamarina, J.C. 2011. CO2 geological storage — Geotechnical implications. *KSCE Journal of Civil Engineering* **15** (4): 707-719. https://doi.org/10.1007/s12205-011-0011-9.

Espinoza, D.N. and Santamarina, J.C. 2010. Water-CO2-mineral systems: Interfacial tension, contact angle, and diffusion-Implications to CO2 geological storage. *Water Resources Research* **46** (7): n/a. https://doi.org/10.1029/2009WR008634.

Espinoza, D.N. and Santamarina, J.C. 2012. Clay interaction with liquid and supercritical CO2: The relevance of electrical and capillary forces. *International Journal of Greenhouse Gas Control* **10**: 351-362. https://doi.org/10.1016/j.ijggc.2012.06.020.

Espinoza, D.N. and Santamarina, J.C. 2017. CO2 breakthrough—Caprock sealing efficiency and integrity for carbon geological storage. *International Journal of Greenhouse Gas Control* **66** (C): 218-229. https://doi.org/10.1016/j.ijggc.2017.09.019.

Farajzadeh, R., Eftekhari, A.A., Dafnomilis, G. et al. 2020. On the sustainability of CO2 storage through CO2 – Enhanced oil recovery. *Applied Energy* **261**: 114467. https://doi.org/10.1016/j.apenergy.2019.114467.

Farokhpoor, R., Bjørkvik, B.J.A., Lindeberg, E. et al. 2013. CO2 Wettability Behavior During CO2 Sequestration in Saline Aquifer -An Experimental Study on Minerals Representing Sandstone and Carbonate. *Energy Procedia* **37**: 5339-5351. https://doi.org/10.1016/j.egypro.2013.06.452.

Fatah, A., Bennour, Z., Ben Mahmud, H. et al. 2020. A Review on the Influence of CO2/Shale Interaction on Shale Properties: Implications of CCS in Shales. *Energies* **13** (12): 3200. https://www.mdpi.com/1996-1073/13/12/3200.

Fatah, A., Mahmud, H.B., Bennour, Z. et al. 2021. Effect of supercritical CO2 treatment on physical properties and functional groups of shales. *Fuel* **303**: 121310. https://doi.org/10.1016/j.fuel.2021.121310.

Fleury, M., Berne, P., and Bachaud, P. 2009. Diffusion of dissolved CO2 in caprock. *Energy procedia* **1** (1): 3461-3468. https://doi.org/10.1016/j.egypro.2009.02.137

Fleury, M. and Brosse, E. 2018. Transport in Tight Rocks. In *Geological Carbon Storage*, 31-43. https://doi.org/10.1002/9781119118657.ch2

Fleury, M., Gautier, S., Gland, N. et al. 2013. Advanced and Integrated Petrophysical Characterization for CO2 Storage: Application to the Ketzin Site. *Oil & Gas Science and Technology* **68** (3): 557-576. https://doi.org/10.2516/ogst/2012084.

Fuhua, S., Ke, M., Yanming, Z.H.U. et al. 2023. Pore structure, adsorption capacity and their controlling factors of shale in complex structural area. *Méitàn kēxué jìshù* **51** (2): 269-282.

Gamadi, T.D., Sheng, J.J., and Soliman, M.Y. 2013. An Experimental Study of Cyclic Gas Injection to Improve Shale Oil Recovery. Paper presented at the SPE Annual Technical Conference and Exhibition, New Orleans, Louisiana, USA, 2013/9/30/. SPE. https://doi.org/10.2118/166334-MS.

Gamadi, T.D., Sheng, J.J., Soliman, M.Y. et al. 2014. An Experimental Study of Cyclic CO2 Injection to Improve Shale Oil Recovery. Paper presented at the SPE Improved Oil Recovery Symposium, Tulsa, Oklahoma, USA, 2014/4/12/. SPE. https://doi.org/10.2118/169142-MS.

Gannaway, G. 2014. NMR Investigation of Pore Structure in Gas Shales. Paper presented at the SPE Annual Technical Conference and Exhibition. https://doi.org/10.2118/173474-STU.

Garcia, J.E. 2001. Density of aqueous solutions of CO2. https://escholarship.org/uc/item/6dn022hb.

Gaus, I. 2010. Role and impact of CO2–rock interactions during CO2 storage in sedimentary rocks. *International Journal of Greenhouse Gas Control* **4** (1): 73-89. https://doi.org/10.1016/j.ijggc.2009.09.015.

Gaus, I., Azaroual, M., and Czernichowski-Lauriol, I. 2005. Reactive transport modelling of the impact of CO2 injection on the clayey cap rock at Sleipner (North Sea). *Chemical Geology* **217** (3-4): 319-337. https://doi.org/10.1016/j.chemgeo.2004.12.016.

Georgiadis, A., Llovell, F., Bismarck, A. et al. 2010a. Interfacial tension measurements and modelling of (carbon dioxide + n-alkane) and (carbon dioxide + water) binary mixtures at elevated pressures and temperatures. *The Journal of Supercritical Fluids* **55** (2): 743-754. https://doi.org/10.1016/j.supflu.2010.09.028.

Georgiadis, A., Maitland, G., Trusler, J.P.M. et al. 2010b. Interfacial Tension Measurements of the (H2O + CO2) System at Elevated Pressures and Temperatures. *Journal of Chemical and Engineering Data* **55** (10): 4168-4175. https://doi.org/10.1021/je100198g.

Ghanizadeh, A., Song, C., Hamdi, H. et al. 2021. Experimental and computational evaluation of cyclic solvent injection in fractured tight hydrocarbon reservoirs. *Scientific Reports* **11** (1): 9497. https://doi.org/10.1038/s41598-021-88247-y.

Gholami, R., Raza, A., Andersen, P. et al. 2021. Long-term integrity of shaly seals in CO2 geo-sequestration sites: An experimental study. *International Journal of Greenhouse Gas Control* **109**: 103370. https://www.sciencedirect.com/science/article/pii/S1750583621001225.

Golkari, A., Riazi, M., Cortés, F.B. et al. 2022. Experimental investigation of interfacial tension and oil swelling for asphaltenic crude oil/carbonated water system. *Egyptian Journal of Petroleum* **31** (2): 51-58. https://www.sciencedirect.com/science/article/pii/S1110062122000174.

Golubev, S.V., Bénézeth, P., Schott, J. et al. 2009. Siderite dissolution kinetics in acidic aqueous solutions from 25 to 100 °C and 0 to 50 atm pCO2. *Chemical Geology* **265** (1-2): 13-19. https://doi.org/10.1016/j.chemgeo.2008.12.031.

Good, R.J. and Mittal, K.L. 1993. *Contact angle, wettability and adhesion : festschrift in honor of Professor Robert J. Good / editor, K.L. Mittal*. Utrecht, The Netherlands: Utrecht, The Netherlands : VSP.

Goodman, A., Hakala, A., Bromhal, G. et al. 2011. U.S. DOE methodology for the development of geologic storage potential for carbon dioxide at the national and regional scale. *International Journal of Greenhouse Gas Control* **5** (4): 952-965. https://www.sciencedirect.com/science/article/pii/S1750583611000405.

Goodman, A., Sanguinito, S., Tkach, M. et al. 2019. Investigating the role of water on CO2-Utica Shale interactions for carbon storage and shale gas extraction activities – Evidence for pore scale alterations. *Fuel* **242** (C): 744-755. https://doi.org/10.1016/j.fuel.2019.01.091.

Guiltinan, E.J., Cardenas, M.B., Bennett, P.C. et al. 2017. The effect of organic matter and thermal maturity on the wettability of supercritical CO 2 on organic shales. *International Journal of Greenhouse Gas Control* **65** (C). https://doi.org/10.1016/j.ijggc.2017.08.006.

Gunter, W.D., Wiwehar, B., and Perkins, E.H. 1997. Aquifer disposal of CO2-rich greenhouse gases: Extension of the time scale of experiment for CO2-sequestering reactions by geochemical modelling. *Mineralogy and Petrology* **59** (1-2): 121-140. https://doi.org/10.1007/BF01163065.

Hansen, F.K. and Rødsrud, G. 1991. Surface tension by pendant drop: I. A fast standard instrument using computer image analysis. *Journal of Colloid and Interface Science* **141** (1): 1-9. https://doi.org/10.1016/0021-9797(91)90296-K.

Hashemi, L., Glerum, W., Farajzadeh, R. et al. 2021. Contact angle measurement for hydrogen/brine/sandstone system using captive-bubble method relevant for underground

hydrogen storage. *Advances in Water Resources* **154**: 103964. https://doi.org/10.1016/j.advwatres.2021.103964.

Hawthorne, S.B., Miller, D.J., Jin, L. et al. 2016. Rapid and Simple Capillary-Rise/Vanishing Interfacial Tension Method To Determine Crude Oil Minimum Miscibility Pressure: Pure and Mixed CO2, Methane, and Ethane. *Energy & Fuels* **30** (8): 6365-6372. https://doi.org/10.1021/acs.energyfuels.6b01151.

He, J., Wang, J., Yu, Q. et al. 2022. Stress-Dependent Permeability of Naturally Micro-Fractured Shale. *Geosciences* **12** (4): 150. https://www.mdpi.com/2076-3263/12/4/150.

Hebach, A., Oberhof, A., Dahmen, N. et al. 2002. Interfacial Tension at Elevated Pressures Measurements and Correlations in the Water + Carbon Dioxide System. *Journal of Chemical and Engineering Data* **47** (6): 1540-1546. https://doi.org/10.1021/je025569p.

Hemmati-Sarapardeh, A., Ayatollahi, S., Ghazanfari, M.-H. et al. 2014. Experimental Determination of Interfacial Tension and Miscibility of the CO2–Crude Oil System; Temperature, Pressure, and Composition Effects. *Journal of Chemical & Engineering Data* **59** (1): 61-69. https://doi.org/10.1021/je400811h.

Henkel, S., Pudlo, D., Werner, L. et al. 2014. Mineral Reactions in the Geological Underground Induced by H2 and CO2 Injections. *Energy Procedia* **63**: 8026-8035. https://doi.org/10.1016/j.egypro.2014.11.839.

Hildenbrand, A. and Krooss, B.M. 2003. CO2 migration processes in argillaceous rocks: pressure-driven volume flow and diffusion. *Journal of Geochemical Exploration* **78-79**: 169-172. https://doi.org/10.1016/S0375-6742(03)00077-3.

Hirai, S., Okazaki, K., Yazawa, H. et al. 1997. Measurement of CO2 diffusion coefficient and application of LIF in pressurized water. *Energy* **22** (2-3): 363-367. https://doi.org/10.1016/S0360-5442(96)00135-1.

Ho, T.A. and Ilgen, A. 2017. Density Fluctuation in Aqueous Solutions and Molecular Origin of Salting-Out Effect for CO2. *The Journal of Physical Chemistry B* **121** (51): 11485-11491. https://doi.org/10.1021/acs.jpcb.7b09215.

Hoffman, B.T. and Kovscek, A.R. 2004. Efficiency and Oil Recovery Mechanisms of Steam Injection into Low Permeability, Hydraulically Fractured Reservoirs. *Petroleum Science and Technology* **22** (5-6): 537-564. https://doi.org/10.1081/LFT-120034187.

Hoffman, B.T. and Reichhardt, D. 2020. Recovery Mechanisms for Cyclic (Huff-n-Puff) Gas Injection in Unconventional Reservoirs: A Quantitative Evaluation Using Numerical Simulation. *Energies* **13** (18): 4944. https://www.mdpi.com/1996-1073/13/18/4944.

Hyde, A.M., Zultanski, S.L., Waldman, J.H. et al. 2017. General Principles and Strategies for Salting-Out Informed by the Hofmeister Series. *Organic Process Research & Development* **21** (9): 1355-1370. https://doi.org/10.1021/acs.oprd.7b00197.

IEA. 2023. Section 45Q Credit for Carbon Oxide Sequestration. *International Energy Agency*, https://www.iea.org/policies/4986-section-45q-credit-for-carbon-oxide-sequestration (accessed October 6 2023).

Iglauer, S., Al-Yaseri, A.Z., Rezaee, R. et al. 2015a. CO2 wettability of caprocks: Implications for structural storage capacity and containment security. *Geophysical Research Letters* **42** (21): 9279-9284. https://doi.org/10.1002/2015GL065787.

Iglauer, S., Pentland, C.H., and Busch, A. 2015b. CO2 wettability of seal and reservoir rocks and the implications for carbon geo-sequestration. *Water Resources Research* **51** (1): 729-774. https://doi.org/10.1002/2014WR015553.

Iglauer, S., Salamah, A., Sarmadivaleh, M. et al. 2014. Contamination of silica surfaces: Impact on water–CO2–quartz and glass contact angle measurements. *International Journal of Greenhouse Gas Control* **22**: 325-328. https://www.sciencedirect.com/science/article/pii/S1750583614000073.

Jacobs, T. 71. Reservoir-on-a-Chip Technology Opens a New Window Into Oilfield Chemistry, 01/01, https://jpt.spe.org/reservoir-chip-technology-opens-new-window-oilfield-chemistry#:~:text=To%20simulate%20reservoir%2Dlike%20conditions,get%20oil%20flowing%2C%20or%20not.71).

Jaeger, P.T., Alotaibi, M.B., and Nasr-El-Din, H.A. 2010. Influence of Compressed Carbon Dioxide on the Capillarity of the Gas−Crude Oil−Reservoir Water System. *Journal of Chemical and Engineering Data* **55** (11): 5246-5251. https://doi.org/10.1021/je100825b.

Jamialahmadi, M., Emadi, M., and Müller-Steinhagen, H. 2006. Diffusion coefficients of methane in liquid hydrocarbons at high pressure and temperature. *Journal of Petroleum Science and Engineering* **53** (1): 47-60. http://www.sciencedirect.com/science/article/pii/S0920410506000246.

Jiang, X. 2011. A review of physical modelling and numerical simulation of long-term geological storage of CO2. *Applied Energy* **88** (11): 3557-3566. https://www.sciencedirect.com/science/article/pii/S0306261911002959.

Jin, L., Hawthorne, S., Sorensen, J. et al. 2017a. Utilization of Produced Gas for Improved Oil Recovery and Reduced Emissions from the Bakken Formation. Paper presented at the SPE Health, Safety, Security, Environment, & Social Responsibility Conference - North America. https://doi.org/10.2118/184414-MS.

Jin, L., Hawthorne, S., Sorensen, J. et al. 2017b. Utilization of Produced Gas for Improved Oil Recovery and Reduced Emissions from the Bakken Formation. Paper presented at the SPE Health, Safety, Security, Environment, & Social Responsibility Conference - North America, New Orleans, Louisiana, USA, 2017/4/18/. SPE. https://doi.org/10.2118/184414-MS.

Jin, L., Hawthorne, S., Sorensen, J. et al. 2017c. Extraction of Oil From the Bakken Shales With Supercritical CO2. Paper presented at the SPE/AAPG/SEG Unconventional Resources Technology Conference, Austin, Texas, USA, 2017/7/24/. URTEC. https://doi.org/10.15530/URTEC-2017-2671596.

Jin, L., Sorensen, J.A., Hawthorne, S.B. et al. 2017d. Improving Oil Recovery by Use of Carbon Dioxide in the Bakken Unconventional System: A Laboratory Investigation. *SPE-168971-PA* **20** (3): 602-612. https://doi.org/10.2118/178948-PA.

JPT. Shale EOR Works, But Will It Make a Difference?, https://pubs.spe.org/en/jpt/jpt-article-detail/?art=3391 (accessed 09/13/2020).

Jung, J.-W. and Jiamin, W.A.N. 2012. Supercritical CO2 and Ionic Strength Effects on Wettability of Silica Surfaces: Equilibrium Contact Angle Measurements. *Energy & Fuels* **26** (SEPOCT): 6053-6059. https://doi.org/10.1021/ef300913t.

Jung, N.-H., Han, W.S., Watson, Z.T. et al. 2014. Fault-controlled CO2 leakage from natural reservoirs in the Colorado Plateau, East-Central Utah. *Earth and Planetary Science Letters* **403**: 358-367. https://www.sciencedirect.com/science/article/pii/S0012821X14004622.

Kaszuba, J., Yardley, B., and Andreani, M. 2013. Experimental perspectives of mineral dissolution and precipitation due to carbon dioxide-water-rock interactions. *Reviews in Mineralogy and Geochemistry* **77** (1): 153-188. https://doi.org/10.2138/rmg.2013.77.5.

Kaveh, N.S., Rudolph, E.S.J., van Hemert, P. et al. 2014. Wettability Evaluation of a CO2/Water/Bentheimer Sandstone System: Contact Angle, Dissolution, and Bubble Size. *Energy & Fuels* **28** (6): 4002-4020. https://doi.org/10.1021/ef500034j.

Kazemzadeh, Y., Parsaei, R., and Riazi, M. 2015. Experimental study of asphaltene precipitation prediction during gas injection to oil reservoirs by interfacial tension measurement. *Colloids and Surfaces A: Physicochemical and Engineering Aspects* **466**: 138-146. https://doi.org/10.1016/j.colsurfa.2014.10.053.

Kim, K., Kundzicz, P.M., and Makhnenko, R.Y. 2023. Effect of CO2 Injection on the Multiphase Flow Properties of Reservoir Rock. *Transport in Porous Media* **147** (2): 429-461. https://doi.org/10.1007/s11242-023-01916-6.

Kim, K. and Makhnenko, R.Y. 2022. Short- and Long-Term Responses of Reservoir Rock Induced by CO2 Injection. *Rock Mechanics and Rock Engineering* **55** (11): 6605-6625. https://doi.org/10.1007/s00603-022-03032-1.

Kim, Y., Wan, J., Kneafsey, T.J. et al. 2012. Dewetting of Silica Surfaces upon Reactions with Supercritical CO2 and Brine: Pore-Scale Studies in Micromodels. *Environmental Science & Technology* **46** (7): 4228-4235. https://doi.org/10.1021/es204096w.

King, M.B., Mubarak, A., Kim, J.D. et al. 1992. The mutual solubilities of water with supercritical and liquid carbon dioxides. *The Journal of Supercritical Fluids* **5** (4): 296-302. https://doi.org/10.1016/0896-8446(92)90021-B.

Kivi, I.R., Makhnenko, R.Y., and Vilarrasa, V. 2022. Two-Phase Flow Mechanisms Controlling CO2 Intrusion into Shaly Caprock. *Transport in Porous Media* **141** (3): 771-798. https://doi.org/10.1007/s11242-022-01748-w.

Kivi, I.R., Vilarrasa, V., and Makhnenko, R. 2021. Effect of Caprock Relative Permeability on Co2 Flow through it. *SINTEF Proceedings*. https://hdl.handle.net/11250/2785918.

Klokov, A., Meckel, T.A., and Treviño, R.H. 2018. Confining system integrity assessment by detection of natural gas migration using seismic diffractions. *International Journal of Greenhouse Gas Control* **75** (C): 32-40. https://doi.org/10.1016/j.ijggc.2018.05.001.

Kolodzie, S., Jr. 1980. Analysis Of Pore Throat Size And Use Of The Waxman-Smits Equation To Determine Ooip In Spindle Field, Colorado. Paper presented at the SPE Annual Technical Conference and Exhibition, Dallas, Texas, 1980/1/1/. SPE. https://doi.org/10.2118/9382-MS.

Kravanja, G., Knez, Ž., and Knez Hrnčič, M. 2018a. The effect of argon contamination on interfacial tension, diffusion coefficients and storage capacity in carbon sequestration processes. *International Journal of Greenhouse Gas Control* **71**: 142-154. https://doi.org/10.1016/j.ijggc.2018.02.016.

Kravanja, G., Škerget, M., Knez, Ž. et al. 2018b. Diffusion coefficients of water and propylene glycol in supercritical CO2 from pendant drop tensiometry. *The Journal of Supercritical Fluids* **133**: 1-8. https://www.sciencedirect.com/science/article/pii/S0896844617304576.

Krieger, I.M., Mulholland, G.W., and Dickey, C.S. 1967. Diffusion coefficients for gases in liquids from the rates of solution of small gas bubbles. *Journal of Physical Chemistry* **71** (4): 1123-1129. https://doi.org/10.1021/j100863a051.

Krooss, B.M., Hildenbrand, A., Alles, S. et al. 2005. - Assessment of the CO2 sealing efficiency of pelitic rocks: Two-phase flow and diffusive transport. In *Greenhouse Gas Control Technologies 7*, ed. E. S. Rubin, D. W. Keith, C. F. Gilboy, M. Wilson, T. Morris, J. Gale and K. Thambimuthu, 2003-2006. Oxford: Elsevier Science Ltd. https://doi.org/10.1016/B978-008044704-9/50259-7

Kumar, R., Ali, S.J., and Mathur, A. 2020. A Rigorous Workflow for Evaluation of Huff and Puff Recovery Efficiency of Immiscible and Miscible Gases in Unconventional Reservoirs by Integrating Core Tests with NMR and GC Analysis. *Proc.*, SPE/AAPG/SEG Unconventional Resources Technology Conference. https://doi.org/10.15530/urtec-2020-3332.

Kvamme, B., Kuznetsova, T., Hebach, A. et al. 2007. Measurements and modelling of interfacial tension for water+carbon dioxide systems at elevated pressures. *Computational Materials Science* **38** (3): 506-513. https://www.sciencedirect.com/science/article/pii/S0927025606000656.

Lake, L., Lotfollahi, M., and Bryant, S. 2019. CO2 Enhanced Oil Recovery Experience and its Messages for CO2 Storage. In, 11-23. https://doi.org/10.1016/B978-0-12-812752-0.00002-2

Lake, L.W. 1989. *Enhanced Oil Recovery*: Prentice Hall.

Lashkarbolooki, M., Riazi, M., and Ayatollahi, S. 2018. Effect of CO2 and crude oil type on the dynamic interfacial tension of crude oil/carbonated water at different operational conditions. *Journal of Petroleum Science and Engineering* **170**: 576-581. https://www.sciencedirect.com/science/article/pii/S0920410518305795.

Leroy, P., Lassin, A., Azaroual, M. et al. 2010. Predicting the surface tension of aqueous 1:1 electrolyte solutions at high salinity. *Geochimica et Cosmochimica Acta* **74** (19): 5427-5442. https://www.sciencedirect.com/science/article/pii/S0016703710003339.

Lesti, M., Tiemeyer, C., and Plank, J. 2013. CO2 stability of Portland cement based well cementing systems for use on carbon capture & storage (CCS) wells. *Cement and Concrete Research* **45**: 45-54. https://doi.org/10.1016/j.cemconres.2012.12.001.

Leung, D.Y.C., Caramanna, G., and Maroto-Valer, M.M. 2014. An overview of current status of carbon dioxide capture and storage technologies. *Renewable & Sustainable Energy Reviews* **39**: 426-443. https://doi.org/10.1016/j.rser.2014.07.093.

Li, C., Pu, H., Zhong, X. et al. 2020a. Interfacial interactions between Bakken crude oil and injected gases at reservoir temperature: A molecular dynamics simulation study. *Fuel* **276**: 118058. https://doi.org/10.1016/j.fuel.2020.118058.

Li, H., Zheng, S., and Yang, D. 2013. Enhanced swelling effect and viscosity reduction of solvent (s)/CO2/heavy-oil systems. *SPE Journal* **18** (04): 695-707. https://doi.org/10.2118/150168-PA.

Li, L., Li, C., and Kang, T. 2019a. Adsorption/Desorption Behavior of CH4 on Shale during the CO2 Huff-and-Puff Process. *Energy & Fuels* **33** (6): 5147-5152. https://doi.org/10.1021/acs.energyfuels.9b00920.

Li, L., Sheng, J.J., Su, Y. et al. 2018. Further Investigation of Effects of Injection Pressure and Imbibition Water on CO2 Huff-n-Puff Performance in Liquid-Rich Shale Reservoirs. *Energy & Fuels* **32** (5): 5789-5798. https://doi.org/10.1021/acs.energyfuels.8b00536.

Li, L., Su, Y., Lv, Y. et al. 2020b. Asphaltene deposition and permeability impairment in shale reservoirs during CO2 huff-n-puff EOR process. *Petroleum Science and Technology* **38** (4): 384-390. https://doi.org/10.1080/10916466.2019.1705855.

Li, L., Su, Y., Sheng, J.J. et al. 2019b. Experimental and Numerical Study on CO2 Sweep Volume during CO2 Huff-n-Puff Enhanced Oil Recovery Process in Shale Oil Reservoirs. *Energy & Fuels* **33** (5): 4017-4032. https://doi.org/10.1021/acs.energyfuels.9b00164.

Li, L., Zhang, Y., and Sheng, J.J. 2017a. Effect of the Injection Pressure on Enhancing Oil Recovery in Shale Cores during the CO2 Huff-n-Puff Process When It Is above and below the Minimum Miscibility Pressure. *Energy & Fuels* **31** (4): 3856-3867. https://doi.org/10.1021/acs.energyfuels.7b00031.

Li, N., Zhang, C.-W., Ma, Q.-L. et al. 2017b. Interfacial Tension Measurement and Calculation of (Carbon Dioxide + n-Alkane) Binary Mixtures. *Journal of Chemical & Engineering Data* **62** (9): 2861-2871. https://doi.org/10.1021/acs.jced.7b00159.

Li, W., Frash, L.P., Welch, N.J. et al. 2021. Stress-dependent fracture permeability measurements and implications for shale gas production. *Fuel* **290**: 119984. https://www.sciencedirect.com/science/article/pii/S001623612032980X.

Li, X., Boek, E., Maitland, G.C. et al. 2012. Interfacial Tension of (Brines + CO2): (0.864 NaCl + 0.136 KCl) at Temperatures between (298 and 448) K, Pressures between (2 and 50) MPa, and Total Molalities of (1 to 5) mol·kg–1. *Journal of Chemical and Engineering Data* **57** (4): 1078-1088. https://doi.org/10.1021/je201062r.

Lifton, V.A. 2016. *10.1039/C6LC00318D*. Microfluidics: an enabling screening technology for enhanced oil recovery (EOR). *Lab on a Chip* **16** (10): 1777-1796. http://dx.doi.org/10.1039/C6LC00318D.

Liu, J., Li, H., Liu, S. et al. 2023. Investigating the Impact of Aqueous Phase on CO2 Huff 'n' Puff in Tight Oil Reservoirs Using Nuclear Magnetic Resonance Technology: Stimulation Measures and Mechanisms. *SPE Journal*: 1-17. https://doi.org/10.2118/217978-PA.

Liu, Y., Li, H.A., and Okuno, R. 2016. Measurements and Modeling of Interfacial Tension for CO2/CH4/Brine Systems under Reservoir Conditions. *Industrial & Engineering Chemistry Research* **55** (48): 12358-12375. https://doi.org/10.1021/acs.iecr.6b02446.

Liu, Y., Mutailipu, M., Jiang, L. et al. 2015. Interfacial tension and contact angle measurements for the evaluation of CO2-brine two-phase flow characteristics in porous media. *Environmental Progress & Sustainable Energy* **34** (6): 1756-1762. https://doi.org/10.1002/ep.12160.

Lu, H., Huang, F., Jiang, P. et al. 2021. Exsolution effects in CO2 huff-n-puff enhanced oil recovery: Water-Oil-CO2 three phase flow visualization and measurements by micro-PIV in micromodel. *International Journal of Greenhouse Gas Control* **111**: 103445. https://doi.org/10.1016/j.ijggc.2021.103445.

Lu, J., Kharaka, Y.K., Thordsen, J.J. et al. 2012. CO_2–rock–brine interactions in Lower Tuscaloosa Formation at Cranfield CO_2 sequestration site, Mississippi, U.S.A. *Chemical Geology* **291** (6): 269-277. https://doi.org/10.1016/j.chemgeo.2011.10.020.

Lu, W., Guo, H., Chou, I.M. et al. 2013. Determination of diffusion coefficients of carbon dioxide in water between 268 and 473 K in a high-pressure capillary optical cell with in situ Raman spectroscopic measurements. *Geochimica et Cosmochimica Acta* **115**: 183-204. https://doi.org/10.1016/j.gca.2013.04.010.

Luo, A., Li, Y., Chen, X. et al. 2022. Review of CO2 sequestration mechanism in saline aquifers. *Natural Gas Industry B* **9** (4): 383-393. https://www.sciencedirect.com/science/article/pii/S2352854022000493.

Lv, P., Liu, Y., Jiang, L. et al. 2016. Experimental determination of wettability and heterogeneity effect on CO2 distribution in porous media. *Greenhouse Gases: Science and Technology* **6** (3): 401-415. https://doi.org/10.1002/ghg.1572.

Lv, P., Liu, Y., Wang, Z. et al. 2017. In Situ Local Contact Angle Measurement in a CO2–Brine–Sand System Using Microfocused X-ray CT. *Langmuir* **33** (14): 3358-3366. https://doi.org/10.1021/acs.langmuir.6b04533.

Mamoudou, S. 2020. *Evaluation of Huff-n-Puff EOR in Various Liquid Rich Shales*. M.S Thesis, University of Oklahoma. https://hdl.handle.net/11244/326661

Mamoudou, S., Perez, F., Tinni, A. et al. 2020. Evaluation of Huff-n-Puff in Shale Using Experiments and Molecular Simulations. *Proc.*, SPE/AAPG/SEG Unconventional Resources Technology Conference. https://doi.org/10.15530/urtec-2020-2923.

Mamoudou, S., Tinni, A., Curtis, M. et al. 2021. Impact of EOR Huff-n-Puff on Rock Microstructure. *Proc.*, SPE/AAPG/SEG Unconventional Resources Technology Conference. https://doi.org/10.15530/urtec-2021-5664.

Mason, E.A. and Kronstadt, B. 1967. Graham's Laws of diffusion and effusion. *Journal of Chemical Education* **44** (12): 740. https://doi.org/10.1021/ed044p740.

Massoudi, R. and King, A.D. 1974. Effect of pressure on the surface tension of water. Adsorption of low molecular weight gases on water at 25.deg. *Journal of Physical Chemistry* **78** (22): 2262-2266. https://doi.org/10.1021/j100615a017.

Medina, B.X., Kohli, A., Kovscek, A.R. et al. 2023. Effects of Supercritical CO2 Injection on the Shale Pore Structures and Mass Transport Rates. *Energy & Fuels* **37** (2): 1151-1168. https://doi.org/10.1021/acs.energyfuels.2c02254.

Miller, Q.R.S., Wang, X., Kaszuba, J.P. et al. 2016. Experimental Study of Porosity Changes in Shale Caprocks Exposed to Carbon Dioxide-Saturated Brine II: Insights from Aqueous Geochemistry. *Environmental Engineering Science* **33** (10): 736-744. https://doi.org/10.1089/ees.2015.0592.

Mills, J., Riazi, M., and Sohrabi, M. 2011. *Wettability of Common Rock-Forming Minerals in a CO2-Brine System at Reservoir Conditions*. https://api.semanticscholar.org/CorpusID:33975412

Min, B., Mamoudou, S., Dang, S., Tinni, A., Sondergeld, C., and Rai, C. Comprehensive Experimental Study of Huff-n-Puff Enhanced Oil Recovey in Eagle Ford: Key Parameters and Recovery Mechanism. Paper presented at the SPE Improved Oil Recovery Conference, Virtual, August 2020. doi: https://doi.org/10.2118/200436-MS

Miocic, J.M., Gilfillan, S.M.V., Frank, N. et al. 2019. 420,000 year assessment of fault leakage rates shows geological carbon storage is secure. *Scientific Reports* **9** (1): 769. https://doi.org/10.1038/s41598-018-36974-0.

Montegrossi, G., Cantucci, B., Piochi, M. et al. 2023. CO2 Reaction-Diffusion Experiments in Shales and Carbonates. *Minerals* **13** (1): 56. https://www.mdpi.com/2075-163X/13/1/56.

Moradi, B., Awang, M., Bashir, A. et al. 2014. Effects of alcohols on interfacial tension between carbon dioxide and crude oil at elevated pressures and temperature. *Journal of Petroleum Science & Engineering* **121**: 103-109. https://doi.org/10.1016/j.petrol.2014.06.017

Mortezaei, K. and Vahedifard, F. 2015. Numerical Simulation of Induced Seismicity in Carbon Capture and Storage Projects. *Geotechnical and Geological Engineering* **33** (2): 411-424. https://doi.org/10.1007/s10706-015-9859-7.

Mouzakis, K.M., Navarre-Sitchler, A.K., Rother, G. et al. 2016. Experimental Study of Porosity Changes in Shale Caprocks Exposed to CO2-Saturated Brines I: Evolution of Mineralogy, Pore Connectivity, Pore Size Distribution, and Surface Area. *Environmental Engineering Science* **33** (10): 725-735. https://doi.org/10.1089/ees.2015.0588.

Mukherjee, S. 2020. *Measurement and analysis of oil-gas diffusion at reservoir conditions: application to huff-n-puff EOR in unconventional reservoirs*. M.S Thesis, University of Oklahoma. https://hdl.handle.net/11244/326601

Mukherjee, S., Dang, S.T., Rai, C. et al. 2020. Revisiting the Concept of Wettability for Organic-Rich Tight Rocks: Application in Formation Damage-Water Blockage. *Petrophysics - The SPWLA Journal of Formation Evaluation and Reservoir Description* **61** (05): 473-481. https://doi.org/10.30632/PJV61N5-2020a5.

Mutailipu, M., Jiang, L., Fu, J. et al. 2018. Effects of Na+, K+, Ca2+, and Mg2+ cations on CO2–brine interfacial tension under offshore storage conditions. *Greenhouse Gases: Science and Technology* **8** (4): 762-780. https://onlinelibrary.wiley.com/doi/abs/10.1002/ghg.1787.

Mutailipu, M., Liu, Y., Jiang, L. et al. 2019. Measurement and estimation of CO2–brine interfacial tension and rock wettability under CO2 sub- and super-critical conditions. *Journal of Colloid and Interface Science* **534** (C): 605-617. https://doi.org/10.1016/j.jcis.2018.09.031.

Narayanan Nair, A.K., Anwari Che Ruslan, M.F., Ramirez Hincapie, M.L. et al. 2022. Bulk and Interfacial Properties of Brine or Alkane in the Presence of Carbon Dioxide, Methane, and Their Mixture. *Industrial & Engineering Chemistry Research* **61** (15): 5016-5029. https://doi.org/10.1021/acs.iecr.2c00249.

NASA. Global Climate Change - Vital Signs on the Planet. *National Aeronautics and Space Administration (NASA)*, https://climate.nasa.gov/vital-signs/carbon-dioxide/#:~:text=Carbon%20dioxide%20in%20the%20atmosphere,in%20less%20than%20200%20years (accessed Retrieved April 6, 2023.

Neeson, M.J., Chan, D.Y.C., and Tabor, R.F. 2014. Compound Pendant Drop Tensiometry for Interfacial Tension Measurement at Zero Bond Number. *Langmuir* **30** (51): 15388-15391. https://doi.org/10.1021/la504406m.

NETL. Carbon Dioxide Enhanced Oil Recovery. *National Energy Technology Laboratory*, https://www.netl.doe.gov/sites/default/files/netl-file/co2_eor_primer.pdf.

NETL. Carbon Storage. *U.S. Department of Energy, National Energy Technology Laboratory*, https://netl.doe.gov/carbon-management/carbon-storage/faqs/carbon-storage-faqs (accessed Retrieved April 6th, 2023.

Newmark, R.L., Friedmann, S.J., and Carroll, S.A. 2010. Water challenges for geologic carbon capture and sequestration (in eng). *Environ Manage* **45** (4): 651-61. https://doi.org/10.1007/s00267-010-9434-1.

Ng, W.Y. and Walkley, J. 1969. Diffusion of gases in liquids: the constant size bubble method. *Canadian Journal of Chemistry* **47** (6): 1075-1077. https://doi.org/10.1139/v69-170.

Nowrouzi, I., Manshad, A.K., and Mohammadi, A.H. 2019. Effects of dissolved carbon dioxide and ions in water on the dynamic interfacial tension of water and oil in the process of carbonated smart water injection into oil reservoirs. *Fuel* **243**: 569-578. https://doi.org/10.1016/j.fuel.2019.01.069.

Odiachi, J., Cruz, F., and Tinni, A. 2021. Experimental Study of Hydrocarbon Vaporization for EOR Applications. *Proc.*, SPE/AAPG/SEG Unconventional Resources Technology Conference. https://doi.org/10.15530/urtec-2021-5674.

Odiachi, J., Cruz, F., and Tinni, A. 2022. Diffusional and Electrical Tortuosity in Unconventional Shale Reservoirs. *Proc.*, SPE Annual Technical Conference and Exhibition. https://doi.org/10.2118/210164-MS.

Oosterkamp, A. and Ramsen, J. 2008. State-of-the-Art Overview of CO 2 Pipeline Transport with Relevance to Offshore Pipelines. https://www.researchgate.net/publication/228688545_State-of-the-Art_Overview_of_CO_2_Pipeline_Transport_with_Relevance_to_Offshore_Pipelines

Pajonpai, N., Bissen, R., Pumjan, S. et al. 2022. Shape design and safety evaluation of salt caverns for CO2 storage in northeast Thailand. *International Journal of Greenhouse Gas Control* **120**: 103773. https://doi.org/10.1016/j.ijggc.2022.103773.

Palandri, J.L. and Kharaka, Y.K. 2004. A Compilation of Rate Parameters of Water-Mineral Interaction Kinetics for Application to Geochemical Modeling. https://doi.org/10.3133/ofr20041068

Pan, B., Li, Y., Wang, H. et al. 2018a. CO2 and CH4 Wettabilities of Organic-Rich Shale. *Energy & Fuels* **32** (2): 1914-1922. https://doi.org/10.1021/acs.energyfuels.7b01147.

Pan, Y., Hui, D., Luo, P. et al. 2018b. Experimental Investigation of the Geochemical Interactions between Supercritical CO2 and Shale: Implications for CO2 Storage in Gas-Bearing Shale Formations. *Energy & Fuels* **32** (2): 1963-1978. https://doi.org/10.1021/acs.energyfuels.7b03074.

Park, J.-Y., Lim, J.S., Yoon, C.H. et al. 2005. Effect of a Fluorinated Sodium Bis(2-ethylhexyl) Sulfosuccinate (Aerosol-OT, AOT) Analogue Surfactant on the Interfacial Tension of CO2 + Water and CO2 + Ni-Plating Solution in Near- and Supercritical CO2. *Journal of Chemical and Engineering Data* **50** (2): 299-308. https://doi.org/10.1021/je0499667.

Park, T., Yoon, S., Jung, J. et al. 2020. Effect of Fluid–Rock Interactions on In Situ Bacterial Alteration of Interfacial Properties and Wettability of CO2–Brine–Mineral Systems for Geologic Carbon Storage. *Environmental Science & Technology* **54** (23): 15355-15365. https://doi.org/10.1021/acs.est.0c05772.

Parkinson, W.J. and De Nevers, N.J. 1969. Partial Molal Volume of Carbon Dioxide in Water Solutions. *Industrial & Engineering Chemistry Fundamentals* **8** (4): 709-713. https://doi.org/10.1021/i160032a017.

Patil, V.V., McPherson, B.J., Priewisch, A. et al. 2017. Factors affecting self-sealing of geological faults due to CO2-leakage. *Greenhouse Gases: Science and Technology* **7** (2): 273-294. https://onlinelibrary.wiley.com/doi/abs/10.1002/ghg.1673.

Pegram, L.M. and Record, M.T. 2007. Hofmeister Salt Effects on Surface Tension Arise from Partitioning of Anions and Cations between Bulk Water and the Air−Water Interface. *The Journal of Physical Chemistry B* **111** (19): 5411-5417. https://doi.org/10.1021/jp070245z.

Pereira, L.M.C., Chapoy, A., Burgass, R. et al. 2016. Study of the impact of high temperatures and pressures on the equilibrium densities and interfacial tension of the carbon dioxide/water system. *The Journal of Chemical Thermodynamics* **93**: 404-415. https://www.sciencedirect.com/science/article/pii/S0021961415001378.

Perera, P.N., Deng, H., Schuck, P.J. et al. 2018. Diffusivity of Carbon Dioxide in Aqueous Solutions under Geologic Carbon Sequestration Conditions. *The Journal of Physical Chemistry B* **122** (16): 4566-4572. https://doi.org/10.1021/acs.jpcb.8b00802.

Perez, F. and Devegowda, D. 2020. A Molecular Dynamics Study of Soaking During Enhanced Oil Recovery in Shale Organic Pores. *SPE Journal* **25** (02): 832-841. https://doi.org/10.2118/199879-PA.

Pfennig, A., Wolf, M., and Kranzmann, A. 2021. Corrosion and Corrosion Fatigue of Steels in Downhole CCS Environment—A Summary. *Processes* **9** (4): 594. https://doi.org/10.3390/pr9040594.

Pokrovsky, O.S., Golubev, S.V., Schott, J. et al. 2009. Calcite, dolomite and magnesite dissolution kinetics in aqueous solutions at acid to circumneutral pH, 25 to 150 [degrees]C and 1 to 55 atm pCO.sub.2: New constraints on CO.sub.2 sequestration in sedimentary basins. *Chemical Geology* **260** (3-4): 317. https://doi.org/10.1016/j.chemgeo.2009.01.013.

Prem, B. and Imran, S. 2018. Interfacial Tension and Contact Angle Data Relevant to Carbon Sequestration. In *Carbon Capture, Utilization and Sequestration*, ed. K. Agarwal Ramesh, Ch. 10. Rijeka: IntechOpen. https://doi.org/10.5772/intechopen.79414

Qian, K., Huang, Y., He, Y. et al. 2022. Experimental Study on the Oil Recovery Performance of CO[sub.2] Huff-and-Puff Process in Fractured Tight Oil Reservoirs. *Geofluids* **2022**. https://doi.org/10.1155/2022/6193082.

Qin, C., Jiang, Y., Luo, Y. et al. 2017. Effect of Supercritical Carbon Dioxide Treatment Time, Pressure, and Temperature on Shale Water Wettability. *Energy & Fuels* **31** (1): 493-503. https://doi.org/10.1021/acs.energyfuels.6b03257.

Qin, C., Jiang, Y., Zhou, J. et al. 2022. Influence of supercritical CO2 exposure on water wettability of shale: Implications for CO2 sequestration and shale gas recovery. *Energy* **242**: 122551. https://doi.org/10.1016/j.energy.2021.122551.

Quayle, O.R. 1953. The Parachors of Organic Compounds. An Interpretation and Catalogue. *Chemical Reviews* **53** (3): 439-589. https://doi.org/10.1021/cr60166a003.

Rahman, T., Lebedev, M., Barifcani, A. et al. 2016. Residual trapping of supercritical CO.sub.2 in oil-wet sandstone. *Journal of Colloid and Interface Science* **469**: 63. https://doi.org/10.1016/j.jcis.2016.02.020.

Ramey, H.J. and Firoozabadi, A. 1988. Surface Tension Of Water-Hydrocarbon Systems At Reservoir Conditions. *Journal of Canadian Petroleum Technology* **27** (3): 41-48. https://doi.org/10.2118/88-03-03.

Rathnaweera, T.D., Ranjith, P.G., and Perera, M.S.A. 2016. Experimental investigation of geochemical and mineralogical effects of CO2 sequestration on flow characteristics of reservoir rock in deep saline aquifers. *Scientific Reports* **6** (1): 19362. https://doi.org/10.1038/srep19362.

Raza, A., Glatz, G., Gholami, R. et al. 2022. Carbon mineralization and geological storage of CO2 in basalt: Mechanisms and technical challenges. *Earth-science Reviews* **229**: 104036. https://doi.org/10.1016/j.earscirev.2022.104036.

Réveillère, A. 2013. Semi-analytical Solution for Brine Leakage Through Passive Abandoned Wells Taking Account of Brine Density Differences. *Transport in Porous Media* **100**: 337-361. https://doi.org/10.1007/s11242-013-0221-3.

Rezaei, F., Rezaei, A., Jafari, S. et al. 2021. On the Evaluation of Interfacial Tension (IFT) of CO₂–Paraffin System for Enhanced Oil Recovery Process: Comparison of Empirical Correlations, Soft Computing Approaches, and Parachor Model (in English). *Energies* **14** (11): 3045. https://doi.org/10.3390/en14113045.

Rezaeyan, A., Tabatabaei-Nejad, S.A., Khodapanah, E. et al. 2015. Parametric analysis of caprock integrity in relation with CO2 geosequestration: capillary breakthrough pressure of caprock and gas effective permeability. *Greenhouse Gases: Science and Technology* **5** (6): 714-731. https://doi.org/10.1002/ghg.1516.

Río, O.I.d. and Neumann, A.W. 1997. Axisymmetric Drop Shape Analysis: Computational Methods for the Measurement of Interfacial Properties from the Shape and Dimensions of Pendant and Sessile Drops. *Journal of Colloid and Interface Science* **196** (2): 136-147. https://doi.org/10.1006/jcis.1997.5214.

Rosenbauer, R.J., Koksalan, T., and Palandri, J.L. 2005. Experimental investigation of CO2-brine-rock interactions at elevated temperature and pressure : Implications for CO2 sequestration in deep-saline aquifers. *Fuel Processing Technology* **86** (14-15): 1581-1597. https://doi.org/10.1016/j.fuproc.2005.01.011.

Roshan, H., Al-Yaseri, A.Z., Sarmadivaleh, M. et al. 2016. On wettability of shale rocks. *Journal of Colloid and Interface Science* **475**: 104-111. https://doi.org/10.1016/j.jcis.2016.04.041.

Rouhibakhsh, K., Darvish, H., Sabzgholami, H. et al. 2018. Application of ANFIS-GA as a novel and accurate tool for estimation of interfacial tension of carbon dioxide and hydrocarbon. *Petroleum Science and Technology* **36** (15): 1143-1149. https://doi.org/10.1080/10916466.2018.1465959.

Salehi, E., Mohammad-Reza, M., Hemmati-Sarapardeh, A. et al. 2022. Modeling Interfacial Tension of N₂/CO₂ Mixture + n-Alkanes with Machine Learning Methods: Application to EOR in Conventional and Unconventional Reservoirs by Flue Gas Injection (in English). *Minerals* **12** (2): 252. https://doi.org/10.3390/min12020252.

Samara, H., Al-Eryani, M., and Jaeger, P. 2022. The role of supercritical carbon dioxide in modifying the phase and interfacial properties of multiphase systems relevant to combined EOR-CCS. *Fuel* **323**: 124271. https://doi.org/10.1016/j.fuel.2022.124271.

Sanguinito, S., Goodman, A., Tkach, M. et al. 2018. Quantifying dry supercritical CO2-induced changes of the Utica Shale. *Fuel* **226** (C): 54-64. https://doi.org/10.1016/j.fuel.2018.03.156.

Santini, M., Guilizzoni, M., and Fest-Santini, S. 2013. X-ray computed microtomography for drop shape analysis and contact angle measurement. *Journal of Colloid and Interface Science* **409**. https://doi.org/10.1016/j.jcis.2013.06.036.

Saraji, S., Goual, L., Piri, M. et al. 2013. Wettability of Supercritical Carbon Dioxide/Water/Quartz Systems: Simultaneous Measurement of Contact Angle and Interfacial Tension at Reservoir Conditions. *Langmuir* **29** (23): 6856-6866. https://doi.org/10.1021/la3050863.

Saraji, S., Piri, M., and Goual, L. 2014. The effects of SO2 contamination, brine salinity, pressure, and temperature on dynamic contact angles and interfacial tension of supercritical CO2/brine/quartz systems. *International Journal of Greenhouse Gas Control* **28**: 147–155. https://doi.org/10.1016/j.ijggc.2014.06.024.

Sell, A., Fadaei, H., Kim, M. et al. 2013. Measurement of CO2 Diffusivity for Carbon Sequestration: A Microfluidic Approach for Reservoir-Specific Analysis. *Environmental Science & Technology* **47** (1): 71-78. https://doi.org/10.1021/es303319q.

Seyyedi, M., Mahmud, H.K.B., Verrall, M. et al. 2020. Pore Structure Changes Occur During CO2 Injection into Carbonate Reservoirs. *Scientific Reports* **10** (1): 3624. https://doi.org/10.1038/s41598-020-60247-4.

Seyyedi, M., Sohrabi, M., and Farzaneh, A. 2015. Investigation of Rock Wettability Alteration by Carbonated Water through Contact Angle Measurements. *Energy & Fuels* **29** (9): 5544-5553. https://doi.org/10.1021/acs.energyfuels.5b01069.

Shabib-Asl, A., Plaksina, T., and Moradi, B. 2020. Evaluation of nanopore confinement during CO2 huff and puff process in liquid-rich shale formations. *Computational Geosciences* **24** (3): 1163-1178. https://doi.org/10.1007/s10596-019-09932-6.

Shah, V., Broseta, D., Mouronval, G. et al. 2008. Water/acid gas interfacial tensions and their impact on acid gas geological storage. *International Journal of Greenhouse Gas Control* **2** (4): 594-604. https://www.sciencedirect.com/science/article/pii/S1750583608000108.

Shang, Q., Xia, S., Cui, G. et al. 2018. Experiment and correlation of the equilibrium interfacial tension for paraffin+CO2 modified with ethanol. *The Journal of Chemical Thermodynamics* **116**: 206-212. https://doi.org/10.1016/j.jct.2017.08.031.

Shen, V.K., Siderius, D.W., Krekelberg, W.P., and Hatch, H.W. Eds., NIST Standard Reference Simulation Website, NIST Standard Reference Database Number 173, National Institute of Standards and Technology, Gaithersburg MD, 20899, http://doi.org/10.18434/T4M88Q (accessed Retrieved on April 9, 2023.

Shen, Z. and Sheng, J.J. 2016. Experimental Study of Asphaltene Aggregation during CO2 and CH4 Injection in Shale Oil Reservoirs. *Proc.*, SPE Improved Oil Recovery Conference. https://doi.org/10.2118/179675-MS.

Shen, Z. and Sheng, J.J. 2017. Investigation of asphaltene deposition mechanisms during CO2 huff-n-puff injection in Eagle Ford shale. *Petroleum Science and Technology* **35** (20): 1960-1966. https://doi.org/10.1080/10916466.2017.1374403.

Shi, Z., Sun, L., Haljasmaa, I. et al. 2019. Impact of Brine/CO2 exposure on the transport and mechanical properties of the Mt Simon sandstone. *Journal of Petroleum Science & Engineering* **177** (C): 295-305. https://doi.org/10.1016/j.petrol.2019.01.112.

Shilov, E., Dorhjie, D.B., Mukhina, E. et al. 2022. Experimental and numerical studies of rich gas Huff-n-Puff injection in tight formation. *Journal of Petroleum Science and Engineering* **208**: 109420. https://www.sciencedirect.com/science/article/pii/S0920410521010664.

Shojai Kaveh, N., Barnhoorn, A., and Wolf, K.H. 2016. Wettability evaluation of silty shale caprocks for CO 2 storage. *International Journal of Greenhouse Gas Control* **49**: 425-435. https://doi.org/10.1016/j.ijggc.2016.04.003.

Sie, C.-y. and Nguyen, Q.P. 2020. Field Gas Huff-n-Puff for Improving Oil Recovery from Eagle Ford Shale Reservoirs. *Proc.*, SPE Improved Oil Recovery Conference. https://doi.org/10.2118/200471-MS.

Sing, K.S.W. 1985. Reporting physisorption data for gas/solid systems with special reference to the determination of surface area and porosity (Recommendations 1984). *Pure and Applied Chemistry* **57** (4): 603-619. https://doi.org/10.1351/pac198557040603.

Smit, B., Reimer, J., Oldenburg, C. et al. 2014. *Introduction to Carbon Capture and Sequestration*.

Smith, L., Billingham, M.A., Lee, C.H. et al. 2011. Establishing and maintaining the integrity of wells used for sequestration of CO2. *Energy Procedia* **4**: 5154-5161. https://doi.org/10.1016/j.egypro.2011.02.492.

Soleymanzadeh, A., Rahmati, A., Yousefi, M. et al. 2021. Theoretical and experimental investigation of effect of salinity and asphaltene on IFT of brine and live oil samples. *Journal of Petroleum Exploration and Production* **11** (2): 769-781. https://doi.org/10.1007/s13202-020-01020-1.

Sondergeld, C., Curtis, M., Dang, S. et al. 2022. Does EOR in unconventionals change the rock? *Fuel* **310**: 122176. https://www.sciencedirect.com/science/article/pii/S0016236121020524.

Sondergeld, C.H., Rai, C.S. 1993. A new exploration tool: Quantitative core characterization. *Pure and Applied Geophysics.* 141, 249–268. https://doi.org/10.1007/BF00998331

Song, C., Clarkson, C.R., Hamdi, H. et al. 2021. Comparison of CO2 and Lean Gas Cyclic Injection ('Huff-n-Puff') in Artificially-Fractured Shale Core Samples. *Proc.*, SPE/AAPG/SEG Unconventional Resources Technology Conference. https://doi.org/10.15530/urtec-2021-5309.

Song, C. and Yang, D. 2013. Performance Evaluation of CO2 Huff-n-Puff Processes in Tight Oil Formations. Paper presented at the SPE Unconventional Resources Conference Canada, Calgary, Alberta, Canada, 2013/11/5/. SPE. https://doi.org/10.2118/167217-MS.

Song, C. and Yang, D. 2017. Experimental and numerical evaluation of CO2 huff-n-puff processes in Bakken formation. *Fuel* **190**: 145-162. https://doi.org/10.1016/j.fuel.2016.11.041.

Song, J.-W. and Fan, L.-W. 2022. Understanding the effects of pressure on the contact angle of water on a silicon surface in nitrogen gas environment: Contrasts between low- and high-temperature regimes. *Journal of Colloid and Interface Science* **607**: 1571-1579. https://doi.org/10.1016/j.jcis.2021.09.021.

Song, J.Y., Jeong, Y.J., and Yun, T.S. 2022. Effects of Anisotropy and CO2 Wettability on CO2 Storage Capacity in Sandstone. *Geofluids* **2022**: 1-11. https://doi.org/10.1155/2022/5900255.

Span, R. and Wagner, W. 2015. A New Equation of State for Carbon Dioxide Covering the Fluid Region from the Triple-Point Temperature to 1100 K at Pressures up to 800 MPa. *Journal of Physical and Chemical Reference Data* **44** (1): 1. https://doi.org/10.1063/1.555991.

Spycher, N., Pruess, K., and Ennis-King, J. 2003. CO2-H2O mixtures in the geological sequestration of CO2. I. Assessment and calculation of mutual solubilities from 12 to

100°C and up to 600 bar. *Geochimica Et Cosmochimica Acta* **67**: 3015-3031. https://doi.org/10.1016/S0016-7037(03)00273-4.

Stavropoulou, E. and Laloui, L. 2022. Evaluating CO2 breakthrough in a shaly caprock material: a multi-scale experimental approach. *Scientific Reports* **12** (1): 10706. https://doi.org/10.1038/s41598-022-14793-8.

Steel, L., Liu, Q., Mackay, E. et al. 2016. CO2 solubility measurements in brine under reservoir conditions: A comparison of experimental and geochemical modeling methods. *Greenhouse Gases: Science and Technology* **6** (2): 197-217. https://doi.org/10.1002/ghg.1590.

Sugden, S. 1921. *10.1039/CT9211901483*. CLXXV.—The determination of surface tension from the rise in capillary tubes. *Journal of the Chemical Society, Transactions* **119** (0): 1483-1492. http://dx.doi.org/10.1039/CT9211901483.

Sun, Q., Bhusal, A., Zhang, N. et al. 2023a. Molecular insight into minimum miscibility pressure estimation of shale oil/CO2 in organic nanopores using CO2 huff-n-puff. *Chemical Engineering Science* **280**: 119024. https://doi.org/10.1016/j.ces.2023.119024.

Sun, Z., Zhou, S., and Li, P. 2023b. Measurement of Gas Diffusion Coefficients in Cores of Fine-Grained Lithologies Considering Stress and Adsorption Effects. *ACS Omega* **8**. https://doi.org/10.1021/acsomega.3c03639.

Sutjiadi-Sia, Y., Jaeger, P., and Eggers, R. 2008. Interfacial phenomena of aqueous systems in dense carbon dioxide. *The Journal of Supercritical Fluids* **46** (3): 272-279. https://doi.org/10.1016/j.supflu.2008.06.001.

Sutton, R. 2009. An Improved Model for Water-Hydrocarbon Surface Tension at Reservoir Conditions. *Proceedings - SPE Annual Technical Conference and Exhibition* **6**. https://doi.org/10.2118/124968-MS.

Szulczewski, M. and Juanes, R. 2009. A simple but rigorous model for calculating CO (sub 2) storage capacity in deep saline aquifers at the basin scale. *Energy Procedia* **1** (1): 3307-3314. https://doi.org/10.1016/j.egypro.2009.02.117.

Teklu, T.W., Alharthy, N., Kazemi, H. et al. 2014. Phase Behavior and Minimum Miscibility Pressure in Nanopores. *SPE-168971-PA* **17** (03): 396-403. https://doi.org/10.2118/168865-PA.

Tewes, F. and Boury, F. 2004. Thermodynamic and Dynamic Interfacial Properties of Binary Carbon Dioxide−Water Systems. *The Journal of Physical Chemistry B* **108** (7): 2405-2412. https://doi.org/10.1021/jp030895c.

Thibeau, S., Bachu, S., Birkholzer, J. et al. 2014. Using Pressure and Volumetric Approaches to Estimate CO2 Storage Capacity in Deep Saline Aquifers. *Energy Procedia* **63**: 5294-5304. https://www.sciencedirect.com/science/article/pii/S1876610214023753.

Thommes, M., Kaneko, K., Neimark, A.V. et al. 2015. Physisorption of gases, with special reference to the evaluation of surface area and pore size distribution (IUPAC Technical Report). **87** (9-10): 1051-1069. https://doi.org/10.1515/pac-2014-1117.

Tian, Y., Chen, Q., Yan, C. et al. 2020. Classification of Adsorption Isotherm Curves for Shale Based on Pore Structure. *Petrophysics - The SPWLA Journal of Formation Evaluation and Reservoir Description* **61** (05): 417-433. https://doi.org/10.30632/PJV61N5-2020a2.

Tinni, A., Odusina, E., Sulucarnain, I. et al. 2015. Nuclear-Magnetic-Resonance Response of Brine, Oil, and Methane in Organic-Rich Shales. *SPE-168971-PA* **18** (03): 400-406. https://doi.org/10.2118/168971-PA.

Tonnet, N., Mouronval, G., Chiquet, P. et al. 2011. Petrophysical assessment of a carbonate-rich caprock for CO2 geological storage purposes. *Energy Procedia* **4**: 5422-5429. https://doi.org/10.1016/j.egypro.2011.02.527.

Tovar, F.D., Barrufet, M.A., and Schechter, D.S. 2021. Enhanced Oil Recovery in the Wolfcamp Shale by Carbon Dioxide or Nitrogen Injection: An Experimental Investigation. *SPE Journal* **26** (01): 515-537. https://doi.org/10.2118/204230-PA.

Tudek, J., Crandall, D., Fuchs, S. et al. 2017. In situ contact angle measurements of liquid CO2, brine, and Mount Simon sandstone core using micro X-ray CT imaging, sessile drop, and Lattice Boltzmann modeling. *Journal of Petroleum Science & Engineering* **155** (C). https://doi.org/10.1016/j.petrol.2017.01.047.

Tutolo, B.M., Luhmann, A.J., Kong, X.-Z. et al. 2015. CO2 sequestration in feldspar-rich sandstone: Coupled evolution of fluid chemistry, mineral reaction rates, and hydrogeochemical properties. *Geochimica et Cosmochimica Acta* **160**: 132-154. https://www.sciencedirect.com/science/article/pii/S0016703715001957.

UN. Climate Change: The Paris Agreement, https://www.un.org/en/climatechange/paris-agreement (accessed Retrieved April 6, 2023.

van der Meer, L.G.H., Hofstee, C., and Orlic, B. 2009. The fluid flow consequences of CO2 migration from 1000 to 600 metres upon passing the critical conditions of CO2. *Energy Procedia* **1** (1): 3213-3220. https://doi.org/10.1016/j.egypro.2009.02.105.

Vaziri Hassas, B. and Miller, J.D. 2019. The effect of carbon dioxide and nitrogen on pyrite surface properties and flotation response. *Minerals Engineering* **144**: 106048. https://www.sciencedirect.com/science/article/pii/S0892687519304595.

Vernik, L. 1994. Hydrocarbon-generation-induced microcracking of source rocks. *Geophysics* **59** (4): 555-563. https://doi.org/10.1190/1.1443616.

Vilarrasa, V. and Rutqvist, J. 2017. Thermal effects on geologic carbon storage. *Earth-science Reviews* **165**: 245-256. https://doi.org/10.1016/j.earscirev.2016.12.011.

Vishal, V. and Bakshi, T. 2023. Confinement effect on CO2 and CH4 permeability in shale. *Energy Geoscience*: 100236. https://www.sciencedirect.com/science/article/pii/S2666759223000823.

Walsh, J.B. 1981. Effect of pore pressure and confining pressure on fracture permeability. *International Journal of Rock Mechanics and Mining Sciences & Geomechanics Abstracts* **18** (5): 429-435. https://doi.org/10.1016/0148-9062(81)90006-1.

Wan, T., Yu, Y., and Sheng, J. 2015. Experimental and numerical study of the EOR potential in liquid-rich shales by cyclic gas injection. *Journal of Unconventional Oil and Gas Resources* **12**: 56-67. https://doi.org/10.1016/j.juogr.2015.08.004.

Wang, H., Alvarado, V., Smith, E.R. et al. 2020. Link Between CO2-Induced Wettability and Pore Architecture Alteration. *Geophysical Research Letters* **47** (18): n/a. https://doi.org/10.1029/2020GL088490.

Wang, M., Wang, L., Zhou, W. et al. 2019. Lean gas Huff and Puff process for Eagle Ford Shale: Methane adsorption and gas trapping effects on EOR. *Fuel* **248**: 143-151. https://doi.org/10.1016/j.fuel.2019.03.084.

Wang, R., Sang, S., Zhu, D. et al. 2017. Pore characteristics and controlling factors of the Lower Cambrian Hetang Formation shale in Northeast Jiangxi, China. *Energy Exploration & Exploitation* **36**: 014459871772381. https://www.jstor.org/stable/90015707.

Wang, S., Edwards, I.M., and Clarens, A.F. 2013. Wettability Phenomena at the CO2–Brine–Mineral Interface: Implications for Geologic Carbon Sequestration. *Environmental Science & Technology* **47** (1): 234-241. https://doi.org/10.1021/es301297z.

Wang, S., Zhou, S., Pan, Z. et al. 2023. Response of pore network fractal dimensions and gas adsorption capacities of shales exposed to supercritical CO2: Implications for CH4 recovery and carbon sequestration. *Energy Reports* **9**: 6461-6485. https://doi.org/10.1016/j.egyr.2023.05.266.

Wei, N., Li, X., Jiao, Z. et al. 2022. A Hierarchical Framework for CO2 Storage Capacity in Deep Saline Aquifer Formations. *Frontiers in Earth Science* **9**. https://doi.org/10.3389/feart.2021.777323.

Weinaug, C.F. and Katz, D.L. 1943. Surface Tensions of Methane-Propane Mixtures. *Industrial and Engineering Chemistry* **35** (2): 239-246. https://doi.org/10.1021/ie50398a028.

Weiss, R.F. 1974. Carbon dioxide in water and seawater: the solubility of a non-ideal gas. *Marine Chemistry* **2** (3): 203-215. https://www.sciencedirect.com/science/article/pii/0304420374900152.

Wigand, M., Carey, J.W., SchÜTt, H. et al. 2008. Geochemical effects of CO2 sequestration in sandstones under simulated in situ conditions of deep saline aquifers. *Applied Geochemistry* **23** (9): 2735-2745. https://doi.org/10.1016/j.apgeochem.2008.06.006.

Wollenweber, J., Alles, S.a., Kronimus, A. et al. 2009. Caprock and overburden processes in geological CO2 storage: An experimental study on sealing efficiency and mineral alterations. *Energy Procedia* **1** (1): 3469-3476. https://doi.org/10.1016/j.egypro.2009.02.138.

Xiao, T., Chen, T., Ma, Z. et al. 2024. A review of risk and uncertainty assessment for geologic carbon storage. *Renewable and Sustainable Energy Reviews* **189**: 113945. https://www.sciencedirect.com/science/article/pii/S1364032123008031.

Xing, W., Song, Y., Zhang, Y. et al. 2013. Research Progress of the Interfacial Tension in Supercritical CO2-water/oil System. *Energy Procedia* **37**: 6928-6935. https://doi.org/10.1016/j.egypro.2013.06.625.

Yang, C. and Gu, Y. 2006. Accelerated Mass Transfer of CO2 in Reservoir Brine Due to Density-Driven Natural Convection at High Pressures and Elevated Temperatures. *Industrial & Engineering Chemistry Research* **45** (8): 2430-2436. https://doi.org/10.1021/ie050497r.

Yang, D. and Gu, Y. 2008. Determination of Diffusion Coefficients and Interface Mass-Transfer Coefficients of the Crude Oil−CO2 System by Analysis of the Dynamic and Equilibrium Interfacial Tensions. *Industrial & Engineering Chemistry Research* **47** (15): 5447-5455. https://doi.org/10.1021/ie800053d.

Yang, D., Gu, Y., and Tontiwachwuthikul, P. 2008. Wettability Determination of the Reservoir Brine−Reservoir Rock System with Dissolution of CO2 at High Pressures and Elevated Temperatures. *Energy & Fuels* **22** (1): 504-509. https://doi.org/10.1021/ef700383x.

Yang, D., Tontiwachwuthikul, P., and Gu, Y. 2005. Interfacial Tensions of the Crude Oil + Reservoir Brine + CO2 Systems at Pressures up to 31 MPa and Temperatures of 27 °C and

58 °C. *Journal of Chemical and Engineering Data* **50** (4): 1242-1249. https://doi.org/10.1021/je0500227.

Yang, Y., Che Ruslan, M.F.A., Narayanan Nair, A.K. et al. 2019. Effect of Ion Valency on the Properties of the Carbon Dioxide–Methane–Brine System. *The Journal of Physical Chemistry B* **123** (12): 2719-2727. https://doi.org/10.1021/acs.jpcb.8b12033.

Yang, Y., Zhu, W., Ji, Y. et al. 2022. Interfacial Properties of H₂O+CO₂+Oil Three-Phase Systems: A Density Gradient Theory Study (in English). *Atmosphere* **13** (4): 625. https://doi.org/10.3390/atmos13040625.

Yang, Z., Liu, X., Hua, Z. et al. 2015. Interfacial tension of CO2 and crude oils under high pressure and temperature. *Colloids and Surfaces A: Physicochemical and Engineering Aspects* **482**: 611-616. https://doi.org/10.1016/j.colsurfa.2015.05.058.

Yao, C., Zhao, J., Ji, Z. et al. 2023. Effect of CO2 Huff-n-Puff Mode with a Horizontal Well on Shale Oil Recovery: A Three-Dimensional Experimental Study. *Energy & fuels* **37** (13): 9318-9328. https://doi.org/10.1021/acs.energyfuels.3c01179

Yekeen, N., Padmanabhan, E., Abdulelah, H. et al. 2021. CO.sub.2/brine interfacial tension and rock wettability at reservoir conditions: A critical review of previous studies and case study of black shale from Malaysian formation. *Journal of Petroleum Science & Engineering* **196**. https://doi.org/10.1016/j.petrol.2020.107673.

Yekeen, N., Padmanabhan, E., Sevoo, T.A.L. et al. 2020. Wettability of rock/CO2/brine systems: A critical review of influencing parameters and recent advances. *Journal of Industrial and Engineering Chemistry* **88**: 1-28. https://doi.org/10.1016/j.jiec.2020.03.021.

Yellig, W.F. and Metcalfe, R.S. 1980. Determination and Prediction of CO2 Minimum Miscibility Pressures (includes associated paper 8876). *SPE-949039-G* **32** (1): 160-168. https://doi.org/10.2118/7477-PA.

Yeow, Y.L., Pepperell, C.J., Sabturani, F.M. et al. 2008. Obtaining surface tension from pendant drop volume and radius of curvature at the apex. *Colloids and Surfaces A: Physicochemical and Engineering Aspects* **315** (1): 136-146. https://doi.org/10.1016/j.colsurfa.2007.07.025.

Yu, Y., Li, L., and Sheng, J.J. 2017. A comparative experimental study of gas injection in shale plugs by flooding and huff-n-puff processes. *Journal of Natural Gas Science and Engineering* **38**: 195-202. http://www.sciencedirect.com/science/article/pii/S1875510016309404.

Zarghami, S., Boukadi, F., and Al-Wahaibi, Y. 2017. Diffusion of carbon dioxide in formation water as a result of CO2 enhanced oil recovery and CO2 sequestration. *Journal of Petroleum Exploration and Production Technology* **7** (1): 161-168. https://doi.org/10.1007/s13202-016-0261-7.

Zeng, T., Guo, Y., and Mohanty, K.K. 2021. Use of Hydrocarbon Gas to Replace CO2 for Shale Oil Huff-n-Puff EOR. *Proc.*, SPE/AAPG/SEG Unconventional Resources Technology Conference. https://doi.org/10.15530/urtec-2021-5447.

Zhang, D. and Song, J. 2014. Mechanisms for Geological Carbon Sequestration. *Procedia IUTAM* **10**: 319-327. https://doi.org/10.1016/j.piutam.2014.01.027.

Zhang, K. and Gu, Y. 2015. Two different technical criteria for determining the minimum miscibility pressures (MMPs) from the slim-tube and coreflood tests. *Fuel* **161**: 146-156. https://doi.org/10.1016/j.fuel.2015.08.039.

Zhang, K., Jia, N., and Liu, L. 2019a. CO2 storage in fractured nanopores underground: Phase behaviour study. *Applied Energy* **238**: 911-928. https://doi.org/10.1016/j.apenergy.2019.01.088.

Zhang, K., Jia, N., Zeng, F. et al. 2019b. A review of experimental methods for determining the Oil–Gas minimum miscibility pressures. *Journal of Petroleum Science & Engineering* **183**: 106366. https://doi.org/10.1016/j.petrol.2019.106366.

Zhang, K., Jia, N., Zeng, F. et al. 2017. A New Diminishing Interface Method for Determining the Minimum Miscibility Pressures of Light Oil–CO2 Systems in Bulk Phase and Nanopores. *Energy & Fuels* **31** (11): 12021-12034. https://doi.org/10.1021/acs.energyfuels.7b02439.

Zhang, K., Tian, L., and Liu, L. 2018. A new analysis of pressure dependence of the equilibrium interfacial tensions of different light crude oil–CO^sub 2^ systems. *International Journal of Heat and Mass Transfer* **121**: 503. https://doi.org/10.1016/j.ijheatmasstransfer.2018.01.014.

Zhao, H., Dilmore, R., Allen, D.E. et al. 2015a. Measurement and Modeling of CO2 Solubility in Natural and Synthetic Formation Brines for CO2 Sequestration. *Environmental Science & Technology* **49** (3): 1972-1980. https://doi.org/10.1021/es505550a.

Zhao, H., Dilmore, R.M., and Lvov, S.N. 2015b. Experimental studies and modeling of CO2 solubility in high temperature aqueous CaCl2, MgCl2, Na2SO4, and KCl solutions. *AIChE Journal* **61** (7): 2286-2297. https://doi.org/10.1002/aic.14825.

Zhao, H., Fedkin, M.V., Dilmore, R.M. et al. 2015c. Carbon dioxide solubility in aqueous solutions of sodium chloride at geological conditions experimental results at 323.15, 373.15, and 423.15 K and 150 bar and modeling up to 573.15 K and 2000 bar. *Geochimica et Cosmochimica Acta* **149** (C): 165-189. https://doi.org/10.1016/j.gca.2014.11.004.

Zhao, X., Chen, Z., Zhou, B. et al. 2023. Multiple Flow Mechanism-Based Numerical Model for CO2 Huff-n-Puff in Shale Gas Reservoirs with Complex Fractures. *Energy & Fuels* **37** (12): 8374-8385. https://doi.org/10.1021/acs.energyfuels.3c00931.

Zhelezny, V.P., Semenyuk, Y.V., Ancherbak, S.N. et al. 2009. The temperature dependence of parachor. *Russian Journal of Physical Chemistry A* **83** (2): 182-186. https://doi.org/10.1134/S0036024409020071.

Zhu, C.-F., Guo, W., Wang, Y.-P. et al. 2021. Experimental study of enhanced oil recovery by CO2 huff-n-puff in shales and tight sandstones with fractures. *Petroleum Science* **18** (3): 852-869. https://doi.org/10.1007/s12182-020-00538-7.

Zhu, Z., Fang, C., Qiao, R. et al. 2020. Experimental and Molecular Insights on Mitigation of Hydrocarbon Sieving in Niobrara Shale by CO2 Huff ‘n’ Puff. *SPE Journal* **25** (4): 1803-1811. https://doi.org/10.2118/196136-PA.

Appendix A

Results of the petrophysical characterization after HnP-EOR tests using produced and enriched field gases on the two Eagle Ford samples is discussed in this section. **Figure 63** shows the MICP pore throat size distributions (PTSD) of the two Eagle Ford samples after the tests. Similarly, the PSD obtained with N_2 adsorption are shown in **Figure 64**. It is clear that fluid removal after HnP yields an increase in pore volume in the nanopore range. The N_2 adsorption PSD appears to reflect better the effect of pressure on the increase in nanopore volume due to fluid removal. **Figure 65** depicts the scanning electron microscopy (SEM) images of a high recovery sample (EF2, produced field gas, 4850 psi or 1000 psi above the MMP) taken at the same location before (**Figure 65(a)**) and after (**Figure 65(b)**) HnP-EOR. Regions of organic matter showed a reduction in porosity associated with potential film coating the sample and clogging the organic pores after HnP-EOR. In **Figure 65(c)**, a plan view image of a region rich in organics was obtained. Further cross-section images (**Figure 65(d)** and **(e)**) using FIB-SEM suggests that the pore blockage occurs mainly at the surface and the porosity remains unaltered with depth. Insights from molecular dynamics (Perez and Devegowda 2020) indicate that fraction of heavy hydrocarbons remains adhered to the surface due to their lower energy and could be deposited as a film as observed in the SEM images.

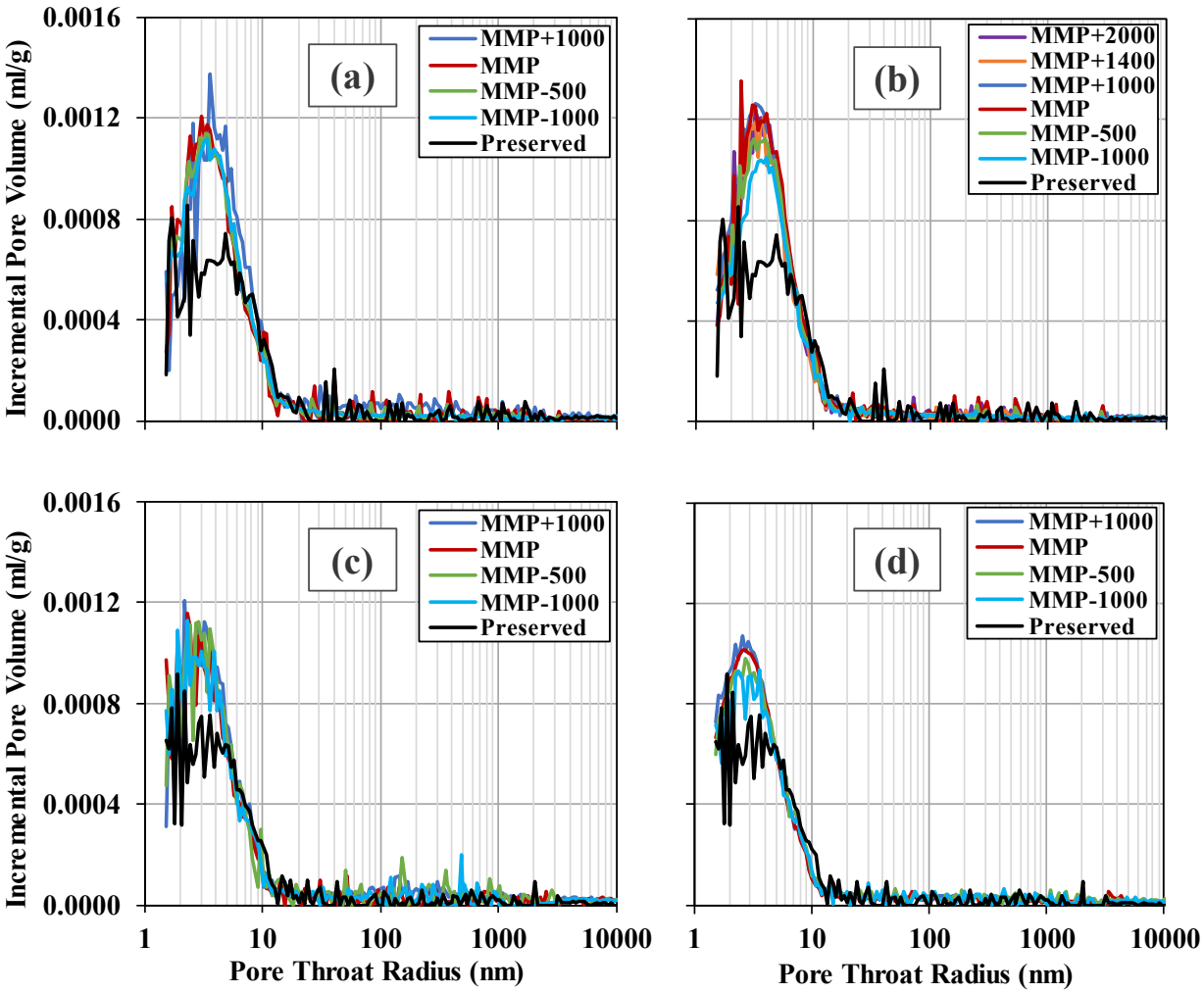

Figure 63. Mercury injection capillary pressure (MICP) pore throat size distribution (PTSD) of the crushed (7-8 mm) Eagle Ford samples (EF1 and EF2) obtained before and after each HnP-EOR test using produced and enriched field gases and varying injection pressures. (a) EF1 using produced field gas. (b) EF1 using enriched field gas. (c) EF2 using produced field gas. (d) EF2 using enriched field gas. All PTSD show an increase in amplitude at the main nanopore range associated with fluid removal. No clear correlation between the amplitude increase and injection pressures was observed.

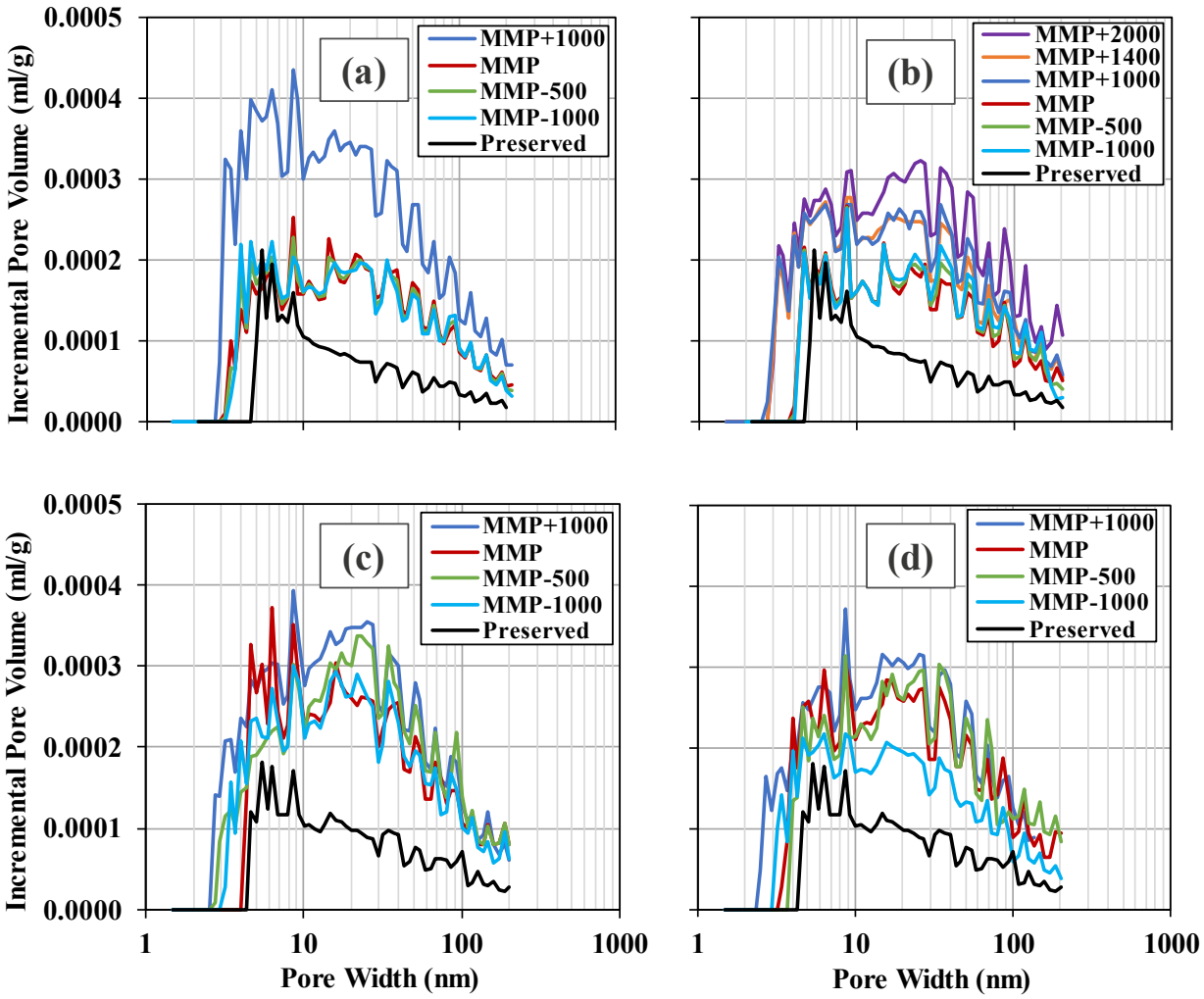

Figure 64. Isothermal nitrogen adsorption pore size distribution (PSD) of the crushed (7-8 mm) Eagle Ford samples (EF1 and EF2) obtained before and after each HnP-EOR test using produced and enriched field gases and varying injection pressures. (a) EF1 using produced field gas. (b) EF1 using enriched field gas. (c) EF2 using produced field gas. (d) EF2 using enriched field gas. An increase in the mesopore (2-50nm) and macropore (>50nm) volume is observed after HnP associated with fluid removal. The increase appears to be amplified with increasing pressure.

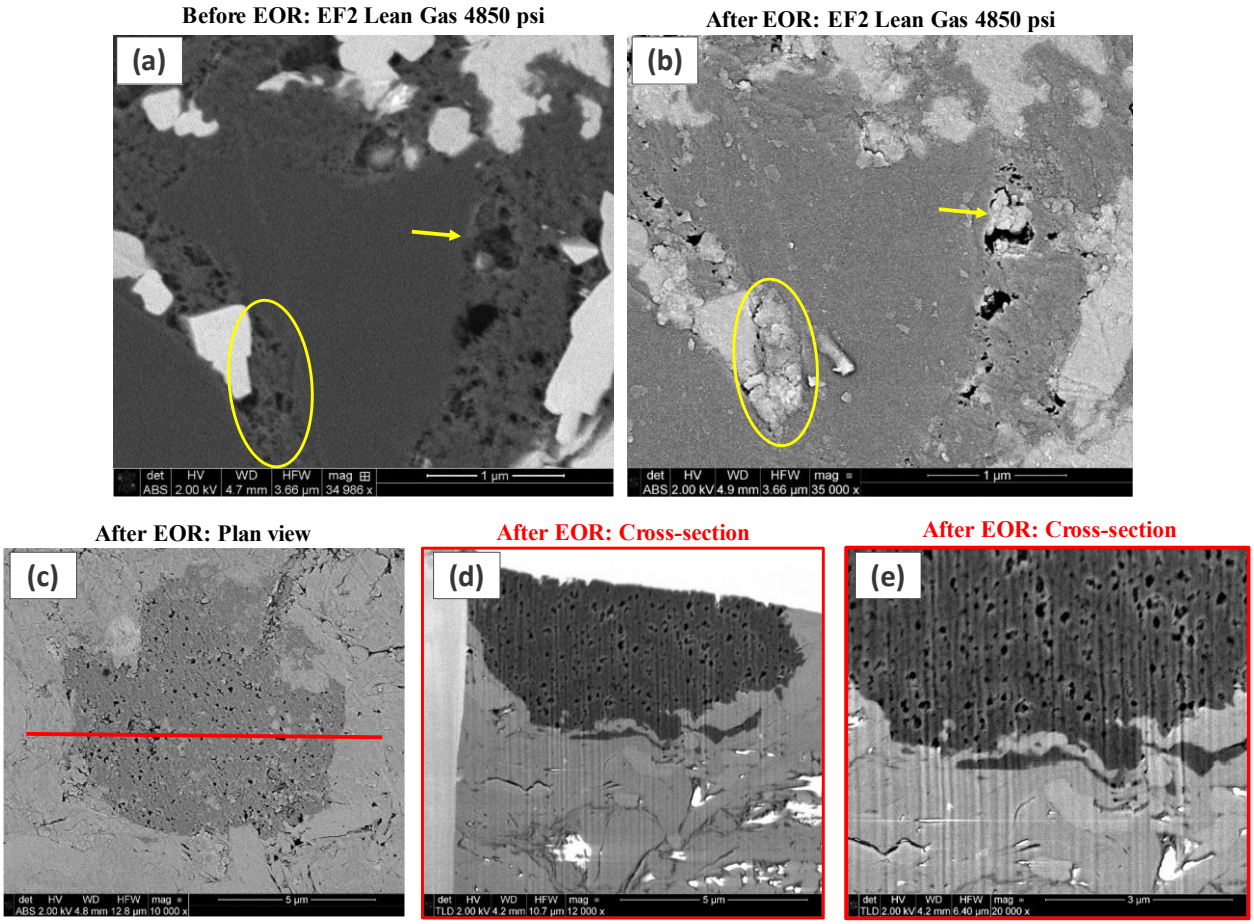

Figure 65. SEM images of a high-recovery sample (EF2, produced field gas, 4850 psi). (a) before EOR. (b) after EOR, displaying reduced porosity and potential surface coating clogging the organic pores. (c) plan view of an organic-rich area. (d) and (e) cross-section images using FIB-SEM reveal that pore blockage is superficial, with deeper porosity remaining unchanged. Molecular dynamics suggest heavy hydrocarbon fractions adhere to the surface (Perez and Devegowda 2020), possibly forming the observed film in the SEM images.

Appendix B

Detailed FTIR mineralogy of the samples used in the CO_2-geostorage study can be found in **Table 7**. It indicates that the Navajo Sandstone (S1) is quartz-rich, Meramec (S2) is quartz/clay-rich, Uinta (S3) is carbonate-rich, Utica (S4) is clay-rich, Woodford (S5) is quartz-rich, and Eagle Ford (S6) is carbonate-rich.

Table 7. Detailed FTIR mineralogy (wt.%) of the samples used in this study.

Sample	Formation	Quartz	Calcite	Dolomite	Illite	Smectite	Kaolinite	Chlorite	Pyrite	Orthoclas	Oligoclas	Mixed	Albite	Anhydrite	Siderite	Apatite	Others
S1	Navajo	79	0	4	0	0	1	2	0	0	1	11	0	0	2	0	0
S2	Meramec	42	13	1	8	0	0	1	0	4	2	17	7	0	5	0	0
S3	Uinta	7	44	4	6	0	0	6	0	0	1	15	4	2	10	2	0
S4	Utica	7	0	0	55	0	0	6	1	6	5	12	0	1	7	0	0
S5	Woodford	67	0	0	4	0	0	0	0	9	0	12	0	1	4	0	2
S6	Eagle Ford	6	63	0	7	0	0	1	6	0	1	0	6	0	8	2	0

Appendix C

The non-steady state one-dimensional diffusion across a porous medium (thickness $2l$) sealed at the edges, where initial concentration of the diffusing substance is zero, and bounded by two parallel planes ($x = \pm l$) of equal and constant surface concentrations (C_1) is stated as follows (Crank 1979):

$$C = C_1, \qquad x = 0, \qquad x = l\,, \qquad t \geq 0 \tag{C.1}$$

$$C = 0, \qquad -l < x < +l, \qquad t = 0 \tag{C.2}$$

Solution to this problem is obtained in the form of a trigonometrical series:

$$\frac{C}{C_1} = 1 - \frac{4}{\pi}\sum_{n=0}^{\infty}\frac{(-1)^n}{2n+1}exp\{-D_{eff}(2n+1)^2\pi^2 t/4l^2\}\,cos\frac{(2n+1)\pi x}{2l} \tag{C.3}$$

where D_{eff} is the effective diffusion coefficient of the diffusing substance in the porous medium. The total volume of the substance (V_t) which has entered the medium at a time t is obtained by:

$$\frac{V_t}{V_\infty} = 1 - \frac{8}{\pi^2}\sum_{n=0}^{\infty}\frac{1}{(2n+1)^2}exp\{-D_{eff}(2n+1)^2\pi^2 t/4l^2\} \tag{C.4}$$

where V_∞ is the total volume at infinite time or obtained when diffusion ceases. Analogously, the concentration profile of diffusing CO_2 across a brine-saturated confining zone (thickness l), from a reservoir-caprock boundary ($x = 0$) saturated in CO_2 ($C_1 = C_{sat}$), toward an upper layer ($x = l$) having negligible CO_2 concentration ($C_2 = 0$), is obtained by:

$$\frac{C}{C_{sat}} = 1 - \frac{x}{l} - \frac{2}{\pi}\sum_{n=1}^{\infty}\frac{1}{n}exp\{-Dn^2\pi^2 t/l^2\}\,sin\frac{n\pi x}{l} \tag{C.5}$$

The equation for the total volume of CO_2 which has diffused in the confining zone (V_t) at a time t has the same form as in **Equation C.4**, with the exception that the volume at the end of diffusion (V_∞) is substituted by the volume of the confining zone if it was saturated in CO_2 (V_{sat}). By integrating the rate at which CO_2 emerges from a unit area of the outer layer $\left\{-D\left(\frac{\partial C}{\partial x}\right)_{x=l}\right\}$, the total volume of CO_2 which has leaked from the confining zone (Q_t) at a time t is obtained:

$$\frac{Q_t}{lC_{sat}} = \frac{Dt}{l^2} + \frac{2}{\pi^2}\sum_{n=1}^{\infty}\frac{cos\, n\pi}{n^2}\{1 - exp(-Dn^2\pi^2 t/l^2)\} \quad \text{(C.6)}$$

Appendix D

Table 8 shows the results of NMR T_2 H_2O-D_2O diffusion measurements on group 2 samples in both horizontal and vertical orientations during $scCO_2$ treatment. Presented data includes measured effective D_2O diffusion coefficients and tortuosities. Additionally, estimates of effective $scCO_2$ diffusion coefficients under subsurface conditions (150 °F, 3000 psi, and 1 M salinity brine) are provided. In **Figure 66**, concentration-distance profiles illustrating the effective diffusion of $scCO_2$ within the confining zone over time, utilizing **Equation C.5** and the estimated effective $scCO_2$ diffusion coefficients for sample S4 in subsurface conditions as detailed in **Table 8**. The modeling approach considers non-steady 1D diffusion, where the storage reservoir-confining zone boundary is saturated in $scCO_2$, while the outer boundary condition for the confining zone maintains a $scCO_2$ concentration of zero. The figure demonstrates that effective diffusion within horizontal samples (parallel to the bedding) penetrates to greater depths over time compared to vertical samples (perpendicular to the bedding). **Figure 66(a)** and **Figure 66(b)** show the estimation of $scCO_2$ penetration using diffusivities for sample S4 before and after 3 weeks of $scCO_2$ treatment, respectively. Without the effect of short-term geochemical reactivity, after 100 years, $scCO_2$ does not extend beyond approximately 5 meters in either sample. Including short-term geochemical reactivity, after 100 years, the $scCO_2$ penetration increases slightly from 5 meters to 7 meters along the horizontal direction.

Table 8. Summary of the results for the NMR T_2 H_2O-D_2O diffusion measurements on group 2 samples in horizontal and vertical orientation during $scCO_2$ treatment. The measured effective D_2O diffusion

coefficients and tortuosities are reported. The table also includes an estimation of effective $scCO_2$ diffusion coefficients at subsurface conditions of 150 °F, 3000 psi, and 1 M salinity brine.

Sample	Orientation	Treatment time (weeks)	$De_{ff,D2O}$ (10^{-10} x m^2/s)	Tortuosity	$De_{ff,scCO2}$ (10^{-10} x m^2/s)
S4	Horizontal	0	3.6 ± 0.5	6.1 ± 0.8	6.6 ± 0.8
		1	4.3 ± 0.5	5.1 ± 0.6	7.9 ± 1.0
		3	5.7 ± 0.5	3.9 ± 0.6	10.4 ± 1.6
	Vertical	0	1.1 ± 0.1	20.8 ± 2.4	1.9 ± 0.2
		1	1.4 ± 0.2	15.9 ± 1.5	2.5 ± 0.2
		3	2.1 ± 0.2	10.9 ± 1.2	3.7 ± 0.4
S5	Horizontal	0	1.4 ± 0.1	15.7 ± 1.4	2.5 ± 0.2
		1	1.4 ± 0.1	15.9 ± 1.2	2.5 ± 0.2
		3	1.3 ± 0.1	17.4 ± 1.4	2.3 ± 0.2
	Vertical	0	1.3 ± 0.1	17.1 ± 1.7	2.3 ± 0.2
		1	1.4 ± 0.2	15.4 ± 1.6	2.6 ± 0.3
		3	1.4 ± 0.2	15.8 ± 2.3	2.5 ± 0.4
S6	Horizontal	0	4.2 ± 0.5	5.2 ± 0.7	7.6 ± 1.0
		1	2.4 ± 0.4	9.2 ± 1.4	4.4 ± 0.6
		3	3.6 ± 0.6	6.2 ± 1.0	6.5 ± 1.1
	Vertical	0	1.5 ± 0.2	14.8 ± 1.9	2.7 ± 0.3
		1	1.3 ± 0.2	16.6 ± 2.4	2.4 ± 0.3
		3	1.8 ± 0.3	12.3 ± 1.9	3.2 ± 0.5

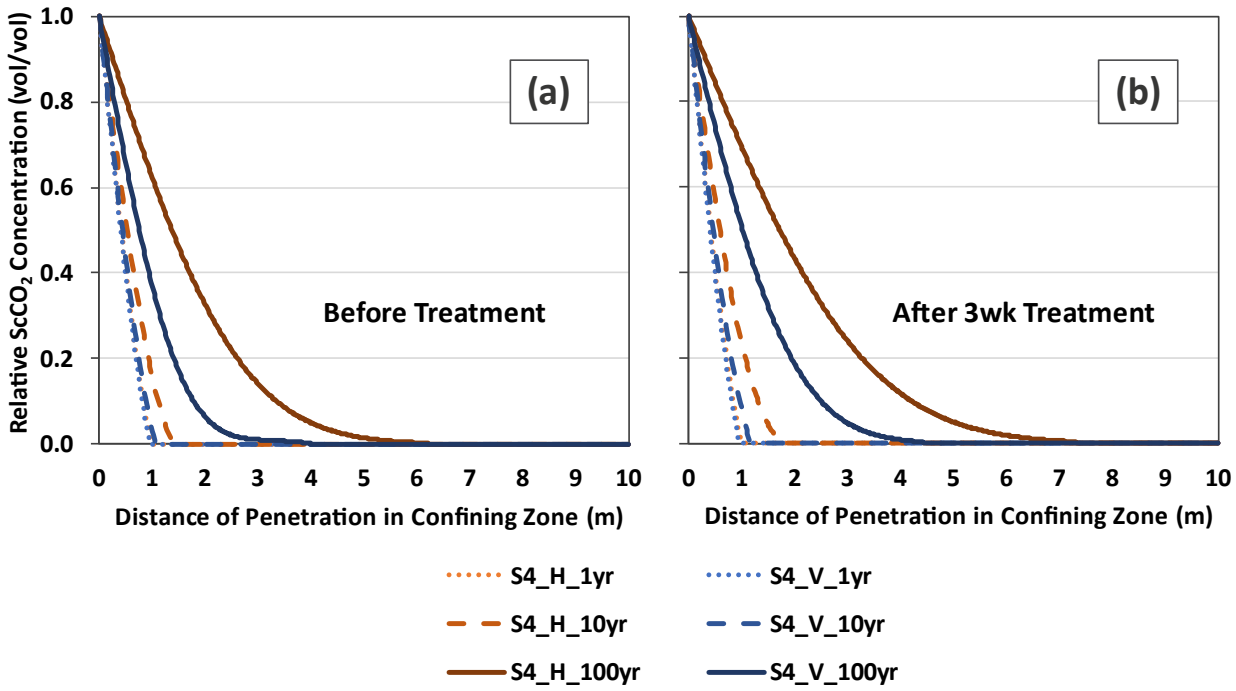

Figure 66. Concentration-distance profiles of the effective diffusion of $scCO_2$ in the confining zone as function of time using **Equation C.5** and the effective $scCO_2$ diffusion coefficient values for sample S4 estimated in subsurface conditions shown in Table 8. Mathematical assumption is a 1D non-steady diffusion where the boundary condition for the storage reservoir – confining zone is saturated in CO_2, while the concentration of CO_2 in the outer boundary condition for the confining zone is zero. The figures show that effective diffusion in horizontal samples (along the bedding) penetrates deeper with increasing time as compared to vertical samples (perpendicular to bedding). (a) Using diffusivities for S4 before $scCO_2$ treatment, after 100 years, $scCO_2$ does not penetrate farther than ~5 m in both samples. (b) Using diffusivities after 3 weeks $scCO_2$ treatment, after 100 years, the maximum penetration depth increases slightly, from 5 m to 7 m. The upscaling of laboratory diffusivity measurements on thin disk samples before and after $scCO_2$ treatment to reservoir scale indicate small impact of short-term geochemical reactivity on the diffusive properties of confining zones.